Organisation and dynamics of a polymeric surfactant at the air-water interface

Sarica, Jordan

Organisation and Dynamics of a Polymeric Surfactant at the Air-Water Interface

September 2003

Jordan Sarica

Graduate Society

University of Durham

A thesis submitted to the University of Durham in partial fulfilment of the regulations for the Degree of Doctor of Philosophy.

Declaration

The work reported in this thesis has been carried out at the Interdisciplinary Research Centre in Polymer Science and Technology, Department of Chemistry, Durham University and at the Rutherford Appleton Laboratory in Oxfordshire between October 2000 and September 2003. This work has not been submitted for any other degree in Durham or elsewhere and, unless stated otherwise, is the original work of the author.

Statement of Copyright

Financial Support

I gratefully acknowledge Durham University for financial support.

Organisation and Dynamics of a Polymeric Surfactant at the Air-Water Interface

Abstract

Polyethylene(oxide) (PEO) is an intriguing polymer, it is water-soluble but exhibits surface-active properties. When capped hydrophobically at one end by a fluorocarbon group, a novel polymeric surfactant is generated. This has been synthesised by combining anionic polymerisation and an end-capping reaction using isophorone diisocyanate.

Three molecular weight polymers were generated, for each of which a hydrogenous and a deuterated version were required. In aqueous solution, these polymeric surfactants formed surface excess layers at the air-water interface and their surface organisation and dynamic behaviour has been investigated.

Surface tension data was obtained using a digital tensiometer and the surface tension isotherm is dependent on both solution concentration and polymer molecular weight. Using neutron reflectometry, the organisation of such adsorbed polymer films at the air-water interface has been obtained over a range of solution concentrations for each polymer molecular weight. Neutron reflectometry data was analysed by both optical matrix and kinematic approximation methods. Both analyses yield the same description, i.e. a two-layer organisation is observed at the air-water interface for all three molecular weight polymers. The PEO layer thickness and the surface organisation are found to be dependent on both solution concentration and molecular weight. The PEO chains are totally immersed in the subphase and strongly anchored at the surface *via* the fluorocarbon end group.

The dynamic behaviour of each PEO adsorbed surface excess at the air-water interface has been studied using surface quasi-elastic light scattering. A resonance between the capillary and dilational waves is observed and the maximum in damping is independent on surface organisation but is molecular weight and solution concentration dependent. The viscoelastic behaviour of the dilational modulus can be described using a simple Maxwell fluid model, from which a relaxation time has been obtained assuming a single relaxational process.

Acknowledgements

I am deeply indebted to a number of people who played a specific role, directly or indirectly, in the production of this thesis.

Firstly, I would like to thank Randal Richards for giving me the opportunity to join his Research group and his continuous support throughout my PhD course. He has been a true inspiration over the past three years.

Many thanks are also due to Lian Hutchings for passing on his anionic polymerisation experience and for running my GPC samples, and to Alan Kenwright for his guidance on NMR. In addition I am grateful to Nigel Clarke for helping me in finalising my thesis.

The SQELS experiments reported here could have not been carried out without the help of James Cook. Likewise the neutron reflectometry work relied on the expertise of the instrument scientists, John Webster and Stephen Holt. Many thanks go to Stuart Leslie for running my SANS samples and his help on dynamic light scattering.

I would like to collectively thank everyone, past and present, who has worked in the Chemistry department. Special thanks must go to Susan Roberts-Bleming who constantly reminds me that any crisis can be solved by having a good gossip around a nice cup of coffee. It has been such a great pleasure to work with you and will miss all the fantastic cakes you brought for our daily chat. Thanks also to my "patriots": Amel Garbi and Stéphanie Cornet.

There are also an endless list of friends that supported me since I moved to England 5 years ago but special thanks to Sandrine Moreau for her unique sense of humour and well for being such a Great Friend, Laurence Paroche for a continuous love and support and Emmanuelle Huot for being so energetic and positive. I will not be where I am today without the help of the kindest and most devoted person I have ever met: Malcolm Stainthorpe you are and always will be my guardian angel. Your support, encouragement and love have been feeding the energy that kept me going. I also want to add at the end of this list someone who has been continuously supporting me in every shape or form since I started my PhD. Darren Sedgeman there is no big enough word to qualify you. You have been so patient and understanding and help me more than you can imagine. You truly are an inspiration.

Finally, I would like to thank my family; papa et maman je vous aime et vous remercie d'être là pour moi, Marina, Mathilde, Catherine et Nathalie, vous êtes et serez toujours un model à suivre. Votre amour, votre support et votre proctection me sont vitals. José tu es ma force et ma joie de vivre et même si un océan nous sépare tu as toujours été là pour me soutenir. Charline, Baptiste, Jules, Camille, Anatole, Justine, Louis et ceux à venir, je suis un tonton comblé et votre amour me donne des ailes. Je vous suis toutes et tous extrêmement reconnaissant.

Contents

I have stolen ideas from every book I have ever read. My principle is researching for a novel is "Read like a butterfly, write like a bee", and if this story contains any honey, it is entirely because of the quality of the nectar I found in the work of better writers.

Philip Pullman

Chapter One

Introduction

1-1 Polymers at Interfaces

Adsorption of polymer molecules at an interface induces a concentration differential at or near the interface influencing both the bulk and interfacial properties of the system. This phenomenon highlights one of the most intriguing properties of polymeric materials when present at surfaces and interfaces and is a subject of much interest[1,2]. An interface is commonly known as a boundary between two portions of matter or space and can be summarised in a formal way in terms of the three states of matter-solid, liquid, and gas as follows:

Gas-Liquid

Gas-Solid

Liquid-Liquid

Liquid-Solid

Solid-Solid

Most of the work reported is for polymers at the air-fluid interface and the majority of studies have used water as the fluid, including the research discussed herein. The air-water interface is often seen as an ideal medium for understanding the behaviour of polymers at an interface as it is a model for more complex systems[3].

Due to the spectacular progress of chemistry throughout the years and more specifically in polymer science and technology, new polymeric materials have emerged on the market with different architectures and properties[4-6]. A new concept has been introduced in the last few years, which is similar to small-molecule surfactant chemistry and is known as polymeric surfactant. The basic idea is to create an amphiphilic polymer in which various parts of the molecule have different affinities for the various parts of the interface. One example is a block copolymer (diblock or triblock) where one of the sequences is strongly adsorbed on the interface and anchors another block that is highly soluble[7,8]. A second way involves small hydrophobic groups grafted on a water soluble polymer either at one or both ends[9,10].

Polyethylene oxide (PEO) is a non-ionic water soluble polymer that is used in a wide range of technical applications[11]. PEO has a surface tension of 31 mN m^{-1} that is much lower than that of water, consequently a surface excess layer is formed in aqueous solutions due to the ability of PEO to adsorb at the air-water interface[12]. Specially modified PEO chains have proven to be some of the most efficient non-

ionic surfactants available[13,14]. Modified PEO with hydrophobic end groups such as residues of alcohols, alkylphenols, esters of fatty acids, mercaptans, alkylamines or alkylamides have been synthesised[14]. However, the highest surface activity at the critical micelle concentration (CMC) at 293 K reported for PEO was obtained by incorporating either a fluorinated[15] or siloxane[16] terminal groups. For example, the surface tension of aqueous solutions was decreased down to 12-15 mN m^{-1} by low molecular weight non-ionic fluorocarbon surfactants[17].

In the mid 20th century there was great interest in tethered polymer layers since it was discovered that the end-grafting of polymer molecules to colloidal particles was an extremely effective way of preventing flocculation[18]. A statement was made: tethered polymer layers can be used to modify the properties of surfaces and interfaces. The subsequent question is: how do the molecules arrange themselves at the interface to modify the surface properties of the solution? It is well known that a polymer chain in a homogeneous solution can adopt a wide range of shapes mainly by rotation about the single bonds in the backbone of the molecule. Compared to an unrestricted chain in solution, adsorbed chains do not enjoy the same magnitude of freedom due to the restriction of the interface; half of the space is inaccessible. The adsorption of polymer at an interface is described as an assembly of tails, loops, and trains, as reported in 1951 by the loop-train-tail model of Jenkel and Rumbach[19]. When the polymer is tethered to an interface, the hydrophobic group is strongly adsorbed on the interface and anchors the remaining part of the molecule that is highly soluble. The remaining section of the polymer that is not attached to the surface forms a tail that is free to move. The principle architecture adopted by a polymer constrained to a plane was described by de Gennes and is called a polymer brush[20]. Polymer brushes[21] are formed when one end of the polymer molecule is constrained to lie in a plane such that the distance between the tethered ends is less than the Flory radius of gyration, R_g (measure of the size of a polymer molecule from its centre of gravity) of the chains. Tethering is sufficiently dense that the polymer chains are crowded and forced to stretch away from the surface or interface due to repulsive excluded volume interactions between chain segments. These stretched configurations are found under thermodynamic equilibrium conditions when the energy gain resulting from the reduction of the excluded volume interactions compensates the entropy penalty from the stretching of the chains from their initial random walk configurations. The height of the resulting solvated brush layer is

commonly found to be several times the unperturbed radius of gyration of the free chains in solution. The interface to which polymer chains are tethered in the polymer brushes may be a solid substrate surface (silicon or quartz) or an interface between two liquids or air-liquid[22]. Solvent can be either present or absent (melt conditions) in polymer brushes. In the presence of a good solvent[23,24], the polymer chains try to avoid contact with neighbouring chains to maximise contact with solvent molecules. Polymer brushes are attractive candidates in many applications, including stabilisation of colloids particles[25], new adhesive materials[26,27], lubricants[28], protein-resistant biosurfaces[29] and drug delivery systems[30].

Correlating the height of the brush with the grafting density (number of grafted molecules per unit area) has been the focus of many theories and experiments. Theoretical calculations[31,32] stipulate that the resulting density profile (density distribution for solvated polymer brushes as a function of distance from the grafting surface) should not be a step function as predicted by scaling theory[20] but should be parabolic. Experimental research has been carried out to elucidate polymer brush structures but also to check the veracity of theoretical predictions. For end-adsorbed polymer brushes, optical probes such as ellipsometry[33] and infrared spectroscopy[9] have given information about the total amount of polymer adsorbed but detail is rather limited since information on a molecular level cannot be extracted due to the low resolution of the experimental methods. X-ray and neutron scattering techniques have been very useful in providing information about the molecular organisation normal to the surface or interface[34-36]. However, neutron reflection is a more powerful technique than X-ray techniques due to its higher spatial resolution but the main advantage is the use of judicious isotopic labelling to get an almost complete description of the polymer organisation[37-39]. Indeed, specular reflection of neutrons relies on the markedly different nuclear scattering lengths for hydrogen and deuterium, allowing deuterium labelling to be used to highlight regions of interest in the system investigated. Numerous systems have been investigated by neutron reflection including surfactants[40], polymers[41] and proteins[42]. PEO and polymethyl methacrylate (PMMA) have both been the subject of many investigations, either as homopolymers[43-46] or copolymers from linear diblock[47] to graft copolymers[48].

Two methods are known to populate an air-water interface with polymeric materials. Firstly, dissolution of a surface active polymer in the subphase with the formation of surface excess, i.e. the concentration of polymer at the surface is greater

than the bulk concentration. Dynamic equilibrium between the surface excess layer and the bulk is achieved by continuous adsorption and desorption of molecules from the surface. Secondly, spreading an insoluble polymer on the liquid surface. Basically, the polymer is dissolved at an appropriate concentration in a volatile solvent insoluble in the liquid substrate and the solution is spread on the substrate. Adsorbed solutions and spread films of PEO have been the centre of many investigations due to the intriguing properties of PEO. Surface properties of linear PEO and copolymers containing PEO have been studied widely[49-58], examining the effects of molecular weight, concentration, substrate conditions and temperature on the coverage of PEO at the air-water interface. Despite its solubility, PEO can also form a stable spread film at the air-water interface[49,50]. Neutron reflectomery studies agreed with the existence of a stable monolayer at the air-water interface for spread film of linear PEO, showing that above a surface concentration of 0.5 mg m^{-2}, the linear PEO chains penetrate the subphase due to a looping of the molecules[59]. Determination of the surface organisation of adsorbed solutions of linear PEO at the air-water interface has been determined by neutron reflectometry experiments[60,61] and differences between the structure of the spread monolayer and adsorbed solutions from the bulk solution were observed, contradicting the previous results reported by Sauer and Yu[54].

Recently, polymer brushes formed at the air-water interface by end capped PEO with hydrophobic groups have been investigated. In 1995, a study on the surface structures of fluorinated carbon end-capped PEO at the air-water interface has been investigated for the first time by Ren *et al.*[62] Monomolecular layers of semi-fluorinated alcohol as well as polymers of PEO end-capped with fluorinated hydrocarbon chains have been used. They were able to use infrared reflectance spectroscopy to investigate the surface organisation of fluorinated end-capped PEO at the air-water interface as reflectance intensities of the CF_2 stretching vibrations of PEO provided a direct measure of the surface concentration as a function of the bulk concentration. Their results confirmed that the functionalised polymers were more highly organised at the interface than the unfunctionalised polymers, with the hydrophobic end groups oriented with the helix axis normal to the surface. They concluded that PEO with perfluoroalkyl end groups have a very high ability to form a brush-like structure at the air-water interface, especially at high surface coverage.

In 1997, Barentin et al.[10] studied spread films of PEO end capped with hydrophobic alkane groups (C_{12} and C_{16}) on a Langmuir trough at the air-water

interface. By comparing the isotherms of monolayers of pure PEO with modified PEO, they were able to prove the importance of the hydrophobic end groups, which anchor the PEO at the surface under compression. By increasing the compression, they noticed that despite their hydrophobic ends, the polymer detached from the interface and was expelled from the adsorbed layer toward the bulk solution. In order to interpret quantitatively their results, they used polymer brush theory (scaling theory) but they were unable to find agreement between the theory and the experiment as the model did not take account of the adsorbed chain configurations (trains and loops). In 1999, they extended their research by making computer simulations of adsorbed polymer solutions of hydrophobically end capped PEO using mean field theory and scaling laws[63]. They concluded that at low grafting density, the adsorbed polymer could be considered as a two-dimensional semi-dilute solution rather than a continuous layer. As the concentration increases, monolayers formed by polymers with free ends were unstable leading to the dissolution of the polymer into the bulk solvent. If the chains were able to graft at the interface, the chains were anchored on the interface and polymer brushes were observed.

In 1998, Su *et al.* investigated the surface activity of perfluorodecanoyl end-capped PEO at the air-water interface[8] and air-polymer interface[64]. In both cases, PEO was either functionalised at one end or at both ends and studied as spread films. For the polymer-air interface, the polymers were analysed by X-ray photoelectron spectroscopy (XPS). As the surface energy of the fluorocarbon end groups is lower than that of the polymer, the modified PEO preferentially adsorbs to the free polymer surface. According to the XPS results, they noticed that perfluoroalkyl chain ends adsorb to the polymer surface in a reasonably close-packed fashion, leaving a zone depleted of fluorine directly below the highly fluorinated surface region. PEO samples, with both ends capped, were found to have a slightly higher surface affinity than PEO capped at one end. They also concluded that there was a slight effect of molecular weight on surface fluorine content, indicating that the conformations of adsorbed chains were brush-like with the degree of brush extension (chain stretching) roughly linear in molecular weight. Investigation of the fluorocarbon end modified PEO at the air-water interface was also reported. The polymeric surfactants were found to be highly surface active (in the concentration range 2-8 mg ml^{-1}, the surface tensions were as low as 13.6 mN m^{-1} at 293 K). Polarized infrared reflectance spectroscopy showed that perfluoroalkyl groups were nearly perpendicular to the air-

water interface. The molecular area per chain was 30-32 $Å^2$ for PEO capped only at one end and 36-40 $Å^2$ for PEO with both ends capped. Finally, they concluded that for PEO with one end capped, the chains form a brush configuration and most of the PEO chains with both ends capped also form a brush conformation as a small percentage (22%) of the chains forms extended loops.

Recently, water-soluble amphiphilic polyethylene oxide-polypropylene oxide-polyethylene oxide (PEO-PPO-PEO) triblock copolymers have been used to build a PEO-brush at the aqueous solution/air interface[65]. The brush thickness has been estimated by using microscopic foam film methodology. It was found that the simple brush theory (polymer brush as a string of blobs) was generally obeyed.

Liquid surfaces are commonly perturbed by thermal fluctuations, which can be decomposed into a series of discrete Fourier modes and are commonly known as capillary waves[66]. The presence of polymeric materials at the surface or interface influences the dynamics of the capillary waves by modifying their frequency and damping. The main technique to quantify the dynamics of polymers at surface and interface is surface quasi-elastic light scattering (SQELS) introduced in the 1970's by Hård[67] but further developed by Earnshaw[68]. The surface dynamics of the system can be divided into four parameters, known as visco-elastic parameters and are decomposed as follow: surface tension, transverse shear viscosity, dilational modulus and dilational viscosity. SQELS experiments allow the determination of these factors and they can be studied as a function of both bulk concentration and frequency.

SQELS has been used to investigate a range of low molecular weight compounds either as spread films or as surface excess in surfactant solutions[69,70]. Most of the experimental works on SQELS have been carried out by mainly two research groups. Yu and co-workers investigated spread films at the air-water interface of various systems including polyethers as well as low molecular weight block copolymer of PEO and styrene[71-73]. The power spectra were fitted by simple Lorentzian functions rather than a skewed Lorentzian curve[74], to extract the surface visco-elastic parameters. Veracity of the results is questionable as an unfounded assumption about the non-existent transverse shear viscosity was made. An improved analysis method was proved by Earnshaw and co-workers[75], by allowing the four parameters to be determined without any assumptions. Most of the experimental works have been carried out on surfactant[76] and polymer[50,51,52,77] systems, including PMMA, PEO as homopolymers[50], linear diblock[51] and graft copolymers[52]. A linear

diblock copolymer of poly(methyl methacrylate) and poly-4-vinyl pyridine quaternised with ethyl bromide has also been investigated[77]. Surprisingly, the dilational viscosity showed quite unusual behaviour as negative values were reported, also observed for low molecular weight surfactants. The implications of a negative dilational viscosity for polymer system are not fully understood and have been interpreted as effective parameters indicating that modification of current theories was required. In an attempt to improve the theoretical analysis, Buzza[78] and co-workers developed a new dispersion equation including two other visco-elastic parameters known as the bending and the coupling modulus and equating the transverse shear viscosity to zero. However, some recent observations[79] suggested that the dispersion equation remains incomplete as negative viscosities were still observed.

1-2 Aim of the Research Project

The surface organisation and dynamics of a fluorocarbon end capped polyethylene oxide are investigated at the air-water interface. The effect of the molecular weight as well as the concentration on the surface organisation of adsorbed solutions of modified PEO would be reported.

Questions addressed are:

- Is a brush like layer formed at the air-water interface?
- Where is the fluorocarbon end group located?
- Is the PEO chain completely immersed in the aqueous phase?

There were three main components in the attempt to answer these questions

1) The synthesis of three fluorocarbon end-capped PEO of specific molecular weight, 2 000, 5 000 and 10 000 g mol^{-1} and evaluation of surface tension of aqueous solutions. In each case both hydrogenous and deuterated polymers were to be produced.

2) Investigation of the surface organisation by neutron reflectometry and comparison of these profiles with theoretical predictions.

3) Investigation of the dynamics of the system using surface quasi-elastic light scattering and correlating these data with the description organisation obtained by neutron reflectometry.

1-3 References

1) Jones, R.A.L.; Richards, R.W. *Polymers at Surfaces and Interfaces*, **1999**, Cambridge University Press.
2) Fleer. G.J.; Cohen Stuart, M.A.; Scheutjens, J.M.H.M.; Cosgrove, T.; Vincent, B. *Polymers at Interfaces*, **1983**, Chapman & Hall, London.
3) Napper, D.H. *Polymeric Stabilisation of Colloidal Dispersions*, **1983**, Academic Press, New York.
4) Feng, Y.; Zhao, J.R.; Wang, Q.; Li, M.; Chen, X.F. *J. of Appl. Poly. Sci.*, **2000**, 475, 75.
5) Kim, Y.H. *J. of Poly. Sci. A*, **1998**, 11, 1685.
6) Sferrazza, M.; Jones, R.A.L.; Penfold, J.; Bucknall, D.B.; Webster, J.R.P. *J. of Materials Chemistry*, **2000**, 10, 127.
7) Richards, R.W.; Rochford, B.R.; Webster, J.R.P. *Polymer*, **1997**, 38, 1169.
8) Miller, A.F.; Richards, R.W.; Webster, J.R.P. *Macromolecules*, **2001**, 34, 8361.
9) Su, Z.; McCarthy, T.J.; Hsu, S.L.; Stidham, H.D.; Fan, Z.; Wu, D. *Polymer*. **1998**, 39, 4655.
10) Barentin, C.; Muller, P.; Joanny, J.F. *Macromolecules*, **1998**, 31, 2198.
11) Bailey, F.E.Jr.; Gallard, R.W. *Poly(ethylene oxide)*, **1976**, Academic Press, New York.
12) Cao, B.H.; Kim, M.W. *Faraday Discuss.*, **1994**, 98, 245.
13) Pirma, I. *Polymeric Surfactants*, **1992**, ed. I. Pirma. Marcel Dekker, New York.
14) Schick, M.J. *Non-ionic Surfactants*, **1967**, ed. Schick, M.J. Marcel Dekker, New York.
15) Selve, C.; Ravey, J.C.; Stebe, M.J.; Moudjahid, C.E.; Moumni, E.L.; Delpuech, J.J. *Tetrahedron*, **1991**, 47, 411.
16) Owen, M.J. *Siloxane Polymer*, **1993**, ed. M.J. Owen, Prentice Hall, Englewood Cliffs, New Jersey.
17) Kuneida, H.; Shinoda, K. *J. Phys. Chem.*, **1976**, 80, 2468.
18) Clayfield, E.J.; Lumb, E.C. *J. Colloid Interface Sci.*, **1966**, 22, 269.

19) Jenkel, E.; Rumbach, B.; *Elektrochem*, **1951**, 55, 612.

20) de Gennes, P.G. *Macromolecules*, **1980**, 13, 1069.

21) Brittain, W.J.; Zhao, B. *Prog. Polym. Sci.*, **2000**, 25, 677.

22) Kent, M.S.; Lee, L.T.; Factor, B.J.; Rondlez, F.; Smith, G.S. *J. Chem. Phys.* **1995**, 103, 2320.

23) Liu, Y.; Quinn, J.; Rafailovich, M.H.; Sokolov, J. *Macromolecules*, **1995**, 28, 6347.

24) Perahia, D.; Wiesler, D.G.; Satija, S.K.; Fetters, L.J.; Sinha, S.K.; Milner, S.T. *Physical Review Letters*, **1994**, 72, 100.

25) Napper, D.H. *Polymeric Stabilisation of Colloid Dispersions*, **1983**, Academic Press, London.

26) Raphaël, E.; de Gennes, PG. *J. Phys. Chem.*, **1992**, 96, 4002.

27) Ji, H.; de Gennes, P.G. *Macromolecules*, **1993**, 26, 520.

28) Joanny, J. F. *Langmuir*, **1992**, 8, 989.

29) Szleifer, I.; Carignano, M.A. *Macromol. Rapid Commun.*, **2000**, 21, 423.

30) Torchilin, V.P. *Journal of Controlled Release*, **2001**, 73, 137.

31) Milner, S.T.; Witten, T.A.; Cates, M.E. *Macromolecules*, **1988**, 21, 2610.

32) Milner, S.T.; Witten, T.A.; Cates, M.E. *Europhysics Letters*, **1988**, 5, 413.

33) Sauer, D.B.; Yu, H.; Kim, M.W. *Langmuir*, **1989**, 5, 278.

34) Bucknall, D.G. *Modern Techniques for Polymer Characterisation*, **1999**, Pethrick, R.A.; Dawkins, J.V. (Eds). John Wiley and Sons Ltd.

35) Richards, R.W. *Scattering Methods in Polymer Science*, **1995**, Ellis Horwood.

36) Russell, T.P. *Materials Science Reports*, **1990**, 5, 171.

37) Higgins, J.S.; Benoit, H.C. *Polymers and Neutron Scattering*, **1994**, Oxford University Press.

38) Thomas, R.K. *Scattering Methods in Polymer Science*, **1995**, Chapter 4, Ed. Richards, R.W. Ellis Horwood.

39) Russel, T.P. *Mat. Sci. Rep. 5*, **1990**, 171.

40) Lu, J.R.; Hromadova, M.; Simister, E.A.; Thomas, R.K. *Macromolecules*, **1993**, 26, 4591.

41) Reynolds, I.; Richards, R.W.; Webster, J.R.P. *Macromolecules*, **1995**, 28, 7845.

42) Atkinson, P.J.; Dickinson, E.; Horne, D.S.; Richardson, R.M. *J. Chem. Soc., Faraday Trans*, **1995**, 91, 2847.

43) Gissing, S.K.; Richards, R.W.; Rochford, B.R. *Colloids and Surfaces A: Physiochem. Eng. Asp.*, **1994**, 86, 171.

44) Henderson, J.A.; Richards, R.W.; Penfold, J.; Shackleton, C.; Thomas, R.K. *Polymer*, **1991**, 32, 3284.

45) Henderson, J.A.; Richards, R.W.; Penfold, J.; Thomas, R.K. *Macromolecules*, **1993**, 26, 65.

46) Henderson, J.A.; Richards, R.W.; Penfold, J.; Thomas, R.K.; Lu, J.R. *Macromolecules*, **1993**, 26, 4591.

47) Richards, R.W.; Rochford, B.R.; Webster, J.R.P. *J. Chem. Soc. Farad. Discuss.* **1994**, 98, 263.

48) Miller, A.F.; Richards, R.W.; Webster, J.R.P. *Macromolecules*, **2001**, 34, 8361.

49) Henderson, J.A.; Richards, R.W.; Penfold, J.; Thomas, R.K.; Lu, J.R. *Macromolecules*, **1993**, 26, 4591.

50) Richards, R.W.; Taylor, M.R. *J. Chem. Soc., Faraday Trans.*, **1996**, 92, 601.

51) Peace, S.K.; Richards, R.W.; Williams, N. *Langmuir*, **1998**, 14, 667.

52) Richards, R.W.; Rochford, B.R.; Taylor, M.R. *Macromolecules*, **1996**, 29, 1980.

53) Richards, R.W.; Peace, S.K. *Polymer*, **1996**, 37, 4945.

54) Sauer, B.B.; Yu, H. *Macromolecules*, **1989**, 22, 786.

55) Kawaguchi, M.; Sauer, B.B.; Yu, H. *Macromolecules*, **1989**, 22, 1735.

56) Huang, Q.R.; Wang, C.H. *Langmuir*, **1996**, 12, 2679.

57) Cao, B.H.; Kim, M.W.; Cummings, H.Z. *J. Chem. Phys.*, **1995**, 102, 9375.

58) Cao, B.H.; Kim, M.W. *Europhys. Lett.*, **1995**, 29, 555.

59) Kawaguchi, M.; Komatsu, S.; Matsuzumi, M.; Takahashi, A.J. *Colloid Interface Sci.*, **1984**, 102, 356.

60) Rennie, A.R.; Crawford, R.J.; Lee, E.M.; Thomas, R.K.; Crowley, T.L.; Roberts, S.; Qureshi, M.S.; Richards, R.W. *Macromolecules*. **1989**, 22, 3466.

61) Lu, J.R.; Penfold, J.; Richards, R.W.; Su, T.J.; Thomas, R.K. *Polymer*, **1996**, 37, 109.

62) Ren, Y. ; Shoichet, M.S. ; McCarthy, T.J. ; Stidham, H.D. ; Hsu, S.L. *Macromolecules*. **1995**, 28, 358.

63) Barentin, C. ; Joanny, J.F. *Langmuir*. **1999**, 15, 1802.

64) Su, Z. ; Wu, D. ; Hsu, S.L. ; McCarthy, T.J. *Macromolecules*. **1997**, 30, 840.

65) Sedev, R. *Colloids and Surfaces* A : Physicochem. Eng. Aspects. **1999**, 156, 65.

66) Earnshaw, J.C. *J. Appl. Optics*, 1997, 36, 7583.

67) Hård, S.; Hammerius, Y.; Nilsson, O. *J. App. Phys.*, **1976**, 47, 2433.

68) Hughes, C.J.; Earnshaw, J.C. *J. Phys. E.: Rev. Sci. Instrum.*, **1993**, 64, 2789.

69) Langevin, D.; *Light Scattering by Liquid Surfaces and Complementary Techniques*, **1992**, Dekker, New York.

70) Earnshaw, J.C. *Polymer Surfaces and Interfaces II*; Feast, W.J.; Munro, H.S.; Richards, R.W.; Eds.; Wiley: New York, **1992**, Chapter5.

71) Kawaguchi, M.; Sano, M.; Yen-Lane, C.; Zogafi, G.; Yu, H. *Macromolecules*, **1986**, 19, 2606.

72) Sauer, B.B.; Yu, H.; Tien, C.F.; Hager, D.F. *Macromolecules*, **1987**, 20, 393.

73) Kawaguchi, M.; Sauer, B.B.; Yu, H. *Macromolecules*, **1989**, 22, 1735.

74) Earnshaw, J.C.; McGivern, R.C.; McLaughlin, A.C.; Winch, P.J. *Langmuir*, **1990**, 6, 649.

75) Earnshaw, J.C.; McGivern, R.C., McLaughlin, A.C.; Winch, P.J. *Langmuir*, **1990**, 6, 650.

76) Earnshaw, J.C.; McCoo, E. *Langmuir*, **1995**, 11, 1087.

77) Brown, A.S.; Richards, R.W.; Buzza, D.M.A.; McLeish, T.C.B. *Faraday Discuss.*, **1999**, 112, 1.

78) Buzza, D.M.A; Jones, J.L.; McLeish, T.C.B.; Richards, R.W. *J. Chem. Phys.*, **1998**, 109, 5008.

79) Milling, A.J.; Richards, R.W.; Hiorns, R.C.; Jones, R.G. *Macromolecules*, **2000**, 33, 2651.

Chapter Two

Theory

2-1 Synthetic Background

2-1-1 Introduction

Seals, insulation, cordage, tire, etc. all share a common heritage: polymers whose physical state can range from rubbery, glassy or crystalline and combinations thereof[1]. The word *polymer* comes from the Greek, *polymeres*, or having many parts[2]. The word describes a long chain molecule with a repeating pattern, or a macromolecule. Such giant molecules consist of many simple chemical units (monomers), covalently bonded in numerous patterns via a polymeric reaction[3].

The last fifteen years have seen impressive progress in the efficiency of polymer synthesis. Regio- and stereoselectivity, molecular weight control and access to more complex architectures of both homopolymer and copolymers (polymers composed of two different monomers) have been achieved (random, diblock, triblock copolymers, graft copolymers, dendrimers, etc...). The physical properties (viscoelasticity, Glass transition temperature...) of such well-defined materials were found to be dependent on both the architecture and the percentage composition of the copolymer.

The technical applications of polymeric materials are well known and continue to expand due to the need for novel polymers. Consequently, polymer synthesis of novel polymeric material has triggered interest from both academic and industrial applications. Polymers can be classified in various ways, and a convenient way is with reference to the manner of their preparation[4]. One class comprises step-growth polymers in which the chains are built up step by step, usually by condensation reactions which occur by molecular mechanisms in which a small molecule, such as water, is split off at each step (esterification reaction). The second class comprises the addition polymers, which are usually prepared by reactions involving the participation of free radicals (anion, cation or radical). One important feature of addition reactions occurs when the active site on the growing polymer chain is available indefinitely for further propagation leading to living polymerisation. Such reactions are employed when precise molecular weight and polydispersities are required.

The living polymerisation method allows complete conversion of all monomer species to polymeric material regardless of the propagation rate provided the system is

impurity-free, as these will cause termination of the propagating chain or initiation of chain transfer reactions. When the initiation step (process generating free radicals) is faster than the propagation step (continuous regeneration of monomer to active site), all polymer chains will grow at identical rates, thus leading to monodisperse material. By simply altering the monomer to initiator ratio, perfect control over the molecular weight is achieved.

2-1-2 Anionic Polymerisation

Anionic polymerisation is one class of living polymerisation where the active propagating site is a carbanion[5]. Monomers must be able to stabilise an anion and therefore monomers containing electron-withdrawing substituents such as diene or styrene or cyclic monomers (ethylene oxide) are preferred as they will be susceptible to anionic polymerisation using the appropriate initiator. Organo-metallic compounds are used as initiators, for example, butyl lithium commonly used in the synthesis of polyisoprene. The initiation step, as shown schematically in scheme 2.2.1, occurs usually by addition of a basic ion, which in the case of cyclic monomer opens the ring, leaving an anionic active site ready to undergo another nucleophile attack.

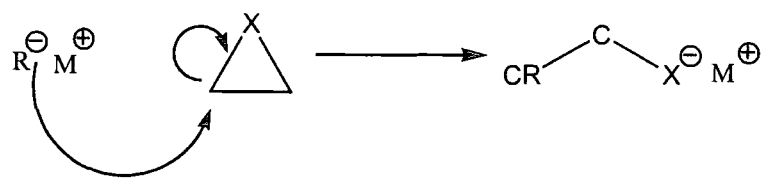

Scheme 2.2.1: Initiation step for anionic polymerisation.

By adding another monomer unit, the chain will grow and this continuous regeneration of reactive intermediates, propagation, is shown in scheme 2.2.2.

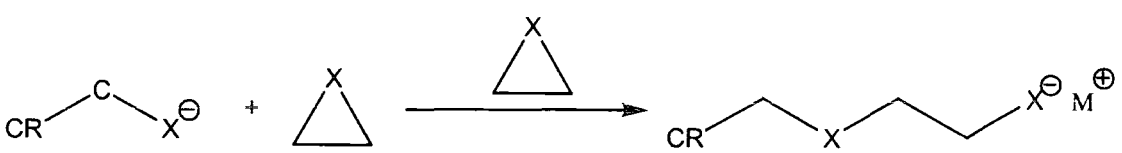

Scheme 2.2.2: Propagation step for anionic polymerisation.

In order to prepare monodisperse polymers it is essential to ensure that the rate of initiation is faster than propagation. This can be achieved by careful and judicious choice of solvent and initiator. A good solvent, for enhanced rate of reaction, is one that solvates the cation of the initiating species, thus maximising the nucleophilicity of the anion and also preventing aggregation of the initiating species.

The propagating chain end in an anionic process remains active until a specific terminating compound is added to stop propagation, i.e. termination. When the terminating agent contains functional groups then this final step is referred to as the end-capping of the polymer chains. However impurities could also stop the reaction as mentioned earlier and active chain ends are particularly water sensitive. To eliminate such impurities, the experimental procedure requires extremely clean glassware, purified reagents and the reaction to be undertaken under a nitrogen atmosphere.

A complete description and practical applications of anionic polymerisation is available by Hsieh and Quirk[6].

2-2 Adsorption

2-2-1 Interfacial Region

In many systems, the interfacial region is characterised by atomic or molecular length scales and obviously differs from low to high molecular weight materials. In a macroscopic sample the distance over which the surface properties differ from the bulk is a few molecular diameters due to the small fraction of molecules that have affinities with the interface rather than the bulk. This statement is also valid for macromolecules. The interfacial region is obviously of longer extent compared to low molecular weight materials and is controlled by two main factors.

On the one hand, there are relatively strong interactions due to the short intersegment distance on adjacent polymer molecules. These interactions (range ~20Å) fall off rapidly as the distance between molecules increases; they are enthalpic in character and determine such properties as compressibility and surface tension. On the other hand, the majority of polymer properties arise from the connection of segments joined together by covalent bonds to form a long chain. Therefore, polymer molecules can adopt an extensive number of configurations as polymer molecules are spatially extended objects. This second length scale is related to the polymer chain dimension, which is generally expressed as a radius of gyration (R_g) or end-to-end distance.

$$R_g^{\,2} = nl^2 \qquad \text{Equation 2.2.1.}$$

$$\text{end-to-end distance} = R_g \times \sqrt{6} \qquad \text{Equation 2.2.2.}$$

where n is the number of repeat unit and l the statistical segment length of the polymer chain.

For flexible polymers, the arrangement of the polymer segments means that the configurational entropy plays a role in determining the equilibrium, minimum free energy, state. By convention (2^{nd} law of thermodynamics), thermodynamic equilibrium equates to the configuration of maximum entropy in an isolated system. When polymer molecules are near an interface, the number of configurations is reduced which leads to a reduction of the entropy. Therefore, the free energy of the

system is influenced. Because polymers are large molecules, we expect the length scale of surface region in polymers to be much greater when compared to small molecules. Indeed, polymer/polymer interfaces and layers of adsorbed polymers at solid/liquid and liquid/air interfaces will be more spatially extended, increasing the length range of the interfacial region.

The surface and interfacial properties of polymers observed are the outcome of the competition between short-range enthalpic interactions and entropic contribution to the overall free energy outlined above.

2-2-2 Surface and Interfacial Tension

The most important quantity characterising a surface is the surface tension, commonly denoted by γ, and has the dimension of a force per unit length (mNm^{-1}). The surface tension in thermodynamic terms is the surface free energy per unit area. It implies that work is required to increase the surface area, that is, to bring molecules from the interior of the phase into the surface region.

Thermodynamically the interfacial tension between two phases 1 and 2 may be defined as an increase in Gibbs free energy of the whole system per unit increase in interfacial area, at constant temperature and pressure and is given by,

$$\gamma = \left(\frac{\partial G}{\partial A}\right)_{T,p,n} \qquad \text{Equation 2.2.3.}$$

At constant temperature (T) and pressure (p), the Gibbs free energy is,

$$G = E + pV - TS = H - TS \qquad \text{Equation 2.2.4.}$$

where E is the internal energy of the system, V the work generated by the system, S, the entropy and H, the enthalpy.

By definition, for any irreversible and spontaneous process at constant temperature and pressure, the Gibbs free energy decreases to the minimum value for

the system. This can be achieved by a decrease of enthalpy (decrease in energy) or an increase of entropy (increase of disorder) or a combination of both.

Therefore, because minimisation of the free energy leads to equilibrium of a particular system, it would be of great interest to define a model that would estimate the contribution of the entropic and energetic factors and thus get some knowledge about the equilibrium conformation of the system. This has been introduced by the Flory-Huggins model[7] for bulk solutions of polymers.

This lattice model for the polymer and its surrounding provides the free energy of the system. In such a lattice fluid model, the bulk phase is divided into cells that can be occupied either by a polymer segment or a solvent molecule. One parameter that results from the theory is χ, the polymer-solvent interaction parameter. It is a dimensionless number, enthalpic in character but related to the internal energy of the system.

When adsorbed monolayers of soluble amphiphile (or surface active material) are formed at a surface or interface, the surface tension is reduced since the adsorbed film increases the thermodynamic stability at the surface[8]. By varying the bulk concentration and by monitoring the changes in surface tension using a digital tensiometer and Wilhelmy plate (refer to Chapter Three, section 3-6), qualitative insight into the molecular organisation of the adsorbed film at the interface can be obtained. These variations in surface tension are plotted as a function of surface concentration thus providing an adsorption isotherm. A schematic adsorption isotherm for low molecular weight surfactant (sodium dodecyl sulfate) is shown in figure 2.2.1.

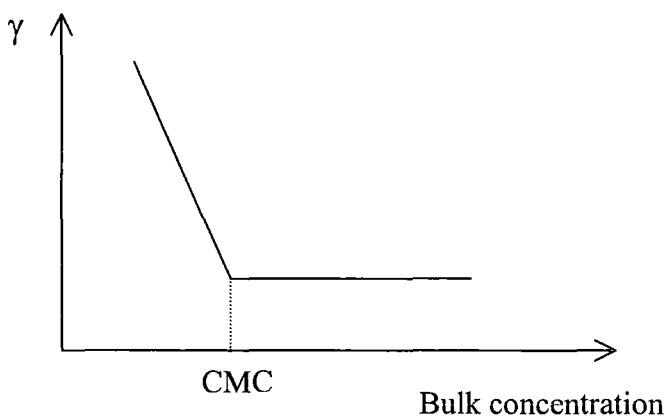

Figure 2.2.1: Schematic representation of adsorption isotherm for low molecular weight surfactant.

As depicted in figure 2.2.1, the surface tension decreases as the bulk concentration increases due to adsorption of molecules at the interface, until a break is observed, thereafter the surface tension remains approximately constant. For low molecular weight surfactant, the break observed in the surface tension isotherm is attributed to the formation of micelles as the interface becomes saturated, and will be discussed in more detail later. The concentration at which the micelles are formed is known as the critical micelle concentration or CMC. Monolayers adsorbed from solution are expected to be in thermodynamic equilibrium with the underlying solution and should therefore obey the Gibbs equation. The variation of surface tension with composition is governed by the Gibbs adsorption isotherm. For ideal adsorption in a binary system (polymer/solvent), the Gibbs adsorption isotherm is given by,

$$\Gamma = -\frac{1}{RT} \times \frac{d\gamma}{d \ln c} \qquad \text{mol m}^{-2} \qquad \text{Equation 2.2.5.}$$

where $\frac{d\gamma}{d \ln c}$ is the slope of $\gamma = f(\ln c)$, T is the temperature in K (293 K), R is the gas constant and Γ is known as the surface concentration or surface excess.

2-2-3 Adsorption of Polymers

The adsorption of polymers onto a range of interfaces has been much studied[9,10]. Indeed, by modifying the surface of a material its adhesive properties are altered by either enhancing or minimising adhesion. These principles are applied in many practical applications such as adhesion (protective coatings), lubrication and stabilisation of colloidal particles[11-13]. An important example of adhesion minimisation involves the development of surface coatings that are resistant to biological contamination.

The properties of a liquid near an interface are inevitably different from its bulk properties. For a polymeric solution (i.e. mixture of polymer and solvent), the most important effect is a change in composition near the interface, i.e.; a concentration differential at or near the interface is induced. An increase in concentration of the solute in the interfacial region is generally called *adsorption*. The term *physisorption* is used when only physical interactions play a role. The opposite

case is the result of a reduction in solute concentration near the interface and is commonly known as *desorption* and *depletion* for polymers.

Adsorption or depletion depends both on the net adsorption energy imposed by the polymer segments, i.e., on the difference between the free energy of segment/surface contacts and that of solvent/surface contacts. If this difference is sufficiently negative, adsorption will occur, otherwise depletion is observed. Because of the large size of polymer molecules, the adsorption phenomenon of polymers is much more complicated than that of small molecules. The theory of polymer adsorption is therefore based on a lattice model, which makes the counting of conformations much simpler. Polymer adsorption from solution is a very large subject and a much more complete treatment is provided by Fleer *et al*[9].

It is well known that the conformations of chains in a homogeneous solution under θ-conditions can be described as an unrestricted, purely random walk. For sufficiently long chains, this results in a Gaussian distribution of segments about the centre of mass. Compared to an unrestricted chain in solution, adsorbed chains do not enjoy the same magnitude of freedom. Indeed due to the restriction of the rigid wall, half of the space is inaccessible. This restriction leads to a lower configurational entropy in the surface region. The adsorption of polymer at an interface is described as an assembly of tails, loops, and trains, as described by the loop-train-tail model of Jenkel and Rumbach[14] as shown schematically in figure 2.2.2.

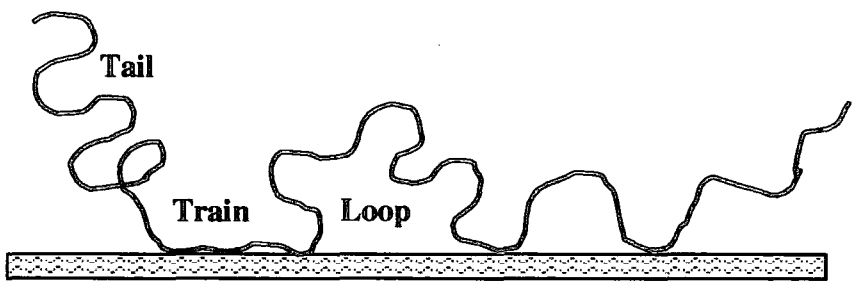

Figure 2.2.2: Schematic representation of the conformation of an adsorbed polymer.

Tails are the sections extending into the bulk with one end anchored to the surface, while trains consist of the segments, which directly attach to the surface, resulting in a flat conformation. A loop is the bridging section between two trains, which also extends into the solution from the surface. From such a model, it is quite

obvious that the train section influences directly the surface energy of the system as it is attached to the surface. Therefore the use of polymers to modify the properties of interfaces has been of great interest in the last few decades; one way is by tethering a polymer molecule at the surface or interface.

The term *tethered polymer* is employed to describe a polymer molecule that is attached to a surface or interface. In many case when polymers are used to stabilise a colloid, they are grafted by one end, constraining one end of the polymer molecule to a plane.

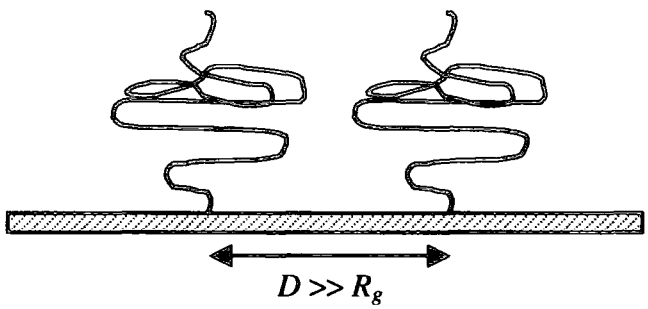

Figure 2.2.3: Schematic representation of a grafted polymer.

Consequently, the behaviour of polymer molecules, when one of their ends is tethered to a surface or an interface, is altered when compared to free chain molecules in solution[9]. Indeed due to the presence of the grafting surface, the configurational space of the chains is limited, influencing the way in which neighbouring chains interact with each other. Consider the case of polymer molecules tethered by one end to a planar substrate and immersed in a thermodynamically good solvent. If the distance between tethered chains (D) is greater than the radius of gyration of the chains, no interaction between neighbouring chains is generated and the polymer chains can adopt either a mushroom configuration (figure 2.2.3) or a pancake configuration as shown in figure 2.2.4.

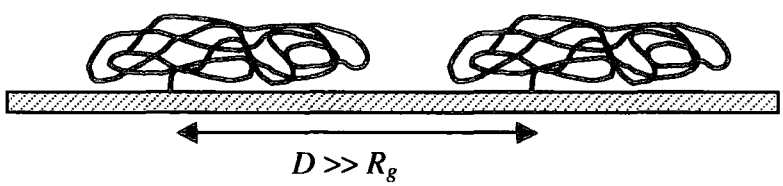

Figure 2.2.4: Schematic illustration of pancakes.

When the distance, D, is less than the radius of gyration the chains interact with each another. A semi-dilute regime is then observed and as a direct consequence of these interactions the free energy of the system increases. Due to excluded volume

interactions between neighbouring chains, the chains start to stretch in the direction normal to the surface to reduce their contact and maximise enthalpically favourable interaction with the solvent molecules. A configurational entropy penalty associated with stretching the chains out from their random walk configurations contributes to the system free energy. The resulting array of interacting chains is known as a polymer brush as depicted in figure 2.2.5.

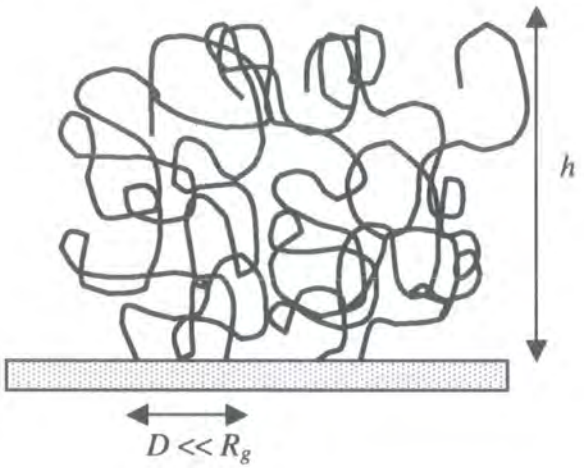

Figure 2.2.5: Schematic illustration of a polymer brush.

The height of the brush, h, is defined as the distance from the grafting surface at which the polymer volume fraction falls to zero. However, as discussed briefly above, the brush height is also dependent on the quality of the solvent. The size of an isolated polymer coil in solution is determined by the thermodynamic quality of the solvent[10]. In a thermodynamically good solvent (interaction between solvent and polymer molecules is attractive), the coil will expand slightly due to repulsive excluded volume interactions between the chain segments as they maximise their contact with the solvent molecules (positive excluded volume). In the case of a thermodynamically poor solvent (interaction between solvent and polymer molecules is repulsive), the interaction between the polymer segments becomes attractive and the coil collapses in on itself in order to minimise segment-solvent interactions (negative excluded volume). For any given polymer-solvent system, the thermodynamic quality of the solvent generally improves with increasing temperature, and the transition between the poor and good solvent regimes occurs at the theta temperature (θ)[10]. At this specific temperature, the excluded volume is zero, and the polymer coil has its unperturbed dimensions. By analogy with the brush

configuration, if the solvent is good, the brush height is expected to be up to several times the unperturbed radius of gyration. When the solvent quality reduces however, the brushes tend to collapse as the segments attempt to reduce their enthalpically unfavourable interactions with the solvent molecules.

The shape of the polymer volume fraction profile, i.e. the distribution of polymer as a function of distance from the grafting surface has been the subject of numerous theoretical models. The relevant models for fluorocarbon end-capped polyethylene oxide (PEOF) will be discussed here.

In 1977, Alexander[15] predicted that the equilibrium thickness of a layer is reached as a direct result of the competition between chain stretching (elastic free energy) and chain-chain repulsion (interaction energy per chain). A scaling argument can be applied to this model but only at low grafting density (semi-dilute regime) as this model does not take the conformations of polymer chains into account and therefore no density profile of the chains at a distance from the grafting surface is available.

$$h \sim Na\sigma^{1/3} \qquad \text{Equation 2.2.6.}$$

where N is the degree of polymerisation of the chain, a is the Kuhn step length of the repeat unit. The grafting density is σ as defined in equation 2.2.7 divided by a^2, i.e. the area occupied by a segment.

$$\sigma = \frac{n_i \times d}{\mathrm{N_A}} \qquad \text{chains per Å}^{-2} \qquad \text{Equation 2.2.7.}$$

where n is the number density of molecules i and d the layer thickness determined by neutron reflectometry experiments (as discussed in section 2-3) and $\mathrm{N_A}$ is Avogadro's number.

As the grafting density increases, excluded volume interactions between neighbouring chains are generated. This concept was introduced by De Gennes[16] in 1980. It presumes that all the chain ends are located at the same distance from the surface. Equilibrium stretching is obtained when the energy gain resulting from the

reduction of the excluded volume interactions compensates the entropy penalty from the stretching of the chains from their initial random walk configurations.

In the stretched wet brush regime[14], the scaling law for a polymer with a degree of polymerisation N is given by,

$$h \sim N(\upsilon\sigma)^{1/3} \qquad \text{Equation 2.2.8.}$$

Equation 2.2.8 differs slightly from equation 2.2.6 as it incorporates the excluded volume, υ, given by,

$$\upsilon = a^3(1-2\chi) \qquad \text{Equation 2.2.9.}$$

As the scaling law equations (2.2.7 and 2.2.8) show, h depends linearly on N and is a function of the grafting density raised to the power 1/3. The scaling theory predicts that all chain length are situated at the same distance from the surface and the near surface depth profile is step like (volume fraction is constant throughout the brush).

Since this first scaling law theory, an analytical self consistent field theory has been produced by Milner *et al.*[17]. In reality, free chain ends are less stretched than most of the polymer chains. A simple hypothesis about free chain ends from the interface is made: the free chain ends may be located at any distance from the interface. The resulting density profile is not a step function, as predicted by scaling laws, but should be parabolic. The resulting density distribution as a function of distance from the grafting surface, z, is shown in figure 2.2.6.

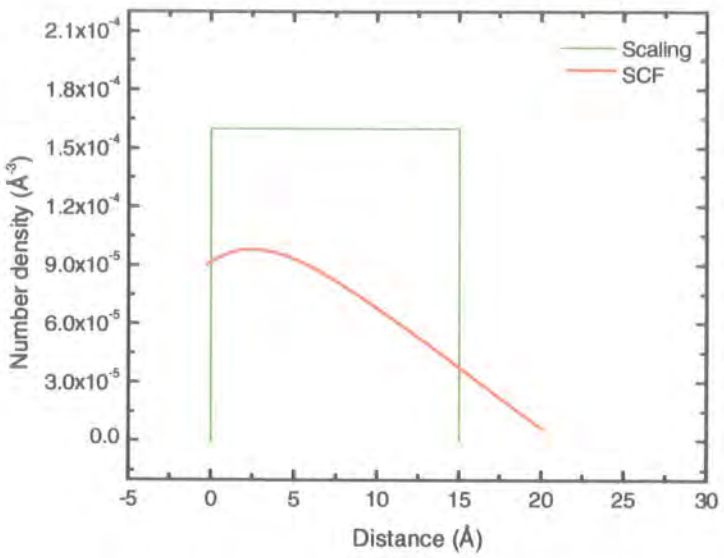

Figure 2.2.6: The resulting density distribution as a function of distance from the grafting surface, z, according to scaling (green) and SCF (red) theories.

Using a Self-Consistent Field method (SCF), Milner *et al.*[17] were able to confirm the parabolic profiles. The main idea is that where polymers are strongly stretched (brush), fluctuations around the most probable paths are small and can therefore be ignored. All the possible configurations of the brush are taken into account as no assumption regarding the monomer distribution is made.

The SCF theory gives the brush height as:

$$h = \left(\frac{12}{\pi^2}\right)^{1/3} N\sigma^{1/3}v^{1/3} \qquad \text{Equation 2.2.10.}$$

Equation 2.2.10 is in agreement with scaling theory because h is still linearly dependent on N and the scaling exponent for the grafting density is 1/3.

Shim and Cates[18] extended this theory as they considered finite extensibility of the chain length at high surface coverage, i.e. $\sigma > 0.05$. They postulated that the density profile was flatter than a pure parabolic distribution but still scales according to equation 2.2.10 for the majority of surface coverage.

2-2-4 Micelle Formation

When amphiphilic molecules are dissolved in water the hydrophobic portions segregate from the solvent by self-aggregation. The aggregated products are known as micelles. Above the CMC the micelle will consist of a hydrophobic core surrounded by hydrophilic groups (the corona). Micelles can be small spheres or disks, long cylinders or ellipsoids. The formation of micelles relies on the ability to dissolve hydrophobic substances within them and can be interpreted via two "phenomena": hydrophobic hydration and hydrophobic effect.

Hydrophobic Hydration

Water is at the heart of the solubility mechanism and can be regarded as a macroscopic network of molecules connected by hydrogen bonds[19]. This description implies that the dissolution of an apolar molecule in water necessitates the formation of a cavity in the three-dimensional hydrogen bonded network. The thermodynamics of such a process are quite characteristic. The entropic penalty for the solvation of alkanes by water is an important fingerprint of hydrophobic hydration[20,21]. However, over the past fifty years, its molecular origin has been interpreted quite differently. In 1945, Frank and Evans[22] published their classical study where the "iceberg model" was invoked to explain the negative entropy of hydration: the water molecules were proposed to be quasi-solidly structured around a nonpolar solute, thus increasing hydrogen bonding in the hydration shell. Theories of hydrophobic hydration have continued to develop. Spectroscopic techniques have been refined and developed, allowing a structural interpretation at a molecular level. Good indications for the absence of hydration cages were obtained by neutron scattering studies[23] and computer simulations[24]. It was found that at room temperature the number and strength of the hydrogen bond interactions in the hydration shell are similar to those in bulk water. Thus, (hydrogen bond) enthalpy losses are kept at a minimum[25]. This condition is achieved by a certain preferred orientation of the water molecules. One OH bond points to the bulk water, the other is oriented tangentially with respect to the surface of the apolar solute. Of course, water molecules in the hydration shell have less translational and rotational degrees of freedom as compared with their bulk

counterparts, and this accounts for the strongly negative entropy of solvation[26]. Another characteristic of hydrophobic hydration is the temperature dependence of the enthalpy of solvation. Increased thermal motions hinder the tangential orientations of water molecules in the first hydration shells surrounding the apolar solute. The number of hydrogen bonds in bulk water also decreases with increasing temperature, but to a lesser extent[27]. Hence, at higher temperatures, the hydration of hydrophobic molecules is accompanied by a greater loss of hydrogen bond interactions, so that a larger enthalpy penalty has to be met. At the same time, the preferred orientation of water molecules in the hydration shell is disturbed, so that the entropic penalty for hydrophobic hydration becomes smaller. Therefore, hydration effects result from a subtle balance of enthalpy and entropy. Both thermodynamic quantities are large and oppose each other.

Hydrophobic Interactions

The tendency of nonpolar molecules to associate in aqueous solutions is called the hydrophobic effect[28]. The idea is that aggregation of nonpolar molecules at low concentrations is hampered by the special orientation of water molecules in the first hydration shell[27,29]. At a certain concentration of solute, the number of water molecules available to form a complete hydrophobic hydration shell is insufficient, leading to interference and mutual obstruction of hydration shells and the inevitable sacrifice of hydrogen bonds. The result is known as demixing[30]. However the state-of-the-art is based on the results of computer simulations, which are contradictory. Indeed, this model accounts qualitatively for the sudden aggregation of hydrophobic solutes in water, at specific concentrations but implies an extended hydrophobic hydration shell. Recently, neutron scattering studies indicate that the hydrophobic hydration shells are relatively small[23]. From a thermodynamic point of view, bulk hydrophobic interactions and phase separation can be treated in terms of the solubility limit, which results from a balance between the positive mixing entropy of the solute and the negative entropy of the water molecules entering the hydration shell from the bulk. Thus, as more and more nonpolar molecules are dissolved in water, their mixing entropy progressively increases. The entropy of the water molecules decreases linearly with solute concentration. Therefore, the total entropy change of the system will become positive at a certain solute concentration, and neglecting enthalpy, this

will be the point where pseudophase separation occurs (hydrophobic effect). The notion of micellization as pseudophase separation due to the presence of an entropic solubility limit might be somewhat more realistic than the idea that micellization occurs as soon as complete hydrophobic hydration shells cannot be independently formed.

2-3 Neutron Reflectometry

Neutron reflectometry is a powerful technique for studying the organisation of polymer at surfaces and interfaces[31,32]. Due to its high spatial resolution (~15-20 Å), this technique is very useful to investigate the organisation of molecules at the air-liquid interface. Because the length scale resolution is proportional to the radiation wavelength (λ_0 10~20 Å), neutron beams are very efficient for polymeric length scales. This technique differs mainly from X-ray reflectometry because neutrons are scattered by nuclei, not electrons.

Neutron reflectometry experiments consist of measuring the intensity of a specularly reflected neutron beam from a surface as a function of the scattering vector *(Q)* normal to the interface on which the beam is incident. The reflectivity, *R(Q)*, of any material is the ratio of the reflected intensity, *I(Q)* to the incident intensity *(I_0)*.

$$R(Q) = \frac{I(Q)}{I_0} \qquad \text{Equation 2.3.1.}$$

When a source of neutrons is incident on a surface, four different processes occur including specular reflection, transmission, bulk scattering and non-specular reflection as depicted in figure 2.3.1.

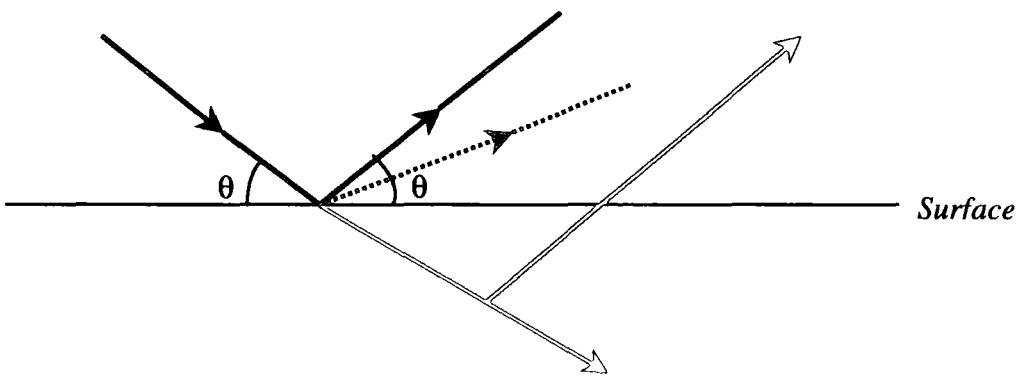

Figure 2.3.1: A schematic diagram of specular reflection (black), transmission (red), scattering from the bulk (green) and non-specular reflection (blue) when a neutron beam hits a surface.

Specular reflection from a surface occurs when the angle of incidence, θ, equals that of reflection. Non-specular reflection occurs due to roughened surface induced by thermal fluctuations. However if the experimental system is mounted on an anti-vibration table, the intensity of non-specular reflection is less than the background signal. Scattering from the bulk is also occurring if a scattering species is present in the subphase and contributes to the background signal. If the beam is not reflected then it is completely transmitted into the subphase.

As implied by equation 2.3.1, the organisation of materials can be probed at various depths normal to the interface simply by monitoring the reflectivity over a range of Q values. But what is Q? This is the magnitude of the scattering vector $\mathbb{Q}$ and is the fundamental variable in a neutron reflectometry experiment. It is defined by,

$$\mathbb{Q} = |Q| = \frac{4\pi}{\lambda}\sin\theta \qquad \text{Equation 2.3.2.}$$

where θ is the grazing angle of incidence and λ the wavelength of the incoming neutron beam.

Q is the magnitude of the vector between the transmitted beam and the specularly reflected beam as illustrated in figure 2.3.2, where k_i and k_r are the wavevectors of the incident and reflected beam respectively.

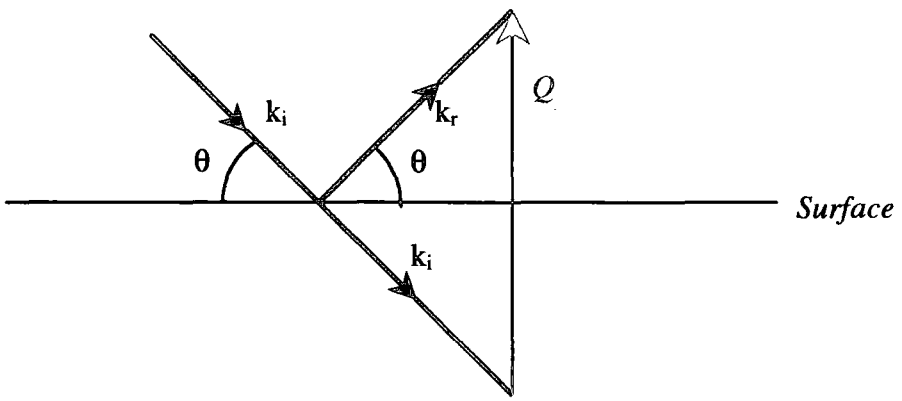

Figure 2.3.2: Representation of the wavevector Q.

According to equation 2.3.2 the scattering vector, Q, can be varied either by changing the wavelength of the incoming neutron beam or the grazing angle of

incidence. All neutron reflectivity experiments reported here were carried out at the ISIS pulsed neuron source at the Rutherford Appleton Laboratory (RAL) using the white beam time-of-flight (TOF) SURF reflectometer, i.e. determine λ at fixed θ.

The instrumentation for neutron reflectometry has been described in detail elsewhere[33]. Only a précis of the experimental details is outlined here.

2-3-1 Instrumental Details

The neutrons at ISIS are produced by a spallation process. This occurs when pulses of protons, with an associated frequency of 50 Hz, are accelerated towards a tantalum target resulting in the spalling ("boiling off") of neutrons. These neutrons are then passed through a 20 K hydrogen moderator where they continually bounce around losing energy at every collision before they are guided to the individual instruments that surround the target. The wavelength range of the beam used on SURF is $0.5 < \lambda / \text{Å} < 6.5$. Therefore, by collecting reflectivity data at three incident angles (0.5°, 0.8° and 1.5°) a Q range of $0.019 < Q / \text{Å}^{-1} < 0.6$ is accessible.

A schematic representation of SURF is given in figure 2.3.3.

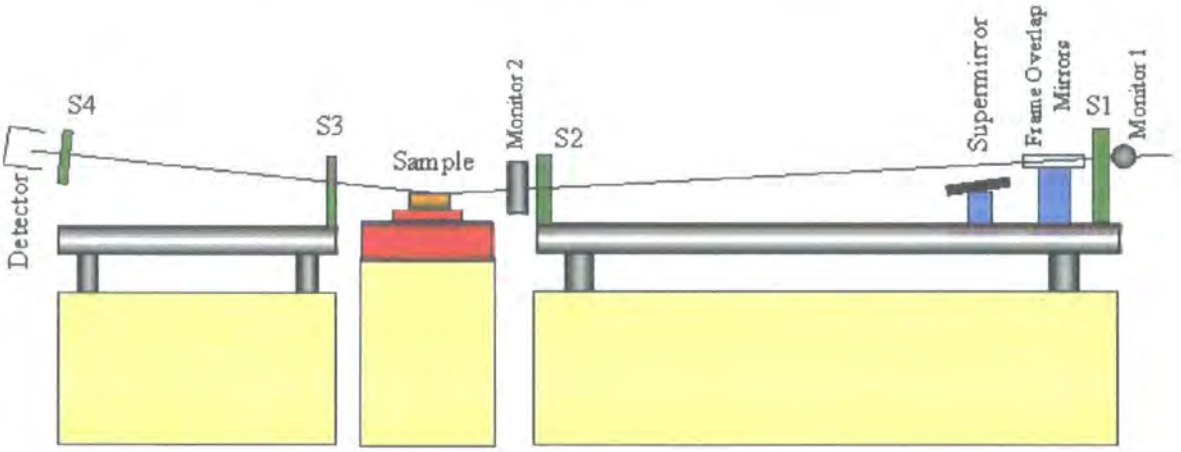

Figure 2.3.3: Schematic representation of SURF reflectometer.

The incoming "raw" neutron beam contains a broad mixture of wavelengths that need to be separated to get the desired wavelength distribution. A single disc known as chopper defines the wavelength band and provides some frame overlap suppression. This disc is not represented in figure 2.3.3; it is placed before monitor 1.

Hence the white beam travel through slit one (S1). However, occasionally neutrons with a long wavelength, known as slow neutrons, escape the chopper. They are removed from the beam by the frame overlap mirrors. This nickel-coated mirror sets to reflect out of the main beam, neutrons greater than 13 Å, allowing only neutrons of the desired wavelength from each pulse to pass through. The super mirror controls the angle of the incoming neutron beam with respect to the horizontal.

The neutrons pass through the second slit (S2) before being incident on the sample interface. The reflected and scattered neutrons are travelling through two further slits before finally falling on the scintillator detector. This measures the intensity of the neutrons as a function of time, t, with $t = 0$ defined as the beginning of every pulse. As the distance of the monitor to the target is known exactly then it is possible to convert time into neutron energy and ultimately wavelength, hence the terminology "time of flight" (TOF) method. The four slits collimate the incident (S1 and S2) and the reflected beam (S3 and S4). The width of each slit is specific to the incident angle and the experiment. In this study, the widths of S1 to S4 were usually set to 1, 0.67, 0, and 0 mm respectively for a neutron beam incident at 0.5°, 1.6, 1.07, 4, 4 mm for 0.8° angle and 3, 2, 2, 3 mm for 1.5° angle.

The resultant reflectivity is defined as the ratio of the intensity of the incident beam (measured by the monitor) to a reflected beam (measured by the detector). The final reflectivity for each angle is calculated automatically using appropriate instrument software and by placing the data on an absolute scale and combining them, a complete reflectivity curve is obtained.

2-3-2 Scattering Length Density

The reflective properties of neutrons are analogous to those of light and are therefore governed by Fresnel's law (basic rules of geometric optics) with subsequent modifications. When discussing the reflection of neutrons, the optical refractive index is replaced by the neutron refractive index of the reflecting substance. The refractive index can be related to the composition of the solution and as the refractive index changes from one bulk value to the other through the interface (the reflectivity changes with penetration depth), a perfect description of the composition distribution normal to the surface is accessible.

The neutron refractive index, n, from a smooth interface between two phases is given by equation 2.3.3.

$$n = 1 - \frac{\lambda^2 Nb}{2\pi} \qquad \text{Equation 2.3.3.}$$

where N is the atomic number density and b is the coherent scattering length of the atom. As mentioned earlier, neutrons are scattered by nuclei, therefore the scattering length values vary randomly across the periodic table. The values of b for nuclei relevant to this study are given in table 2.3.1.

Nucleus	b / 10^{-4} Å
C	0.67
O	0.58
F	0.566
^{1}H	-0.37
^{2}H	0.68

Table 2.3.1: The coherent scattering length values required for this study.

It is interesting to notice that the coherent scattering length of ^{1}H is negative whereas that of ^{2}H is positive. The difference between these two isotopes is fundamental to the neutron reflectometry experiments and will be discussed further.

The scattering length density is determined by the composition of the reflecting material and is given by,

$$\rho = \sum b_i n_i \qquad \text{Equation 2.3.4.}$$

where n is the number density of species i.

The scattering length density is one of the most fundamental parameters in neutron reflectometry as the surface refractive index depends on it (equation 2.3.3). Indeed, the change in neutron refractive index for polymers is not large and a contrast between the polymer and its surrounding must be generated to observe an effect on

the reflectivity. The magnitude and sign of the scattering length density influences the amplitude of the reflected beam (a high positive scattering length enhances the amplitude of the neutron beam leading to a stronger reflection of the neutron). Because the scattering lengths of hydrogen and deuterium are significantly different (see table 2.3.1), deuterium labelling can be used to generate a contrast in the refractive index of various components. Materials mainly composed of hydrogen, such as water and hydrogenous polymers, have a negative scattering length density. Thus it is possible to add D_2O to H_2O to adjust the scattering length density of the resulting system to be that of air ($\rho_{air} = 0$). The resulting contrast is known as null reflecting water (nrw) as there is no reflection from the air-water interface. For a solution of deuterated polymer in nrw, reflection will only occur if there is adsorption of the deuterated material at the surface.

Values for the scattering length and scattering length densities pertinent to this study are given in table 2.3.2.

Species	Σb_i (Å)	$\rho / 10^{-6}$ Å^{-2}
H_2O	-1.68E-04	-0.56
D_2O	1.92E-04	6.35
air	0	0
2k HPEOF	3.46E-03	0.82
2k DPEOF	1.67E-02	4.32
5k HPEOF	6.10E-03	0.69
5k DPEOF	4.16E-02	5.08
10k HPEOF	1.02E-02	0.64
10k DPEOF	8.88E-02	5.44

Table 2.3.2: Scattering length and scattering length densities for materials used in this study. The notation *n*k IPEOF is given in Chapter Three, section 3.1.

2-3-3 Specular Reflection

At the interface between two media the grazing angle of incidence, θ_0, is related to the angle of refraction, θ_1, using Snell's law and the relationship is given by,

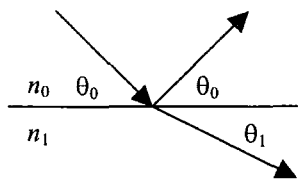

$$n_0 \cos\theta_0 = n_1 \cos\theta_1 \qquad \text{Equation 2.3.5.}$$

where n_0 and n_1 are the refractive index of media 0 and 1 respectively.

If medium 0 is air, then n_0 is 1 and equation 2.3.5 becomes,

$$\cos\theta_0 = n_1 \cos\theta_1 \qquad \text{Equation 2.3.6.}$$

When n_1 is less than one, there will be a critical angle above which specular reflection of all incident neutrons will occur. At this critical angle, θ_c, θ_1 is zero, therefore,

$$\cos\theta_c = n_1 \qquad \text{Equation 2.3.7.}$$

The air-water interface has a very small critical angle since the refractive index of both the upper and lower media are approximately one. The cosine term from equation 2.3.7 can be expanded to give,

$$\theta_c = \lambda\sqrt{\frac{\rho_d}{\pi}} \qquad \text{Equation 2.3.8.}$$

where ρ_d is the scattering length density of the subphase.

For an air-D_2O interface the critical angle occurs at a critical momentum transfer, Q_c , of 0.0179 $Å^{-1}$. The lowest Q value obtained experimentally here was circa 0.019 $Å^{-1}$, therefore the critical angle could not be encountered during experimental studies.

When an adsorbed polymer film is present between two media (0 and 2), the organisation of monolayer 1 can be probed using neutron reflectometry. A schematic representation of such system is shown in figure 2.3.4.

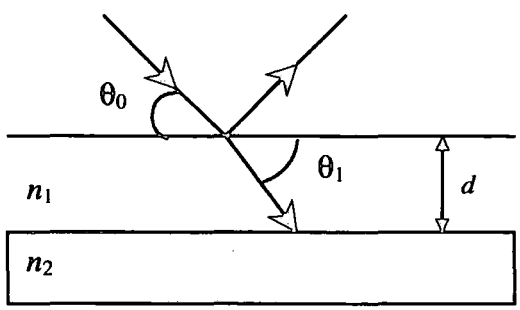

Figure 2.3.4: The specular reflection from an adsorbed film, n_1, at an interface between two media n_0 and n_2.

The reflectivity, R, for such system is analysed as a function of scattering vector and can be expressed according to Fresnel, resulting in equation 2.3.9.

$$R = \left| \frac{r_{01} + r_{12} \exp(2i\beta)}{1 + r_{01} r_{12} \exp(2i\beta)} \right|^2 \qquad \text{Equation 2.3.9.}$$

where the reflected and transmitted amplitudes of the beam at each interface (between 0 and 1, and 1 and 2) are represented by the Fresnel coefficients r_{01} and r_{12} respectively. β is the phase shift or optical path length of the beam, which can be calculated as the neutron traverses each layer, i, by using,

$$\beta = \left(\frac{2\pi}{\lambda} \right) d \sin\theta_i \qquad \text{Equation 2.3.10.}$$

where d is the thickness of the monolayer.

For an i-j interface, the Fresnel coefficients are given by,

$$r_{ij} = \frac{n_i \sin\theta_i - n_j \sin\theta_j}{n_i \sin\theta_i + n_j \sin\theta_j} \qquad \text{Equation 2.3.11.}$$

Combining equation 2.3.9 and 2.3.11, the overall reflectivity of the adsorbed monolayer is available,

$$R = \frac{r_{01}^2 + r_{12}^2 + 2r_{01}r_{12}\cos 2\beta}{1 + r_{01}^2 r_{12}^2 + 2r_{01}r_{12}\cos 2\beta} \qquad \text{Equation 2.3.12.}$$

Above the critical angle, equation 2.3.12 shows that the reflectivity R has maxima and minima when $\cos 2\beta = \pm 1$. If the equation for the phase shift (equation 2.3.10) is substituted into equation 2.3.12, it is clear that the separation of the maxima is dependent on the layer thickness and Q_c of the specific system. As discussed earlier, Q is dependent on the scattering angle and therefore on the scattering length density and the phase shift through equations 2.3.8 and 2.3.10. Consequently, a

complete description (composition and layer thickness) of the near surface can be extracted from a reflectivity profile. From a practical point of view, data cannot be Fourier transformed directly in order to obtain the composition distribution as phase information is lost from the data and the Q range is limited due to a high incoherent background signal.

Neutron reflectometry data are frequently interpreted by using models, i.e., a model composition distribution normal to the interface is generated and its reflectivity calculated and compared with the experimental data. This process is aided by two main techniques: the optical matrix method[34] and the kinematic approximation[35].

The optical matrix method is exact and uses theoretical models to fit the data. With the kinematic approximation, the reflectivity is expressed in terms of partial structure factors. Each method is outlined below.

2-3-4 The Optical Matrix Method

This method simulates a reflectivity curve based on a theorical model where the surface depth profile can be decomposed into a series of discrete layers of known thickness and number density. This profile is shown in figure 2.3.5.

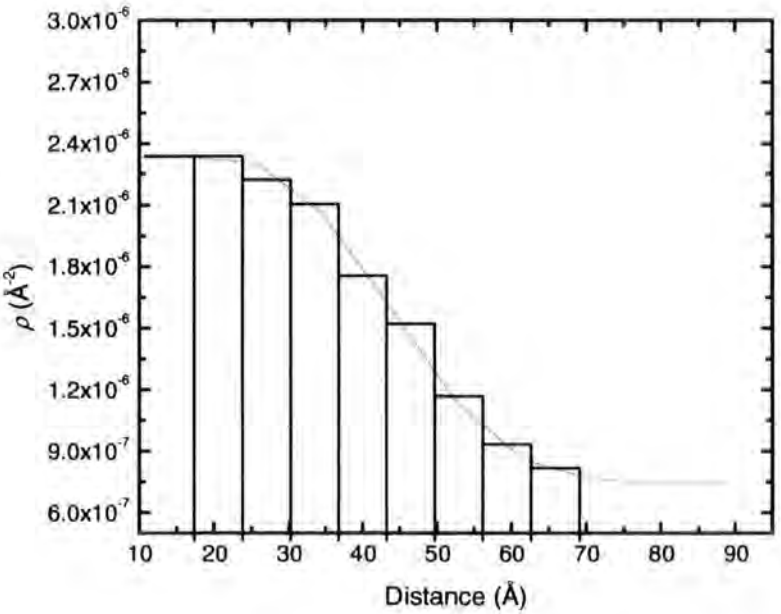

Figure 2.3.5: Gradual change in scattering length density (red) and its approximation as a series of discrete layers.

Each layer is represented by a characteristic matrix and has been described by Born and Wolf[36]. For example the characteristic matrix for a single layer, *j*, is,

$$M_j = \begin{bmatrix} \cos\beta_j & -(i/k)\sin\beta_j \\ -ik_i \sin\beta_i & \cos\beta_j \end{bmatrix} \qquad \text{Equation 2.3.13.}$$

where $k_i = n_i \sin\theta_i$.

When a model consists of multiple layers, the overall optical matrix is the product of all the individual matrices;

$$[M] = [M_1]\,[M_2]....[M_n] = \begin{bmatrix} M_{11} & M_{21} \\ M_{12} & M_{22} \end{bmatrix} \qquad \text{Equation 2.3.14.}$$

The overall reflectivity is given by,

$$R = \left| \frac{(M_{11} + M_{12}k_s)k_a - (M_{21} + M_{22})k_s}{(M_{11} + M_{12}k_s)k_a + (M_{21} + M_{22})k_s} \right| \qquad \text{Equation 2.3.15.}$$

where the subscripts *a* and *s* refer to the upper and the lower phase respectively and M_{ii} are the elements of $[M]$.

However, interfaces are never perfectly smooth and therefore are not infinitely sharp. For polymers in solution, the interface is not only influenced by the adsorbing specimen and the surrounding media (air in this study) but also by consecutive layers of polymers. This refers to a diffuse interface between the polymers. The roughness of the surface generally decreases the specular reflectivity[37]. This can be accounted for by a factor somewhat like a Debye-Waller factor[38],

$$I = I_0 \exp\left(-Q^2 \langle \sigma_r \rangle^2\right) \qquad \text{Equation 2.3.16.}$$

where I and I_0 are the reflected intensity of the beam with and without surface roughness, and σ_r is the root mean square roughness.

This equation can be incorporated into equation 2.3.13 but complexity arises when more than three layers are modelled. To overcome this problem, a more suitable method was introduced by Abeles[39] by dividing the interface into additional layers that incorporate the root mean square roughness. A different characteristic matrix from equation 2.3.13 is defined in terms of Fresnel coefficient and phase factors[40].

$$M_j = \begin{bmatrix} \exp(i\beta_{j-1}) & r_j \exp(i\beta_{j-1}) \\ r_j \exp(-i\beta_{j-1}) & \exp(-i\beta_{j-1}) \end{bmatrix} \qquad \text{Equation 2.3.17.}$$

where the reflectivity becomes,

$$R(Q) = \frac{M_{21}M_{21}^*}{M_{11}M_{11}^*} \qquad \text{Equation 2.3.18.}$$

The generated profiles are then compared with experimental data. The model parameters, describing the near surface organisation, are then varied (the initial model consists of one uniform layer with a layer thickness, d, and a scattering length density, ρ) and additional lamellae are introduced as necessary until the best-fit values for those parameters are obtained.

For a uniform layer, the scattering length density is given by,

$$\rho = \sum \rho_i \phi_i \qquad \text{Equation 2.3.19.}$$

where ϕ_i is the volume fraction and the superscript i represents the component present in the layer.

The number density, n_i, is related to ρ and the scattering length, b_i, and is given in equation 2.3.20.

$$\rho = \sum n_i b_i \qquad \text{Equation 2.3.20.}$$

Knowing n_i, the surface concentration can be calculated for each species present in the layer. The appropriate surface excess concentration equation for a uniform monolayer will be discussed in Chapter Four.

However, even if the optical matrix gives the exact reflectivity, uncertainty about the uniqueness of the model used to fit the data is always present because including more layers will always give a better fit to the data and therefore many models may fit the data well. To overcome this problem, reflectivity curves for all three polymer-subphase contrasts collected are fitted for different contrasts using the same model (multilayer model). The consistency of the layer thickness is used as a criterion for the validity of the model. Furthermore, the optical matrix method provides only the overall thickness and composition of the layer. It would be of great interest to get some insight into the distribution of the polymer segments or water at the surface. This can be obtained by the kinematic approximation.

2-3-5 The Kinematic Approximation

The kinematic approximation was developed by Thomas from an initial outline by Crowley[35]. By comparison with the optical matrix method, the kinematic approximation is able to provide a more rapidly informative analysis of the data since subtle differences between surface structures are made more apparent.

This approach is also model dependent and is only valid when the reflectivity is weak (generally $< 10^{-3}$) and $Q >> Q_C$ (where Q_C is the critical value below which total reflection is observed). Under these conditions, the specular component of reflectivity, $R(Q)$, is,

$$R(Q) = \frac{16\pi^2}{Q^2}\left|\rho(Q)\right|^2 \qquad \text{Equation 2.3.21.}$$

where $\rho(Q)$ is the one dimensional Fourier transform of $\rho(z)$, the scattering length density distribution normal to the interface.

$\rho(Q)$ can be expressed as,

$$\rho(Q) = \int_{-\infty}^{\infty} \exp(iQz)\rho(z)dz \qquad \text{Equation 2.3.22.}$$

$$\rho(z) = \sum_i n_i(z)b_i \qquad \text{Equation 2.3.23.}$$

where $n_i(z)$ is the number density of species i at a distance z, normal to the interface.

By combining, equations 2.3.22 and 2.3.23, we have,

$$\begin{aligned}\rho(Q) &= \sum b_i \int_{-\infty}^{\infty} \exp(iQz)n_i(z) \\ &= \sum b_i n_i(Q)\end{aligned} \qquad \text{Equation 2.3.24.}$$

Inserting equation 2.3.24 into equation 2.3.21 and writing $\rho(Q)$ in terms of $\sum b_i n_i(Q)$, $R(Q)$ can be expressed as follow,

$$R(Q) = \frac{16\pi^2}{Q^2}\sum_i\sum_j b_i b_j h_{ij}(Q) \qquad \text{Equation 2.3.25.}$$

where h_{ij} is known as the partial structure factor.

Alternatively, equation 2.3.21 can be written in terms of the gradient of the scattering length density profile, $\rho' = d\rho/dz$,

$$R(Q) = \frac{16\pi^2}{Q^4}\left|\rho'(Q)\right|^2 \qquad \text{Equation 2.3.26.}$$

where,

$$\rho'(Q) = \int_{-\infty}^{\infty} \exp(iQz)\frac{d\rho}{dz}dz \qquad \text{Equation 2.3.27.}$$

Consequently, $R(Q)$ can also be expressed as,

$$R(Q) = \frac{16\pi^2}{Q^4} \sum_i \sum_j b_i b_j h'_{ij}(Q) \qquad \text{Equation 2.3.28.}$$

When $i = j$, the self partial structure factor for species i, h_{ii}, is obtained. This describes the distribution of these species (i and j) in the surface layer, i.e., the composition and the thickness of the regions containing the species. $h'_{ij}(Q)$ is the gradient in the self partial structure factor, given by,

$$h'_{ii}(Q) = \left|n'_i(Q)\right|^2 \qquad \text{Equation 2.3.29.}$$

and $h'_{ii}(Q)$ is related to the partial structure factor by,

$$h_{ii}(Q) = Q^2 h'_{ii}(Q) = (n_i(Q))^2 \qquad \text{Equation 2.3.30.}$$

where $n_i(Q)$ is the one-dimensional Fourier transform of the number density distribution of component i in the surface layer.

When $i \neq j$, the cross partial structure factor, $h_{ij}(Q)$ is obtained, giving information on the distribution of species i and j relative to each other, i.e., information about the separation between the two components.

$$h'_{ij}(Q) = h'_{ji}(Q) = \mathrm{Re}\left|n'_i(Q) n'_j(Q)\right| \qquad \text{Equation 2.3.31.}$$

Imagine a polymer (p), and the subphase w (water), the kinematic expression for the total reflectivity of the system becomes,

$$R(Q) = \frac{16\pi^2}{Q^4}\left[b_p^2 h'_{pp}(Q) + b_w^2 h'_{ww}(Q) + 2b_p b_w h'_{pw}(Q)\right] \qquad \text{Equation 2.3.32.}$$

To characterise fully the polymer organisation (determination of both self and cross partial structure factors) a set of three experimental contrasts[41] at the same bulk concentration of polymer is required to solve equation 2.3.32. This is achieved by changing the isotopic composition (interchanging hydrogen and deuterium labelling), as different values for b_p and b_w can be obtained. Therefore two polymers are required: the fully deuterated and fully hydrogenated version. Two different subphases are also used: D_2O and nrw (b_w = 0). The resulting three experimental contrast conditions relevant to this study are,

1- Hydrogenous polymer in D_2O.
2- Deuterated polymer in nrw.
3- Deuterated polymer in D_2O.

As discussed previously, the kinematic approximation only applies in regions where $Q >> Q_c$ but also raw data need to be corrected before analysis as multiple scattering within the material could limit the use of the kinematic approximation. Especially for highly reflecting surface (D_2O), multiple scattering is inevitable. To overcome such a limitation, Crowley[42] introduced a correction factor (equation 2.3.33) that scales the experimental data by the reflectivity of a smooth surface, using the kinematic reflectivity $R_s(Q)$ and the Fresnel reflectivity R_f, calculated using exact methods.

$$R(Q) = \left[\frac{1+\left(1-\frac{Q_c^2}{Q^2}\right)}{2}\right]\frac{R_{\text{exp}} - R_f}{1-R_f} + R_s(Q) \qquad \text{Equation 2.3.33.}$$

where,

$$R_f = \left[\frac{Q-(Q^2-Q_c^2)^{1/2}}{Q+(Q^2-Q_c^2)^{1/2}}\right] \qquad \text{Equation 2.3.34.}$$

and,

$$R_s = \frac{(\rho_2-\rho_1)^2 \times 16\pi^2}{Q^4} \qquad \text{Equation 2.3.35.}$$

ρ_2 and ρ_1 is simply the difference in scattering length density between two media, i.e. D_2O and air respectively (in this study).

Interpretation of the data in the partial structure factor necessitates the use of a model that predicts the distribution of the components (polymer and subphase) from the interface, i.e. $n(z)$, hence $n(Q)$ upon Fourier transformation. Numerous models have been applied to experimental data including a uniform layer, Gaussian distribution, single parabola distribution, double uniform layer, double Gaussian distribution, double uniform parabolas and hyperbolic tangent profile (tanh). By knowing $n(Q)$ the correspondent partial structure factor can be determined (equation 2.3.30). Details of each model and their applications to experimental profiles are given in Chapter Four, section 4-3-2.

The cross-partial structure factor provides information regarding the relative positions of two components (namely the centre-to-centre separation between the components) and their distribution at the near surface[43]. The cross-partial structure factor between two distributions is expressed as,

$$h_{ij}(Q) = \mathrm{Re}\{n_i(Q)n_j(Q)\exp(\mathrm{i}Q\delta)\} \qquad \text{Equation 2.3.36.}$$

where δ is the distance between the centre of the distribution of the two components.

If n(z) is even about the centre, i.e. a symmetrical model (for example a Gaussian distribution) then the Fourier transform is an even function. This is generally observed for amphiphilic molecules confined to the interface. The other possibly is that n(z) is odd, i.e. asymmetric subphase distribution (example tanh profile) then the Fourier transform is imaginary. If it is assumed that $n_p(z)$ and $n_w(z)$ are exactly even and odd respectively, then the cross-partial structure factor can be written,

$$h_{pw}(Q) = \pm\left(h_{pp}h_{ww}\right)^{1/2}\cos(Q\delta) \qquad \text{Equation 2.3.37.}$$

If $n_p(z)$ and $n_A(z)$ are exactly even,

$$h_{pw}(Q) = \pm\left(h_{pp}h_{AA}\right)^{1/2}\sin(Q\delta) \qquad \text{Equation 2.3.38.}$$

The ± operator results from uncertainty about the phase and introduces some inevitable ambiguity.

The kinematic approximation is therefore a very instructive analysis as both the number density distribution of each component and their separations become accessible.

2-4 Surface Quasi-elastic Light Scattering (SQELS)

SQELS is a well-established technique that has been successfully applied to polymer dynamics to determine the dynamic behaviour of polymers at interfaces.

Liquid surfaces are continually perturbed by thermal fluctuations, which can be decomposed into a series of discrete Fourier modes and are commonly known as capillary waves[44]. The amplitude of capillary waves is quite small (~2 Å for water) and these capillary waves generally have a wavelength of circa 100 μm and an associated frequency in the order of 100 kHz. When a light beam is projected on the surface, it is scattered efficiently by the capillary waves and can be analysed either in time or frequency domain to give the frequency, ω_0, and the damping, Γ, of the capillary wave. For a pure liquid these parameters are dependent on its surface tension (γ_0), the density (ρ) and the viscosity (η).

A propagating capillary wave with a vertical displacement, ξ, from its equilibrium plane at a time t is described by,

$$\xi(x,t) = \xi_0 \exp(i(qx + \omega t)) \qquad \text{Equation 2.4.1.}$$

where q is the surface wave number of the capillary wave which has a frequency, ω, and propagates in the x-direction.

ω is a complex quantity composed of the capillary wave real frequency ω_0 (subject to a decay process) and the damping, Γ.

$$\omega = \omega_0 + i\Gamma \qquad \text{Equation 2.4.2.}$$

In equation 2.4.1, the parameter q is the surface wavenumber of a capillary wave and is given by,

$$q = \frac{2\pi}{\lambda} \qquad \text{Equation 2.4.3.}$$

where λ is the wavelength of the capillary wave.

When light is incident on the surface, it is scattered due to the displacement on the surface caused by the capillary waves. This is shown in figure 2.4.1.

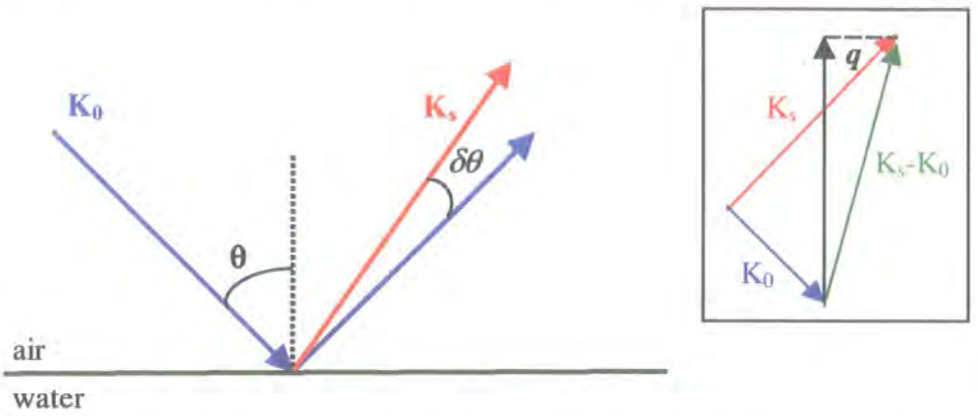

Figure 2.4.1: Representation of the result of an incident beam (0), scattered (s) on an air-water interface and definition of the scattering vector q.

The angle of scatter $\delta\theta$ is related to q and the incident angle (as shown in the resultant vector diagram in figure 2.4.1) by,

$$q = 2K_0 \sin\left(\frac{\delta\theta}{2}\right)\cos\theta \qquad \text{Equation 2.4.4.}$$

When a surface film is present, the properties of the capillary wave are modified as the material changes the frequency and the damping of the capillary waves. Although up to five hydrodynamic modes[45] can be supported by a monolayer covered surface only two are of crucial importance in this study. They are known as lateral compression (longitudinal mode) and vertical compression (transverse mode) and are illustrated in figure 2.4.2.

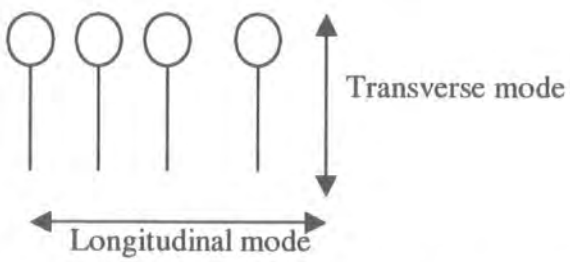

Figure 2.4.2: Schematic representation of the transverse and longitudinal modes.

Capillary wave are dispersive and for any frequency dependent property, the wave number, q, and the frequency, ω_0, of the capillary waves are related by a dispersion equation. This has been demonstrated by Lucassen-Reynders and Lucassen in 1969[44] and a general expression for an air-water interface covered with a surface film is given in equation 2.4.5.

$$D(\omega) = \left[\varepsilon q^2 + i\eta\omega(m+q)\right]\left[\gamma q^2 + i\eta\omega(m+q) - \omega^2\rho/q\right] + \left[\eta\omega(q-m)\right]^2 = 0$$

Equation 2.4.5.

where the parameter m is defined by,

$$m = \mathrm{Re}\left|(q^2 + i\omega q/\eta)\right|^{1/2} \qquad \text{Equation 2.4.6.}$$

and ρ and η are the density and viscosity of water, and ε and γ are the moduli for the dilational and capillary waves respectively.

The solution of the dispersion equation leads to two physical roots in terms of the surface tension (γ), the liquid density (ρ) and the liquid viscosity (η). The first one refers to the capillary waves[46] (transverse motion) and the second to the dilational waves[47] (longitudinal motion). To a first approximation, the equations 2.4.7 (capillary mode) and 2.4.8 (dilational mode) are given in the complex form ($\omega = \omega_0 + i\Gamma$),

Capillary mode $$\omega = \sqrt{\frac{\gamma q^3}{\rho}} + i\frac{2\eta q^2}{\rho} \qquad \text{Equation 2.4.7.}$$

Dilational mode $$\omega = \frac{1}{2}\left(\sqrt{3} + i\right)\left(\frac{\varepsilon^2 q^4}{\eta\rho}\right)^{1/3} \qquad \text{Equation 2.4.8.}$$

According to equations 2.4.7 and 2.4.8, it is evident that the capillary waves are mainly controlled by the surface tension whilst the dilational waves are influenced mostly by the dilational modulus ε at low q values. ε corresponds to the Gibbs static elasticity, $\varepsilon_{0ST} = \Gamma\left(\frac{d\pi}{d\Gamma}\right)$ (for further details, refer to Chapter Five, section 5-3-4).

Both moduli are complex quantities and can be expanded using linear response theory to include energy dissipation.

$$\gamma = \gamma_0 + i\omega\gamma' \qquad \text{Equation 2.4.9.}$$

$$\varepsilon = \varepsilon_0 + i\omega\varepsilon' \qquad \text{Equation 2.4.10.}$$

where γ_0 and ε_0 are the interfacial tension and elastic modulus respectively and ε' and γ' are the dilational and transverse shear viscosity respectively.

The motion of the dilational mode is weakly coupled to the capillary mode to an extent depending upon the coupling coefficient[48], η = (q-m) for an air-liquid interface. It is therefore technically incorrect to refer to the motion as consisting of purely translational or longitudinal waves, therefore the terms capillary and dilational modes are preferred.

Only capillary waves scatter light efficiently as they are predominantly transverse in nature. However, as depicted in equation 2.4.5, the dispersion equation has two real roots corresponding to capillary waves and dilational waves. Therefore, when analysing the capillary wave scattering, both modes are present due to the coupling between them. The best experimental conditions, giving the opportunity to observe dilational wave characteristics, is when the two modes are in resonance, i.e. the capillary and dilational waves have identical frequencies. Resonance occurs when $\varepsilon_0 / \gamma_0 = 0.16$ and produces a maximum in the damping and frequency of the capillary wave.

Having introduced the form of the dispersion equation ($D(\omega)$), the relationship between $D(\omega)$ and the scattered light needs to be established.

The power spectrum of light scattered from the surface by the capillary waves and expressed in terms of the dispersion function is given by equation 2.4.11.

$$P(\omega) = \frac{-2k_B T}{\omega} \mathrm{Im}\left\{\frac{i\eta\omega(q+m)+\varepsilon q^2}{D(\omega)}\right\} \qquad \text{Equation 2.4.11.}$$

where k_B is the Boltzman's constant and T is the absolute temperature.

The resulting spectrum of light has the shape of a skewed Lorentzian function[49] whose central frequency gives the frequency of the capillary wave, ω_0, and the line width, the capillary wave damping, Γ. Since this expression for the spectrum contains the dispersion equation, by suitable fitting, all four surface viscoelastic parameters are accessible.

It is possible to record the power spectrum of light by the correlation function, $g(\tau)$ which is the Fourier transform of $P(\omega)$ (equation 2.4.12).

$$g(\tau) = FT\left[P(\omega, \gamma_0, \gamma', \varepsilon_0, \varepsilon')\right] \qquad \text{Equation 2.4.12.}$$

Even though the capillary waves scatter light efficiently, the intensity of scattering remains weak and the intensity falls off rapidly as q^{-2}. To be able to record the scattered light, it is therefore mixed with a reference beam of light and results in a heterodyne signal[50,51] detected by a photomultiplier tube (further details in section 2-4-3). Recording the scattered light in the time domain results in the correlation function having the shape of a damped cosine function, with a frequency ω_0 and a damping factor Γ. The experimental correlation function obtained, $g(\tau)$ is given in equation 2.4.13 and contains contribution from both heterodyning and homodyning.

$$g(\tau) = (I_s + I_r)^2 + I_s I_r g^1(\tau) + I_s^2 \left| g^2(\tau) - 1 \right| \qquad \text{Equation 2.4.13.}$$

where I_s and I_r are the intensity of the scattered and reference beams respectively, and τ is the delay time. $g^1(\tau)$ is the Fourier transform of the power spectrum referred to earlier and involves only the heterodyne contribution. To ensure that the homodyne contribution (I_s^2 term) is minimal the ratio of I_s / I_r must be greater than 10^{-3}. This is achieved by attenuating the light beam using neutral density filters.

2-4-1 The Cosine Fit

As the Lorentzian power spectrum corresponds to an exponentially damped cosine in the time domain, $g(\tau)$, the correlation function, can be described by the following equation[52],

$$g(\tau) = B + A \times \cos(\omega_0 \tau + \phi) \times \exp\left(\frac{-\beta^2 \tau}{4^2}\right) + C\exp(-\alpha\tau) - D\tau^2$$

Equation 2.4.14.

Where ϕ arises from the skewed nature of the power spectrum (deviation of the power spectrum from the true Lorentzian shape). The background level, B, is modified by the term $D\tau^2$ to account for "droop" on the correlation function caused by external mechanical vibrations. Such external vibration can be limited by mounting the experimental system on a vibration isolation unit on top of an optical table. A is the function amplitude and the Gaussian term, $\exp\left(\frac{-\beta^2\tau}{4^2}\right)$, takes into account the broad nature of the scattered intensity of light due to finite size of the incident beam sampling multiple capillary wave fluctuations. The term $C\exp(-\alpha\tau)$ incorporates the fast relaxation processes that become apparent at short correlation channel widths (2 μs).

This technique allows the determination of the frequency and the damping of the capillary waves by fitting an equation of this form to the experimental data. However, although this method allows the determination of Γ and ω_0, there is no information about the three-viscoelastic parameters (γ, ε, ε'). The extraction of the viscoelastic parameters necessitates a more complex fitting routine known as a spectral fit[53].

2-4-2 Spectral Fit

The equation used for analysing the data is similar to equation 2.4.14, excepted that the cosine term is replaced with the Fourier transform of the power spectrum. It is given in equation 2.4.15.

$$g(\tau) = B + A \times FT\left[P(\omega, \gamma_0, \gamma', \varepsilon_0, \varepsilon')\right] \times \exp\left(\frac{-\beta^2 \tau}{4^2}\right) + C\exp(-\alpha\tau) - D\tau^2$$

Equation 2.4.15.

No assumptions have to be made to analyse the data as this analysis uses the entirety of the light scattering data. To analyse the data, the three parameters are estimated (assuming $\gamma' = 0$ in this study) from which a power spectrum is generated. This is numerically Fourier transformed to give the correlation function which is then fitted in to the experimental data by using a least-squares fitting routine until the best fit is obtained, thus leading to the determination of the three-viscoelastic parameters.

2-4-3 Instrumental Details

All surface quasi-elastic light scattering (SQELS) measurements were performed using light scattering apparatus constructed in Durham University. A schematic representation of the apparatus is given in figure 2.4.3.

All of the optical components and the sample environment are mounted on an optical table, inside a large steel framed and tinted Perspex cabinet. The principle of light scattering experiments is to focus polarised light from a 400 mW solid state diode pumped laser (λ_0 = 532 nm) onto the water surface using a series of lenses and mirrors and to collect the scattered light for further analysis. Initially the laser light is reflected down the optical rail and through the half wave plate (W) and polariser (P). The wave plate rotates the plane of polarised light to attenuate the power of the laser whilst the polariser removed any remaining horizontal polarised light. The light then passed through the first lens (L1), which focussed the beam to pass through the diffraction grating (DG) to provide a series of reference light sources for heterodyne correlation at the photomultiplier tube (PMT). The resulting diverging beams are attenuated by using neutral density filter (NDF) in order to reach optimum conditions for heterodyne correlation. The main beam and diffracted beams are subsequently re-converged by the second lens (L2) and are reflected by mirrors 1 and 2 (M1 and M2) onto the liquid surface. M1 reflects the light by 90° so the beam is travelling vertically when it falls onto M2, where it is reflected onto the liquid surface. A circular and thermostatically controlled (298 K) stainless steel trough equipped with a lid having a

window on the top for the incident and scattered laser beams was placed on a vibration isolation unit to minimise the external vibrations. The light was reflected from the liquid surface and scattered proportionally with the dynamic properties of the liquid surface.

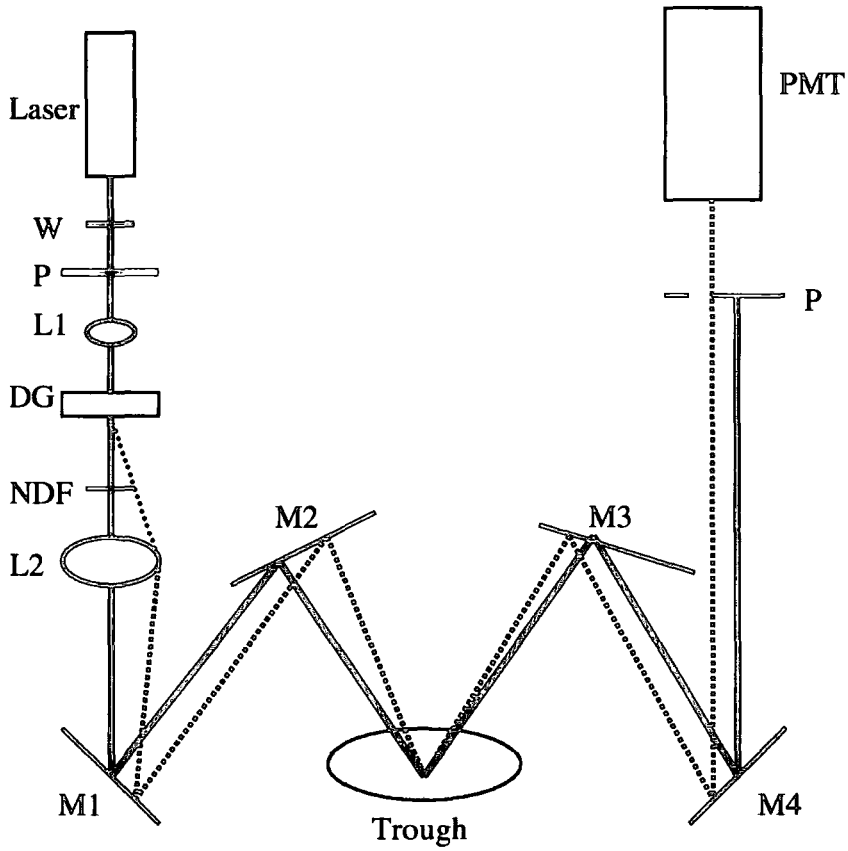

Figure 2.4.3: Schematic representation of the SQELS apparatus.

The light was then reflected by mirrors 3 and 4 (M3 and M4). M4 reflects the light at 90° so the path of the beam is once again parallel with the optical rail. As the beam travels further down the rail, divergence occurs leading to a horizontal array of spots at the PMT. Each beam corresponds to a different scattering angle, θ, and is coincident with light scattered at that same angle and thus a range of scattering vectors, q, can be explored. A pinhole (P) is placed in front of the PMT and by adjustment of mirrors M3 and M4, placed on a motor controlled mount, the diffracted beams can be focussed onto the detector in turn. This provides a means of probing behaviour over a range of q, and therefore wave frequencies. The output from the PMT is analysed by a Brookhaven correlator (model BI9000), connected to a PC. The drawback of BI9000 is that the channel widths are fixed at 10, 5, 2, or 1 μs with a

maximum of 256, 200, 72 or 42 linearly spaced data channels respectively. The final form of the data of the raw data, $g(\tau)$, is stored on a PC and fitted subsequently using cosine and spectral fits.

2-5 References

1) Cowie, J.M.G. *Polymers: Chemistry and Physics of Modern Materials*, 2nd Edition, **1997**, Blackie Academic and Professional, Glascow.
2) Merriam-Webster Dictionary, **1997**.
3) Billmeyer, F.W. *Textbook of Polymer Science*, **1984**, John Wiley and Sons, Singapore.
4) Odian, G. *Principles of Polymerisation, 3rd Edition*, **1991**, John Wiley & Sons, New York.
5) Cram, D.J. *Fundamentals of Carbanion Chemistry*, **1965**, Academic Press, New York.
6) Hsieh, H.L.; Quirk, R.P. *Anionic Polymerisation, Principles and Practical Applications*, **1996**, Marcel Dekker, New York.
7) Flory, P.J. *J. Chem. Phys.*, **1941**, 9, 660.
8) Shaw, D.J. *Colloid and Surface Chemistry, Fourth Edition*, **1996**, Butterworth-Heinemann.
9) Fleer, G.J.; Cohen Stuart, M.A.; Scheutjens, J.M.H.M.; Cosgrove, T.; Vincent, B. *Polymers at Interfaces*, **1993**, Chapman & Hall, London.
10) Jones, R.A.L.; Richards, R.W. *Polymers at Surfaces and Interfaces*, **1999**, Cambridge University Press, UK.
11) Lee, L.H. *Adhesion and Adsorption of Polymers*, **1980**, Plenum Press, New York.
12) Napper, D.H. *Polymeric Stabilisation of Colloid Dispersions*, **1983**, Academic Press, London.
13) de Gennes, P.G.; Puech, P.H.; Brochard-Wyart, F. *Langmuir*, **2003**.
14) Jenkel, E.; Rumbach, B.; *Elektrochem*, **1951**, 55, 612.
15) Alexander, S.J. *J. Phys. (Paris)*, **1977**, 38, 977.
16) de Gennes, P.G. *Macromolecules*, **1980**, 13, 1069.
17) Milner, S.T.; Witten, T.A.; Cates, M.E. *Macromolecules*, **1988**, 21, 2610.
18) Shim, D.F.K.; Cates, M.E. *J. Phys. France*, **1980**, 50, 3535.
19) Besseling, N.A.M.; Lyklema, J. *J. Phys. Chem. B*, **1997**, 101, 7604.
20) Butler, J.A.V. *Trans. Faraday Soc.*, **1937**, 33, 229.

21) Kronberg, B.; Costas, M.; Silveston, R. *Pure Appl. Chem.*, **1995**, 67, 897.

22) Frank, H.S.; Evans, M.W. *J. Chem. Phys.*, **1945**, 13, 507.

23) De Jong, P.H.K.; Wilson, J.E.; Neilson, G.W.; Buckingham, A.D. *Mol. Phys.*, **1997**, 91, 99.

24) Meng, E.C.; Kollman, P.A. *J. Phys. Chem.*, **1996**, 100, 11460.

25) Haymet, A.D.J.; Silverstein, K.A.T.; Dill, K.A. *Faraday Discuss.*, **1996**, 103, 117.

26) Zichi, D.A; Rossky, P.J. *J. Chem. Phys.*, **1986**, 84, 2814.

27) Haymet, A.D.J.; Silverstein, K.A.T.; Dill, K.A. *J. Am. Chem. Soc.* **1998**, 120, 3166.

28) Tanford, C. *The Hydrophobic Effect Formation of Micelles and biological membranes, Second Edition*, **1980**, John Wiley & Sons, New York.

29) Maliniak, A.; Laaksonen, A.; Korppi-Tommola, *J. Am. Chem. Soc.*, **1990**, 112, 86.

30) Blokzijl, W.; Engberts, J.B.F.N. *Angew. Chem., Int. Ed. Engl.*, **1993**, 32, 1545.

31) Lu, J.R.; Thomas, R.K.; Penfold, J. *Adv. Colloids and Interface Sci.*, **2000**, 84, 143.

32) Higgins, J.S.; Benoît, H.C. *Polymers and Neutron Scattering*, **1994**, Oxford University Press.

33) Penfold, J. *Physica B*, **1991**, 173, 1.

34) Lovell, M.R.; Richardson, R.M. *Current Opinion in Coll. And Inter. Sci*, **1999**, 4, 197.

35) Crowley, T.L.; Lee, E.M.; Simister, E.A.; Thomas, R.K.; Penfold, J.; Rennie, A.R. *Colloids and Surfaces*, **1990**, 52, 85.

36) Born, M.; Wolf, E. *Principles of Optics,* **1980**, Oxford University Press, Pergamon.

37) Nevot, L.; Croce, P. *Phys. Appl.*, **1980**, 15, 761.

38) Crowley, T.L.; Ryan, T.W. *J. Phys. D*, **1987**, 20, 61.

39) Abeles, F. *Ann. de Physique*, **1948**, 3, 504.

40) Heavens, O.S. *Optical Properties of Thin Films*, **1955**, Butterworths.

41) Crowley, T.L.; Lee, E.M.; Simister, E.A.; Thomas, R.K. *Physica B*, **1991**, 174, 143.

42) Crowley, T.L. *J. Phys. Chem.*, **1962**, 66, 1858.

43) Simister, E.A.; Lee, E.M.; Thomas R.K. *J. Phys. Chem.*, **1992**, 96, 1373.

44) Lucassen-Reynders, E.H.; Lucassen, J. *Advan. Colloid Interface Sci.*, **1969**, 2, 347.

45) Goodrich, F.C. *Proc. R. Soc*, **1981**, 374, 341.

46) Earnshaw, J.C.; McGivern, R.C. *J. of Colloid and Inter. Sci.*, **1988**, 36, 123.

47) Lamb, H. *Hydrodynamics*, **1945**, Dover.

48) Kramer, L. *J. Chem. Phys.*, **1971**, 55, 2097.

49) Langevin, D. *Light Scattering by Liquid Surfaces and Complementary Techniques, Chapter two*, **1992**, Marcel Decker, New York.

50) Bouchiat, M.A.; Meunier, J. *J. Phys. (Paris)*, **1971**, 32, 561.

51) Earnshaw, J.C.; McGivern, R.C. *J. Appl. Phys.*, **1987**, 20, 82.

52) Kramer, L. *J. Chem. Phys.*, **1971**, 55, 2097.

53) Earnshaw, J.C.; McGivern, R.C.; McLaughlin, A.C.; Winch, P.J. *Langmuir*, **1990**, 6, 649.

Chapter Three

Synthesis and Characterisation

3-1 Introduction

Polyethylene oxide (PEO) is a water soluble polymer that spontaneously forms a surface excess layer when dissolved in water[1]. Previous work reported that modifying PEO by end capping one end or both ends of the polymer chain, not only enhances the surface properties of the polymer molecule[2-4] but also affect its bulk properties[5, 6]. In particular modified PEO incorporating fluorocarbon groups have proven to be highly surface active[7-9]. When polymer chains are grafted by one end or both ends to a surface at sufficiently high grafting density excluded volume interactions between molecules cause them to stretch, forming a brush-like layer[10]. Hence PEO chains with one end capped by perfluorodecanoyl groups may form a brush structure at the air/water interface.

A suitable method is required to synthesise the desired polymers. The first part of this chapter will cover the experimental method used to synthesise PEO with three different molecular weights, circa 2000 g mol^{-1}, 5 000 g mol^{-1} and 10 000 g mol^{-1}, for each molecular weight a hydrogenous and a deuterated version was required. For all polymers an appropriate end capping procedure is described and the problems encountered are detailed. The characterisation of the polymers and a brief description of the characterisation techniques used and the structure and composition of the final polymers will be given in the second part of this chapter.

For ease of reference the notation *n*k IPEO(F) will be used where *n* corresponds to the molecular weight (*n* = 2, 5, or 10), I is the isotopic species (D or H) and F the fluorocarbon group (C_6F_{13}) when PEO is end functionalised.

3-2 Synthesis of PEO via anionic living polymerisation

Chemicals and solvents

All chemicals were obtained from Aldrich Ltd and were used without further purification unless stated otherwise. Solvents were dried using standard conditions detailed in the literature[11].

Experimental method

Synthesis of the initiator

The initiator used for the following synthesis was diphenyl methyl potassium (DPMK) [12] as shown in scheme 3.2.1.

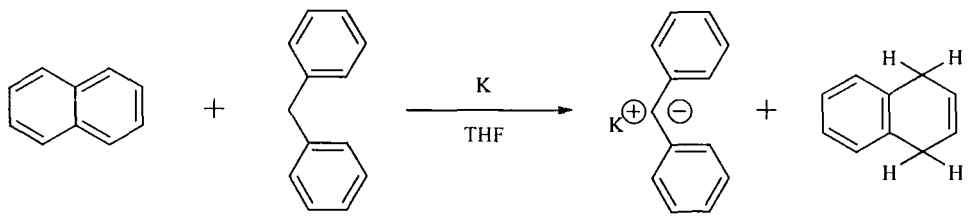

Scheme 3.2.1: Synthesis of diphenyl methyl potassium

To ensure complete conversion of the naphthalene the molar ratio of naphthalene, potassium and diphenylmethane was 0.125: 0.5: 0.33 respectively. Naphthalene was placed in a 3 neck round bottomed flask equipped with stirrer, septum, condenser tube and bubbler under a dry nitrogen purge. Dry THF was added via cannula and the solution cooled to 273 K in an ice bath. Potassium was carefully added into the flask resulting in the solution becoming dark green accompanied by an increase in the temperature. The contents of the flask were then stirred overnight whilst maintained at 273 K.

Diphenylmethane was added dropwise through the septum, the solution becoming a dark red/orange colour. The solution was stirred for two days at room temperature under a nitrogen purge. To remove the excess unreacted potassium, the solution was cannulated out of the flask into a storage bottle sealed by a rubber septum and under a nitrogen atmosphere leaving the excess potassium in the round bottomed flask. The potassium was neutralised by addition of hexane/isopropanol. The initiator solution was stored in a fridge.

Calibration of the initiator

A sample of poly(ethylene oxide) of nominal molecular weight 5 000 g mol^{-1} was synthesised using known quantities of initiator and monomer. By a combination of size exclusion chromatography (SEC) and ^1H NMR analysis, the initiator concentration was calculated. SEC provides the average molecular weights and the polydispersity index of the polymer. To check that the initiator does not include other initiating species (residual potassium or naphthyl potassium), ^1H NMR was used. If only diphenyl methyl potassium initiator is present, we expect 2 main signals: δ~7 ppm for the diphenylmethyl units attached to the end of the polymer and δ~3.5 ppm for the CH_2-CH_2 units of the poly(ethylene oxide) group. From the peak integrals, the number of protons can be determined and the proton ratio of ethylene oxide (EO) monomer to diphenyl group gives the number of repeat units, *n*, the molecular weight can then be calculated.

Using the molecular weights calculated from SEC and ^1H NMR data, the concentration of the initiator was obtained.

Anionic polymerisation of EO

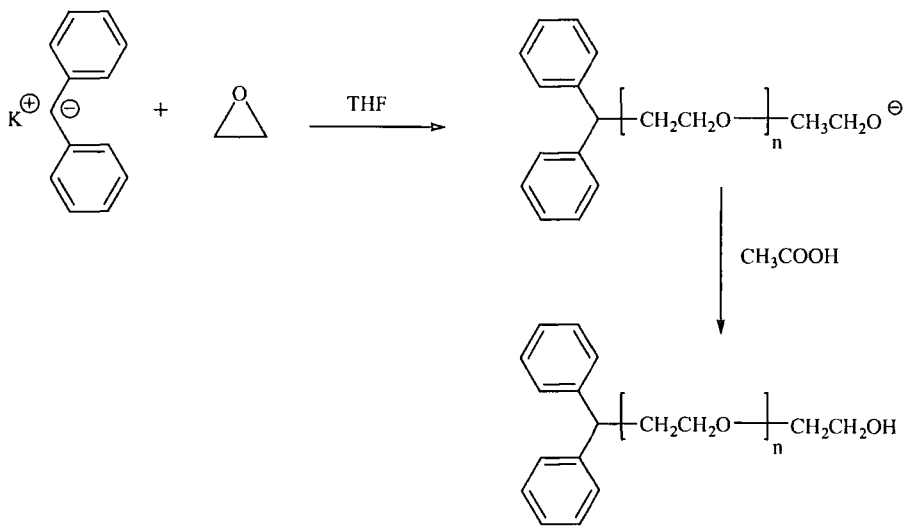

Scheme 3.2.2: Anionic ring opening polymerisation of ethylene oxide.

The first step of this synthesis consists of the purification of ethylene oxide. Due to its high volatility (b.pt. = 286.2 K) and its toxicity (odourless), EO was

manipulated with extreme caution. As supplied, it was first transferred under vacuum into a round bottomed flask fitted with a Young's tap and containing a few grams of potassium hydroxide and a stirrer. The receiving flask was frozen by liquid nitrogen allowing the transfer of EO. The flask was then transferred quickly to the vacuum line and the contents stirred at 273 K overnight.

EO was vacuum distilled on the line to a similar flask containing CaH_2 to remove any water present in EO. The EO was degassed thoroughly by means of repeated freeze-thaw cycles on the vacuum line. The polymerisation of EO was carried out in the reaction flask shown in figure 3.2.3.

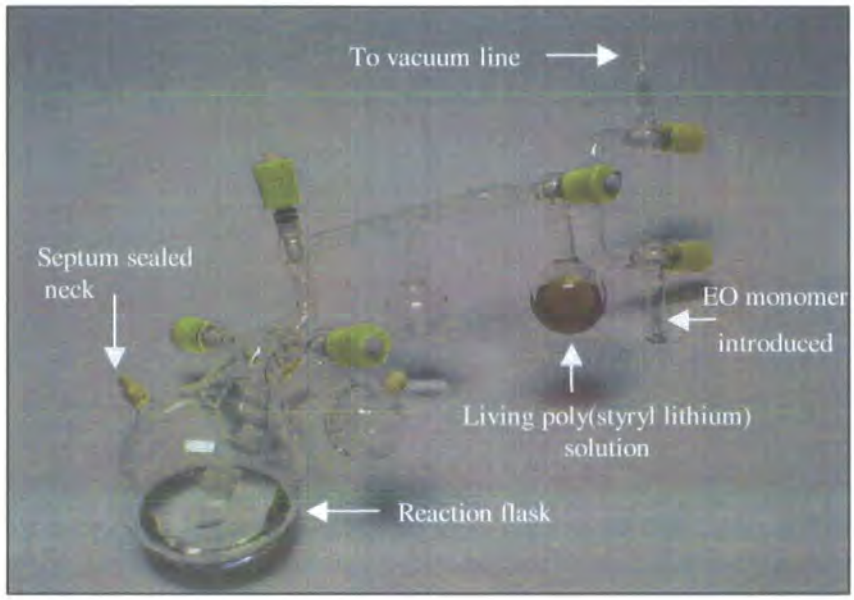

Figure 3.2.3: Reaction flask used for the polymerisation of ethylene oxide

The reaction flask was washed with methanol/acetone and dried. The flask was placed on the vacuum line and evacuated. Immediately before synthesis, the reaction flask was cleaned with a solution of living polystyryl lithium in benzene whilst under vacuum. This solution consists of a small quantity of styrene monomer dissolved in benzene and polymerised anionically by the injection of a few microlitres of 2.5 M n-butyllithium initiator (Aldrich). When the glassware was clean, dry THF (dried over freshly squeezed sodium wire and few crystals of benzophenone) was vacuum distilled into the reaction flask. Before being transferred into the reaction flask, EO required a final purification by transferring to a similar flask equipped with a septum. Dibutyl magnesium was then injected through the septum to remove any

residual water in EO. The flask was then removed from the vacuum line and attached to the reaction flask (see figure 3.2.3). EO was transferred into the reaction flask, which was then cooled in an ice bath. The volume of initiator (V) required was determined by using equation 3.2.1.

$$V = \frac{(m/M)}{c} \qquad \text{Equation 3.2.1.}$$

where m is the mass (g) of EO, M the desired polymer molar mass (g mol^{-1}) and c is the concentration (mol dm^{-3}) of the initiator solution.

The required initiator volume was injected rapidly through the septum and the solution stirred overnight at room temperature. The flask was then warmed to 383 K in an oil bath and held at this temperature for two days with continual stirring to ensure complete conversion of the monomer. The living polymer was terminated by addition of degassed acetic acid to provide a polymer with a hydroxyl group at one end. The polymer was precipitated by pouring the terminated reaction solution into cold hexane, filtered off and dried under vacuum for 3 days at room temperature. All polymers prepared were characterised using SEC, elemental analysis, ^{1}H and ^{19}F NMR. The same procedure was applied to all polymers irrespective of molecular weight or deuteration.

3-3 Initial End Capping Attempt

The end capping reaction via perfluoroheptanoyl chloride acid had been reported in the literature[4] and since this was a facile synthetic route this was attempted first following precisely the procedures outlined in the literature and shown in scheme 3.3.1.

End capping reaction via perfluoroheptanoyl chloride acid.

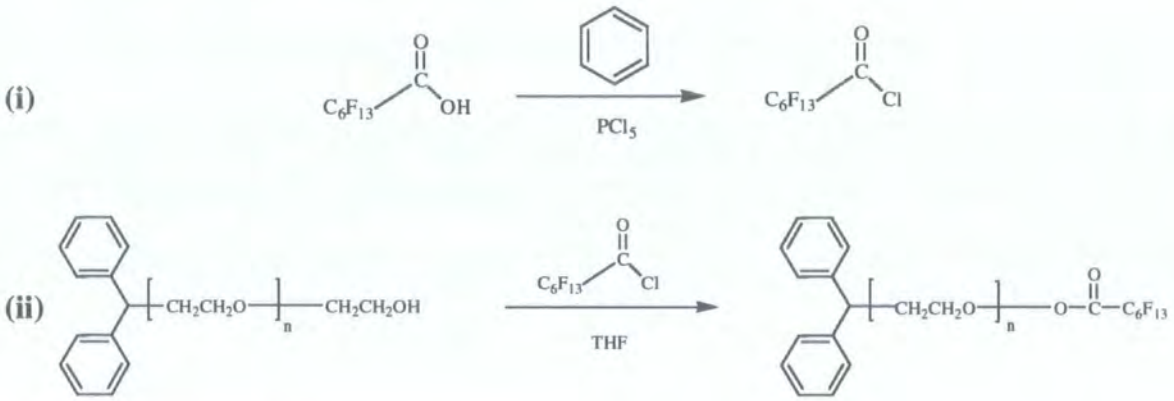

Scheme 3.3.1: End capping reaction via perfluoroheptanoyl chloride acid

The perfluoroheptanoyl end capped PEO (PEOF) by this procedure was characterised via ^{19}F NMR. A characteristic spectrum is shown in figure 3.3.2.

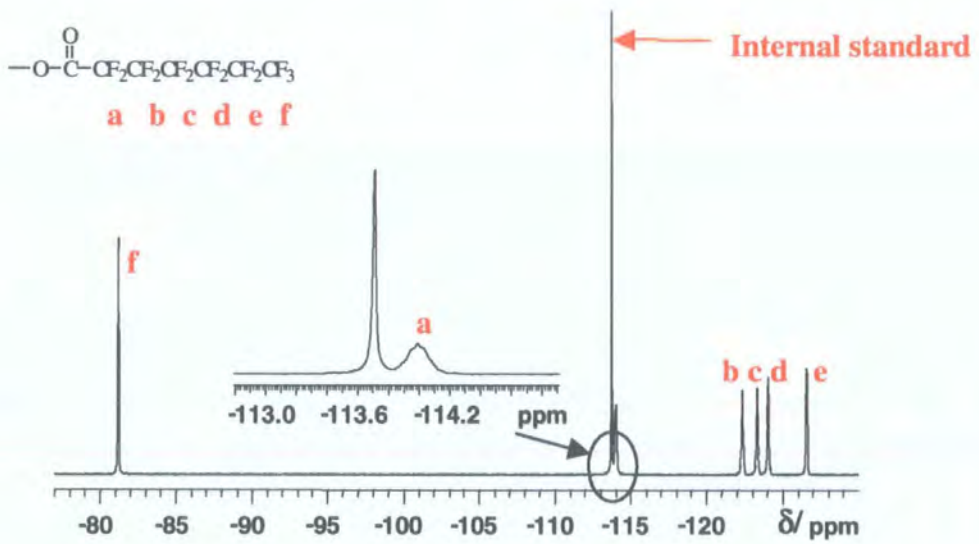

Figure 3.3.2:^{19}F NMR of perfluoroheptanoyl end capped PEO (HPEOF).

Evidence of fluorine content in the sample was quantified via $C_4F_4Cl_4$ as the internal standard and the integration ratio of the characteristic peaks was 88.05 to 100 resulting in 0.95 ± 0.2 % fluorocarbon groups per polymer chains.

However, after dissolution in water for surface tension measurements, the PEOF was recovered and the ^{19}F NMR spectrum redetermined. Figure 3.3.3 shows that only the ^{19}F signal due to the internal standard was observed.

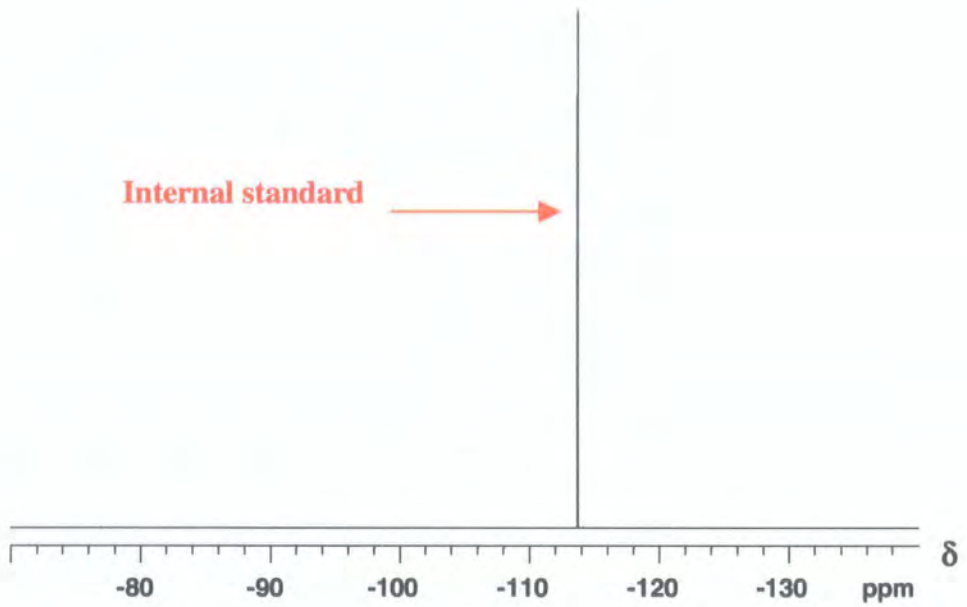

Figure 3.3.3: ^{19}F NMR of recovered HPEOF.

Loss of fluorocarbon in the sample via ester hydrolysis seems to be the most plausible explanation.

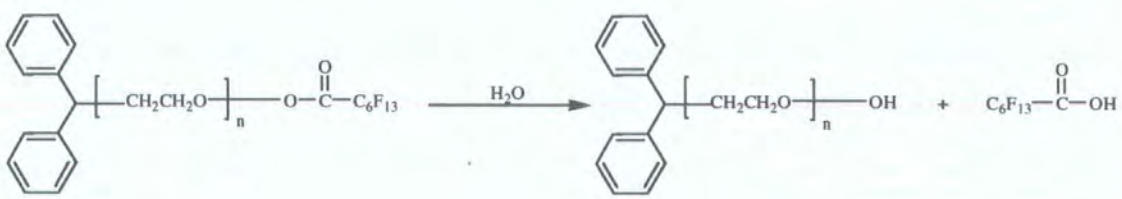

Scheme 3.3.4: Hydrolysis of the ester bond.

A suitable synthetic technique was therefore required in order to improve the stability of the fluorocarbon link to the PEO chain. Isophorone diisocyanate seemed to be the ideal candidate to create a stronger linkage as a peptide bond is generated. One

of the most common examples of the stability of such linkage occurs in DNA, which has been described elsewhere[13].

3-4 End capping reaction via Isophorone Diisocyanate

Materials

Isophorone diisocyanate was purified by vacuum distillation (13.3 Pa, 383 K). The synthesis of the PEO has been outlined above.

Experimental method

End functionalisation was carried out according to the procedure detailed by Xu et al[14]. Two major steps are required for the end capping reaction and are shown in scheme 3.4.1.

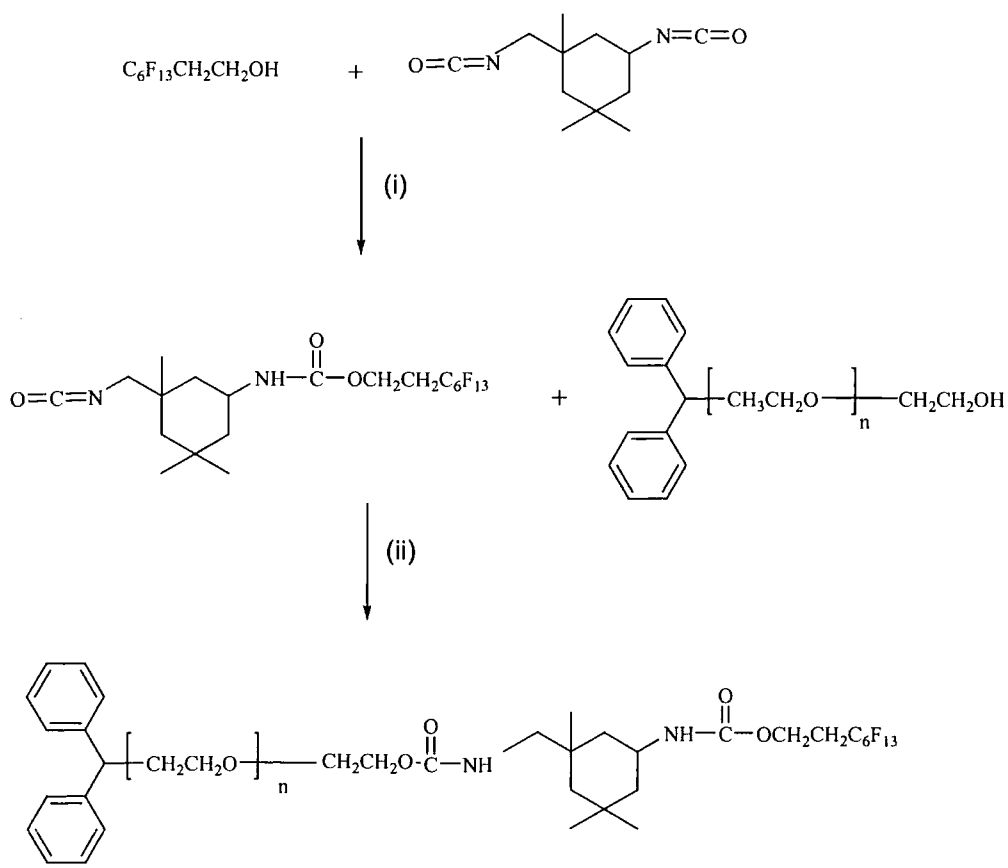

Scheme 3.4.1: End capping reaction of PEO.

(i) Step 1. The preparation of tridecafluorooctanoylisophorone monoisocyanate.

To a three necked round bottomed flask equipped with condenser and nitrogen source at 195 K, tridecafluoro-1-octanol was added. Isophorone diisocyanate (6-fold excess) was injected into the flask and the reaction mixture stirred at 343 K for 12 hours and then the excess isophorone diisocyanate removed by vacuum distillation at 383 K. To ensure the removal of isophorone diisocyanate was complete, hexane was added, the solution refluxed for 1 hour and cooled to 253 K, and the supernatant cannulated out. This operation was repeated three times and the flask was held under reduced pressure for several hours with a nitrogen purge, resulting in a waxy solid in 70% yield.

(ii) Step 2. End capping of PEO

The hydroxyl terminated PEO was placed in a three necked round bottomed flask and dried under vacuum at 378 K overnight. When cooled, the reaction flask was equipped with condenser and nitrogen source to which dry ethylene glycol dimethyl ether was added. Tridecafluorooctanyl isophorone monoisocyanate was dissolved in dry ethylene glycol dimethyl ether and cannulated in the reaction flask. The whole content was then heated to reflux with stirring. Three drops of dibutyltin dilaurate were added as a catalyst and the reaction was refluxed overnight under nitrogen. The solution was allowed to cool and then poured into excess hexane. The precipitated polymer was collected on a glass frit and redissolved in refluxing hexane. This operation was repeated three times. The polymer was then washed two times in refluxing methyl-tert-butyl ether and dissolved in refluxing ethyl acetate and allowed to crystallise on cooling. The polymer (85%) was collected on a glass frit , dispersed in hexane, filtered again and dried in vacuum oven for three days at room temperature.

The extent of functionalisation by the fluorocarbon for each polymer was determined by ^{19}F NMR and 1,4 difluorobenzene as internal standard.

3-5 Characterisation

All end-capped polymers prepared were characterised using size exclusion chromatography (SEC), elemental analysis, ^{1}H and ^{19}F NMR. A brief outline of the characterisation techniques together with molecular weights and efficiency of end capping is given.

3-5-1 Size Exclusion Chromatography (SEC)

Each polymer was analysed by SEC using dimethyl formamide (DMF) as the mobile phase on a Viscotek column TDA 300 machine with Trisec GPC software. The column was equipped with a Polymer Labs Gel (pore size 10^{3}-10^{6} Å) and a Water R403 differential refractometer (flow rate~ 1.0ml/min).

The chromatograms of the three unfunctionalised hydrogenous polymers are shown in figure 3.5.1.

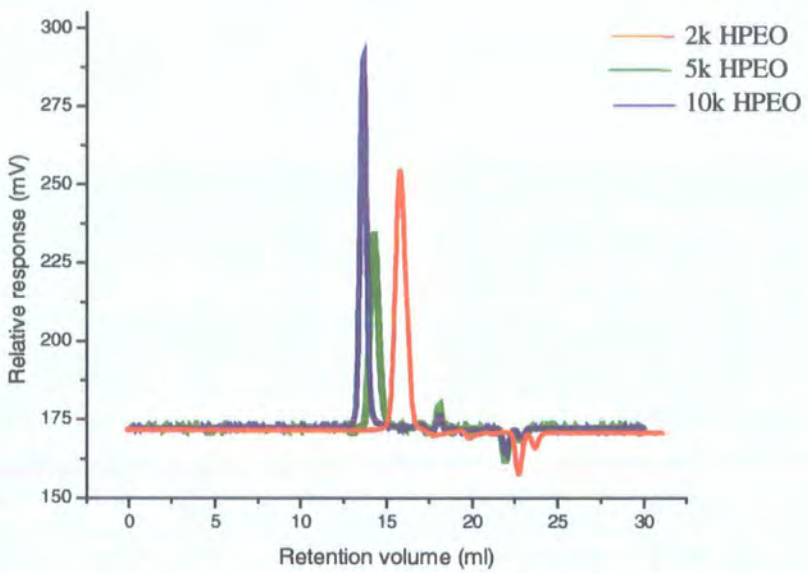

Figure 3.5.1: SEC traces for 2k, 5k and 10k HPEO.

Chromatograms are unimodal in shape for the three different molecular weight polymers. It can be observed (figure 3.5.1), that the elution time for higher molecular weight polymers is less than that of lower molecular weight polymers as anticipated.

Table 3.5.1 shows the SEC results for the range of PEO polymers synthesised (protonated and deuterated) before end-capping.

Polymer	$\overline{M_w}^a$	$\overline{M_n}^b$	$\overline{M_w}/\overline{M_n}^c$	$n_{calc.}{}^d \pm 1$
2k HPEO	2090	1960	1.07	44
2k DPEO	1860	1730	1.08	36
5k HPEO	5060	4770	1.06	108
5k DPEO	4570	4340	1.05	90
10k HPEO	9600	9050	1.06	206
10k DPEO	9800	9230	1.06	192

a- Weight average molar mass

b- Number average molar mass

c- Polydispersity

d- Degree of polymerisation calculated from $\overline{M}_n$

Table 3.5.1: SEC results for protonated and deuterated PEO.

A typical SEC chromatogram for 2k HPEOF, is shown in figure 3.5.2 and a small high molecular weight shoulder is evident.

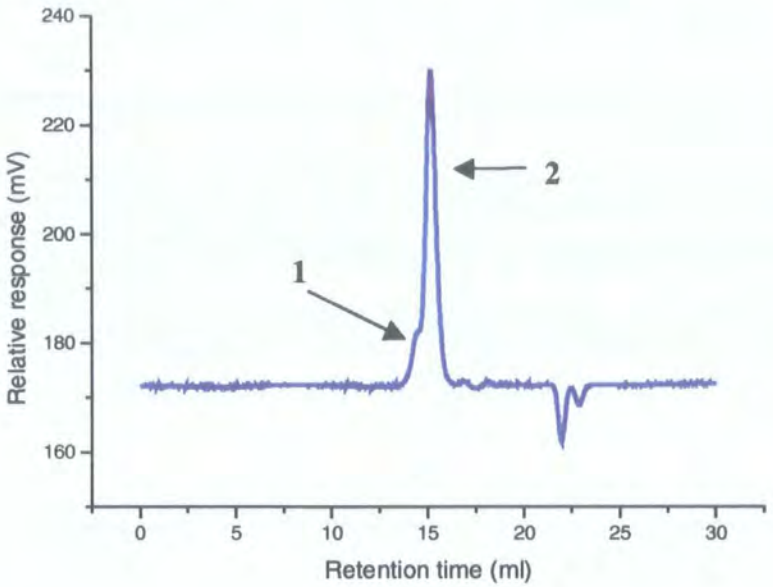

Figure 3.5.2: SEC chromatogram for HPEOF.

The bimodal shape of the chromatogram was observed for the three polymers, suggesting that a coupling reaction between remaining isophorone diisocyanate (despite the procedures used to remove it) and PEO had occurred during the end capping reaction, as shown in scheme 3.5.3.

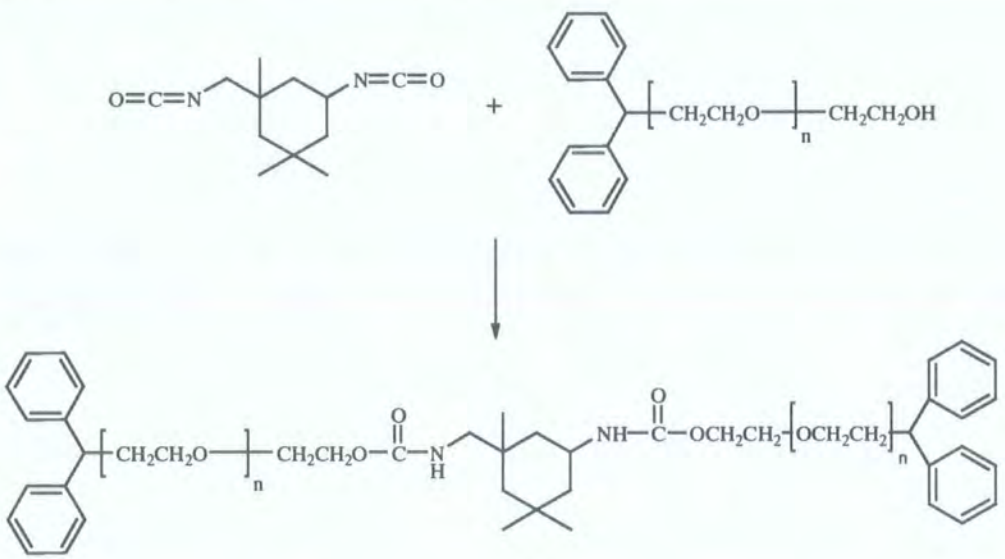

Scheme 3.5.3: Coupling reaction occurring during end capping reaction.

The coupling reaction results in the formation of a polymer with a molecular weight twice that of the original. However, the molecular weight of the two polymers are very close and further purification using fractionation methodologies would have been impossible due to the small difference in molecular weights of the polymers.
The extent of coupling was determined by using equation 3.5.1.

$$\%_{coupling} = {}^{m_1}\!/_{m_2} \qquad \text{Equation 3.5.1.}$$

where m_1 and m_2 are the mass of the peak 1 and peak 2 respectively as shown in figure3.5.2.

The Extent of coupling as well as the SEC results for deuterated and protonated fluorocarbon end-capped PEO are shown in table 3.5.2.

Polymer	$\overline{M_w}$	$\overline{M_n}$	$\overline{M_w}/\overline{M_n}$	$n_{calc.} \pm 1$	% coupling ± 5%
2k HPEOF	2660	2370	1.12	54	12
2k DPEOF	2890	2470	1.17	52	16
5k HPEOF	6320	5430	1.16	123	15
5k DPEOF	5480	4840	1.13	101	15
10k HPEOF	10800	8940	1.17	203	13
10k DPEOF	12400	10800	1.15	225	14

Table 3.5.2: SEC results for protonated and deuterated PEOF.

3-5-2 Elemental analysis

Elemental analysis was applied to determine the percentage of carbon, hydrogen and fluorine present in the modified protonated PEO. To calculate the theoretical percentage of carbon in the material, equation 3.5.2.1 was used.

$$\%C = \frac{(33 \times 12) + (2 \times 12 \times n)}{\overline{M}_n} \qquad \text{Equation 3.5.2.1.}$$

$\overline{M}_n$ corresponds to the number average molar mass of the polymer and has been determined by SEC. By using the same equation and the values obtained for the percentage of carbon in the material, it is also possible to calculate the degree of polymerisation, *n*, of the PEO and to compare it with the theoretical value. By repeating measurements of an identical sample, it was possible to calculate an error for each sample.

The results are listed in table 3.5.2.1.

Theoretical				**Experimental**			
n	% C	% H	% F	*n*	% C	% H	% F
54	86.33	13.01	12.60	53 ± 3	85.20 ±0.30	13.52 ± 0.03	12.82 ± 0.12
123	70.19	11.13	5.18	120 ± 4	68.45 ± 0.41	11.23 ± 0.05	5.02 ± 0.10
203	58.21	9.40	2.73	202 ± 3	57.87 ± 0.33	9.53 ± 0.03	2.45 ± 0.13

Table 3.5.2.1: Results from elemental analysis of the protonated PEOF.

The results from elemental analysis are in good agreement with the theoretical values. However the hydrogen contents are marginally higher in the experimental results, probably due to adsorption of atmosphere moisture during sample preparation for elemental analysis

3-5-3 Nuclear Magnetic Resonance (NMR)

^1H and ^{19}F NMR spectra were recorded at 400 MHz using a Varian VXR 400 spectrometer. Samples were prepared as ~5% solutions in deuterated chloroform ($CDCl_3$, Aldrich).

A characteristic spectrum of PEO is shown in figure 3.5.3.1 and resonance of the methylene protons of PEO is observed at δ 3.64 ppm.

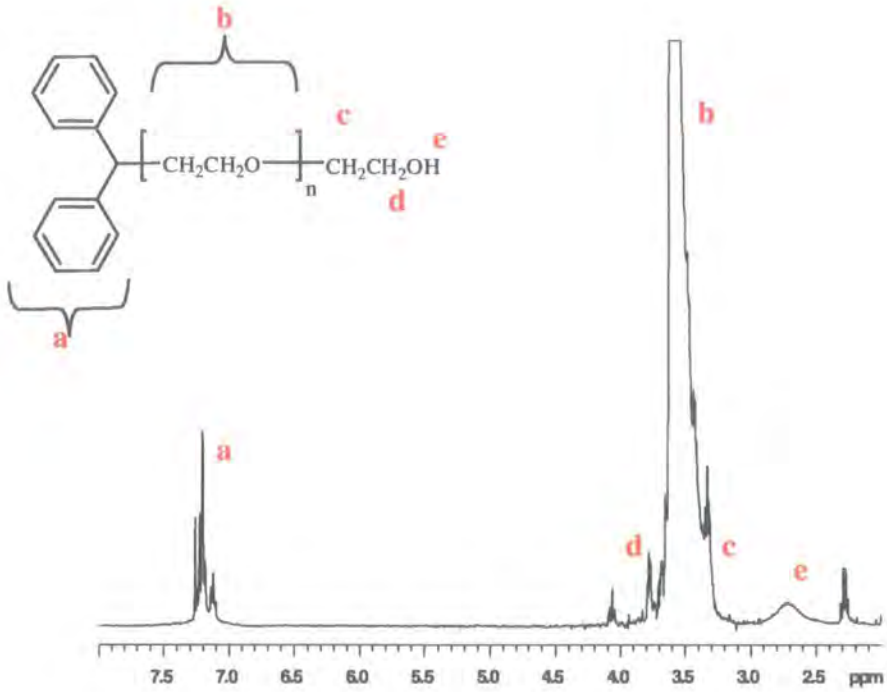

Figure 3.5.3.1: ^{1}H NMR spectrum of PEO.

A typical ^{19}F NMR spectrum of end-capped PEO is shown in figure 3.5.3.2.

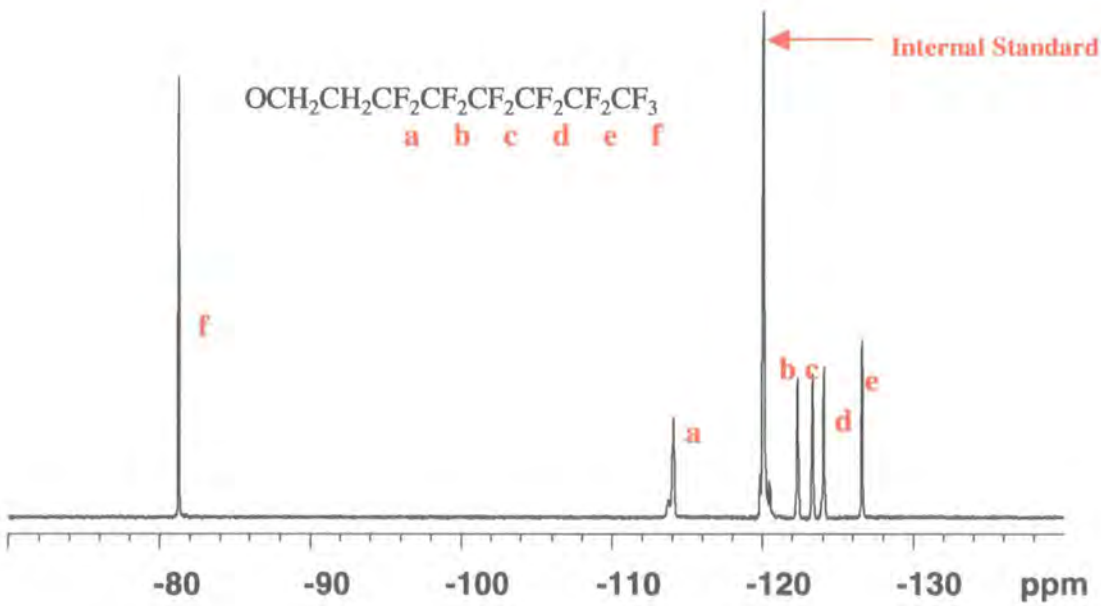

Figure 3.5.3.2: ^{19}F NMR spectrum of PEOF.

Resonance of the 1,4-difluorobenzene (internal standard) is observed at δ -120 ppm. The characteristic peaks for tridecafluorooctanoyl group are as follows: 5 $-CF_2-$ signals observed at δ –114, -122, -123.5, -124, –126.5 ppm and 1 $-CF_3-$ group shown at δ -81.5 ppm.

The number of mol of fluorocarbon group in PEOF, n_{F1}, was determined using the ^{19}F NMR spectrum showed above and calculated using equation 3.5.4.1.

$$n_{F1} = {}^{I_s}\!/_{I_p} \times n_S \qquad \text{Equation 3.5.4.1.}$$

where I_s and I_F are the integrals of the standard and $-CF_2-$ signals respectively. n_S is the number of moles of internal standard calculated knowing the exact volume and density of the standard.

Knowing the exact mass of polymer in the sample, m, the number of moles of PEOF, n_{F2}, can be determined using equation 3.5.4.2.

$$n_{F2} = {}^{m}\!/_{\overline{M_n}} \qquad \text{Equation 3.5.4.2.}$$

where $\overline{M_n}$ is the average molecular weight of PEOF.

The ratio ${}^{n_{F1}}\!/_{n_{F2}}$ is the extent of fluorination; table 3.5.3.1 shows the values obtained.

Polymer	**Fluorocarbon ends per polymer molecule ± 0.2**
2k HPEOF	1.10
2k DPEOF	0.90
5k HPEOF	1.10
5k DPEOF	0.83
10k HPEOF	0.90
10k DPEOF	0.80

Table 3.5.3.1: Extent of fluorination in tridecafluorooctanoyl end-capped PEO.

3-6 Physical properties

Surface Tension Measurements

Surface tension values for aqueous solutions of the polymers were collected using a Krüss K10 digital tensiometer. The temperature of the subphase was regulated at 298 K by using a Haake thermostat water circulator and the surface tension was measured by using a rectangular Wilhelmy plate. Glassware was previously washed by soaking in permanganic acid (mixture of sulphuric acid and few crystals of potassium permanganate) overnight. The vessels were then rinsed several times with ultra high quality (UHQ) water (Elga Technology, High Wycombe, UK) and finally dried at room temperature. The polymer solution was dissolved in UHQ water in a volumetric flask and left overnight to ensure complete dissolution of the material. The dissolved polymer was poured into a 25 ml dish and diluted *in situ*. A range of concentrations between 0.001% and 3% $^{w}/_{v}$ of modified and unmodified PEO were investigated, all required a finite time to reach the equilibrium surface tension as shown in figure 3.6.1.

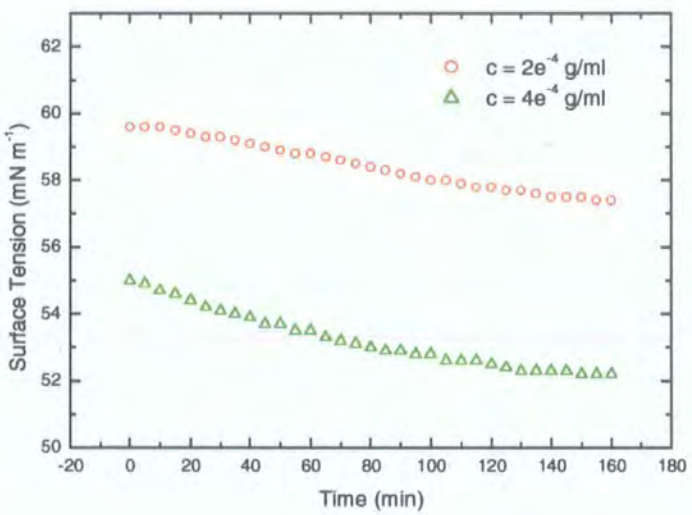

Figure 3.6.1: Approach to equilibrium surface tension for aqueous solutions of 5k PEO F.

Similar approaches to equilibrium were observed for the other PEOF molecular weights, an equilibrium time of ~140 min was required for each

concentration of polymer investigated, whereas ~30 min was sufficient for both deuterated and hydrogenous unmodified PEO

Reproducibility was estimated by repeated measurements of the surface tension of UHQ water, and the uncertainty in surface tension was found to be ± 0.1 mN m^{-1}.

3-7 References

1) Cao, B.H.; Kim, M.W. *Faraday Discuss.* **1994**, 98, 245.

2) Barentin, C.; Muller, P.; Joanny, J.F. *Macromolecules.* **1998**, 31, 2198.

3) Su, Z.; Wu, D.; Hsu, S.L.; McCarthy, T.J. *Macromolecules.* **1997**, 30, 840.

4) Su, Z.; McCarthy, T.J.; Hsu, S.L.; Stidham, H.D.; Fan, Z.; Wu, D. *Polymer.* **1998**, 19, 4655.

5) Zhou, J.; Zhuang, D.; Yuan, X.; Jiang, N.; Zhang, Y. *Langmuir.* **2000**, 16, 9653.

6) Beaudoin, E.; Borisov, O.; Lapp, A.; Billon, L.; Hiorns, R.C.; Francois, J. *Macromolecules.* **2002**, 35, 7436.

7) Bernett, M.K.; Zisman, W.A. *J. Phys. Chem.*, **1967**, 71, 2075.

8) W. A. Zisman, *Advances in Chemistry*, American Chemical Society, Washington DC, (1963).

9) Kuneida, H.; Shinoda, K. *J. Phys. Chem.* **1976**, 80, 2468.

10) DeGennes, P.G. *Macromolecules.* **1980**, 13, 1069.

11) M. Casey, J. Leonard, B. Lygo and G. Procter, (Ed.), *Advanced Practical Organic Chemistry*, Blackie Ltd. (1990).

12) P. H. Richardson, *PhD thesis*, Durham University (1993).

13) Menchen, S.; Johnson, B.; Winnik, M.A.; Xu, B. *Electrophoresis.* **1996**, 17, 14.

14) Xu, B.; Li, L.; Yekta, A.; Masoumi, Z.; Kanagalingam, S.; Winnik, M.A.; Zhang, K.; Macdonald, P.M. *Langmuir.* **1997**, 13, 2447.

Chapter Four

Neutron Reflectometry

4-1 Introduction

Neutron reflectometry data on aqueous solutions of the fluorocarbon end-capped polymers were collected using the SURF reflectometer at the ISIS pulsed neutron source, Rutherford Appleton Laboratory, Didcot, UK. Hydrogenous and deuterated polymers were investigated in null reflecting water (deutero polymer only) and heavy water (both polymers) leading to three isotopic combinations. Three different molecular weight polymers for a series of concentrations up to 0.1% and 1% $^{w}/_{v}$ were investigated. At concentration above 1% $^{w}/_{v}$, phase separation was observed for the lowest molecular weight polymer as oily droplets visible to the naked eye dispersed throughout the aqueous phase. Solutions were poured into a 25 ml Teflon trough inside sealed containers with quartz inlet and outlet windows for the incident and reflected neutron beams. The resultant reflectivity is defined as the ratio of the intensity of the incident beam (measured by monitor) to the reflected beam (measured by a time of flight (TOF) detector) as discussed in Chapter Two, section 2-3-1. Data were converted to absolute reflectivity using calibration factors obtained from fitting to the reflectivity from heavy water. By using three different angles of incidence (0.5°, 0.8°and 1.5°) of the neutron beam, the range of scattering vector ($Q = |\mathbf{Q}|$) explored was $0.019 \leq Q / \text{Å}^{-1} \leq 0.6$. The data collection was instrument controlled through a command file that collected data for a pre-determined integrated incident neutron flux, and altered the geometry of the system when changing angle. Data collection times varied depending not only on the beam current but also on the polymer and the subphase under study. In general data collection times ranged from 30-60 minutes for low angle data to 2-4 hours for high angle data.

The background for each profile was determined by taking the average reflectivity value when the reflectivity had reached a constant value, usually for Q values greater then ~0.4 Å^{-1}. This background signal was subtracted from the raw data and then three combined data files (obtained from each angle of incidence investigated) were saved as ASCII files for the subsequent analysis.

4-2 Results

4-2-1 Surface Tension

The surface tensions for all three molecular weight PEOF compared to that of the surface tension of unmodified polyethylene oxide (PEO) are shown in figure 4.2.1.1.

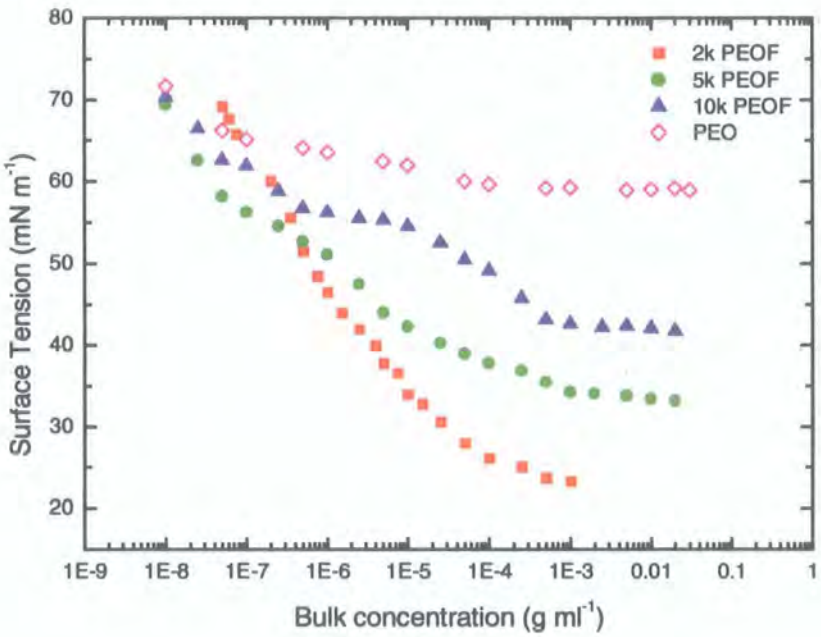

Figure 4.2.1.1: Surface tensions of aqueous solution of fluorocarbon end capped polyethylene oxides and unmodified PEO.

At very low concentrations, the surface tension is essentially that of pure water for all polymers. As the bulk concentration increased, the surface tension of both 2k and 5k PEOF falls off rapidly until a fairly sharp break is observed at higher concentrations followed by constant value of the surface tension. 10k PEOF does not quite show the same trend when compared to 2k and 5k PEOF, as the decrease in surface tension with increasing the bulk concentration is not as monotonic as the two lower molecular weight polymers. A broad shoulder is observed between ~10^{-6} and ~10^{-4} g ml^{-1}, followed by a decrease in surface tension until constant surface tension is observed at circa 10^{-3} g ml^{-1}. The surface tension of unmodified polyethylene oxide exhibits quite

different behaviour, a steady decrease in surface tension being observed with increasing bulk concentration until a constant value of ~60 mN m^{-1} is obtained. A number of studies on the adsorption of PEO from solutions have been reported in the literature. Lovell et al.[1], Couper and co-workers[2], Glass[3], Kim and Cao[4], Daoust et al[5], Rennie et al.[6] and Thomas and co-workers[7] have examined the effect of molecular weight, concentration, substrate conditions and temperature on the coverage of PEO at the air-water interface. The packing of PEO at the surface and consequently reduction of surface tension was attributed to the relative contribution of enthalpy and entropy[1] but also to a change in the nature of the hydrogen bonding with water[4]. It was also speculated that, whatever the molecular weight, portions of the polymer are oriented out of the aqueous phase into the air and molecular weight dependence of the surface tension was observed for concentrated solutions only.

4-2-2 Neutron Reflectometry

Deuterated Fluorocarbon End-Capped Polyethylene Oxide (DPEOF) in Null Reflecting Water (nrw).

The neutron reflectivity for DPEOF in NRW for solutions of 2k, 5k, 10k molecular weight PEOF with concentration are shown in figure 4.2.2.1, 4.2.2.2 and 4.2.2.3 respectively.

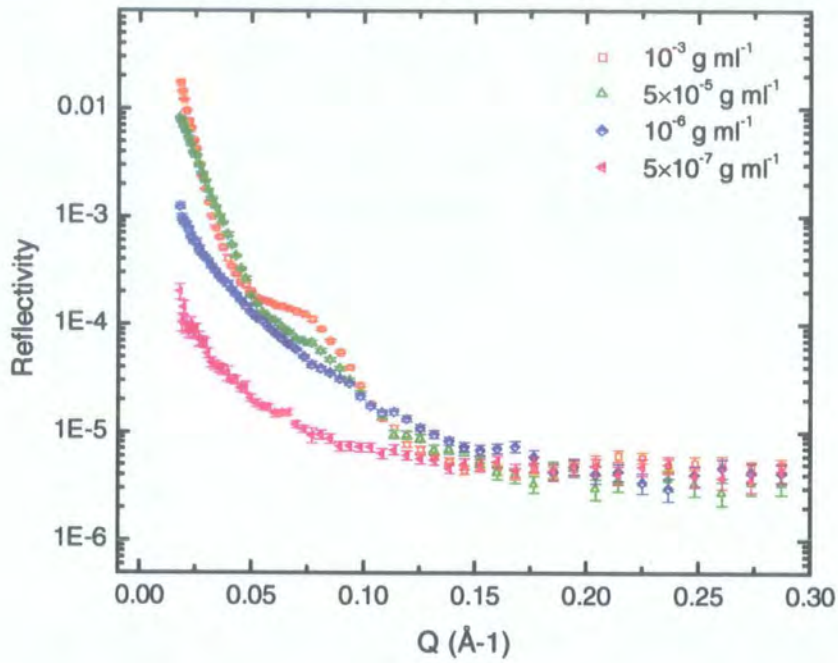

Figure 4.2.2.1: Reflectivity profiles for 2k DPEOF in nrw for a range of bulk concentrations.

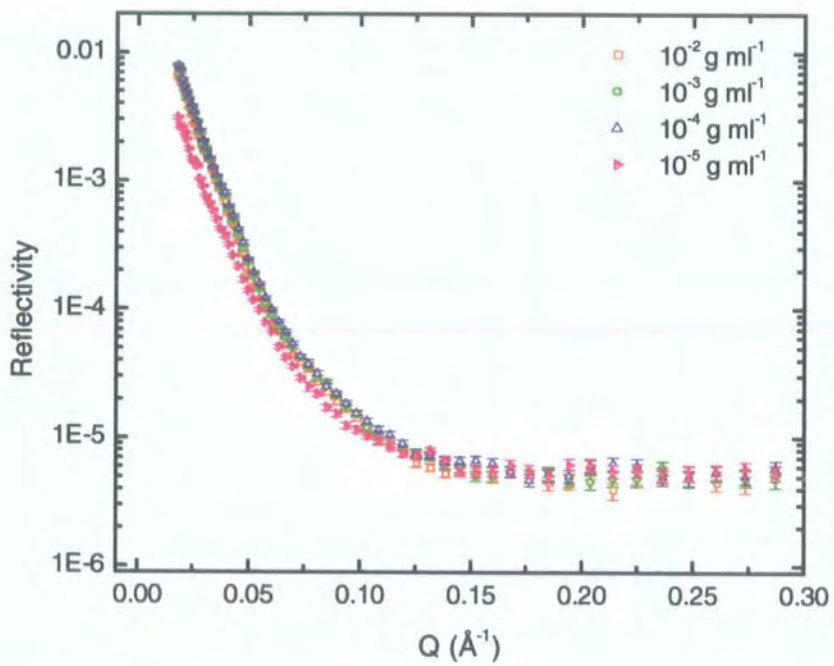

Figure 4.2.2.2: Reflectivity profiles for 5k DPEOF in nrw for a range of bulk concentrations.

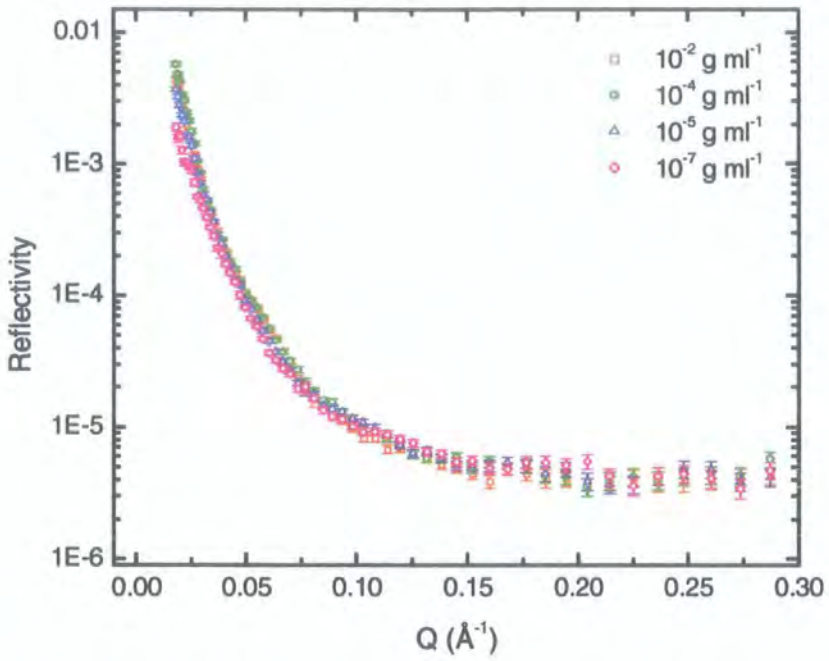

Figure 4.2.2.3: Reflectivity profiles for 10k DPEOF in nrw for a range of bulk concentrations.

Some concentrations have been deliberately omitted from figures 4.2.2.1-3 for clarity; above $Q = 0.3$ Å^{-1}, constant values in $R(Q)$ were observed.

The profiles for 5k and 10k DPEOF do not vary much with increasing bulk concentration. At very low concentration a decrease in the magnitude of the reflectivity is observed. The reflectivity profiles for 2k DPEOF have quite distinct features as the bulk concentration changes; a distinct fringe being observed at high concentrations. The difference in reflectivity between the three molecular weights becomes apparent in figure 4.2.2.4.

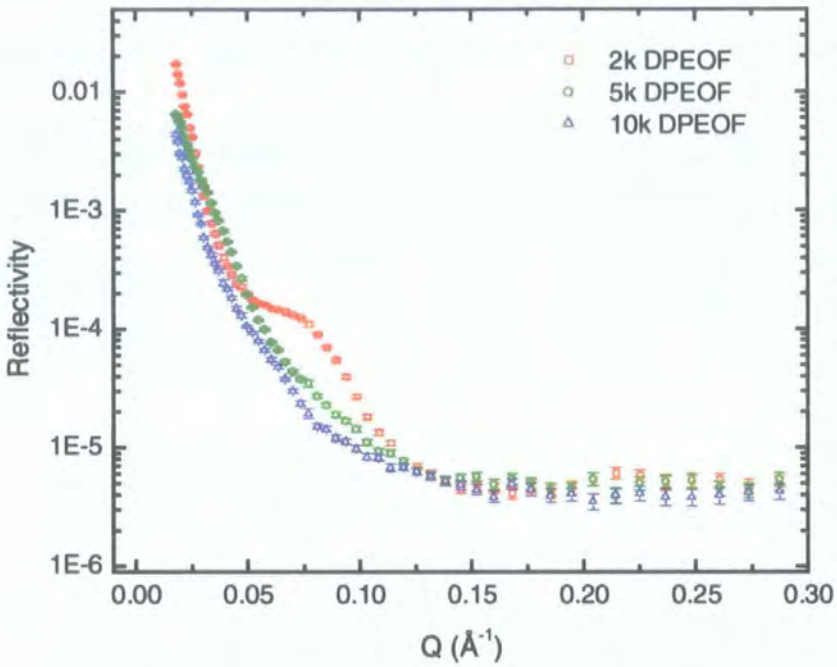

Figure 4.2.2.4: Reflectivity data for all three DPEOF polymers in nrw at a bulk concentration of 10^{-3} g ml^{-1}.

For 2k DPEOF, a distinct fringe is observed between 0.06 and 0.08 Å^{-1}, the reflectivity for 5k DPEOF has evidence of a residual fringe between $0.03 \leq Q$ / Å$^{-1} \leq 0.06$. However, the reflectivity for 10k DPEOF is very similar to that observed for unmodified polyethylene oxide[7] i.e., the reflectivity decreases continuously with increasing Q until background signal is reached.

From figure 4.2.2.1 for the 2k DPEOF, the fringe initially located at circa $Q \approx 0.07$ Å^{-1} for the highest concentration becomes less well defined as the bulk concentration decreases and at 10^{-5} g ml^{-1} (data not shown in figure 4.2.2.1) and below there is no evidence for a fringe at all in the reflectivity profile. Figure 4.2.2.5 shows the reflectivity for all three molecular weight polymers at the same bulk concentration of 10^{-5} g ml^{-1}.

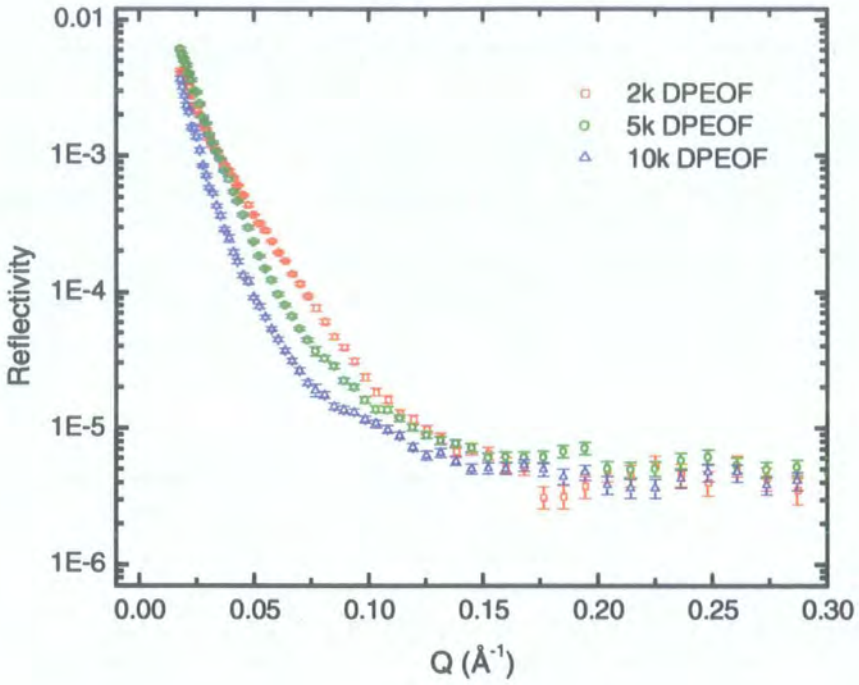

Figure 4.2.2.5: Reflectivity data at a concentration of 10^{-5} g ml^{-1} in null reflecting water for all three molecular weight polymers.

Even though the fringe has disappeared for 2k DPEOF, the reflectivity is still very different when compared to 5k and 10k DPEOF polymers.

Hydrogeneous Fluorocarbon End-Capped Polyethylene Oxide (HPEOF) in D_2O.

The neutron reflectivity for HPEOF in D_2O for solutions of 2k, 5k, 10k molecular weight PEOF with concentration are shown in figure 4.2.2.6, 4.2.2.7 and 4.2.2.8.

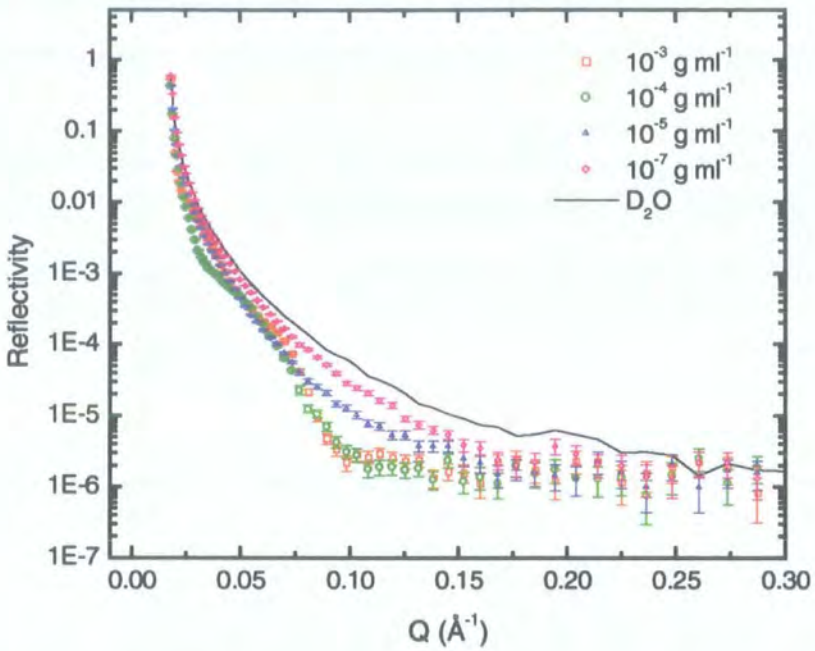

Figure 4.2.2.6: Reflectivity profiles for 2k HPEOF in D_2O at various bulk concentrations.

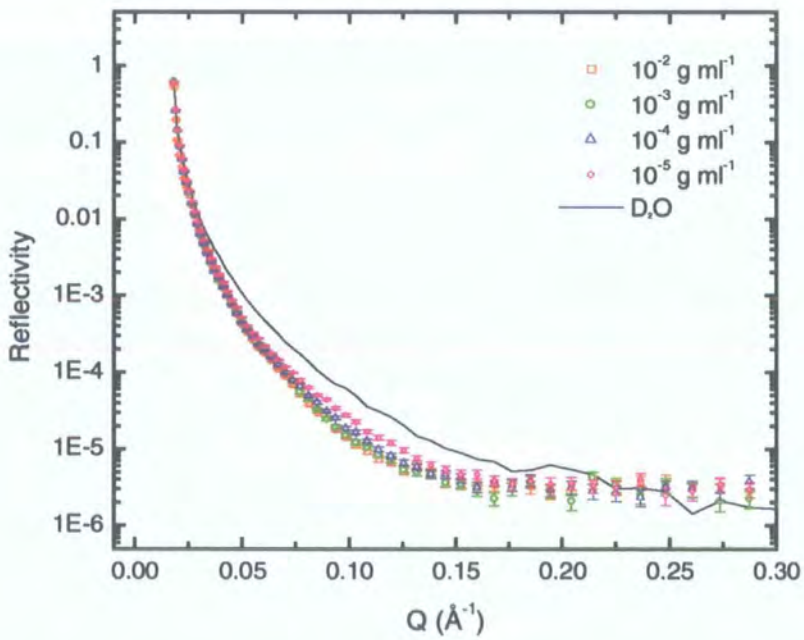

Figure 4.2.2.7: Reflectivity profiles for 5k HPEOF in D_2O at various bulk concentrations.

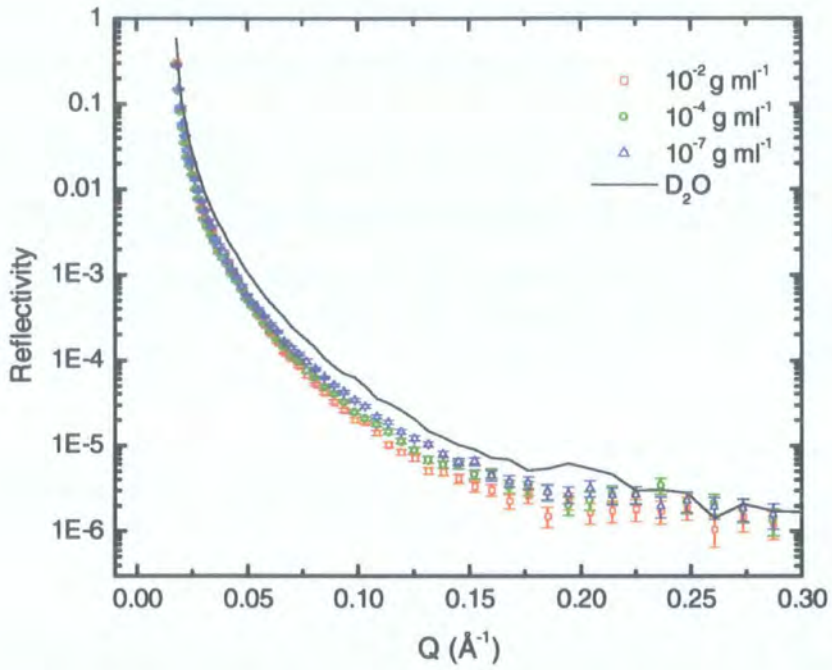

Figure 4.2.2.8: Reflectivity profiles for 10k HPEOF in D_2O at various bulk concentrations.

For solutions of fluorocarbon end-capped HPEO in D_2O, the subphase reflectivity is dominant and changes due to the presence of the polymeric material are subtle until $Q \approx 0.1$ Å^{-1} where a reduction of the reflectivity relative to pure D_2O is observed for all three polymers due to the displacement of D_2O molecules by the weakly reflecting protonated species. Again, this reduction is the sharpest for 2k HPEOF. For the two higher molecular weight polymers, the reflectivity decreases smoothly with increasing Q. Differences in the reflectivity profile for 2k HPEOF are more pronounced compared to 5k and 10k HPEOF as depicted in figure 4.2.2.8 for a concentration of 10^{-3} g ml^{-1}.

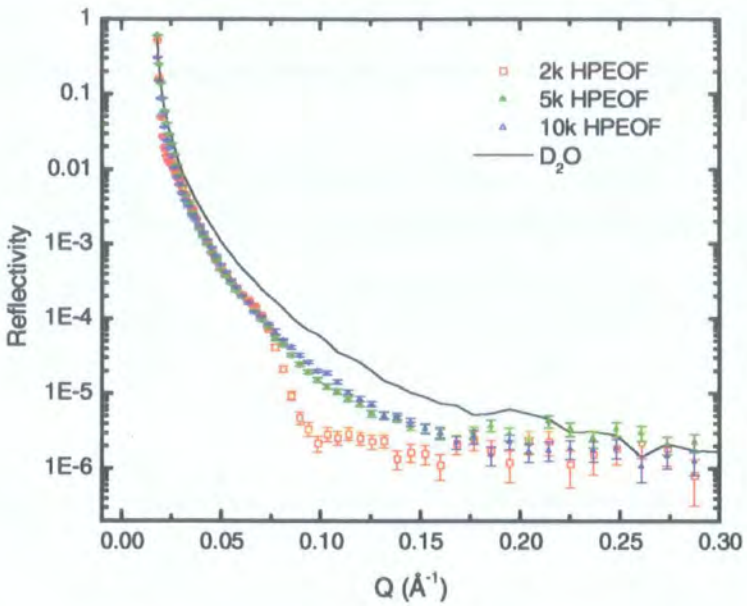

Figure 4.2.2.8: Reflectivity data at a concentration of 10^{-3} g ml^{-1} in D_2O for all three molecular weight polymers.

The difference in reflectivity profile between 2k HPEOF and the two higher molecular weight polymers is still evident at low bulk concentrations as depicted in figure 4.2.2.9.

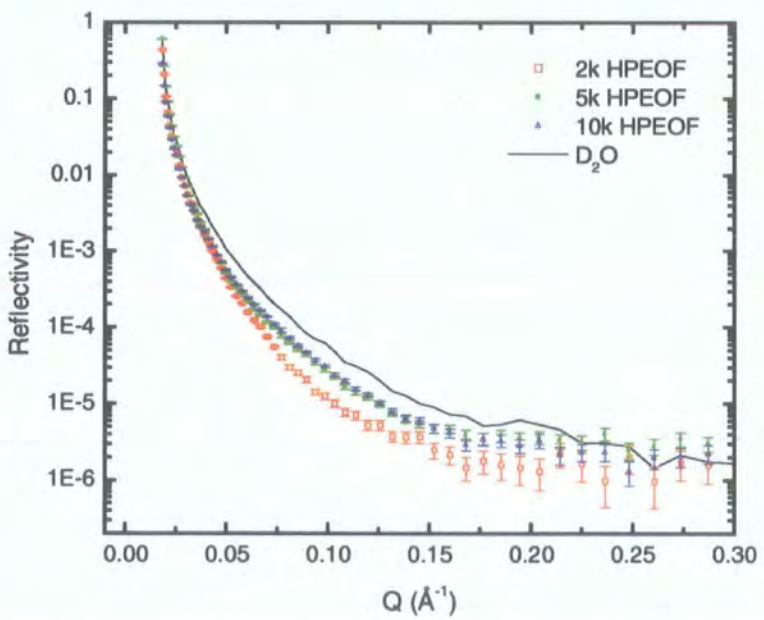

Figure 4.2.2.9: Reflectivity data at a concentration of 10^{-5} g ml^{-1} in D_2O for all three molecular weight polymers.

Deuterated Fluorocarbon End-Capped Polyethylene Oxide (DPEOF) in D_2O.

The neutron reflectivity for D PEOF in D_2O for solutions of 2k and 5k DPEOF with concentration are shown in figure 4.2.2.10a-b. 10k DPEOF neutron reflectivity being very similar to 5k DPEOF was not included deliberately.

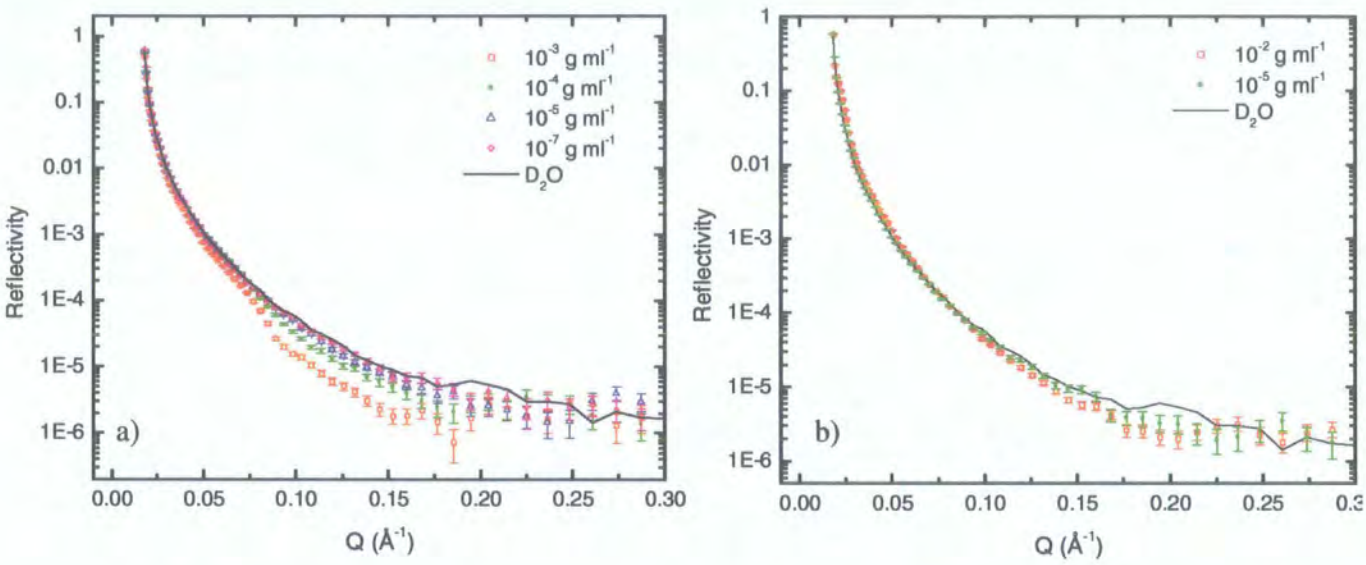

Figure 4.2.2.10: Reflectivity profiles for a) 2k DPEOF and b) 5k DPEOF in D_2O with variation in bulk concentration.

For the solution of fluorocarbon end-capped D PEOF in D_2O, the subphase reflectivity is dominant and changes due to the polymer are subtle until $Q \approx 0.1$ Å^{-1} where a reduction of the reflectivity relative to pure D_2O is observed for all three molecular weight polymers, but more pronounced for 2k DPEOF. For 5k and 10k DPEOF, the change in reflectivity with bulk concentration is very small due to the small difference in scattering length density between 5k and 10k DPEOF ($\rho = 5.08\times10^{-6}$ Å^{-2} and $\rho = 5.44\times10^{-6}$ Å^{-2} respectively), and the subphase ($\rho = 6.35\times10^{-6}$ Å^{-2}) whereas the difference in scattering length density between 2k DPEOF ($\rho = 4.32\times10^{-6}$ Å^{-2}) and the subphase is more pronounced.

4-3 Discussion

Quantitative analysis for aqueous solutions of 2k, 5k and 10k PEOF were obtained using both optical matrix method and kinematic approximation as described in Chapter Two. Briefly, both analyses are complimentary and allowed the determination of the surface organisation of PEOF at the air-water interface by giving information about the number, composition and thickness of layers present in the system under investigation. The optical matrix method provides the overall thickness and composition layer but even though the optical matrix gives the exact reflectivity, uncertainty about the uniqueness of the model used to fit the data is raised as including more layers will always give a better fit to the data and therefore many models may fit the data well. To overcome this problem, the kinematic approximation is used as more details regarding the distributions of PEOF and water molecules at the air-water interface as well as the separation between these two distributions can be obtained separately.

The following section will discuss the results obtained for the three molecular weight polymers using both analyses.

4-3-1 Optical Matrix Analysis

The neutron reflectivity can be calculated exactly for any model of the neutron scattering length density ρ normal to the interface using the optical matrix method[8]. The raw reflectivity profiles were fitted using the optical matrix analysis without further manipulation. The fitting programs WETEST, LAYERS and SURFACE were used throughout and an outline of the general procedure is given here.

Optical matrix analysis of the reflectivity data was undertaken using the minimum number of layers to fit the reflectivity data. Each layer was characterised by a thickness, d, a scattering length density, ρ, and a mean square Gaussian roughness between each layer. The calculated reflectivity was non-linearly least square fitted to the data by adjusting d and ρ. From the best-fit values, the volume fraction (ϕ_i) and number density (n_i) of the species were calculated in addition to the layer thickness (refer to equations 2.3.19 and 2.3.20, Chapter Two). Knowing n_i the surface

concentration or surface excess, Γ_i (g m^{-2}), can be calculated for each of the species i present in the layer (equation 4.3.1.1).

$$\Gamma_i = \frac{n_i m_i d}{N_A} \qquad \text{Equation 4.3.1.1.}$$

where m_i is the molecular weight of species i and N_A is the Avogadro's number.

However, as discussed previously, uncertainty about the uniqueness of the model that fits the data is always present because including more layers will always give a better fit to the data. To overcome this problem, reflectivity curves for all three polymer subphase contrasts collected are fitted using the same model, i.e. a uniform layer model was always used initially to produce an acceptable fit to the data and additional layers subsequently incorporated until good agreement was achieved between the model and experimental reflectivity profiles. Consistency of layer thickness and volume fractions between the three experimental contrasts was used as a criterion for the validity of the model. 2k DPEOF being the polymer with the most complex reflectivity data will be discussed in detail for all contrasts. Identical fitting procedures were adopted for 5k and 10k DPEOF polymers and are included in the discussion.

In general, the data for the most concentrated solution of D PEOF in nrw was fitted first as the data collected at low bulk concentrations were subject to relatively large signal to noise ratio, especially when the subphase was nrw. A typical one layer fit is shown in figure 4.3.1.1 for 2k DPEOF in nrw at a bulk concentration of 10^{-3} g ml^{-1}.

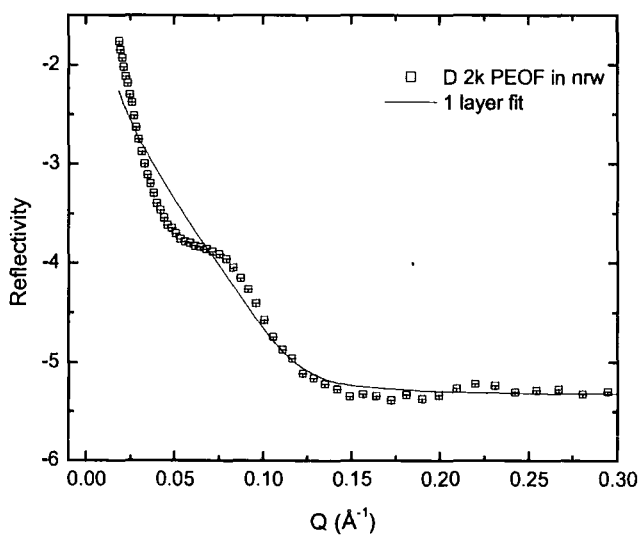

Figure 4.3.1.1: Single uniform layer fit (solid line) to the experimental reflectivity profile for an adsorbed solution of bulk concentration 10^{-3} g ml^{-1} for 2k DPEOF in nrw.

It can be seen clearly that a uniform layer model does not fit the reflectivity profile well and the same observation was observed for the other polymer-subphase contrasts (H and D PEOF in D_2O). To improve the fit, a second uniform layer was introduced, figures 4.3.1.2a-c.

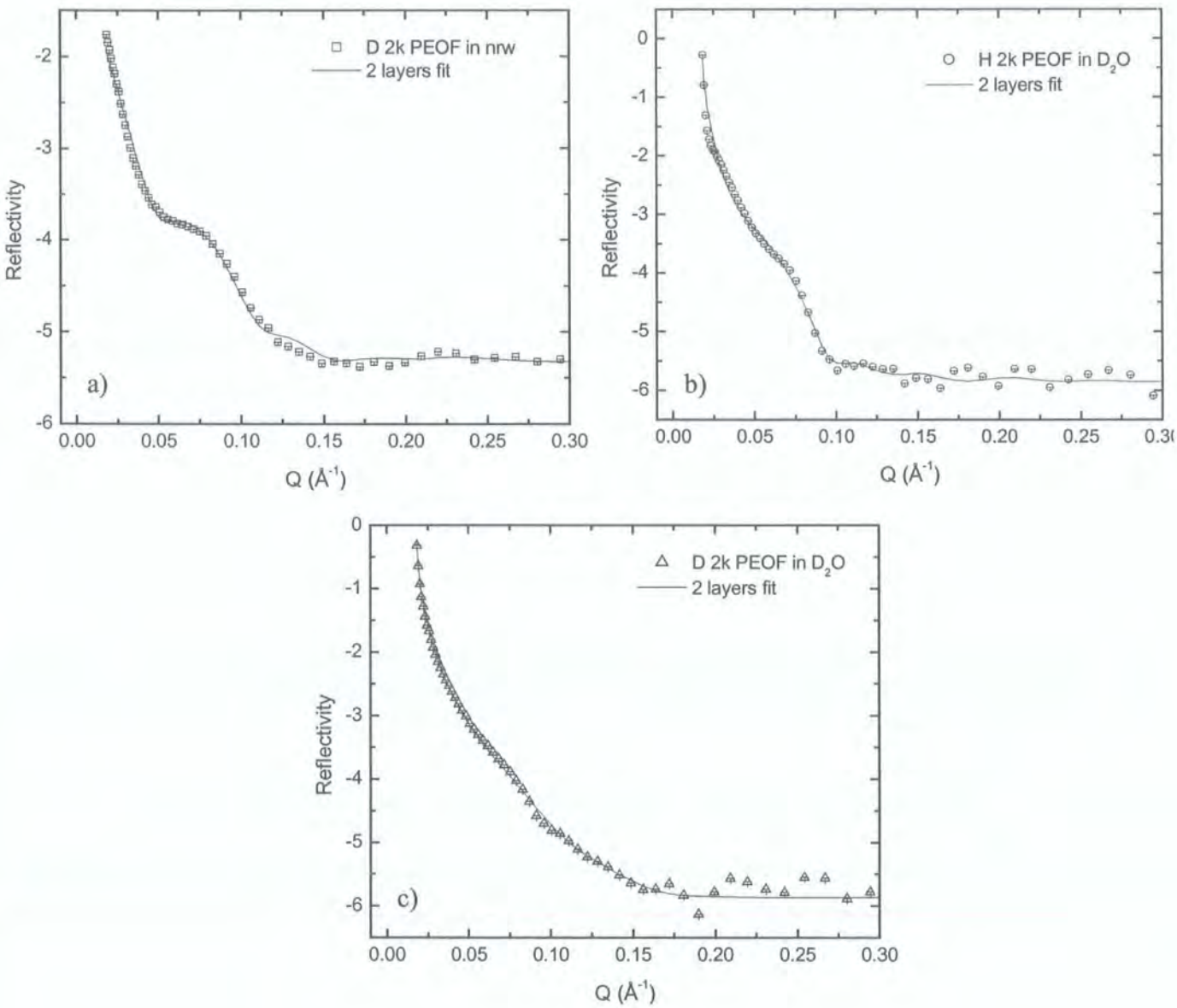

Figure 4.3.1.2: Double uniform layer fit (solid line) to the experimental reflectivity profile for an adsorbed solution of bulk concentration 10^{-3} g ml^{-1} for a) 2k DPEOF in nrw, b) 2k HPEOF in D_2O and c) 2k DPEOF in D_2O.

The model parameters for each fit are given in table 4.3.1.1.

Contrast	Layer	$d \pm 2$ (Å)	$\rho \pm 0.02$ (10^{-6} Å^{-2})	Interfacial roughness (Å)
D NRW	1	38	3.39	8
	2	85	1.08	11
H D_2O	1	37	2.01	7
	2	82	4.75	10
D D_2O	1	36	5.02	5
	2	83	6.06	13

Table 4.3.1.1: Parameters of the double uniform layer fit for 2k PEOF of bulk concentration 10^{-3} g ml^{-1}.

The improvement of the fits is self-evident, and the model clearly reproduces the trend of the three reflectivity profiles. Layer thickness is consistent within error for all three contrasts indicating that the model seems to be appropriate. The best way to check the veracity of the model is to compare the volume fraction composition of each layer. The volume fraction of PEOF and water were determined by using the three equations 4.3.1.2-6

D PEOF in nrw

$$\rho = \rho_{dPEO}\phi_{dPEO} + \rho_w\phi_{w1} \qquad \text{Equation 4.3.1.2.}$$

For D PEOF in nrw, $\rho_w = 0$, and substituting in equation 4.3.1.2

$$\phi_{dPEO} = \frac{\rho}{\rho_{dPEO}} \text{ and } \phi_{w1} = 1 - \phi_{EO} \qquad \text{Equations 4.3.1.3-4.}$$

H PEOF on D_2O

$$\rho = \rho_{hPEO}\phi_{hPEO} + \rho_w\phi_{w2} \qquad \text{Equation 4.3.1.5.}$$

D PEOF on D_2O

$$\rho = \rho_{dPEO}\phi_{dPEO} + \rho_w\phi_{w3} \qquad \text{Equation 4.3.1.6.}$$

Knowing ϕ_{PEO} from equation 4.3.1.3 and substituting in equation 4.3.1.5 and 4.3.1.6, ϕ_{w2} and ϕ_{w3} can be determined and compared to each other; identical values within error should be obtained if the model is appropriate. The scattering length densities relevant to this study are given in Chapter Two, table 2.3.2. The volume fractions obtained for a double uniform layer model for 2k PEOF at a bulk concentration of 10^{-3} g ml^{-1} are shown in table 4.3.1.2.

Contrast	Layer	$\phi_{PEO} \pm 0.03$	$\phi_w \pm 0.02$
D NRW	1	0.78	0.22
	2	0.28	0.72
H D_2O	1	0.79	0.21
	2	0.27	0.73
D D_2O	1	0.75	0.25
	2	0.27	0.73

Table 4.3.1.2: Volume fractions obtained for a double uniform layer model for 2k PEOF at a bulk concentration of 10^{-3} g ml^{-1}.

Consistency in the volume fraction is observed for all contrasts reinforcing the idea that a double uniform layer model correctly fit the reflectivity profiles. According to table 4.3.1.1, the scattering length density of the upper layer (layer 1) for 2k DPEOF in nrw is relatively high indicating the presence of the deuterated PEO species. The magnitude of the scattering length density for 2k DPEOF in nrw is greater than the lower layer, suggesting a denser layer of deuterated species at the near surface and the PEO molecules become more diluted as deeper in the subphase. This idea is reinforced by the fitting parameters obtained for 2k HPEOF in D_2O. The scattering length density of the upper layer is reduced relative to that of D_2O, indicating the presence of hydrogenous PEO molecules near the surface. Hence we appear to have a two-layer organisation for 2k PEOF with an upper layer adjacent to the air consisting of water and a large amount of PEO. The lower layer is essentially highly diluted PEO. At a bulk concentration of 10^{-3} g ml^{-1} a sharp interface develops between the upper layer and the air interface, whereas a small but bigger interfacial roughness between the upper and lower layers is observed suggesting a low degree of interpenetration between the layers.

By using equations 2.3.20 (Chapter Two) and 4.3.1.1 for 2k DPEOF in nrw, the number density, n, and the surface excess, Γ, were calculated and are shown in table 4.3.1.3 for the all concentration range investigated.

c (g ml^{-1})	Layer	$d \pm 2$ (Å)	$\rho \pm 0.02$ (10^{-6} Å^{-2})	Interfacial roughness (Å)	$\phi_{PEO(F)}$	ϕ_w	$n_{EO} \times 10^{-4} \pm 2 \times 10^{-5}$ (Å^{-3})	$\Gamma_T \pm 0.03$ (mg m^{-2})	$\Gamma_{upper} \pm 0.04$ (mg m^{-2})
1E-03	1	38	3.39	8	0.78	0.22	1.58	4.80	2.96
	2	85	1.08	11	0.28	0.72	0.65		
5E-04	1	39	2.92	7	0.75	0.25	1.61	4.81	2.61
	2	76	1.30	10	0.30	0.70	0.87		
1E-04	1	34	3.14	6	0.74	0.26	1.63	4.37	2.45
	2	70	1.34	9	0.31	0.69	0.80		
5E-05	1	35	2.75	10	0.72	0.28	1.65	3.41	2.21
	2	65	0.90	8	0.21	0.79	0.54		
4E-05	1	37	2.46	11	0.64	0.36	1.65	3.08	2.09
	2	63	0.76	8	0.18	0.82	0.46		
3E-05	1	34	2.64	13	0.63	0.37	1.70	2.94	2.06
	2	59	0.74	10	0.17	0.83	0.44		
2E-05	1	37	2.60	10	0.67	0.33	1.71	2.19	2.19
1E-05	1	35	2.80	8	0.65	0.35	1.70	2.05	2.05
5E-06	1	31	2.40	8	0.62	0.38	1.61	1.71	1.71
1E-06	1	23	2.14	5	0.55	0.45	1.44	1.13	1.13
5E-07	1	14	1.54	8	0.40	0.60	1.03	0.49	0.49

Table 4.3.1.3: Layer thickness, scattering length density, interfacial roughness, volume fraction, number density and surface excess (both total surface excess, Γ_T, and upper layer surface excess Γ_{upper}) from double uniform layers for 2k PEOF with bulk concentration.

As shown in table 4.3.1.3, for bulk solution concentrations up to 2×10^{-5} g ml^{-1} and below, a single uniform layer model was sufficient to fit the reflectivity profile as depicted in figures 4.3.1.3a-c.

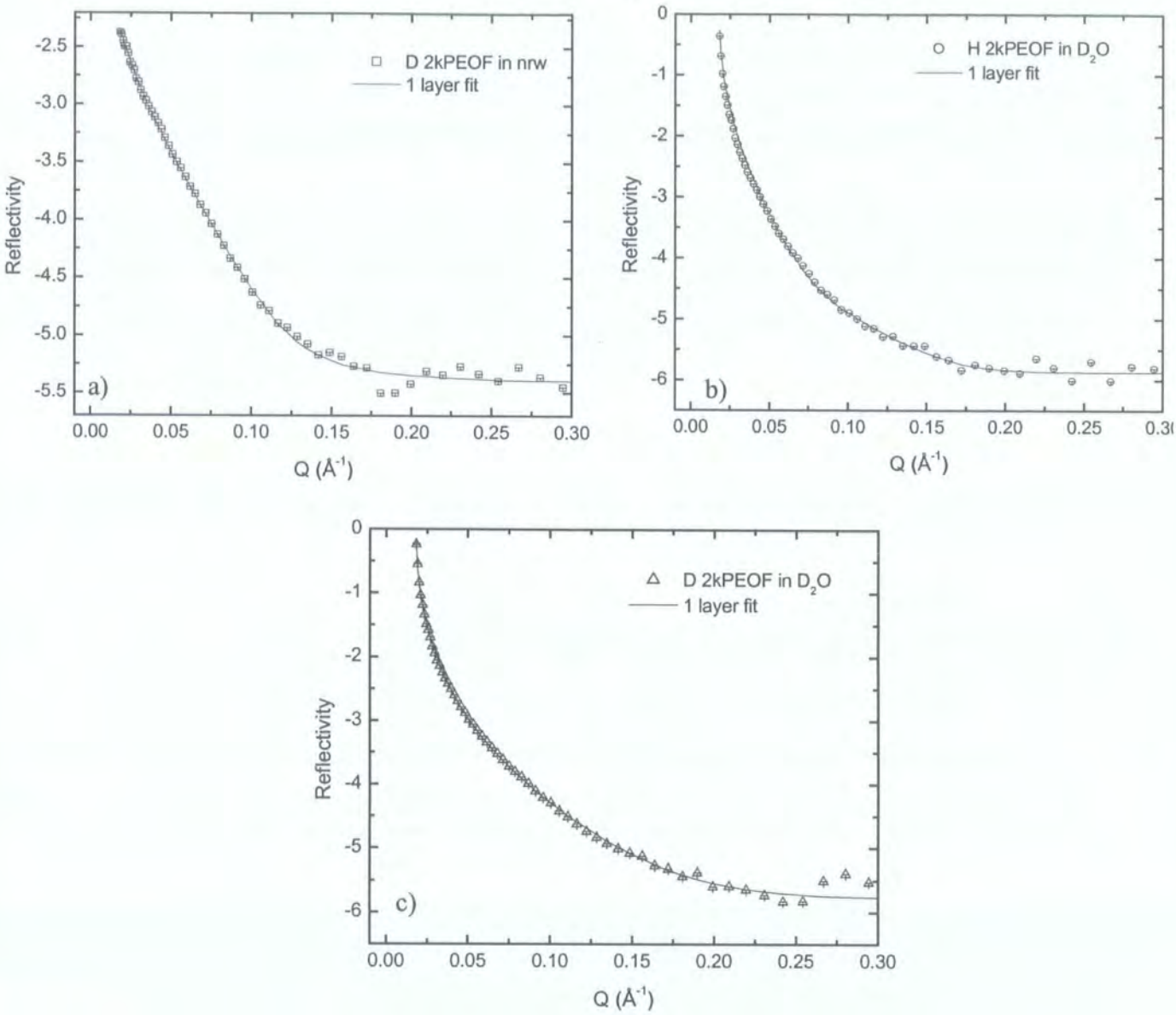

Figure 4.3.1.3: Single uniform layer fit (solid line) to the experimental reflectivity profile at a bulk concentration of 2×10^{-5} g ml^{-1} for a) 2k DPEOF in nrw, b) 2k HPEOF in D_2O and c) 2k DPEOF in D_2O.

The change from one monolayer to two layers is made apparent when plotting the number density of PEO molecules as a function of the penetration depth (figure 4.3.1.4).

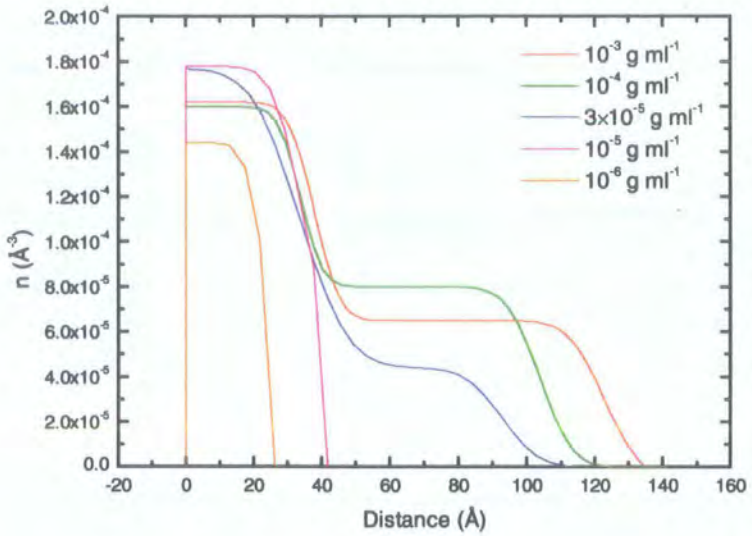

Figure 4.3.1.4: Number density distributions from optical matrix analysis of reflectivity data for aqueous solutions of 2k DPEOF with the bulk concentrations indicated.

Above 2×10^{-5} g ml^{-1}, the transition from one layer to two layers is undeniable, as figure 4.3.1.4 shows clearly the formation of a second layer with two maximums being observed in the number density distribution. For very low concentrations (10^{-6} and 10^{-5} g ml^{-1}) the number density increases with bulk concentration going from 1.4×10^{-4} Å^{-3} to 1.8×10^{-4} Å^{-3} respectively. At a bulk concentration of 3×10^{-5} g ml^{-1} the number density of the upper layer starts to decrease slightly to finally reach a constant value of 1.6×10^{-4} Å^{-3} for higher concentrations. The number density of the lower layer increases with bulk concentration until a decrease is observed at 10^{-3} g ml^{-1} with the magnitude going from 8×10^{-5} Å^{-3} to 7×10^{-5} Å^{-3}. Those observations clearly suggest a stretching of the adsorbed polymer molecules rather than incorporation of more polymers into the upper layer and to illustrate this suggestion the layer thickness (upper and lower layer) is plotted as a function of bulk concentration (figure 4.3.1.5).

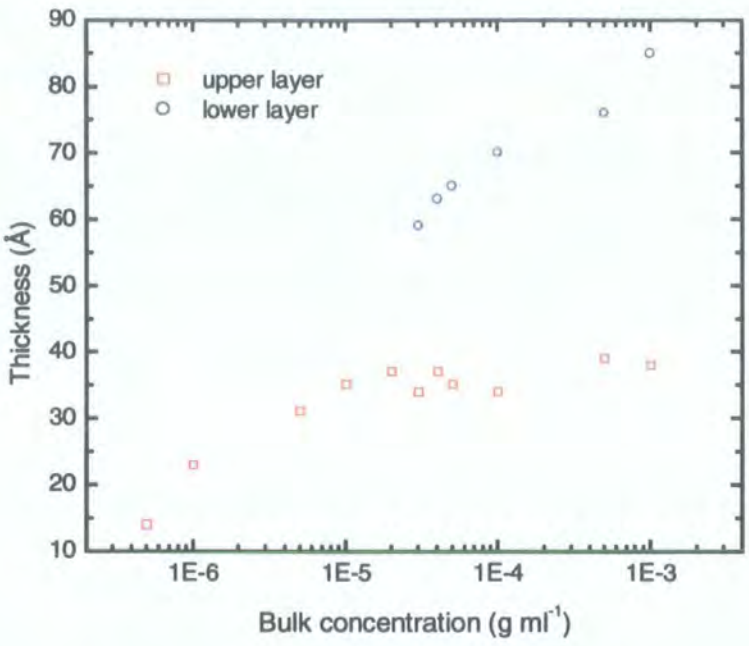

Figure 4.1.3.5: Layer thickness for the upper and lower layer as a function of the bulk concentration for 2k PEOF.

Both thicknesses increase with bulk concentration. The layer thickness of the upper layer increases steady with bulk concentration until 5×10^{-5} g ml^{-1} where constant value is observed with d = 40 Å. Above 3×10^{-5} g ml^{-1} a second layer forms, the thickness of which also increases with bulk concentration; very thick lower layers (up to 85 Å) are observed with no constant value being reached at 10^{-3} g ml^{-1}. An increase in layer thickness with bulk concentration is observed at very low concentration suggesting that the PEO chains have already started to explore the subphase to avoid thermodynamically unfavourable interactions on the surface. Both layer thicknesses increase rapidly and linearly with the bulk concentration but it is evident however that the rate of stretching begins to slow down for the upper layer as the concentration exceeds 3×10^{-5} g ml^{-1}. Both number density of molecules situated at the near surface and upper layer thickness are approximately constant above 3×10^{-5} g ml^{-1} suggesting that the interface is saturated as addition of more material does not affect the number density and layer thickness of the upper layer.

Qualitatively, the organisation of the fluorocarbon end-capped PEO differs dramatically from the organisation of unmodified PEO[6,7]. The investigation by

neutron reflectometry of adsorbed solution of PEO with two molecular weights (17 800 and 87 000 g mol^{-1}) at a fixed concentration of 0.1 wt % led to the conclusion that a two layer organisation was observed with thickness of 18 ± 2 Å and 35 ± 5 Å for the first and second region respectively. A two layer organisation is also observed for 2k PEOF but the magnitude of the thickness in this case are much higher than those observed for significantly higher molecular weight PEO. This suggests that the PEO chains in 2k PEOF are stretched to a greater extend and a hydrophobic group placed at one end of the molecule considerably enhances the adsorption of aqueous solution of PEO to the air-water interface. This statement is confirmed when comparing the surface excess of both hydrophobically end-capped PEO and PEO. According to table 4.3.1.3, the surface excess layer is increasing with bulk concentration until a constant value is observed at $c = 5\times10^{-4}$ g ml^{-1} with $\Gamma_{upper} = 2.96$ ± 0.03 mg m^{-2}. From neutron reflectometry experiments on higher molecular weight PEO[7], Γ was found to be 0.53 ± 0.05 mg m^{-2} at the same bulk concentration. The difference between the surface excess for unmodified PEO and 2k PEOF is a factor ~5 greater indicating that more polymers are adsorbed at the interface when hydrophobically end-capped. It is also evident, by comparing Γ_T and Γ_{upper} (table 4.3.1.3), that the polymer in the upper layer makes the major contribution to the surface excess over the whole concentration range.

A physical picture of the arrangement predicted from double monolayer fits is given by plotting the volume fraction as a function of the distance in the bulk for different concentrations. This is shown in figures 4.3.1.6.

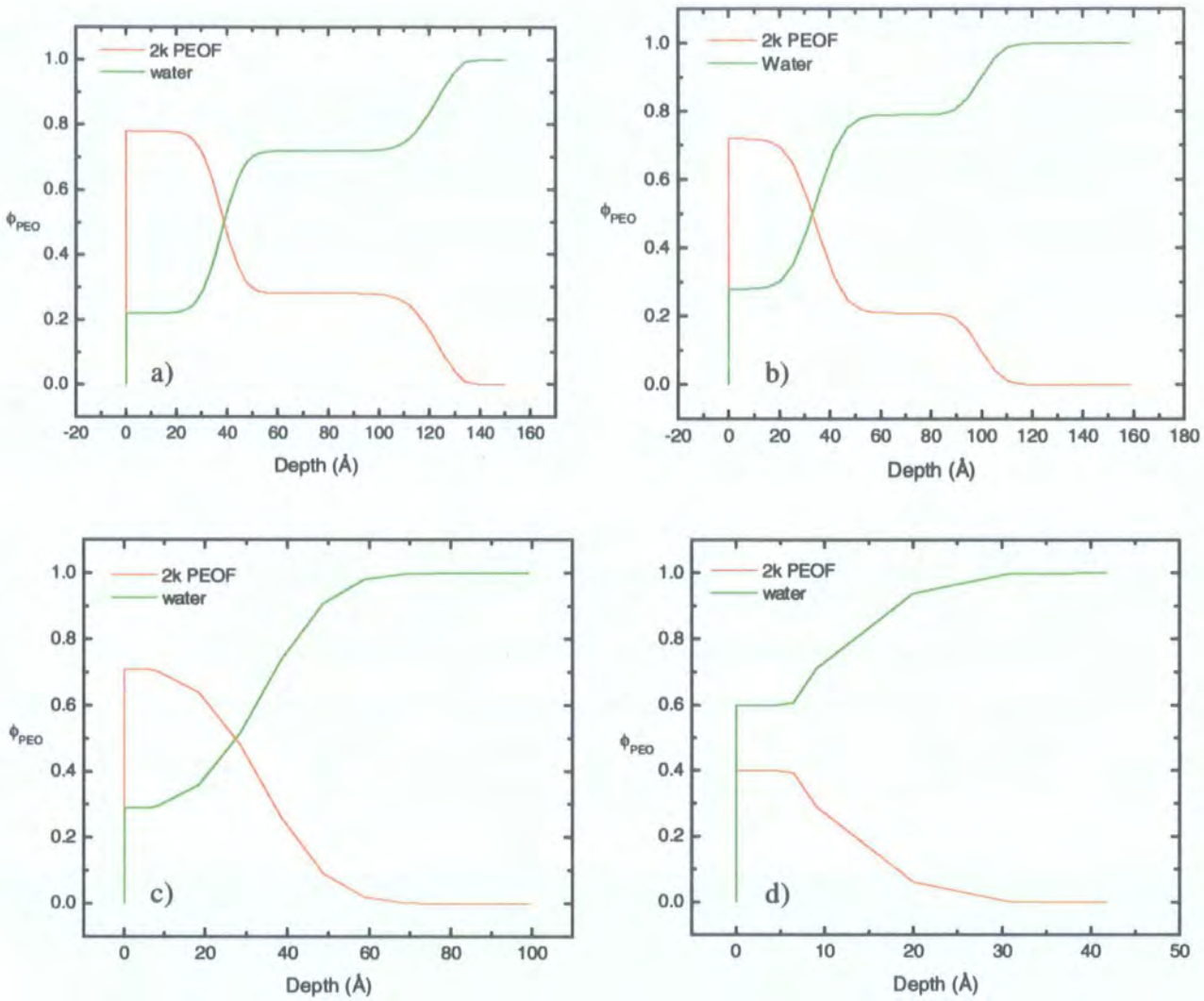

Figure 4.3.1.6: Volume fraction profile for a selection of bulk concentrations a) 10^{-3} g ml^{-1}, b) 5×10^{-5} g ml^{-1}, c) 10^{-5} g ml^{-1} and d) 5×10^{-7} g ml^{-1} for 2k PEOF.

The volume fraction of PEOF increases with bulk concentration but remains constant above a bulk concentration of 5×10^{-5} g ml^{-1}. The volume fraction of water decreased with increase in bulk concentration and the interface is dominated by water molecule at very low concentration. Water molecules are displaced from the interface by the adsorption of polymer molecules at the air-water interface as the bulk concentration increases. Volume fraction of PEO in the lower layer is almost constant for bulk concentrations above 3×10^{-5} g ml^{-1} (not shown in figure 4.3.1.6) but a stretching is apparent as the lower layer thickness increases.

By using the product of the number density n and layer thickness d of the upper layer, the number of molecules per unit area, n_m ($Å^{-2}$) can be determined (equation 4.3.1.7).

$$n_m = n \times d \qquad \text{Equation 4.3.1.7.}$$

The area per molecule is given by equation 4.3.1.8

$$a_m = \frac{1}{n_m} \qquad \text{Equation 4.3.1.8.}$$

The square root of a_m ($Å^2$) gives the distance D (Å) between molecules (equation 4.3.1.9).

$$D = \sqrt{a_m} \qquad \text{Equation 4.3.1.9.}$$

The results are shown in table 4.3.1.4.

Concentration (g ml^{-1})	n_m ($Å^{-2}$)	a_m ($Å^2$)	D (Å)
1.E-03	8.66E-03	115.42	10.74
5.E-04	7.64E-03	130.82	11.44
1.E-04	7.17E-03	139.39	11.81
5.E-05	6.48E-03	154.44	12.43
4.E-05	6.11E-03	163.80	12.80
3.E-05	6.02E-03	166.17	12.89
2.E-05	6.44E-03	155.33	12.46
1.E-05	6.23E-03	160.51	12.67
5.E-06	4.99E-03	200.36	14.15
1.E-06	3.31E-03	301.93	17.38
5.E-07	1.44E-03	693.48	26.33

Table 4.3.1.4: Number of molecules per unit area (n_m), area per segment molecules (a_m) and distance between molecules (D) for 2k PEOF.

The radius of gyration, R_g, relevant to this study were determined using the relationship determined by Kawaguchi *et al.*[9] given in equation 4.3.1.10 and shown in table 4.3.1.5.

$$R_g^2 = 4.08 \times 10^{-18} \times M_w^{1.16} \qquad \text{Equation 4.3.1.10.}$$

where M_w is the molecular weight of the polymer.

Polymer	R_g (Å)
2kPEOF	18.1
5kPEOF	28
10kPEOF	41.8

Table 4.3.1.5: Flory radius of gyration R_g for 2k, 5k and 10k PEOF.

According to table 4.3.1.4, both the area per molecule and the distance between molecules decrease with bulk concentration, suggesting that the polymer chains are stretching into the subphase. As discussed in Chapter Two, section 2-2-3, a brush conformation is expected when $D < R_g$ and this is observed at very low concentration (c = 5×10^{-6} g ml^{-1}) where D = 14.2 Å and R_g = 18.1 Å.

From the double monolayer fit to 2k PEOF data, the following observations were made:

- A two-layer organisation is observed at high concentration with a transition from one monolayer to two monolayers evident at 3×10^{-5} g ml^{-1}.
- From both number density and layer thickness values, a stretching of PEO chains into the subphase seems to be occurring. This picture is supported by the volume fraction distribution of PEO and water molecules at the near surface.
- From both surface tension and surface excess values, the adsorption characteristic of PEO is significantly enhanced when hydrophobically end-capped at one end.
- From the calculations of D (distance between molecules) and R_g, a brush configuration (upper layer) is expected above 10^{-6} g ml^{-1}.

But what about the effect of molecular weight on the surface organisation of PEOF at the air-water interface?

A summary of the results obtained for 5k and 10k PEOF is presented here and the following discussions focussed on examining the influence of the molecular weight of fluorinated PEO on the near surface organisation.

The optical matrix method was applied to both 5k and 10k PEOF and same fitting procedure was followed. Over all the concentration range investigated, a double uniform layer fit was sufficient except for 5k PEOF where a single uniform layer fit sufficed for bulk concentrations of 5×10^{-7} g ml^{-1} and 10^{-7} g ml^{-1}. The results such as the layer thickness, the scattering length density, the interfacial roughness, the volume fraction, the number density and the surface excess are given in appendix 1 and 2 for 5k and 10k PEOF respectively (tables A.1 and A.2).

Major differences were observed in the layer thickness and are shown in figure 4.3.1.7.

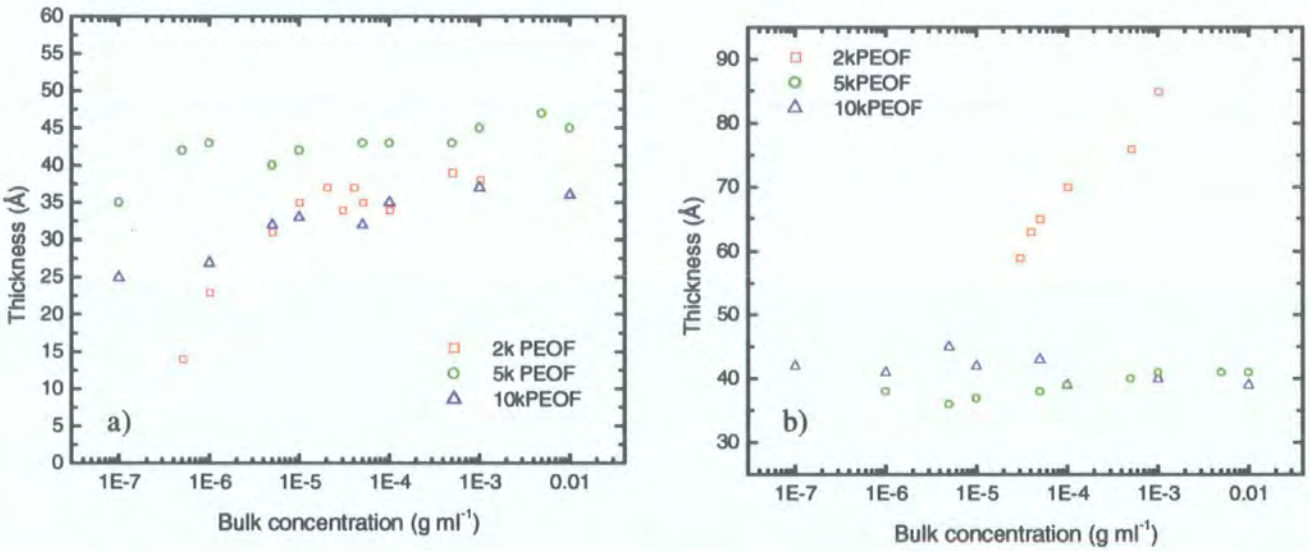

Figure 4.3.1.7: Comparison of the upper (a) and lower (b) layer obtained from double uniform layer fit for 2k, 5k and 10k PEOF with bulk concentration.

A slight increase in the thickness of the upper layer with bulk concentration is observed for 5 k and 10k PEOF. For concentration above 10^{-6} g ml^{-1}, the upper layer thickness of 2k and 10k PEOF are almost identical whereas the upper layer thickness of 5k PEOF is slightly bigger. However, the rate of stretching is slower for 5k and 10k PEOF than 2k PEOF at low bulk concentrations (5×10^{-6} and 10^{-6} g ml^{-1}). Constant values

in layer thickness are observed at low concentration with $d = 43 \pm 3$ Å and $d = 35 \pm 3$ Å for 5k and 10k PEOF respectively. The difference in layer thickness is striking for the lower layer as shown in figure 4.3.1.7 b. 10k PEOF have a constant lower layer thickness of circa 40 ± 3 Å over the all concentration range whereas a second layer of constant thickness $d = 38 \pm 3$ Å is only apparent at $c = 10^{-6}$ g ml^{-1} (and above) for 5k PEOF. This lower layer appears at higher concentrations (~3×10^{-5} g ml^{-1}) for 2k PEOF with a lower layer thickness double the ones observed for higher molecular weight polymers. These observations suggest that as the molecular weight increases, the interface get saturated more quickly due to the adsorption of PEO chains at the near surface.

For higher molecular weight polymers, there is still considerably more polymer adsorbed compared to unmodified PEO. For these polymers, the total surface excess shown in table A.1 and A.2 is almost constant over the all concentration range albeit low concentrations for 5k PEOF. The upper surface excess decreases with an increase in molecular weight as shown in figure 4.3.1.8.

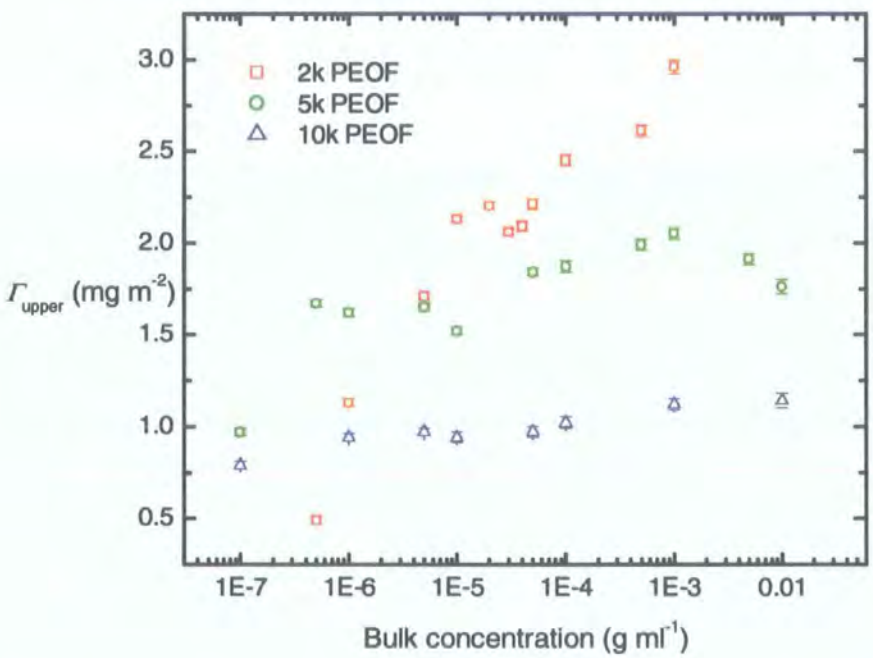

Figure 4.3.1.8: Upper layer surface excess, Γ_{upper}, for 2k, 5k and 10k PEOF with bulk concentration.

For all polymers the polymer in the upper layer makes the major contribution to the surface excess layer. The upper surface excess for 10k PEOF increases slightly with

bulk concentrations starting at 0.75 mg m^{-2} to reach a constant value of 1.10 mg m^{-2} at higher bulk concentrations. A gradual increase to a constant surface excess of ~1.8 mg m^{-2} is observed for 5k PEOF whereas a continuous increase in the surface excess for 2k PEOF is noted with no evidence of approach to an asymptotic value. It is evident that lower molecular weight polymers are adsorbed to a greater extent suggesting that more PEO chains are adsorbed at the air-water interface. The upper layer thickness indicated that the stretching is the most pronounced for 2k PEOF as almost identical layer thickness is observed for higher molecular weight polymers indicating that in addition to PEO chains the lower surface energy fluorocarbon groups influence significantly the surface organisation of hydrophobically end-capped PEO at the air-water interface.

The dependence of the surface tension and surface excess on bulk concentration is shown in figure 4.3.1.9.

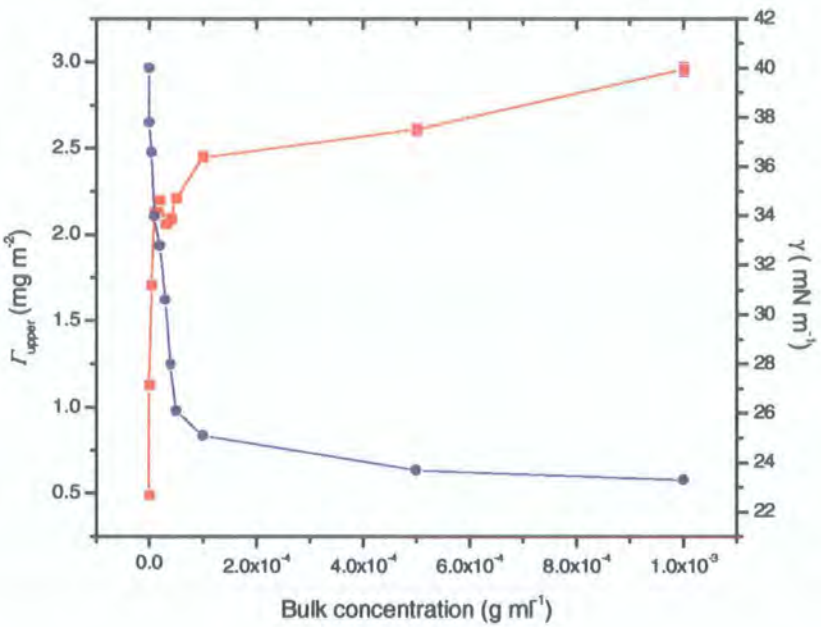

Figure 4.3.1.9: Comparison of surface excess upper layer (red: left axes) to the surface tension data (blue: right axes) both as a bulk concentration (bottom axes) for 2k PEOF.

The dependence of the surface excess concentration on bulk concentration in the upper layer of 2k PEOF mirrors the surface tension behaviour reasonably well with an asymptotic surface excess concentration being observed in the same concentration

range where the surface tension approaches a constant value. This is also true to a certain extent for 5k PEOF but with a continued fall in surface tension, as the surface excess concentration remains constant. This latter behaviour is also evident for 10k PEOF where there is a decrease in surface tension but no change at all in the surface excess concentration in either layer. Those observations suggest that the lowest molecular weight polymer is adsorbed to the interface by the fluorocarbon end whereas the higher molecular weight polymers adsorb by a combination of fluorocarbon ends and ethylene oxide segments with the lower surface energy fluorocarbon ends replacing the ethylene oxide segments at higher concentrations thereby reducing the surface tension with no change in the surface excess concentration. As discussed in Chapter Two (section 2-2-2), monolayers adsorbed from solution are expected to be equilibrium monolayers and should therefore obey the Gibbs equation (equation 4.3.1.11).

$$\Gamma = -\frac{1}{RT} \times \frac{d\gamma}{d\ln c} \times \overline{M_n} \qquad \text{Equation 4.3.1.11.}$$

where $\frac{d\gamma}{d\ln c}$ is the slope of $\gamma = f(\ln c)$, T is the temperature in K (293 K), R is the gas constant and $\overline{M_n}$ is the average number molecular weight determined from SEC.

It is interesting to compare the neutron surface excess with that deduced from the plot of figure 4.3.1.10 using the Gibbs equation.

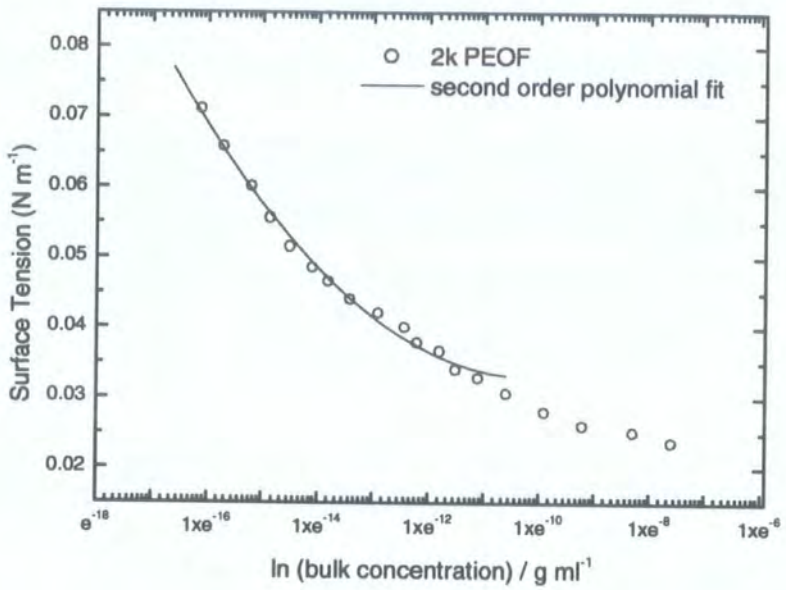

Figure 4.1.3.10: Surface tensions of 2k PEOF in aqueous solution. The line is a polynomial fit to the data below the CMC.

The results returned for Γ from a second order polynomial fit did not correspond at all with the surface excess values obtained by neutron reflectometry as shown in figure 4.3.1.11.

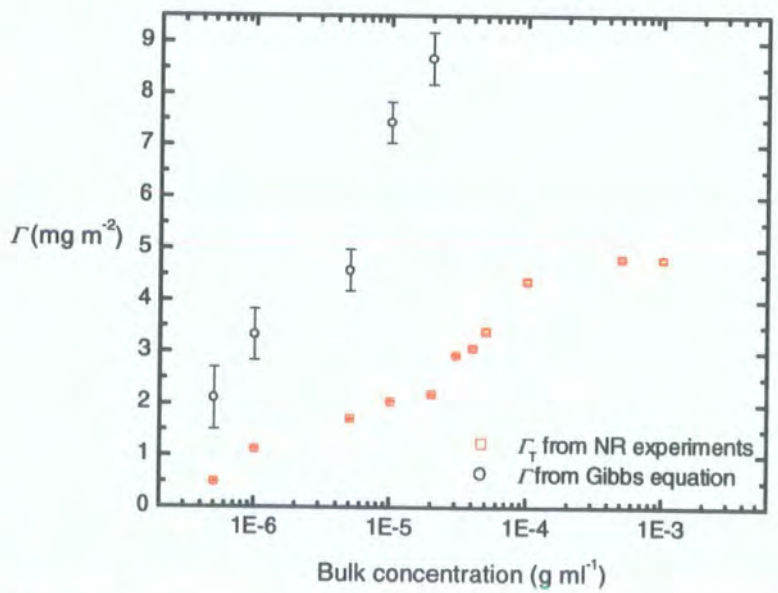

Figure 4.3.1.11: Comparison of surface excess determined by neutron reflectometry (Γ_T) and Gibbs equation (Γ).

Unrealistic values were obtained, being twice as big as the values obtained by neutron reflectometry suggesting that the Gibbs equation failed in interpreting the data. Anomalies in surface excesses determined from neutron reflection and the Gibbs equation have been reported for an anionic surfactant[10] and a fluorocarbon surfactant[11] but none has been noted for polymer systems. Anomalies in surface excesses were explained by impurities in the system having a direct effect on the Gibbs equation due to the assumption made regarding the activity coefficient. Indeed the Gibbs equation can only be used in the dilute regime where they are no intermolecular interactions between molecules and the solute activity can be replaced by the concentration. The same fitting procedure was realised on 5k and 10k PEOF and the same observations were made. It was therefore concluded that, for this particular system, the Gibbs equation analysis failed probably due to the activity coefficient varying significantly with concentration.

The number of molecules per unit area, area per molecule and the distance between molecules for the upper layer of 5k PEOF and 10k PEOF solutions are given in appendix 3 (table A.3.a and A.3.b respectively). According to tables A.3.a-b, both the area per molecule and the distance between molecules decrease slightly with increasing bulk concentration, suggesting that the polymer chains are stretching into the subphase. When comparing the Flory radius of gyration R_g with the distance between grafted molecules, both 5k and 10k PEOF agree with $R_g > D$ over almost the entire concentration range, except for the lowest concentration for 10k PEOF. This indicates that a stretching of the polymer chains into the subphase is occurring but only slightly as the layer thickness remains almost constant for 5k and 10k PEOF at the near surface. Indeed the layer thickness of the upper layer is only $1.5 \times R_g$ at high bulk concentrations, suggesting that a flatter structure is observed for 5k and 10k PEOF compared to 2k PEOF due to competition between the fluorocarbon group and the PEO chains at the air-water interface. A more pronounced stretching is observed for 2k PEOF, as the upper layer thickness is $2 \times R_g$ at concentrated solutions. It seems that the molecular weight is low enough to enable the PEO chains to be displaced from the surface by the lower surface energy fluorocarbon group, allowing more polymers to be adsorbed at the air-water interface and consequently reducing the distance between neighbouring PEO chains that have to stretched into the subphase in order to avoid contact between them.

The nature of the lower layer needs to be clarified. The surface tension data (figure 4.2.1.1) shows similar behaviour as that of low molecular weight surfactant molecules decreasing with increasing bulk concentration. At a critical concentration the surface tension becomes constant and micelles are formed above this critical micelle concentration (CMC).

Dynamic light scattering[13] was performed on the three fluorinated end-capped PEO to check the evidence of micelle formation and the results are shown in figure 4.3.1.12.

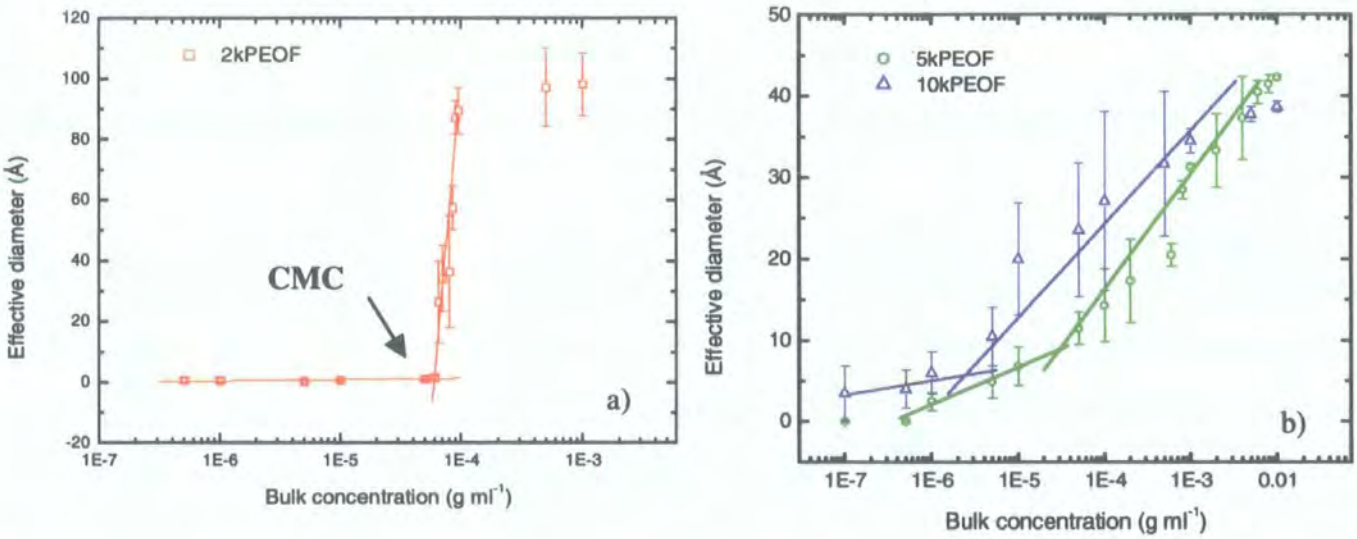

Figure 4.3.1.12: Effective diameter of micelle formation for a) 2k and b) 5k and 10k PEOF with bulk concentration determined by dynamic light scattering experiment.

The CMC determined by the intersection of two linear fits, as shown in figure 4.3.1.12, is given in table 4.1.3.6 for each polymer.

Polymer	CMC ± 0.20 (g ml^{-1})
2kPEOF	5.20×10^{-5}
5kPEOF	3.00×10^{-5}
10kPEOF	2.10×10^{-6}

Table 4.3.1.6: CMC for 2k, 5k, 10kPEOF determined by dynamic light scattering.

It could be argued that 5k and 10k PEOF are not forming micelles in the bulk as the break corresponding to the CMC is not as sharp as the one observed for 2k PEOF and the

diameter is still increasing at high concentrations with no asymptotic value being approached. It seems more than likely that 5k and 10k PEOF polymers are adopting a random coil configuration rather than micelle formation in the bulk. For 2k PEOF, the trend of figure 4.3.1.12a follows the one expected with a sharp break and asymptotic values being observed. The CMC mirrors well the formation of the lower layer observed by neutron reflectometry experiments for 2k PEOF but not for higher molecular weight polymers. According to table A.1 and A.2, this layer is quite diffuse for 5k PEOF and even more diffuse for 10k PEOF. The thickness and composition of this lower layer is relatively constant for both 5k and 10k PEOF. However, the 2k PEOF differs significantly from these higher molecular weight polymers because the thickness increases over the whole concentration range with no asymptotic value being approached. All polymers show evidence of "aggregate" formation and probably micelle formation for the lower molecular weight polymer and since the second layer is observed at concentrations that correspond to, or greater than the CMC and the dimensions of this layer far exceed the radii of gyration of the polymers, the most probable explanation is the adsorption of "aggregates" at the underside of the original adsorbed layer of individual molecules. In an attempt to obtain some knowledge of the size and nature of these arrangements small-angle neutron scattering data was collected for each polymer at a concentration of 10^{-3} g ml^{-1} and are shown in figure 4.3.1.13.

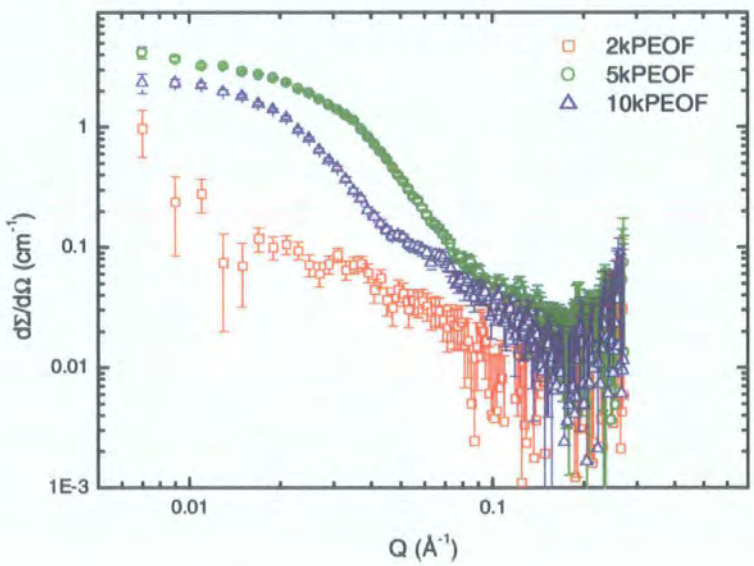

Figure 4.3.1.13: Small angle neutron scattering data for solution of each hydrogenous polymer on D_2O at a concentration of 10^{-3} g ml^{-1}.

The scattering from the two higher molecular weight polymers is quite different to that of the 2k PEOF suggesting that the arrangements have distinctly different morphology. From double logarithmic plots of these data the scaling relations between the scattering cross section ($d\Sigma/d\Omega$) and the scattering vector gives exponents of -1.6 ± 0.04 ($0.03 \leq Q$ / Å ≤ 0.07) and -2 ± 0.06 ($0.02 \leq Q$ / Å ≤ 0.05) respectively. No such exponent can be obtained from the scattering for 2k PEOF, maybe due to the weak scattering signal. The exponents of –1.6 and –2 for 5k and 10k PEOF respectively suggest that for the latter exponent a flexible random coil conformation is adopted whilst the former is near the scaling expected for wormlike micelles (cylindrical micelles should have a scaling exponent of –1)[12]. However due to the very low concentrations investigated, the scattering cross section rapidly falls to background leading to uncertainty about the model to adopt for these data as spherical, cylindrical or Gaussian coils models are as good as each other. Moreover, in the Q range where the signal to noise ratio is acceptable, there are no distinctive features that would enable discrimination between the various possibilities. Consequently all we can rely on is the determination of the radii of gyration of the micelles from Guinier plots[13,14]. An example is shown in figure 4.3.1.14.

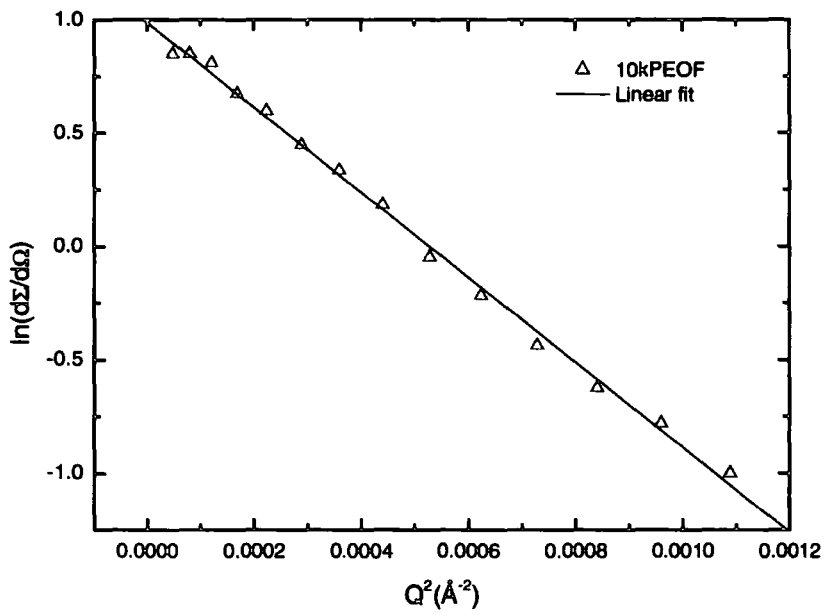

Figure 4.3.1.14: Guinier plot for 10k PEOF at a concentration of 10^{-3} g ml^{-1}.

The results for all three molecular weight polymers are given in table 4.3.1.7.

	R_g (Å) ± 15		
Concentration (g ml^{-1})	2kPEOF	5kPEOF	10kPEOF
1.00E-03	75	97	275
5.00E-04	88	100	281
1.00E-04	86	110	289
5.00E-05	65	105	287

Table 4.3.1.7: Flory radii of gyration, R_g, obtained by Guinier approximation for 2k, 5k and 10k PEOF with bulk concentration.

These values are far larger than the radius of gyration expected for single molecules and much bigger than the lower layer thickness observed for 5k and 10k PEOF. However, the radii of gyration of the micelles are half the values expected for an all trans configuration (223 Å and 524 Å for 5k and 10k PEO respectively) suggesting that the arrangement of 5k and 10k PEOF in the lower layer is not fully stretched. This suggest that significant overlap between the two layers occurs resulting in a less well defined micellar structure that is partially mixed with tails from molecules in the upper layer.

The reflectivity data, the sharpness of the transition from the upper layer to lower layer and the small-angle scattering data for the 2kPEOF polymer suggests that the micelles for this polymer have a well-defined morphology. The radii of gyration of the micelles correspond to the all trans configuration of unmodified 2k PEO (~85 Å) suggesting that the shell of the micelles is made of highly stretched PEO chains regrouped around a fluorocarbon core.

Above a bulk concentration of 10^{-3} g ml^{-1}, phase separation was observed for 2k PEOF as macroscopic oily droplets dispersed throughout the aqueous phase were observed resulting in a heterogeneous solution. Hydrophobically end-capped PEO have been investigated previously and no phase separation was mentioned by Xu and co-workers[15] as well as Zhang *et al.*[16] for fluorinated end-capped PEO with higher molecular weights. However, perfluoroalkyl end-capped PEO have been investigated and recent results[17] showed that phase separation was observed for molecular weight of 10 000 and 20 000 g mol^{-1}. They concluded that phase separation was dependent on the degree of functionalisation, hydrophobic strength of the end group and PEO molecular weight. This process was governed by the hydrophobe-hydrophile balance of PEOF and by the extent

of end-fuctionalisation (a 10% incompletely end-capped 20k PEOF did not phase separate). The phase separation observed for 2k PEOF suggests strong hydrophobicity of the fluorocarbon groups and to check the extent of hydrophobicity, the influence of the temperature on the phase separation was investigated by putting three sealed-test tubes containing about 5 ml of aqueous solutions of 2k, 5k and 10k PEOF ($c = 10^{-3}$ g ml^{-1}) in a thermostatic bath and varying the temperature between 20°C and 80°C. The temperature inside the tube was checked using a digital thermometer and the results are shown in table 4.3.1.8. The temperature at which a homogeneous aqueous PEO solution starts to turn cloudy is referred to as the cloud point temperature. Above those temperatures, the solutions become cloudy due to phase separation, the "cloud point" phenomenon[18]. When PEO dissolves in water, the polymer chain is surrounded by a layer of highly oriented water molecules, which can be disrupted at elevated temperatures (see Chapter Two, section 2-2-3). The breakdown of the water layer will favour PEO-PEO interactions and induce phase separation. Due to the release of structural water molecules, this mechanism is entropically driven. As temperature increases and above CMC, this entropy effect dominates, and hence, the system will undergo phase separation in order to reduce the extent of this unfavourable water structuring. The occurrence of cloudiness signifies the macroscopic phase separation of the PEO-H_2O system into two phases; a polymer-rich phase and a polymer-lean phase.

Polymer	Cloud Point Temperature (°C)
2k PEOF	26.0 ± 0.1
5k PEOF	52.1 ± 0.1
10k PEOF	73.8 ± 0.1

Table 4.3.1.8: Determination of the cloud point temperature (CPT) for 2k, 5k and 10k PEOF at solution concentration of 10^{-3} g ml^{-1}.

As shown in table 4.3.1.8, the cloud point temperature decreases remarkably as the molecular weight decreases going from ~74°C for 10k PEOF to ~26°C for the lower molecular weight polymer. Phase separation of a dilute aqueous PEO solution occurs at a temperature close to 100°C[18]; the CPT is significantly suppressed by the incorporation of

a fluorocarbon group at the end of PEO chains reinforcing the crucial role of the hydrophobe-hydrophile balance in phase separation.

4-3-2 Kinematic Approximation

Using the optical matrix method important information regarding the surface organisation of end fluorinated PEO were determined. Despite those results, the kinematic approximation[19] was also used to analyse the data as it provides a more direct analysis and quantitative values for any separations between regions containing different species are relatively easily obtained.

Reflectivity data for each combination of deuterated and hydrogenous polymer and water were expressed in the form of equation 4.3.2.1 using the appropriate scattering lengths for each combination and after incorporating the corrections where D_2O was the solvent.

$$R(Q) = \frac{16\pi^2}{Q^2}\left[b_p^2 h_{pp}(Q) + b_w^2 h_{ww}(Q) + 2b_p b_w h_{pw}(Q)\right] \qquad \text{Equation 4.3.2.1.}$$

where h_{pp} and h_{ww} are the self partial structure factors of the polymer and water respectively, h_{pw} the cross partial structure factor and b_i the coherent scattering length of the molecule i.

To extract each of these three partial structure factors requires neutron reflectivity data at three different contrasts obtained by various combinations of hydrogenous and deuterated polymer and subphase. Therefore for the adsorbed solutions of deuterated fluorinated end-capped PEO on nrw, the reflectivity can be expressed as,

$$R(Q) = \frac{16\pi^2}{Q^2} b_p^2 h_{pp} \qquad \text{Equation 4.3.2.2.}$$

For the adsorbed solutions of protonated fluorinated end-capped PEO on D_2O (assuming that the contribution to the specular reflection is negligible, i.e. b_p is sufficiently small and can be approximated to 0 Å), the reflectivity is given by,

$$R(Q) = \frac{16\pi^2}{Q^2} b_w^2 h_{ww} \qquad \text{Equation 4.3.2.3.}$$

The combination of deuterated polymer in D_2O lifts the contribution of the cross partial structure factor. By solving simultaneously each of the three expressions for $R(Q)$, the individual partial structure factors can be obtained.

The background contributions were subtracted from all reflectivity profiles and for those systems where the solvent is deuterated, the correction procedure of Crowley and co-workers[20] (further details available in Chapter Two, section 2-3-5) was applied to the experimental data before expressing them in terms of partial structure factors.

Again, 2k DPEOF will be discussed in detail, identical fitting procedures being applied to 5k and 10k DPEOF polymers and will be included in the main discussion.

PEO Self Partial Structure Factor (h_{pp})

Partial structure factors obtained for 2k DPEOF (DPEOF in nrw contrast) at selected concentrations are shown in figure 4.3.2.1.

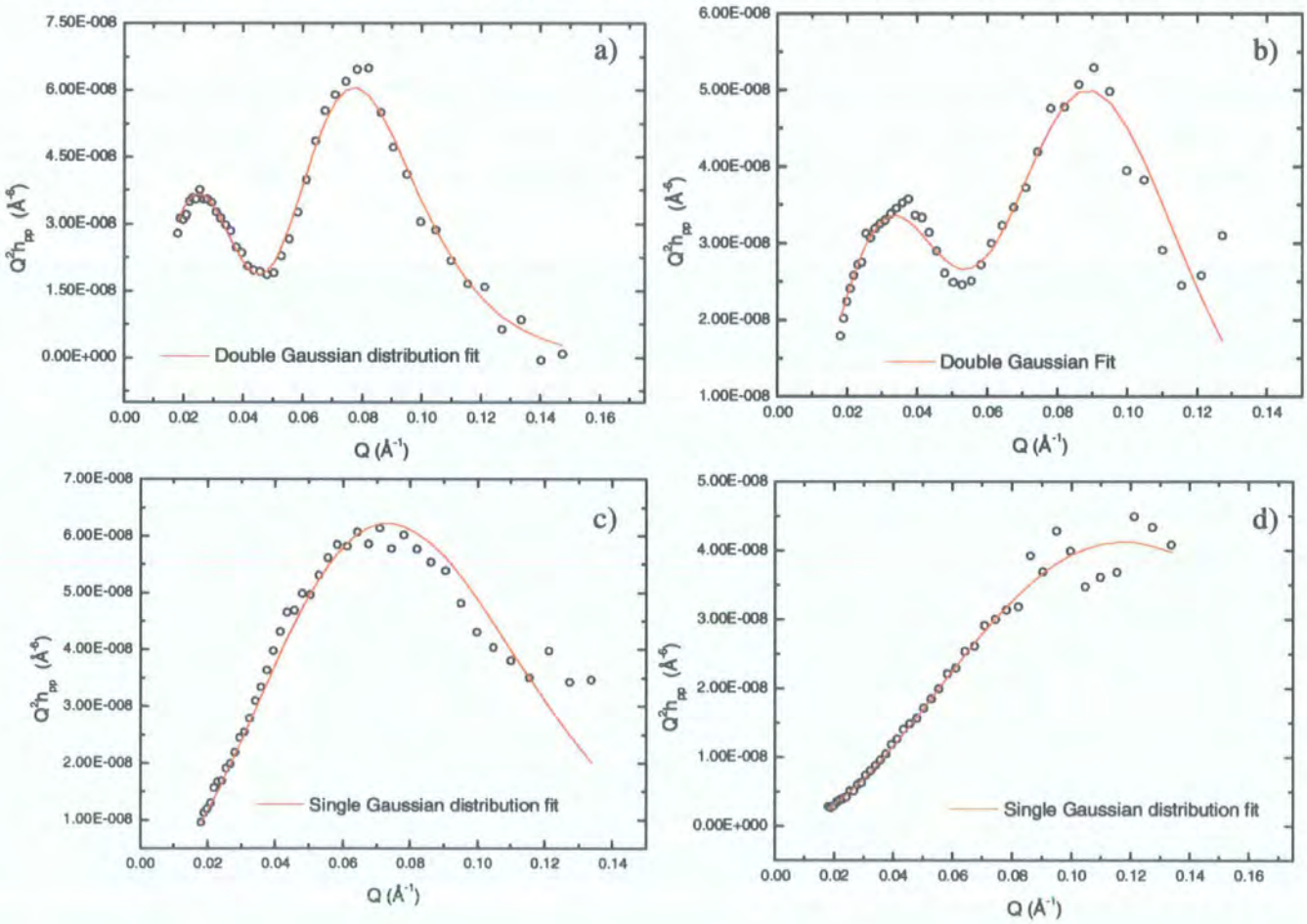

Figure 4.3.2.2: Partial structure factors (h_{pp}) for 2k DPEOF at selected solution concentrations. a) 10^{-3} g ml^{-1}; b) 5×10^{-5} g ml^{-1}; c) 10^{-5} g ml^{-1} and d) 10^{-6} g ml^{-1}. The red line corresponds to non-linear least squares fits of the model partial structure factors to the data.

As the bulk concentration increases, changes in the partial structure factor are evident. At low concentrations (figure 4.3.2.1d) the partial structure factor increases linearly with Q. As the concentration increases, a maximum is observed as shown in figure 4.3.2.1 c, centred at $Q \sim 0.08$ Å^{-1}. For solution concentrations greater than ~2×10^{-5} g ml^{-1} (not shown in figure 4.3.2.1) the partial structure factors become very different with two maxima being observed, one centred between 0.08 and 0.09 Å^{-1} and the other at lower Q (~0.02-0.04 Å^{-1}) with smaller amplitude. The maximum in the partial structure factor at higher Q does not move in Q as the concentration increases and is approximately coincident with the single maximum observed for lower concentrations. This consistency is not observed for the maximum at lower Q as it moves to lower Q values with increase in bulk concentration and for $c = 10^{-3}$ g ml^{-1} the maximum is cut off by the low Q limit of the reflectometer.

A variety of functional forms have been used to interpret the partial structure factors of PEOF and the following section will briefly describe the theoretical distribution used to quantitatively analyse the data. Indeed by choosing the most appropriated functional form, the number density and layer thickness of the polymer layers can be extracted.

a) Single Uniform Density Layer (SUD)

The number density distribution is described by,

$n_i(z) = n_{i1}$ for $-\sigma/2 \le z \le \sigma/2$, 0 for all other z.

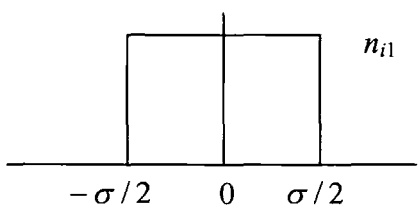

Equation 4.3.2.1.

The partial structure factor is,

$$Q^2 h_{ii}(Q) = 4n_{i1}^2 \sin^2\left(\frac{Q\sigma}{2}\right)$$ Equation 4.3.2.2.

where n_{i1} is the number density of polymer molecule i at the maximum of the distribution and σ is the full width at half height of the distribution which correspond to the layer thickness.

b) Single Gaussian Distribution (SGD)

The distribution is given by,

$$n(z) = n_1 \exp\left(\frac{-4z^2}{\sigma^2}\right) \qquad \text{Equation 4.3.2.3.}$$

where n_1 is the number density of polymer molecules at the maximum of the Gaussian peak, σ is the full width at half height of the distribution and defines the layer thickness.

The associated partial structure factor is,

$$Q^2 h_{pp}(Q) = n_1^2 \frac{\pi Q^2 \sigma^2}{4} \exp\left(\frac{-Q^2\sigma^2}{8}\right) \qquad \text{Equation 4.3.2.4.}$$

For solutions with concentrations greater than 2×10^{-5} g ml^{-1}, a variety of functional forms have been used to interpret theses data and simple model such as double uniform layer, double Gaussian or a double uniform parabola were used.

c) Double Uniform Layer Distribution (DUD)

The number density distribution of a double uniform layer of polymer molecules at the surface is given by,

$$\begin{aligned}
n_i(z) &= 0 && z \le -\delta - \tau/2 \\
&= n_{i2} && -\delta - \tau/2 \le z \le -\delta + \tau/2 \\
&= 0 && -\delta + \tau/2 \le z \le -\sigma/2 \\
&= n_{i1} && -\sigma/2 \le z \le \sigma/2 \\
&= 0 && z \ge \sigma/2
\end{aligned}$$

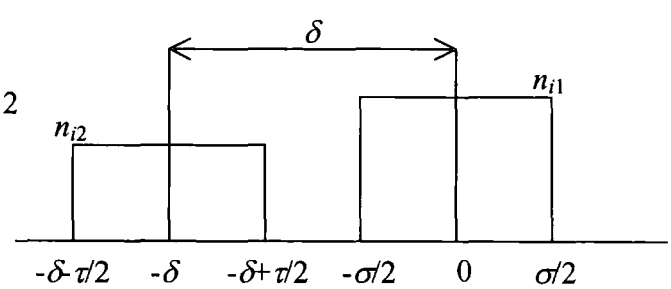

Equation 4.3.2.5.

If no separation, δ can be substituted by $\sigma + \tau/2$.

The partial structure factor is described by,

$$Q^2 h_{ii}(Q) = 4n_{i1}^2 \sin^2\left(\frac{Q\sigma}{2}\right) + 4n_{i2}^2 \sin^2\left(\frac{Q\tau}{2}\right) + 8n_{i1}n_{i2} \sin\left(\frac{Q\sigma}{2}\right)\sin\left(\frac{Q\tau}{2}\right)\cos(Q\delta)$$

Equation 4.3.2.6.

where n_{i1} and n_{i2} are the number density of polymer molecules i in layer 1 and layer 2 respectively that have full widths at half height of σ and τ (thickness). δ is the distance between the centres of each distribution.

d) Double Gaussian Distribution (DGD)

For a double Gaussian distribution of polymer molecules at the near surface, the number density distribution is given by,

$$n(z) = n_1 \exp\left(\frac{-4z^2}{\sigma^2}\right) + n_2 \exp\left(\frac{-4(z+\delta)^2}{\tau^2}\right)$$

Equation 4.3.2.7.

The partial structure factor is given by,

$$Q^2 h_{pp}(Q) = n_1^2 \frac{\pi Q^2\sigma^2}{4}\exp\left(\frac{-Q^2\sigma^2}{8}\right) + n_2^2 \frac{\pi Q^2\tau^2}{4}\exp\left(\frac{-Q^2\tau^2}{8}\right) + n_1 n_2 \frac{\sigma\tau\pi Q^2}{2}\exp\left(\frac{-Q^2(\sigma^2+\tau^2)}{16}\right)\cos(Q\delta)$$

Equation 4.3.2.8.

e) Double Uniform Parabolas Distribution (DPD)

The number density distribution is described as follow,

$$
\begin{aligned}
n_i(z) &= 0 && z \le -\delta - \tau \\
&= n_{i2}\left(1 - \frac{(z+\delta)^2}{\tau^2}\right) && -\delta - \tau \le z \le -\delta + \tau \\
&= 0 && -\delta + \tau \le z \le -\sigma \\
&= n_{i1}\left(1 - \frac{z^2}{\sigma^2}\right) && -\sigma \le z \le \sigma \\
&= 0 && z \ge \sigma
\end{aligned}
$$

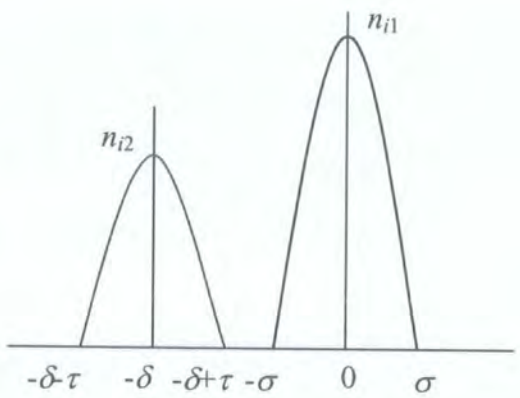

Equation 4.3.2.9.

Hence the associated partial structure factor is,

$$
\begin{aligned}
Q^2 h_{ii}(Q) = {} & \frac{16 n_{i1}^2}{Q^4\sigma^4}(\sin(Q\sigma) - Q\sigma\cos(Q\sigma))^2 + \frac{16 n_{i2}^2}{Q^4\tau^4}(\sin(Q\tau) - Q\tau\cos(Q\tau))^2 \\
& + \frac{32 n_{i1} n_{i2}}{Q^4\sigma^2\tau^2}(\sin(Q\sigma) - Q\sigma\cos(Q\sigma))(\sin(Q\tau) - Q\tau\cos(Q\tau))\cos(Q\delta)
\end{aligned}
$$

Equation 4.3.2.10.

NB. δ can be replaced by $\sigma + \tau$ if no separation required.

Typical number density profiles for each model (excepted double uniform parabolas distribution) are given in figure 4.3.2.3a-d for a range of concentrations that are representative of the series investigated: 10^{-3}, 5×10^{-5}, 10^{-5} and 10^{-6} g m^{-1}. The values obtained from the fits for the layer thicknesses, number densities and "goodness of the fit" (χ) are given in table 4.3.2.1a-d.

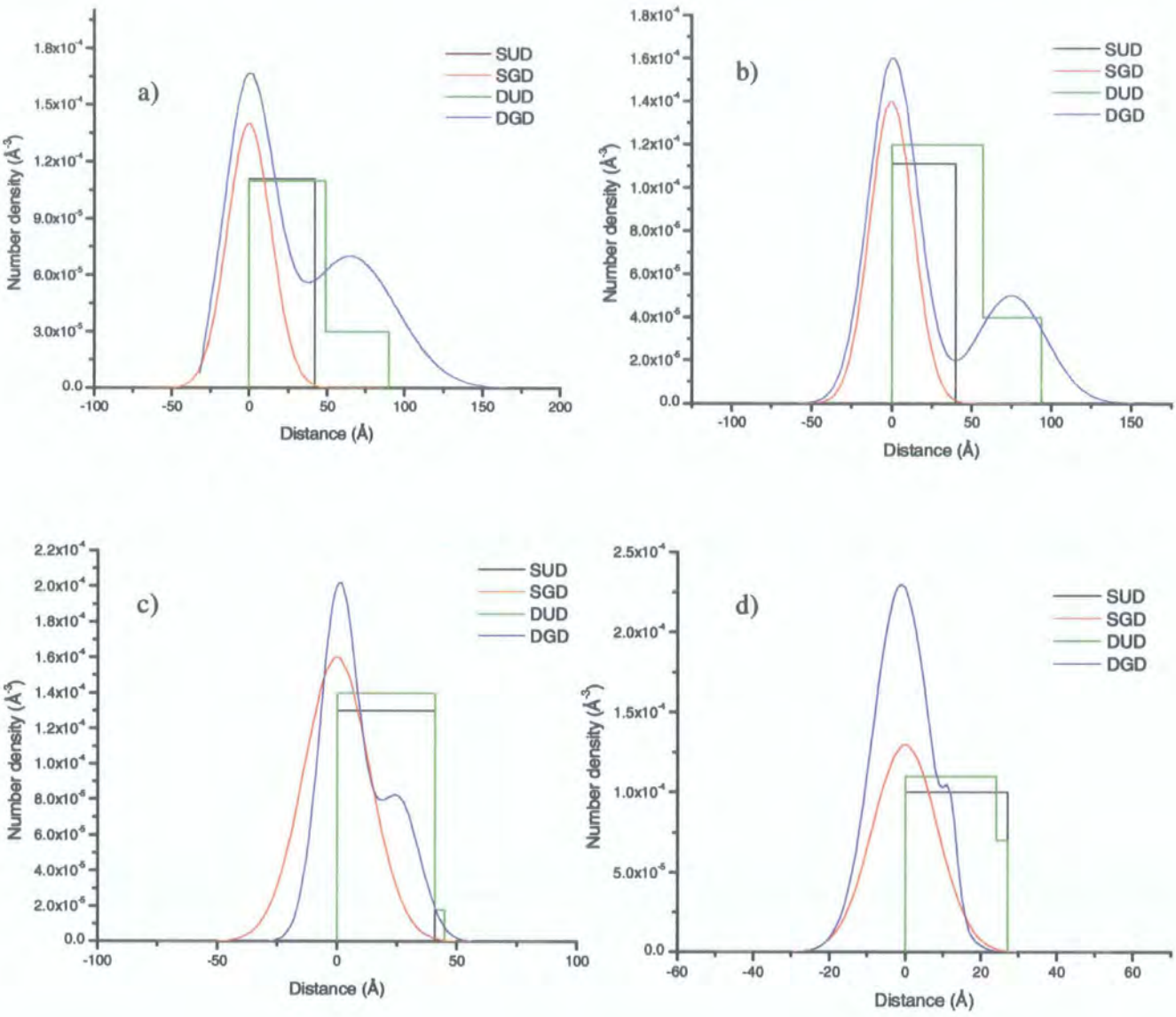

Figure 4.3.2.3: Comparison between the number density profiles of 2k PEOF obtained for various layer model distributions at a bulk concentration of a) 10^{-3} g ml^{-1}, b) 5×10^{-5} g ml^{-1}, c) 10^{-5} g ml^{-1} and d) 10^{-6} g ml^{-1}.

Model	$\sigma \pm 1$ (Å)	n_1 (Å^{-3}) $\pm 2\times10^{-5}$	$\tau \pm 3$ (Å)	n_2 (Å^{-3}) $\pm 2\times10^{-6}$	χ
SUD	42	1.10E-04	-	-	1.67E-16
SGD	40	1.40E-04	-	-	1.84E-16
DUD	49	1.10E-04	41	3.00E-05	7.60E-17
DGD	45	1.60E-04	85	7.00E-05	2.28E-18
DPD	29	9.46E-11	39	5.78E-11	2.60E-17

a) $c = 10^{-3}$ g ml^{-1}

Model	$\sigma \pm 1$ (Å)	n_1 (Å^{-3}) $\pm 2\times10^{-5}$	$\tau \pm 3$ (Å)	n_2 (Å^{-3}) $\pm 2\times10^{-6}$	χ
SUD	40	1.10E-04	-	-	1.54E-16
SGD	38	1.40E-04	-	-	1.35E-16
DUD	57	1.20E-04	37	4.00E-05	6.54E-17
DGD	43	1.60E-04	62	5.00E-05	9.63E-18
DPD	20	4.49E-10	39	6.40E-11	2.26E-17

b) $c = 5\times10^{-5}$ g ml^{-1}

Model	$\sigma \pm 1$ (Å)	n_1 (Å^{-3}) $\pm 2\times10^{-5}$	$\tau \pm 3$ (Å)	n_2 (Å^{-3}) $\pm 2\times10^{-6}$	χ
SUD	41	1.30E-04	-	-	4.66E-18
SGD	39	1.60E-04	-	-	1.52E-18
DUD	41	1.40E-04	4	1.80E-05	1.22E-17
DGD	23	2.00E-04	26	8.00E-05	2.06E-17
DPD	25	3.33E-10	37	-8.21E-12	2.06E-17

c) $c = 10^{-5}$ g ml^{-1}

Model	$\sigma \pm 1$ (Å)	n_1 (Å^{-3}) $\pm 2\times10^{-5}$	$\tau \pm 3$ (Å)	n_2 (Å^{-3}) $\pm 2\times10^{-6}$	χ
SUD	27	1.00E-04	-	-	3.85E-18
SGD	24	1.30E-04	-	-	3.49E-18
DUD	24	1.10E-04	3	7.00E-05	3.50E-17
DGD	21	2.30E-04	9	5.00E-05	3.49E-17
DPD	18	1.20E-09	61	-2.90E-13	3.52E-17

d) $c = 10^{-6}$ g ml^{-1}

Table 4.3.2.1: Layer thickness, number density, "goodness of the fit" values of the fits of 2k PEOF for selected bulk concentrations using different layer model distributions.

After comparing the profiles obtained and the model parameters for each bulk concentration, the following observations were made. For bulk concentration of 10^{-5} g ml^{-1} and above, all models predict almost identical magnitudes of near surface density but contrasting penetration depths. This emphasises the difficulty in identifying the precise distribution of PEO chains in the subphase. However, by comparing the "goodness of fit" parameter, χ, from the least squares fitting routine, it appears that the double Gaussian distribution gave the better fit as shown in table 4.3.2.1a-b. Indeed, the results reveal that the χ values are significantly lower for any double Gaussian model fit, indicating that the fits of the calculated models are closer to the experimental data. It can also be noted that the parameters returned from a double uniform parabolas distribution are extremely low with negative number density returned at low concentration. These unrealistic values suggest that this distribution is not suitable for the system investigated. For bulk concentration of 10^{-5} g ml^{-1} and below, the magnitude in number density returned from theoretical models is almost identical except for the double Gaussian distribution where an increase in number density is observed. However all models agree that the layer thickness of the upper layer remains almost constant over the all concentration range whereas the layer thickness of the lower layer increases with bulk concentration and is almost non-existent at low bulk concentration suggesting that a single monolayer distribution seems to be the most appropriate. This is reinforced by comparing the χ values as single distributions (uniform density layer and Gaussian distribution of polymer molecules) offer lower values. Qualities of the fits are indistinguishable between either of the model functions but the Gaussian distribution was chosen due to its physically viable description. Support for this assumption comes from computer simulations of monolayers of hexadecyltrimethylammonium chloride[21] and tetradecyltrimethylammonium bromide[22].

Therefore, the single Gaussian distribution and double Gaussian distribution were used to fit the data. The fits were obtained by adjusting n_1, n_2, σ and τ with $\delta = (\sigma + \tau)/2$ with the number of parameters depending on whether a single or double Gaussian was required (please refer to figure 4.3.2.2a-d). The results are given in table 4.3.2.2.

c (g ml^{-1})	$d \pm 2$ (Å)	$n_i \pm 3\times10^{-6}$ (Å^{-3})
1.00E-03	σ 45	n_1 1.60E-04
	τ 85	n_2 7.00E-05
5.00E-04	σ 47	n_1 1.70E-04
	τ 79	n_2 8.00E-05
1.00E-04	σ 45	n_1 1.60E-04
	τ 67	n_2 7.00E-05
5.00E-05	σ 43	n_1 1.60E-04
	τ 62	n_2 5.00E-05
3.00E-05	σ 43	n_1 1.60E-04
	τ 58	n_2 4.00E-05
2.00E-05	σ 42	n_1 1.60E-04
1.00E-05	σ 37	n_1 1.60E-04
5.00E-06	σ 35	n_1 1.70E-04
1.00E-06	σ 24	n_1 1.30E-04
5.00E-07	σ 16	n_1 7.00E-05

Table 4.3.2.2: Number densities (n_1 and n_2) of polymer molecules at the maximum of each Gaussian peak and widths (σ and τ) at half height of Gaussian distributions for 2k DPEOF with bulk concentration.

The same models were also applied to the self partial structure factors obtained for the 5k DPEOF and 10k DPEOF, for the latter polymer the quality of the fits was not as good due to the rather more diffuse distribution of the polymer at the air-water interface for these higher molecular weight polymers. However, a single layer model was not appropriate for the 10k DPEOF polymer at any concentration and only valid for the two lowest concentrations solutions of 5k DPEOF. The results of the number densities and layer thicknesses for 5k DPEOF and 10k DPEOF are given in appendix 4 and 5, table A.4 and A.5 respectively.

The dependence of the number density on solution concentration is shown in figures 4.3.2.4a-c for all three D PEOF.

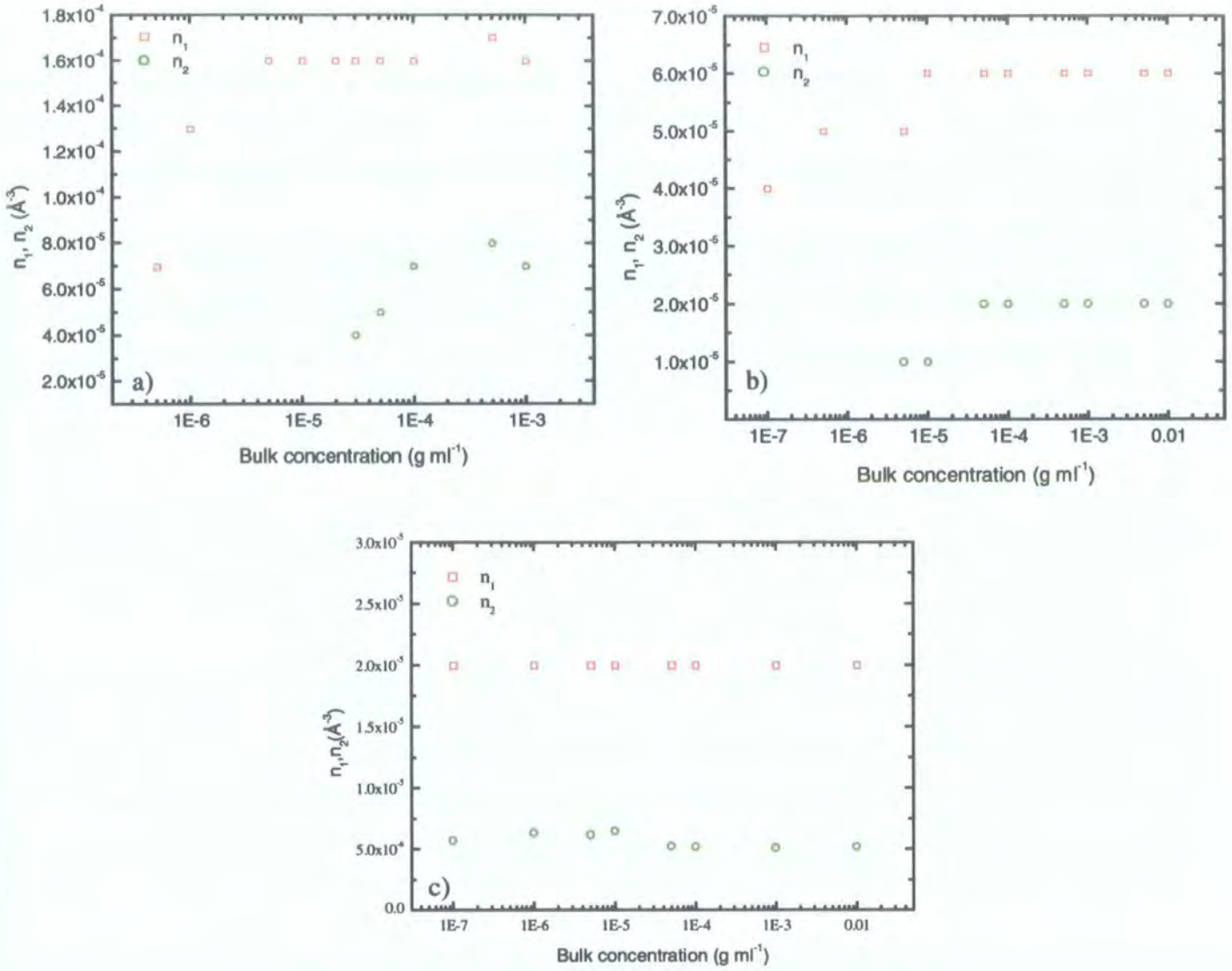

Figure 4.3.2.4: Number densities at maximum of each Gaussian fitted to experimental partial structure factors as a function of solution concentration for a) 2k DPEOF, b) 5k DPEOF and c) 10k DPEOF.

The behaviour of the number density at distribution maximum is dependent on the polymer, for the 2k DPEOF the upper layer number density (n_1) increases rapidly with concentration until a constant value of circa 1.6×10^{-4} Å^{-3} is observed for concentrations above ~10^{-6} g ml^{-1} whereas the lower layer number density (n_2) increases gradually to what appears to be a constant value of ~7×10^{-5} Å^{-3}. Magnitudes of number densities for 5k DPEOF are less than half the one observed for 2k DPEOF and a more gradual increase with concentration is evident with a constant value of circa 6×10^{-5} Å^{-3} being reached at $c = 10^{-5}$ g ml^{-1}. The lower layer has a constant number density of 2×10^{-5} Å^{-3} being reached over a very narrow range of

bulk solution concentration. Number densities of the 10k DPEOF polymer are further reduced and a constant value is observed for both layers over the whole concentration range. The upper layer having a number density of 2×10^{-5} Å^{-3} and that of the lower layer is 5×10^{-6} Å^{-3}, an order of magnitude smaller than that of the 2k DPEOF lower layer number density. The dependence of the distribution full widths at half height (σ and τ) on solution concentration is shown in figures 4.3.2.5a-c for all three DPEOF.

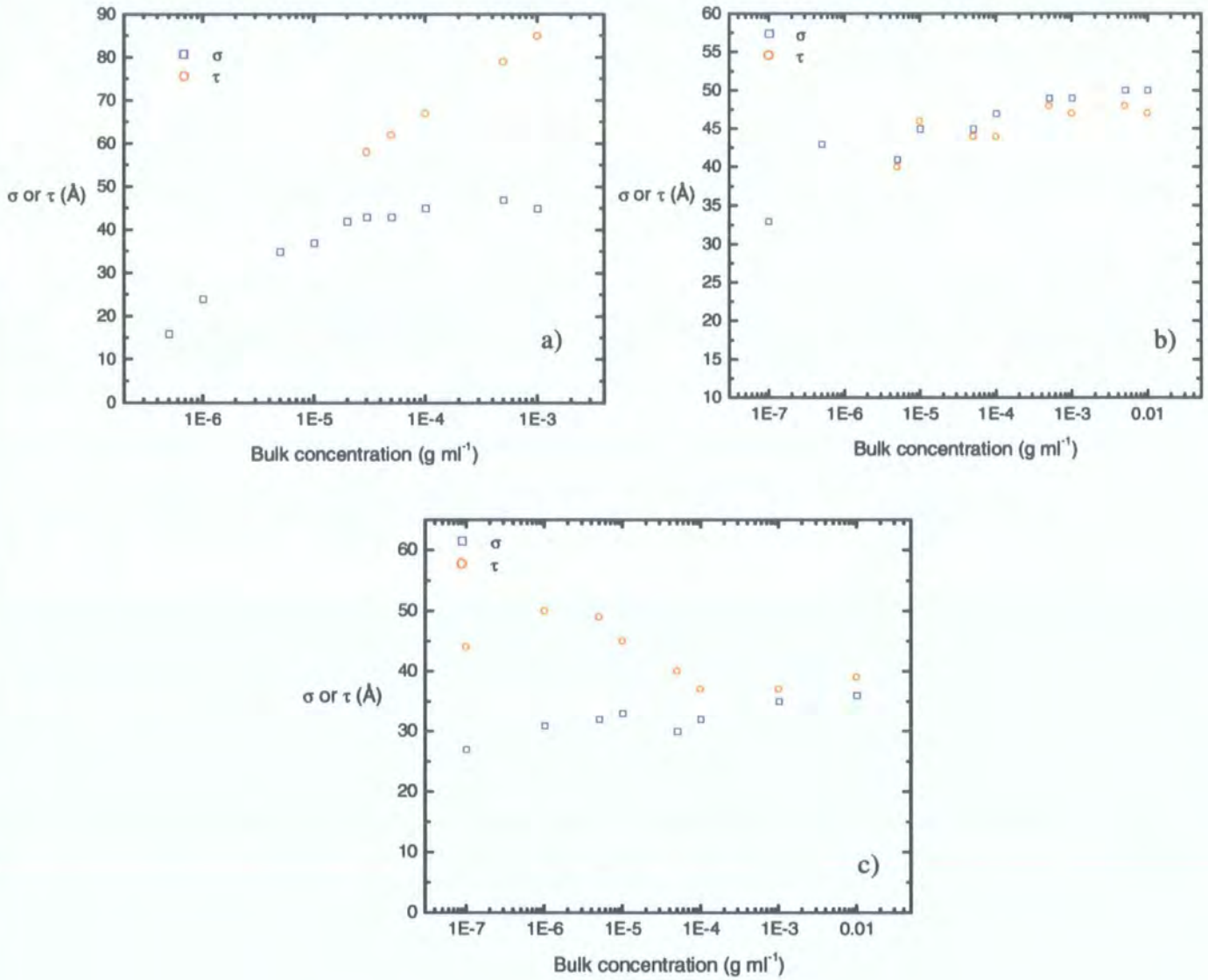

Figure 4.3.2.5: Widths of Gaussian distributions (σ and τ) fitted to experimental partial structure factors as a function of solution concentration for a) 2k DPEOF, b) 5k DPEOF and c) 10k DPEOF.

The behaviour of the full widths is also dependent on the polymer; for 2k DPEOF the upper layer (σ) increases smoothly until the first appearance of a second layer and thereafter it remains constant. The second layer (τ) increases linearly over the concentrations range 3×10^{-5} to 10^{-3} g ml^{-1}. Full widths for the 5k DPEOF polymer differs significantly from 2k DPEOF as both upper and lower layers have much the same values of the distribution width over the concentrations range 5×10^{-6} to 10^{-2} g ml^{-1} where two layers are observed. For concentrations less than 10^{-6} g ml^{-1} only a single layer is evident with the thickness increasing rapidly to approximately the same value as for higher concentrations. The 10k DPEOF polymer have some similarities to a certain extent with the distribution width behaviour of 5k DPEOF as the lower layer width is almost constant at 37 ± 2 Å for the entire concentration range investigated. A slight but noticeable increase in the upper layer distribution width is observed over the concentration range explored but remains essentially constant around 35 ± 2 Å for concentrations of 5×10^{-5} g ml^{-1} and above. The lower magnitudes of the number density combined with the larger layer dimensions for 10k DPEOF are confirming the diffuse nature distribution of the polymer at the air-water interface.

By using equations 4.3.2.4 and 4.3.4.7 the number density distribution for 2k DPEOF can be plotted and is shown in figure 4.3.2.6.

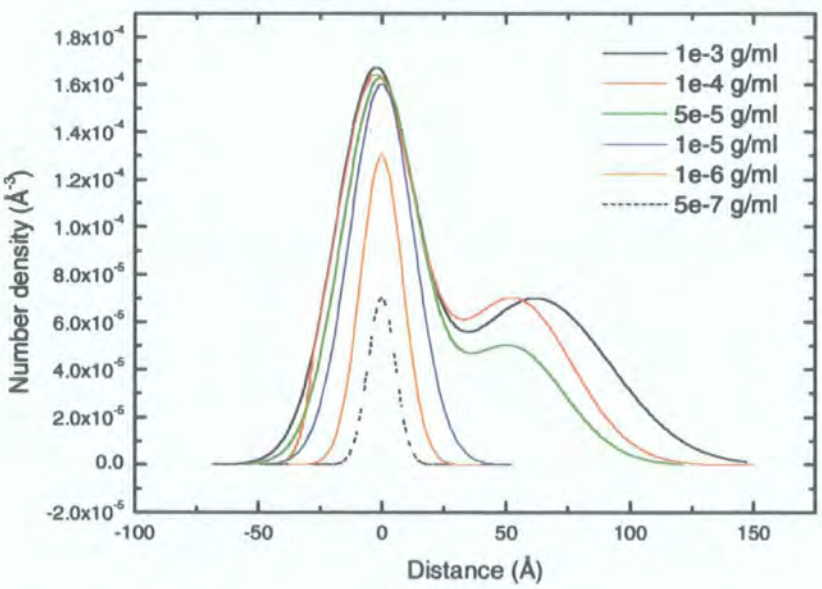

Figure 4.3.2.6: Number density distributions from double Gaussian distribution of reflectivity data for aqueous solutions of 2k DPEOF with the bulk concentrations indicated.

The number density distribution for the 2k DPEOF polymer confirms the two layer organisations observed by the optical matrix analysis, as the formation from one monolayer to two monolayers with increase in bulk concentration is evident. Similarities between the number density distributions from the double Gaussian fits to the partial structure factors and those calculated from the optical matrix method (figure 4.3.1.4) are clearly evident. However the double Gaussian distributions are somewhat broader especially at the air-water interface due probably to the fact that the roughness at the interface in the optical matrix method is fixed to the rms amplitude of capillary wave fluctuations on a water surface, i.e. 2.5 Å. The same agreement was found between the number density distributions from the double Gaussian fits to the partial structure factors and those calculated from the optical matrix method analysis for both 5k and 10k DPEOF polymers.

The number density distribution for all three molecular weight polymers is however very different (figure 4.3.2.7) when compared to each other, confirming the dependence of the surface organisation of PEO at the air-water interface on molecular weight.

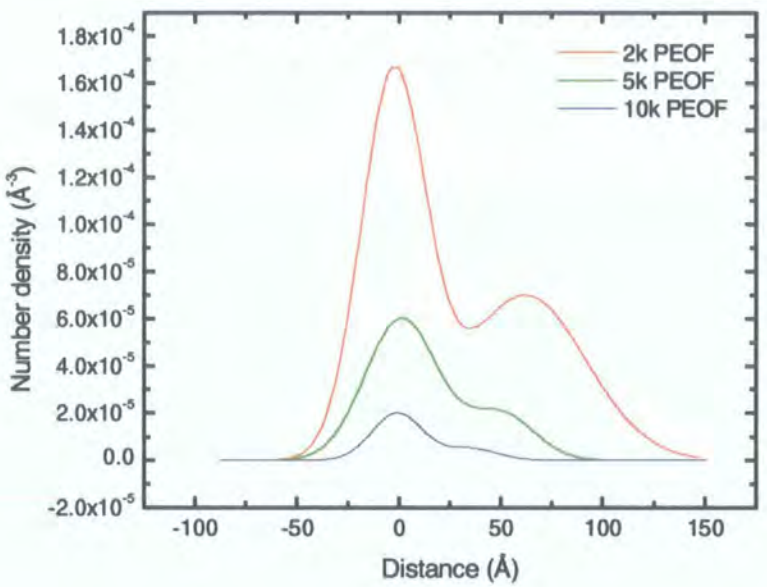

Figure 4.3.2.7: Number density distribution for 2k, 5k and 10k DPEOF at a bulk concentration of 10^{-3} g ml^{-1}.

The results obtained from the kinematic approximation mimics well the results obtained from the optical matrix analysis. Both analyses returned the same magnitude in number density of PEOF in both layers and layer thickness is reproduced well within errors.

The best way to illustrate this argument is by comparing the surface excess returned by both analyses. The total surface excess, Γ (mg m^{-2}), from the kinematic approximation analysis was determined by using equation 4.3.2.11 and 4.3.2.12 according to the distribution of the polymer layer (double or single Gaussian distribution respectively).

$$\Gamma = \frac{\sqrt{\pi/2}}{N_A}(n_{i1}\sigma + n_{i2}\tau) \times \overline{M_n} \times 10^{20} \quad \text{Equation 4.3.2.11.}$$

$$\Gamma = \frac{\sqrt{\pi/2}}{N_A}(n_{i1}\sigma) \times \overline{M_n} \times 10^{20} \quad \text{Equation 4.3.2.12.}$$

where n_{i1} and n_{i2} are the number density of the upper and lower layer respectively and σ and τ their appropriate thickness. $\overline{M}_n$ is the number average molecular weight determined via size exclusion chromatography.

The total surface excess obtained from both analyses is plotted for 2k PEOF as a function of the bulk concentration (figure 4.3.2.8).

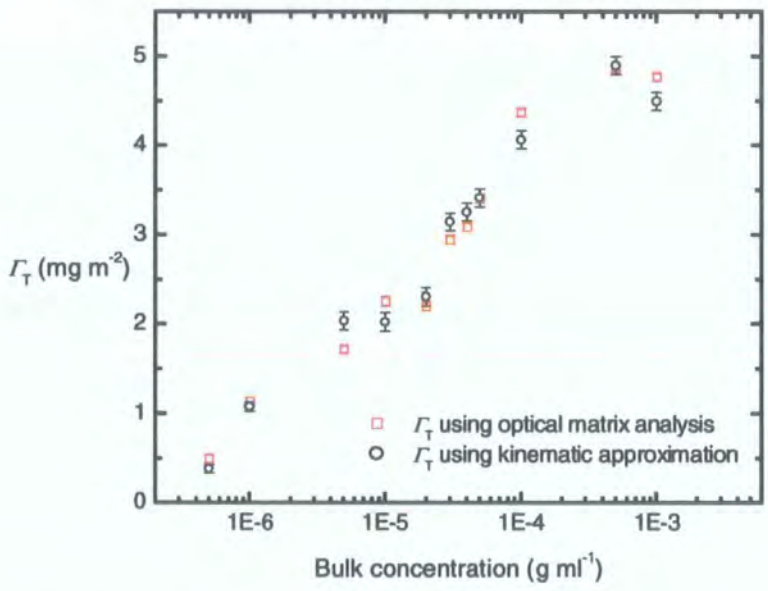

Figure 4.3.2.8: Comparison of the total surface excess calculated from optical matrix analysis and kinematic approximation for 2k PEOF as a function of bulk concentration.

It is evident that the total surface excess returned from both analyses is similar within experimental errors. The same agreements were found for the higher molecular weight polymers suggesting that the results obtained from both analyses are realistic. The total surface excess determined from kinematic approximation for 5k and 10k PEOF is given in appendix 4 and 5, table A.4 and A.5 respectively.

Having confirmed that the parameters describing the PEOF organisation at the air-water interface are reasonable, it would be of great interest to have some information regarding the distribution of water molecules within the polymer layer at the air-water interface.

Water Self Partial Structure Factor (h_{ww})

The background subtracted and Crowley corrected data are presented in terms of the self-partial structure factors obtained for water in figure 4.3.2.9 for a selection of solution concentrations for 2k HPEOF.

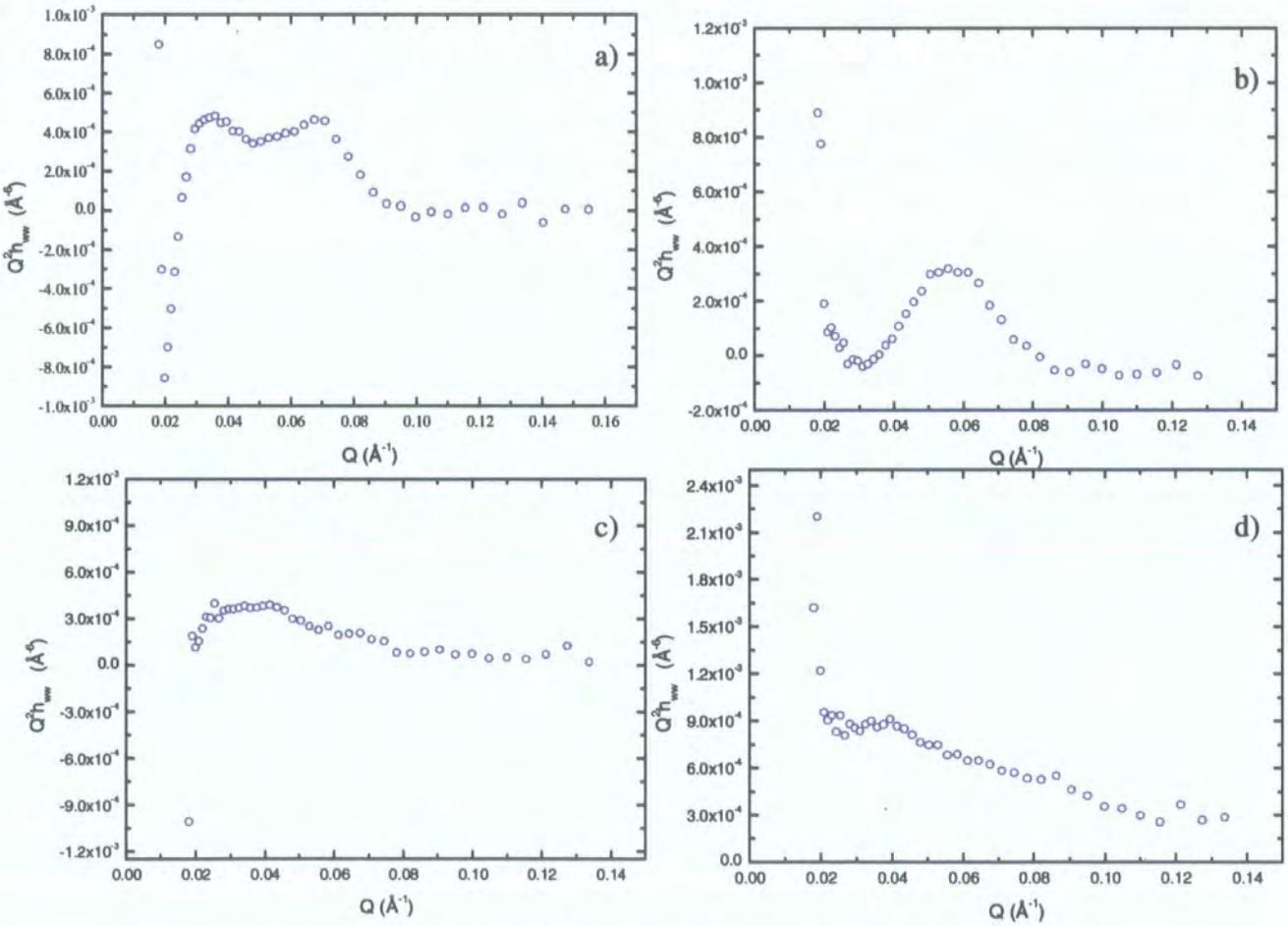

Figure 4.3.2.9: Partial structure factors (h_{ww}) for 2k HPEOF at selected solution concentrations. a) 10^{-3} g ml^{-1}; b) 5×10^{-5} g ml^{-1}; c) 10^{-5} g ml^{-1}; d) 10^{-6} g ml^{-1}

It is clear from figure 4.3.2.9a-d that the behaviour exhibited is unusual as all data display a maximum at low Q, and this has been observed for all three polymers. Theoretically, as Q tends toward zero the water self-partial structure factor data should approach a value of 1.1×10^{-3} $Å^{-6}$, which is the square root of the bulk density of heavy water (0.0332 $Å^{-3}$). In general, due to the displacement of water molecules by protonated polymer, the magnitude of the self-partial structure decreases with increasing solution concentrations. The trend of the water self-partial structure factor is even more unusual at higher concentrations where two maximum are observed centred at $Q \approx 0.03$ and 0.07 $Å^{-1}$ respectively. The magnitude of the experimental partial structure factor is surprisingly small and keeps changing with solution concentration. Higher values are found for the most concentrated solutions but still an order of magnitude lower than theoretical predictions. Similar, but not so pronounced, behaviour has been reported for PEO[23-25] systems containing polymer films but is not specific to PEO systems, as this effect has been reported in other polymer systems [26,27]and recently in EO containing surfactants[28-30]. The possible sources of systematic error in such experiments have been evaluated and discussed in detail elsewhere[31,32]. The potential failure of the kinematic approximation at low Q is accounted for in the correction devised by Crowley[20] and the 4 first experimental data points shown in figure 4.3.2.9 could be attributed to Q approaching Q_c (see Chapter Two section 2-3-5 for more details). Other sources of systematic error include incorrect background subtraction, variations in surface coverage from measurement to measurement, contamination, isotope effects, or inappropriate labelling. As incorrect background subtraction will only affect the data at high Q[33], this assumption was disregarded, as it is not responsible for the major discrepancies observed in figure 4.3.2.9. The other potential factors can be accommodated or corrected, and are also not the source of error. Instrumentation errors being introduced during experimental set up could be the reason of such discrepancies. To check this assumption, the reflectivity data collected from a pure water surface from SURF reflectometer was plotted in the partial structure form and compared to the data from a simulated profile as shown in figure 4.3.2.10.

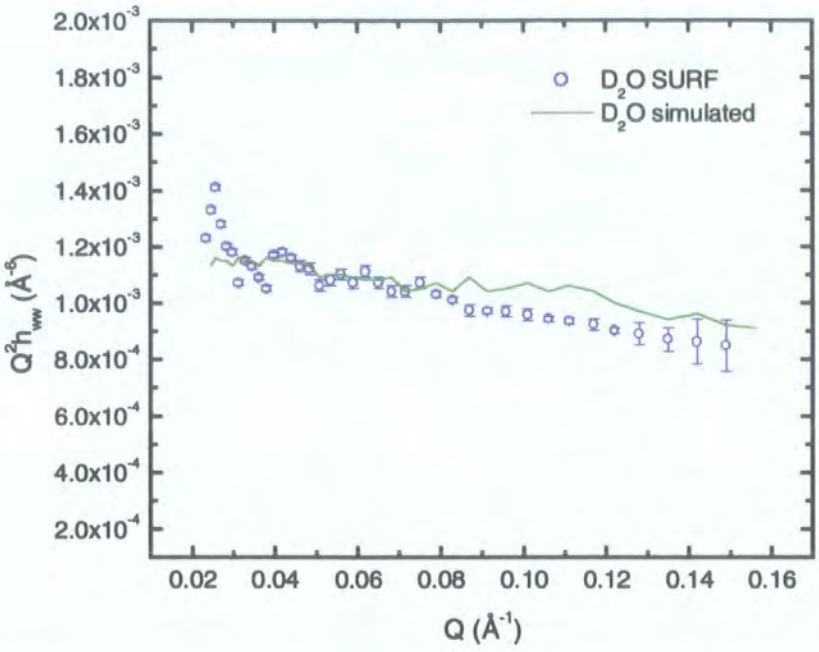

Figure 4.3.2.10: Comparison of simulated and experimental neutron reflectivity data in kinematic approximation form for water self-partial structure factor of a clean surface.

By comparing the partial structure profiles, small differences are observed in the Q range between 0 and 0.14 $Å^{-1}$ but are not important enough to justify the unusual trend of the experimental structure factor observed for aqueous solutions of 2k PEOF. The partial structure factor of a clean D_2O surface follows the trend expected in theory, i.e. a slight decrease in the magnitude of the self-partial structure with increasing Q and a value of h_{ww} ~ 1.1×10^{-3} $Å^{-6}$ observed at low or zero Q. As the unusual and unique trend of the experimental water self-partial structure factor was reproduced for all polymers, it seems that the features are connected to the PEOF/subphase arrangement rather than a mere artefact of the data. The only explanation of such behaviour could be attributed to the effect of the fluorocarbon group on the water molecules distribution, suggesting that the ethylene oxide units are not the only molecules to be considered when analysing the water self-partial structure factor.

In an attempt to improve the description of solvent distribution, 6 contrasts were used to explore the full power of the partial structure factor approach[30]. The kinematic approximation for this case then gives the specular reflectivity $R(Q)$ as in equation 4.3.2.13.

$$R(Q)=\frac{16\pi^2}{Q^2}\{\ b_p^2 h_{pp}(Q)+b_f^2 h_{ff}(Q)+b_w^2 h_{ww}(Q)+2b_p b_f h_{pf}(Q)+2b_p b_w h_{pw}(Q)+2b_f b_w h_{fw}(Q)\ \}$$

Equation 4.3.2.13.

where *p*, *f*, and *w* refer to the polymer chain, fluorocarbon group and water respectively.

The contrasts used and reflectivity profiles obtained are shown in figure 4.3.2.11.

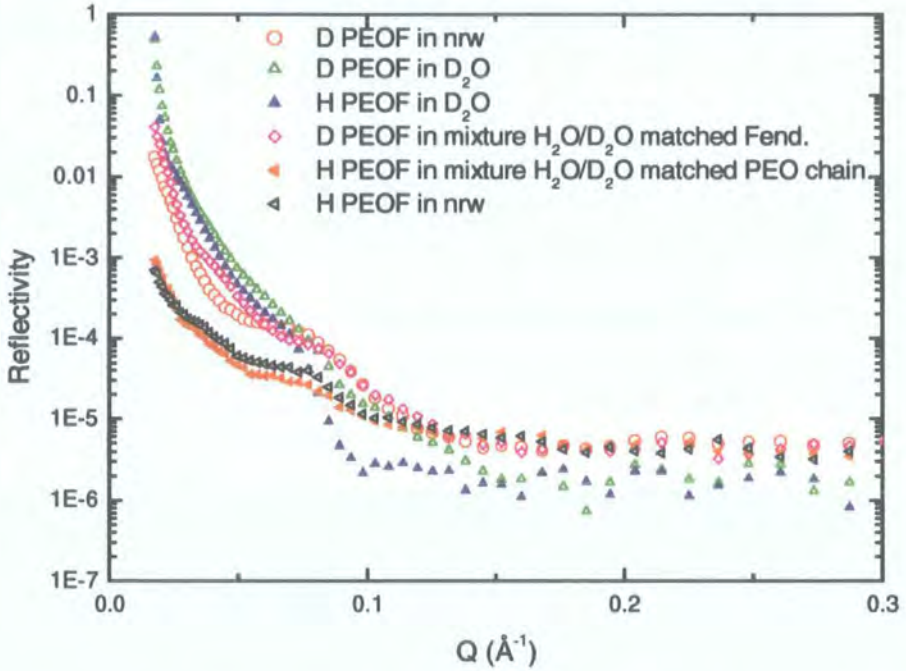

Figure 4.3.2.11: 6 experimental contrasts used for 2k PEOF (also used for 5k and 10k PEOF) to improve the solvent distribution of the water self-partial structure factor from kinematic approximation.

Unfortunately, the 6 partial structure factors obtained were not interpretable by physically realistic models, perhaps due to the very similar reflectivity of the HPEOF in nrw and HPEOF in H_2O/D_2O mixture matched PEO chains combinations. Therefore, only the combinations that gave the highest reflectivities were used resulting in using equation 4.3.2.1.

As it proved difficult to fit the unusual features observed in the water self-partial structure factors, some experimental points (usually for high concentrations between 0.02<

Q / Å^{-1}< 0.04) were disregarded. A variety of functional forms have been used to interpret these data, models used were single uniform water layer, hyperbolic tangent water profile (tanh) and double uniform water layer were.

a) Single Uniform Water Layer

The number density distribution of water molecules in the layer is described as follow,

$$\begin{aligned} n_s(z) &= 0 && z \le -d_{s1}/2 \\ &= ns_1 && -d_{s1}/2 \le z \le d_{s1}/2 \\ &= n_{s0} && z \ge d_{s1}/2 \end{aligned}$$

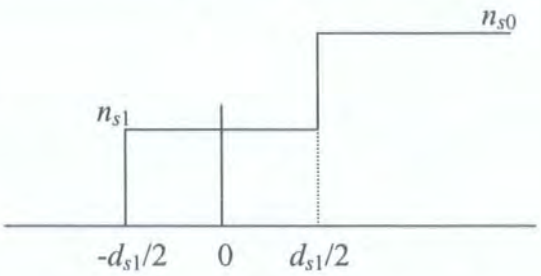

Equation 4.3.2.14.

The associated partial structure factor is given by,

$$Q^2 h_{ww}(Q) = n_{s0}^2 + 4n_{s1}(n_{s1} - n_{s0})\sin^2\left(\frac{Qd_{s1}}{2}\right) \qquad \text{Equation 4.3.2.15.}$$

where ns_0 is the number density of the bulk (0.0332 Å^{-3}), ns_1 is the number density of the water molecules in the layer and ds_1 the thickness of the layer.

b) Hyperbolic Tangent Subphase Profile (tanh)

The model consists of a smooth transition from the number density to the bulk subphase given by,

$$n_s(z) = ns_0\left(0.5 + 0.5\tanh\left(\frac{z}{d_{s1}}\right)\right) \qquad \text{Equation 4.3.2.16.}$$

where z is the distance and d_{s1} the thickness of the polymer layer in the subphase.

The only parameter that can be varied is d_{s1} as ns_0 is fixed to the number density of the bulk. A simulated tanh distribution is shown in figure 4.3.2.12.

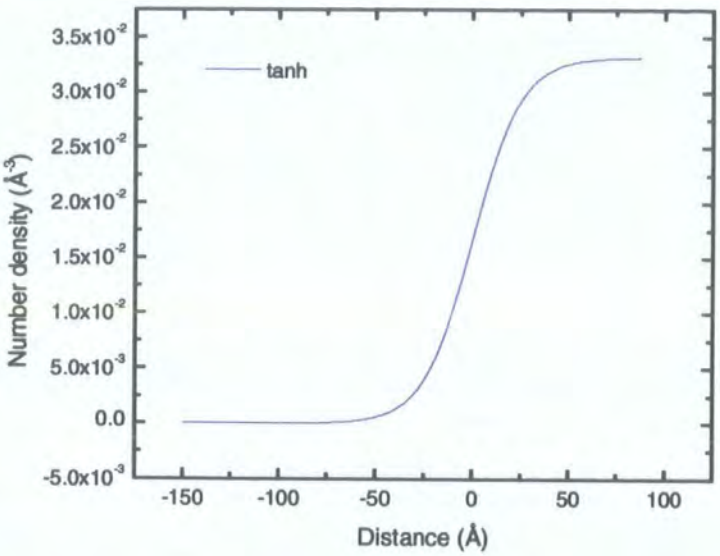

Figure 4.3.2.12: Simulated representation of number density profile for a tanh layer (thickness 25 Å).

The self-partial structure factor is given by,

$$Q^2 h_{ww}(Q) = ns_0^2 \left(\frac{d_{s1} \pi Q}{2} \right)^2 \operatorname{cosech}^2 \left(\frac{d_{s1} \pi Q}{2} \right) \qquad \text{Equation 4.3.2.17.}$$

where $$\operatorname{cosech} = \frac{1}{\sinh Q} \qquad \text{Equation 4.3.2.18.}$$

For solution concentrations below 10^{-5} g ml^{-1} both single uniform water layer and hyperbolic tangent water profiles were used to fit the data. It was apparent that a single uniform water layer fit was not appropriate as shown in figure 4.3.2.13.

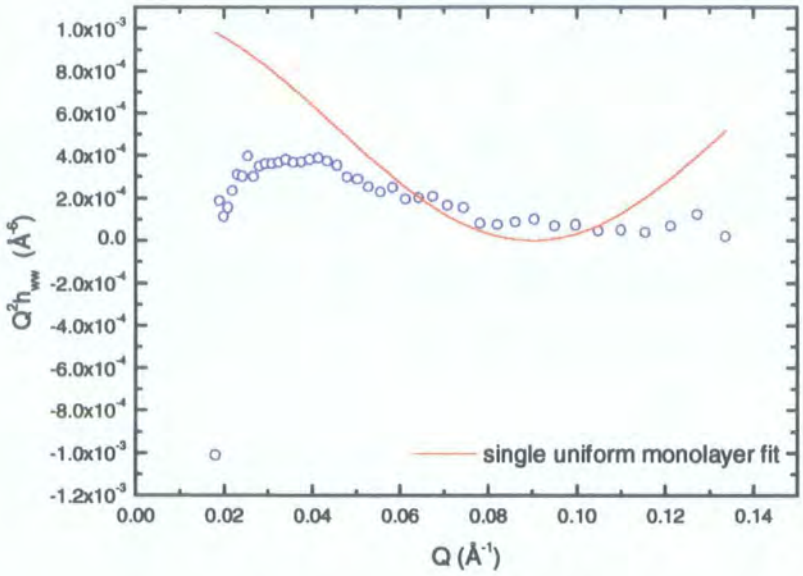

Figure 4.3.2.13: Single uniform water layer fit for water self-partial structure factor of 2k HPEOF/subphase at a solution concentration of 5×10^{-6} g ml^{-1}.

However, a hyperbolic tangent water profile was sufficient to describe the experimental data and the best non-linear least squares fits of these model partial structure factors to the data are shown in figure 4.3.2.14.

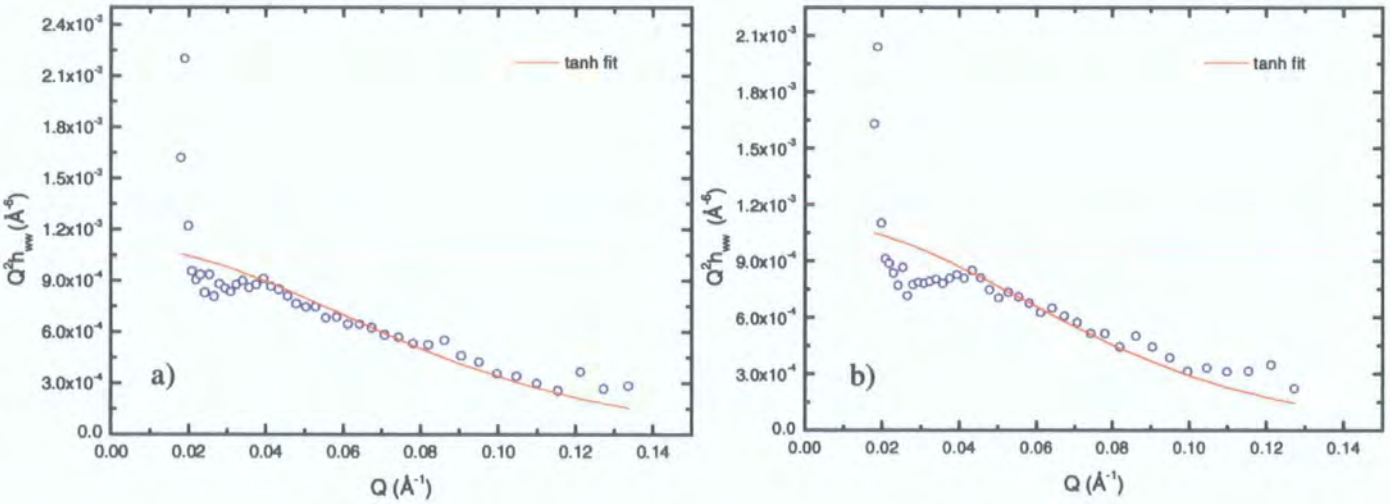

Figure 4.3.2.14: Water self-partial structure factors fitted using tanh profile for a solution concentration of a) 10^{-6} g ml^{-1} and b) 5×10^{-7} g ml^{-1}.

For concentrations between 10^{-3} and 10^{-5} g ml^{-1}, the fit was only acceptable for a double uniform water layer distribution and a schematic representation of the number density profile for a double uniform water layer is shown in figure 4.3.2.15.

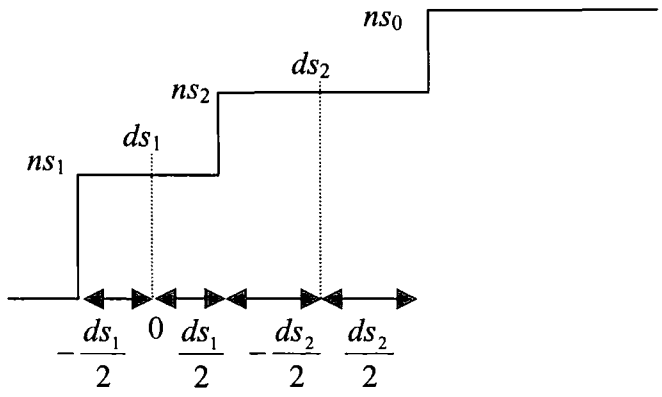

Figure 4.3.2.15: Schematic representation of the number density profile for a double uniform water layer.

Where ns_0 is the number density of the bulk (0.0332 $Å^{-3}$) ns_i is the number density of water molecules and ds_i their appropriate thickness. The number density of such a double layer is given by,

$$\begin{aligned} n_s(z) &= 0 && z \le -ds_1/2 \\ n_s(z) &= ns_1 && -ds_1/2 \le z \le ds_1/2 \\ n_s(z) &= ns_2 && ds_1/2 \le z \le d_{s1}/2 + d_{s2} \\ n_s(z) &= ns_0 && z \ge d_{s1}/2 + d_{s2} \end{aligned}$$

Equation 4.3.2.19.

which leads to a self-partial structure factor of,

$$\begin{aligned} Q^2 h_{ww}(Q) = {} & ns_1^2 + (ns_1 - ns_2)^2 + (ns_2 - ns_0)^2 + 2ns_1(ns_2 - ns_1)\cos(Qds_1) \\ & + 2(ns_1 - ns_2)(ns_2 - ns_0)\cos(Qds_2) + 2ns_1(ns_0 - ns_2)\cos(Q(ds_2 + ds_1)) \end{aligned}$$

Equation 4.3.2.20.

The fits were obtained by adjusting ns_i and ds_i and the best non-linear least squares fits of these model partial structure factors to the data are shown in figure 4.3.2.16.

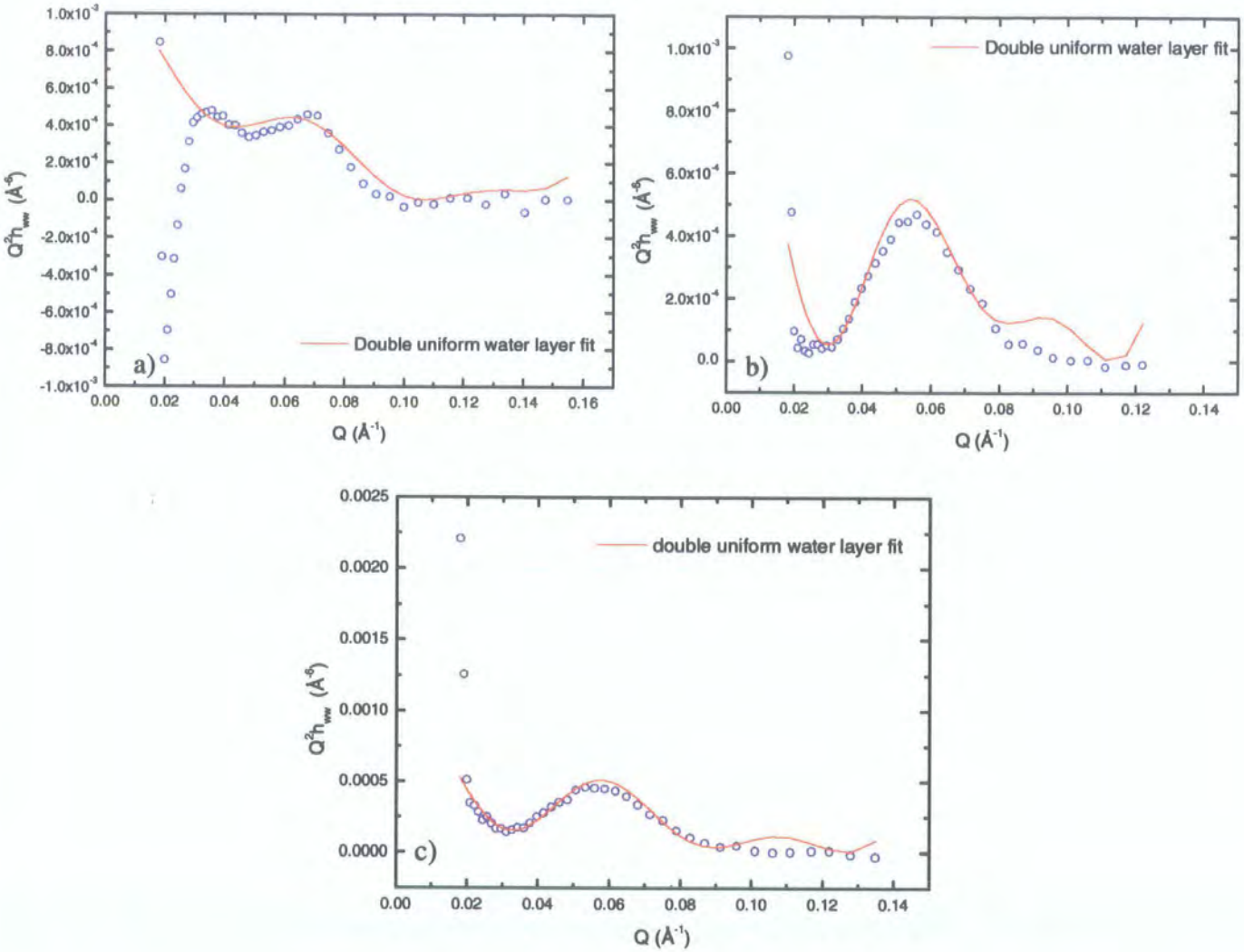

Figure 4.3.2.16: Double uniform water layer fit for a solution concentration of a) 10^{-3} g ml^{-1}, b) 10^{-4} g ml^{-1}and c) 5×10^{-5} g ml^{-1}.

The results obtained for the water self-partial structure factors are given in table 4.3.2.3 for all solution concentrations.

c (g ml^{-1})	$ds_i \pm 2$ (Å)	$ns_i \pm 2\times10^{-3}$ (Å^{-3})
1.00E-03	ds_1 28	ns_1 4.40E-03
	ds_2 70	ns_2 1.90E-02
5.00E-04	ds_1 32	ns_1 4.50E-03
	ds_2 81	ns_2 1.96E-02
1.00E-04	ds_1 32	ns_1 8.70E-03
	ds_2 83	ns_2 2.10E-02
5.00E-05	ds_1 32	ns_1 8.71E-03
	ds_2 83	ns_2 2.07E-02
3.00E-05	ds_1 32	ns_1 7.30E-03
	ds_2 81	ns_2 2.10E-02
2.00E-05	ds_1 34	ns_1 8.00E-03
	ds_2 81	ns_2 2.20E-02
1.00E-05	ds_1 34	ns_1 8.80E-03
	ds_2 77	ns_2 2.00E-02
5.00E-06	ds_1 25	ns_1 3.32E-02
1.00E-06	ds_1 24	ns_1 3.32E-02
5.00E-07	ds_1 13	ns_1 3.32E-02

Table 4.3.2.3: Number densities (ns_1 and ns_2) of water molecules with appropriate thickness (ds_i), obtained by double uniform layer fit and tangent hyperbolic layer profile for 2k HPEOF with bulk concentration.

The same models were also applied to the water self-partial structure factors obtained for the 5k HPEOF and 10k HPEOF, for the latter polymer the quality of the fits was not as good due to the rather more diffuse distribution of the polymer at the air-water interface for these higher molecular weight polymers. However, a tanh model was not appropriate for either 5k HPEOF or 10k HPEOF polymers at any concentration. Only a double uniform water layer fit gave an acceptable fit and the results of the number densities and layer thicknesses for 5k HPEOF and 10k HPEOF are given in appendix 6 and 7, table A.6 and A.7 respectively.

The comparison between PEOF layer thickness and water layer thickness is given in table 4.3.2.4.

c (g ml^{-1})	PEOF ± 2 (Å)		Water ± 2 (Å)	
1.00E-03	σ	54	ds_1	28
	τ	85	ds_2	70
5.00E-04	σ	47	ds_1	32
	τ	79	ds_2	81
1.00E-04	σ	45	ds_1	32
	τ	67	ds_2	83
5.00E-05	σ	43	ds_1	32
	τ	62	ds_2	83
3.00E-05	σ	43	ds_1	32
	τ	58	ds_2	81
2.00E-05	σ	42	ds_1	34
			ds_2	81
1.00E-05	σ	37	ds_1	34
			ds_2	77
5.00E-06	σ	35	ds_1	25
1.00E-06	σ	24	ds_1	24
5.00E-07	σ	16	ds_1	13

Table 4.3.2.4: Comparison between PEOF layer thickness (σ and τ) and water layer thickness (ds_i) obtained from kinematic approximation.

In table 4.3.2.4, information regarding the distribution of water molecules in the polymer layer is shown. At low bulk concentrations (fitted via tanh profile), the layer thicknesses are similar within experimental error, implying that the water molecules are homogeneously distributed within the PEOF layer. As the concentration increases and above 10^{-5} g ml^{-1} a two-layer organisation is observed with the upper layer thickness being constant over the remaining concentration range investigated. The layer thickness is slightly lower than PEOF layer thickness suggesting that some water molecules had been expelled from the PEOF upper layer maybe due to the displacement of water molecules from the interface by the fluorocarbon end group. The lower layer thickness of water is larger than

PEOF lower layer thickness and almost constant with bulk concentrations excepted for 10^{-3} g ml^{-1} where a decrease in layer thickness is observed. It is expected that the lower layer thickness of water should be larger than the PEOF lower layer thickness due to the diffuseness of the water layer. The drop in layer thickness observed at high concentrations could be explained as follow. The first explanation could be attributed to some water condensation on the tip of the PEO chains due to repulsion engendered by the fluorocarbon end group. The second reason could be attributed to the poorly fitted region at low Q where a drop in the magnitude of h_{ss} is observed (figure 4.3.2.16a). The fit was only applicable by ignoring some experimental data points as explained earlier.

For higher molecular weight polymers, a two-layer organisation is observed over the all concentration range investigated. The upper layer thickness of water, for both 5k and 10k PEOF polymers, is smaller than the lower layer thickness of water and remains constant with an increase in bulk concentration due to the adsorption of PEOF at the air-water interface excluding water molecules from the surface. The lower layer thickness remains also constant as the bulk concentration increases and larger values in the lower layer thickness are observed for 5k PEOF when compared to the PEOF lower layer thickness due to the more diffuse nature of water layer. Both lower layer thickness of water and PEOF lower layer thickness are almost identical for 10k PEOF and remain constant over the entire concentration range investigated suggesting that the distribution of water molecules within the PEOF layer is homogeneous.

An increase of the water number density in uniform steps from the interface is observed for all three molecular weight polymers as shown in figure 4.3.2.17.

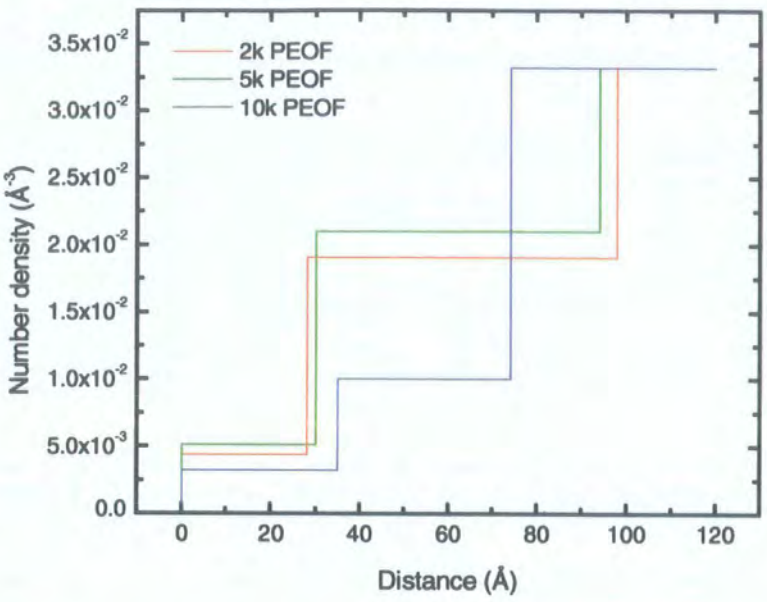

Figure 4.3.2.17: Number density distribution of water molecules at the air-water interface for aqueous solutions of 2k, 5k and 10k HPEOF at a bulk concentration of 10^{-3} g ml^{-1}.

The dependence of the number density distribution of water molecules at the air-water interface with molecular weight is evident but the main difference is observed for the highest molecular weight polymer with the number density of the second layer being twice smaller than that observed for 2k and 5k PEOF.

From the results obtained from h_{ww} fittings, it seems apparent that the water penetrates substantially into the polymer distributions. The degree of immersion for the three molecular weight polymers can be estimated.

Cross Partial Structure Factor (h_{pw})

Cross partial structure factors obtained for 2k PEOF at selected concentrations are shown in figure 4.3.2.18.

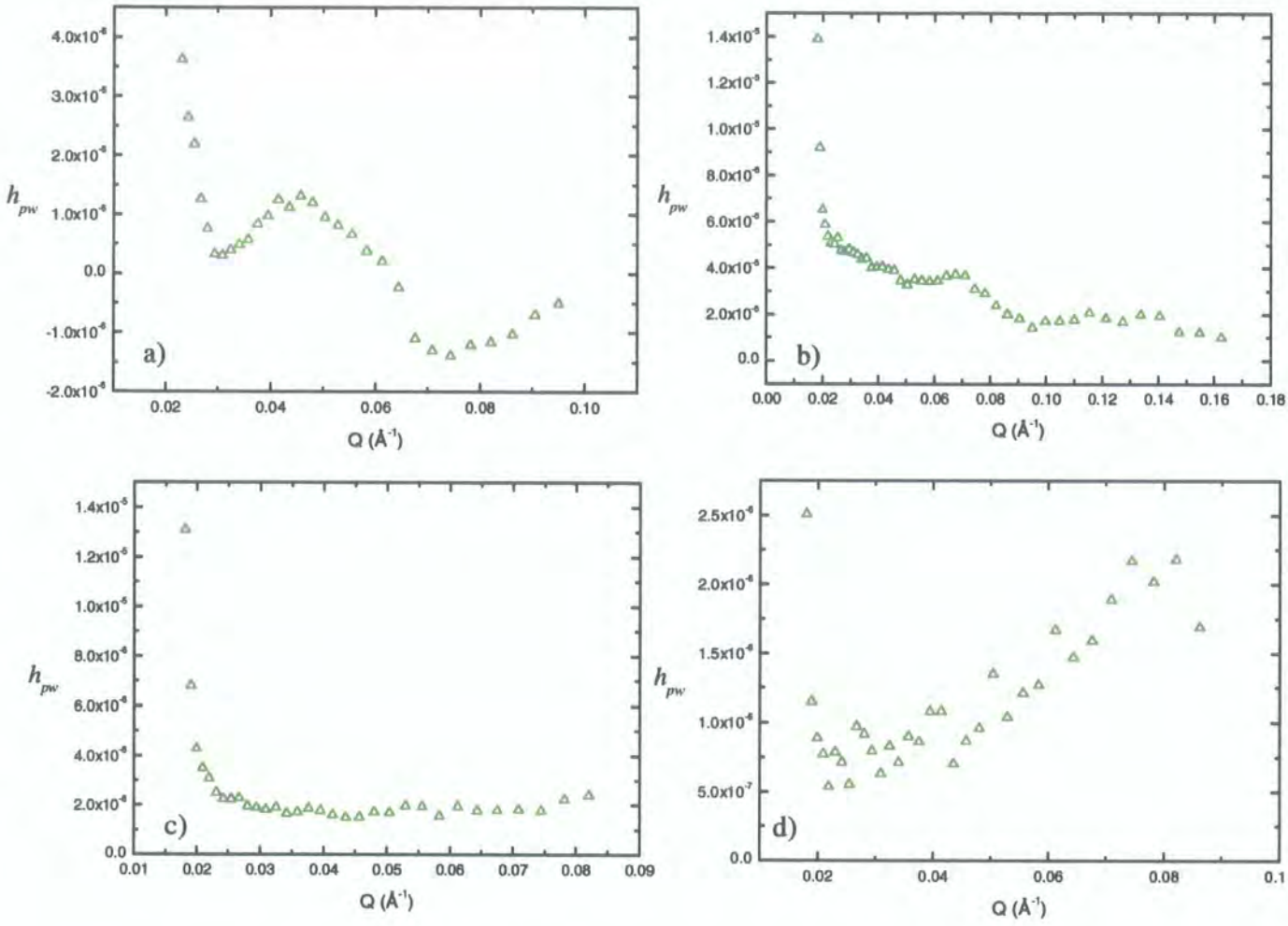

Figure 4.3.2.18: Cross partial structure factor (h_{pw}) for 2k PEOF at selected solution concentrations. a) 10^{-3} g ml^{-1}; b) 10^{-4} g ml^{-1}; c) 10^{-5} g ml^{-1}; d) 5×10^{-7} g ml^{-1}

It is evident from such results that the cross partial structure factors exhibit also some unusual features as the magnitude and shape change with solution concentration. Since the water self-partial distribution was unusual, those results were expected, as the cross partial structure factor is the product of both h_{pp} and h_{ww} given by,

$$h_{pw}(Q) = \pm\left(h_{pp}(Q)h_{ww}(Q)\right)^{1/2}\sin(Q\delta) \qquad \text{Equation 4.3.2.21.}$$

where δ is the separation of the centres of the polymer and solvent distributions.

Since δ is the separation between the centre of the chain distribution and the midpoint of the water distribution, these values indicate the extent of penetration of the PEO chains by the solvent

Equation 4.3.2.21 is used assuming that the Gaussian and double uniform water monolayer or tanh functions are respectively exactly even and exactly odd. However the distributions may not be exactly even/odd, and deviations from this assumption may affect the accuracy with which δ can be determined[34].

Simulated cross partial structure factors were generated by using experimental values of h_{pp} (Q) and $h_{ww}(Q)$ in equation 4.3.2.21. By varying the value of δ, the simulated values were compared with the experimental partial structure factors, and examples of these fits are shown in figure 4.3.2.19.

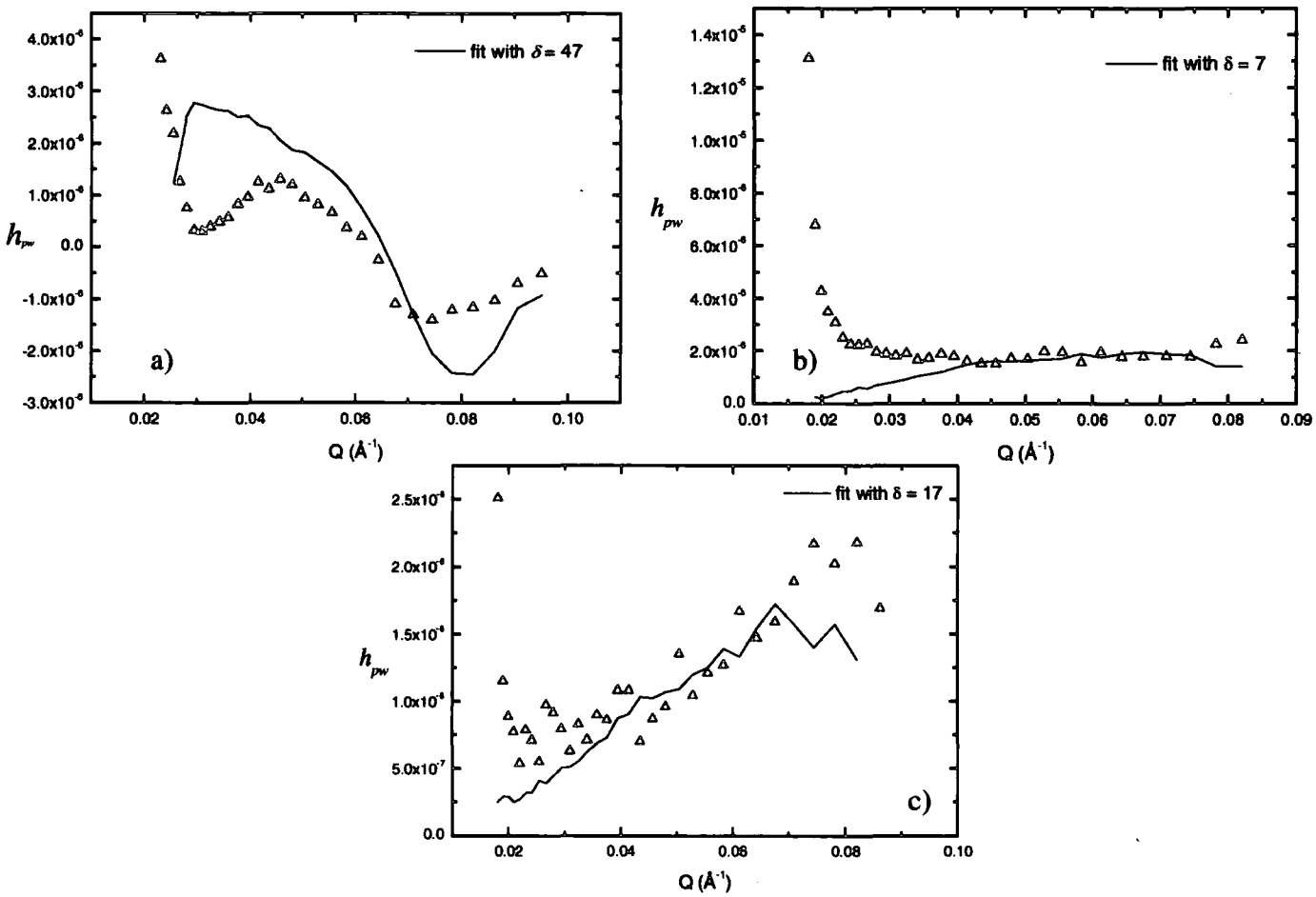

Figure 4.3.2.19: Fit of the cross partial structure factor of 2k PEOF/water by adjusting the separation parameter δ with solutions concentrations a) 10^{-3} g ml^{-1}; b) 10^{-5} g ml^{-1}; and c) 5×10^{-7} g ml^{-1}.

The fit returned did not reproduce particularly well the partial structure factor of 2kPEOF/water at high concentrations but the shape of the fit however is respected. The same difficulties were present for the two higher molecular weight polymers for concentrated solutions (usually above 10^{-4} g ml^{-1}). The main reason is probably due to the difficulty in assessing the description of the water self-partial distribution at high concentrations due to the more diffuse nature of the polymer layers.

However, δ were determined for the three molecular weight polymers and the results for 2k PEOF is given in table 4.3.2.5 whereas the results for 5k and 10k PEOF are given in appendix 8, table A.8a and A.8b respectively.

c (g ml^{-1})	$\delta \pm 0.5$ (Å)
1.E-03	47
5.E-04	30
1.E-04	15
5.E-05	20
4.E-05	10
3.E-05	12
2.E-05	8
1.E-05	7
5.E-06	10
1.E-06	15
5.E-07	17

Table 4.3.2.5: δ values obtained from kinematic approximation for 2k PEOF with bulk concentration.

A simple estimate of the extent of immersion of the PEO chains in the solvent may be made by using the layer thicknesses of both PEOF and water molecules as shown in table 4.3.2.4. Thus if there is no overlap of the two distributions for a given bulk concentration, i.e. no immersion of PEO chains in the water, the separation of the two distributions should be the sum of the two half-thicknesses. For 2k PEOF at 5×10^{-6} g ml^{-1}, this is 30 Å. Since δ is only 10 Å, the two distributions must overlap by 20 Å. Since the thickness of the PEO chains is 35 Å, about 60% of the chain must be immersed in the water. A schematic representation is shown in figure 4.3.2.20.

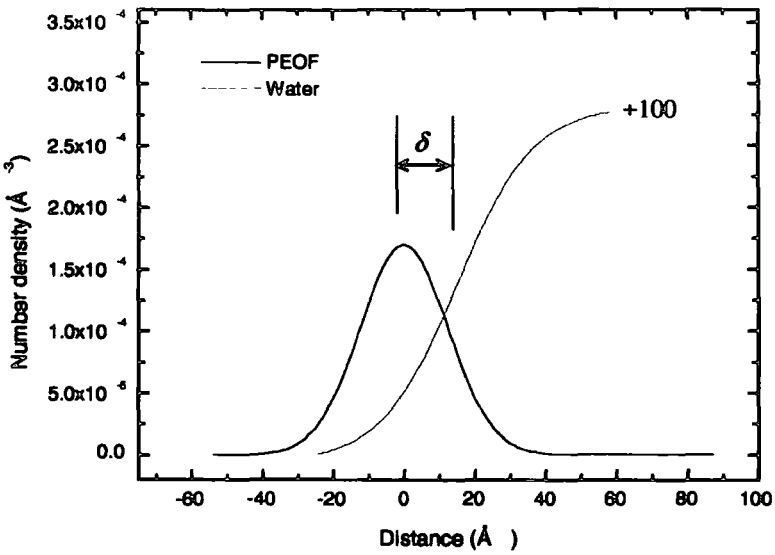

Figure 4.3.2.20: Schematic illustration of number density as a function of distance (z) for PEOF layer on a water subphase at a bulk concentration of 5×10^{-6} g ml^{-1} with δ= 10 Å.

The measured separation of the water and PEO distributions increases with increasing bulk concentration, indicating a greater penetration of PEO chains into the subphase. At 10^{-3} g ml^{-1}, the PEO chains are totally immersed in the subphase and a schematic representation is shown in figure 4.3.2.21.

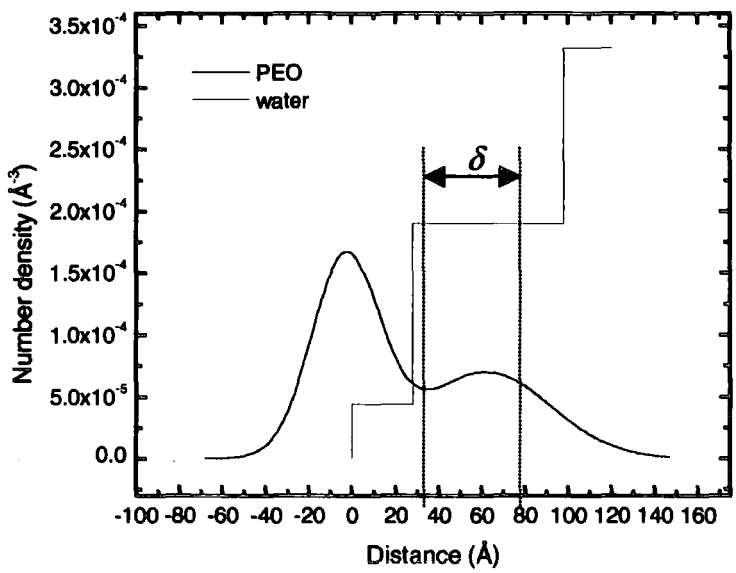

Figure 4.3.2.21: Schematic illustration of number density as a function of distance (z) for PEOF layer on a water subphase at a bulk concentration of 10^{-3} g ml^{-1} with δ= 47 Å.

For double distribution (double Gaussian distribution and double uniform water layer), the centre of each distribution was determined by using equation 4.3.2.22 (PEO) and 4.3.2.23 (water),

$$\overline{Z_n} = \frac{\sum z_i n_i}{\sum n_i}$$ Equation 4.3.2.22.

$$\overline{Z_{nw}} = \frac{\sum z_i n_i}{\sum n_i}$$ Equation 4.3.2.23.

The same results were observed for higher molecular weight polymers and it was therefore concluded that PEO chains are totally immersed into the subphase as the bulk concentration increases and the extent of immersion is solution concentration dependent.

4-3-3 Comparison of Fluorocarbon End-Capped PEO Behaviour to Brush Theory.

All the previous quantitative analyses used to describe the organisation of end fluorinated polymers at the air-water interface, agree on the fact that the upper layer thickness is dependent on both solution concentration and polymer molecular weights. Both the optical matrix analysis and kinematic approximation show that the upper layer thickness for the lowest molecular weight polymer increases with bulk concentration, an asymptotic thickness being approached at higher concentrations. A more gradual increase of the upper layer thickness was observed for higher molecular weight polymers, a constant layer thickness being achieved at higher concentrations. For all polymers, the upper layer thickness is circa twice that of the equivalent layer thickness for unmodified polyethylene oxide adsorbed at the air-water interface[7]. Since the end fluorinated PEO is adsorbed by one end to the interface between the air and the subphase, the possibility that PEOF forms a brush like layer seems distinct.

Brush theory introduced in Chapter Two, section 2-2-3, states that brush like layer configurations are found under thermodynamic equilibrium conditions due to configurational rearrangements minimising the free energy of surface layer of the system as the grafting density increases. Alexander[35] and de Gennes[36] theories predict that the brush height (h) scales linearly with the degree of polymerisation (N) and the cube root of the grafting density (σ), i.e. $h \propto N\sigma^{1/3}$. Milner and co-workers[37,38] used a self consistent field (SCF) method to determine the concentration profiles for polymer brushes and the relationship between h, N and σ is shown in equation 4.3.3.1 where υ is the excluded volume parameter.

$$h = \left(\frac{12}{\pi^2}\right)^{1/3} N(\sigma\upsilon)^{1/3} \qquad \text{Equation 4.3.3.1.}$$

SCF theory shows that the polymer volume fraction in the brush has a parabolic decay with increasing distance from the grafting surface in contrast to the step-function profiles predicted by Alexander and de Gennes. Therefore if the tethered chains are interacting and strongly stretched, then the behaviour of PEOF should theoretically follow the SCF predictions suggesting that an increase in both σ and N will lead to an increase of

h. Milner argument also highlights the role of the thermodynamic quality of the solvent (υ) in determining the brush height and equation 4.3.3.1 holds when the brushes are immersed in a good solvent, i.e. the brush height increases with improving solvent quality. In this study, PEOF is dissolved in water, which is known to be a good solvent for PEO, therefore the above relationship is valid for the system under investigation.

From the upper surface excess (Γ_{upper}) values determined from both optical matrix method and kinematic approximation, the normalised grafting density, σ^* can be calculated by using,

$$\sigma^* = \pi R_g \Gamma_{upper} N_A \qquad \text{Equation 4.3.3.2.}$$

where R_g is the radius of gyration obtained by using the experimental relation of Kawaguchi *et al*[9] (see table 4.3.1.5).

The transition to a brush-like layer for polymer grafted to an interface is predicted to take place at $\sigma^* = 2$ [39-42]. To obtain the scaling exponent, σ/R_g was plotted as a function of σ^* and least squares fits of the data are shown in figure 4.3.3.1.

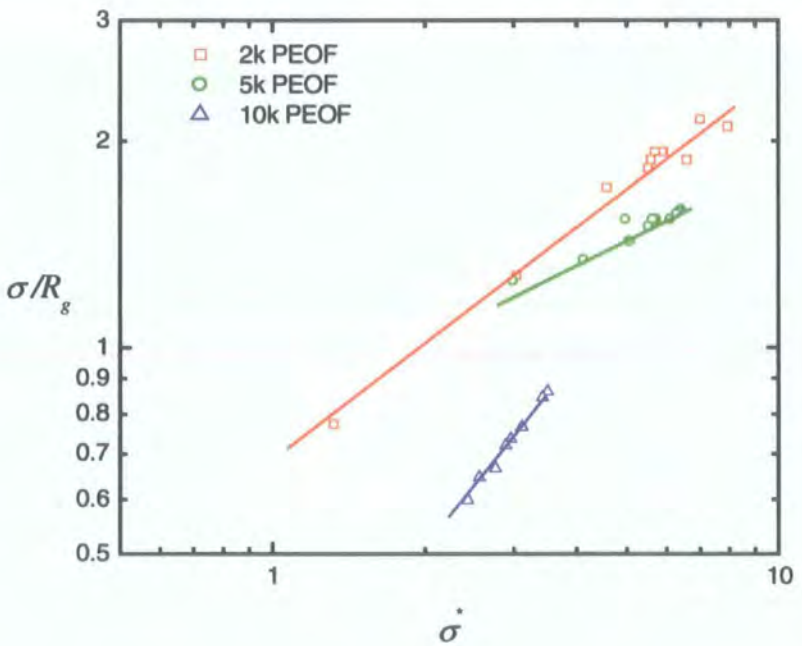

Figure 4.3.3.1: Double logarithmic plot of PEO upper layer thickness, σ, normalised by radius of gyration of equivalent molecular weight PEO as a function of normalised surface coverage, σ^* and least squares fits to the data (lines).

The following scaling exponent were found,

2k PEOF $\frac{\sigma}{R_g} \sim \sigma^{*0.60}$

5k PEOF $\frac{\sigma}{R_g} \sim \sigma^{*0.33}$

10k PEOF $\frac{\sigma}{R_g} \sim \sigma^{*0.90}$

Some uncertainties could arise regarding the choice of σ rather than the brush height h, which could lead to some uncertainties[37-38]. However, the values of σ from the partial structure factors are very similar to the layer thickness obtained from the optical matrix fits to the reflectivity data and justify the use of σ here as the effective layer thickness. The scaling exponent obtained for 5k PEOF agrees with theoretical predictions suggesting the formation of a brush-like layer at the air-water interface. However, the layer thickness of 5k PEOF polymer at maximum extension is $1.5R_g$, which does not constitute significant stretching of the polymer to be classified as a brush-like layer and therefore, the scaling exponent value seems fortuitous. The scaling exponent obtained for 10k PEOF is three times bigger than theoretical predictions but as the values of σ/R_g are always less than 1 for 10k PEOF, it could be debated that there is no evidence of a brush-like layer formation. The layer thickness of 10k PEOF at maximum stretching is also $1.5R_g$, leading to the same conclusions made for 5k PEOF. However it is clear that the adsorption characteristic of fluorinated end-capped PEO is enhanced by the low surface energy fluorocarbon group as the layer thickness is circa twice that of equivalent layer thickness for unmodified PEO. A more extended but still not stretched arrangement is adopted for 5k and 10k PEOF due to the adsorption of fluorocarbon groups at the air-water interface. For 2k PEOF the scaling exponent returned from least square fit to the data (figure 4.3.3.1) is ~2 times bigger than theoretical predictions suggesting that a very strong stretching is occurring. The layer thickness increases with solution concentrations up to circa 5×10^{-5} g ml^{-1} where constant values in the upper layer thickness are observed ($\sigma > 2R_g$). At low concentrations, the layer thickness is indicative of a 'pancake' like-layer configuration where both ethylene oxide segments and the fluorocarbon end of the polymer molecule are adsorbed at the air-water interface. As the solution concentration increases the ethylene oxide are displaced from the surface with the polymer being strongly

anchored at the air-water interface by the fluorocarbon group and the molecular weight of the polymer is sufficiently low that at higher concentrations, all ethylene oxide units can eventually be displaced from the interface by the fluorocarbon end of the polymer molecule resulting in the formation of a brush-like layer at the air-water interface. At circa 3×10^{-5} g ml^{-1}, no further PEO can be adsorbed and since the concentration exceeds its critical micelle concentration, micelles are formed in the bulk.

There have been numerous studies where tethered polymers immersed in good solvent have been used to test scaling predictions and they have had mixed success. Kent and co-workers[40,43] have studied similar dependencies using higher molecular weight polystyrene immersed in ethyl benzoate at much higher σ^* but rather weaker dependencies on normalised grafting density were observed ($\sigma/R_g \propto \sigma^{*\,0.22}$). Polymer brushes formed by spread films of end-capped PEO at the air-water interface have been investigated by Barentin *et al.*[44]. They used the scaling theory to interpret quantitatively their results but were unable to find agreement between the theory and the experiment. Agreement with scaling predictions was achieved by Taunton and co-workers[45], Field *et al.*[46], and more recently Richards *et al*[47]. Richards and co-workers studied the surface organisation of spread film of an amphiphilic graft copolymer at the air-water interface and good agreements between the brush height and normalised grafting density were obtained by single chain mean field theory ($\sigma/R_g \propto \sigma^{*\,0.35}$).

It is therefore evident that scaling predictions used for tethered polymers in good solvent have had mixed success. This work indicates that both molecular weight and bulk concentrations influence brush behaviour and that scaling predictions were not observed for 2k and 10k PEOF with values being much bigger than theoretical predictions. It was therefore concluded that the interfacial arrangement of fluorocarbon end-capped PEO was not well described by the brush-like layer theory. However, it could be debated that a brush configuration is possible for 2k PEOF as significant stretching is observed above 10^{-6} g ml^{-1}. Whereas, there is no evidence for the formation of a stretched brush like layer for 5k and 10k PEOF at the air-water interface.

4-4 Conclusions

Neutron reflectometry has been applied to determine the surface organisation of adsorbed solutions of end fluorinated PEO (PEOF) at the air-water interface. Two different methods have been used to analyse the data including the optical matrix analysis and the kinematic approximation.

Both methods predicted that the surface organisation of PEOF was dependent on both molecular weight and solution concentration and that a hydrophobic group placed at one end of the molecule considerably enhances the adsorption of aqueous solutions of polyethylene oxide at the air-water interface. For a molecular weight of circa 2 000 g mol^{-1} a transition from one monolayer to two monolayers is observed with an increase in solution concentration. The thickness and concentration of the first layer observed for concentrations below ~3×10^{-5} g ml^{-1}, increases with an increase in solution concentration and a considerable stretching of the molecules is implicated since the final thickness is more than twice the radius of gyration of the polymer. Above a bulk concentration of ~3×10^{-5} g ml^{-1}, a second layer is formed below the first layer and the thickness of this layer increases with solution concentration and is twice the thickness of the upper layer. The total surface excess of 2k PEOF increases continuously with increasing bulk concentration. The surface excess associated with the upper layer approaches an asymptotic value at a concentration of ~3×10^{-5} g ml^{-1} that mirrors well the dependence of surface tension on concentration.

For higher molecular weight polymers, there is still considerably more polymer adsorbed than for unmodified polyethylene oxide. A two-layer organisation is also observed over all the concentration range except for concentrations below 10^{-6} g ml^{-1} for 5k PEOF. The thicknesses of both 5k and 10k PEOF are much lower than for the lower molecular weight PEO suggesting that a competition between ethylene oxide segments and fluorocarbon end group takes place at the air-water interface resulting in a "flatter" structure. There is also little variation in the dimension of these layers over the bulk concentration range explored. For 10k PEOF, the layer thicknesses are of the same magnitude as the radius of gyration. For this polymer the surface excess (both total and that attributable to the upper layer alone) is constant although the surface tension decreases over much of the concentration range. This reinforced the idea of competition at the air-water interface between ethylene oxide

segments and fluorocarbon end groups as at higher bulk concentrations, the adsorbed ethylene oxide segments are displaced from the interface with the air by the lower surface energy fluorocarbon groups resulting in lowering the surface tension without more polymer materials being added. The surface excess layers are much more diffuse for these higher molecular weight polymers and some mixing of polymer molecules in the upper and lower layers is evident. The extent of PEO chain penetration into the subphase increases with increasing bulk concentration with PEO chains being totally immersed at high bulk concentrations with the fluorocarbon group being anchored at the air-water interface. This was observed for all three molecular weight polymers.

Both dynamic light scattering and small angle neutron scattering experiments have proved evidence of micelle formation for 2k PEOF, a well defined structure being undeniable but difficult to assess due to the weak scattering for 2k PEOF. For higher molecular weight polymers, a less well-defined arrangement is observed probably due to overlapping between the two layers.

From the dependence of the layer thickness on normalised grafting density, the scaling exponent predicted for a brush like layer conformation was only observed for 5k PEOF. However as the layer thickness of the upper layer is only $1.5R_g$, a stretched brush like layer organisation is not consistent. For the polymer with molecular weight of circa 2 000 g mol^{-1}, the scaling exponent is 0.60 indicative of a highly stretched conformation, which supports adsorption at the air-water interface of this polymer due to fluorocarbon end groups. A bigger scaling exponent was obtained for 10k PEOF but a brush configuration was not consistent with the layer thickness observed at maximum extension (only $1.5R_g$).

4-5 References

1) Lovell, E.L.; Hibbert, H.J. *J. Am. Chem. Soc.*, **1940**, 62, 2144.
2) Couper, A.; Eley, D.D. *J. Polym. Sci.*, **1948**, 3, 345.
3) Glass, J.E. *J. Phys. Chem.*, **1968**, 72, 4459.
4) Cao, B.H.; Kim, M.W. *Faraday Discuss.*, **1994**, 98, 245.
5) Daoust, H.; St-Cyt, D. *Macromolecules*, **1984**, 17, 596.
6) Rennie, A.R.; Crawford, R.J.; Lee, E.M.; Thomas, R.K.; Crowley, T.L.; Roberts, S.; Qureshi, M.S.; Richards, R.W. *Macromolecules*, **1989**, 22, 3466.
7) Lu, J.R.; Penfold, J.; Richards, R.W.; Su, T.J.; Thomas, R.K. *Polymer*, **1996**, 37, 109.
8) Sears, V.F. *Neutron Optics.*, **1989**, Oxford University Press, Oxford.
9) Kawaguchi, S.; Ito, K.; Imai, G.; Suzuki, J.; Miyahara, A.; Kitano, T. *Polymer*, **1997**, 38, 2885.
10) An, S.W.; Lu, J.R.; Thomas, R.K.; Penfold J. *Langmuir*, **1996**, 12, 2446.
11) Downer, A.; Eastoe, J.; Pitt, A.R.; Simister, E.A.; Penfold, J. *Langmuir*, **1999**, 15, 7591.
12) Hamley, I.W.; Pedersen, J.S.; Booth, C.; Nace, V.M. *Langmuir*, **2001**, 17, 6386.
13) King, S.M. *Modern Techniques of Polymer Characterisation*, **1999**, ed. R.A. Pethrick and G.V. Dawkins, Wiley, London.
14) Guinier, A.C.R. *Hebd. Séance Acad. Sci. Paris*, **1937**, 204, 1115.
15) Xu, B.; Li, L.; Yekta, A.; Masouni, Z.; Kanagalingam, S.; Winnik, M.A.; Zhang, K.; Macdonald, P.M. *Langmuir*, **1997**, 13, 2447.
16) Zhang, H.; Hogen-Esch, T.E. *Langmuir*, **1998**, 14, 4972.
17) Calvet, D.; Collet, A.; Viguier, M.; Berret, J.F.; Serero, Y. *Macromolecules*, **2003**, 36, 449.
18) Pang, P.; Englezos, P. *Colloids and Surfaces A: Physicochem. Eng. Aspects*, **2002**, 204, 23.
19) Lee, E.M.; Milnes, J.E. *J. Appl. Cryst.* **1995**, 28, 518.

20) Crowley, T.L.; Lee, E.M.; Simister, E.A.; Thomas, R.K.; Penfold, J.; Rennie, A.R. *Colloids and Surfaces*, **1990**, 52, 85.

21) Bocker, J.; Schlenkrisch, M.; Bopp, P.; Brickmann, J. *J. Phys. Chem.*, **1992**, 96, 9915.

22) Tarek, M.; Tobias, D.J.; Klein, M.L. *J. Phys. Chem.*, **1995**, 99, 1393.

23) Henderson, J.A.; Richards, R.W.; Penfold, J.; Thomas, R.K. *Acta Polymer*, **1993**, 44, 184

24) Richards, R.W.; Rochford, B.R.; Webster, J.R.P. *Faraday Discussions*, **1994**, 98, 263.

25) Miller, A.F. *Ph.D. Thesis*, University of Durham, **2000**.

26) Henderson, J.A.; Richards, R.W.; Penfold, J.; Thomas, R.K. *Macromolecules*, **1993**, 26, 65.

27) Peace, S.K.; Richards, R.W.; Kiff, F.T.; Webster, J.R.P.; Williams, N. *Polymer*, **1999**, 40, 207.

28) Hines, J.D.; Garrett, P.R.; Rennie, A.R.; Thomas, R.K.; Penfold, J. *J. Phys. Chem. B*, **1997**, 101, 7121.

29) Hines, J.D.; Garrett, P.R.; Rennie, A.R.; Thomas, R.K.; Penfold, J. *J. Phys. Chem. B*, **1998**,102, 8834.

30) Thomas, R.K.; Penfold, J. *Phys. Chem. Chem. Phys.*, **2002**, 4, 2648.

31) Lu, J.R.; Lee, E.M.; Thomas, R.K. *Acta Crystallogr.*, **1996**, A52, 11.

32) Lu, J.R.; Thomas, R.K. *Nucl. Instrum. Methods*, **1995**, A354, 147.

33) Simister, E.A.; Lee, E.M.; Thomas, R.K.; Penfold, J. *J. Phys. Chem.*, **1993**, 97, 6024.

34) Simister, E.A.; Lee, E.M.; Thomas, R.K.; Penfold, J. *Macromol. Rep.* **1992**, A29 (Suppl. 2), 155.

35) Alexander, S.J. *J. Phys. (Paris)*, **1977**, 38, 977.

36) de Gennes, P.G. *Macromolecules*, **1980**, 13, 1069.

37) Milner, S.T.; Witten, T.A.; Cates, M.E. *Macromolecules*, **1988**, 21, 2610.

38) Milner, S.T.; Witten, T.A.; Cates, M.E. *Macromolecules*, **1989**, 22, 853.

39) Szleifer, I. *Europhysics Letters*, **1998**, 44, 721.

40) Kent, M.S.; Lee, L.T.; Factor, B.J.; Rondelez, F.; Smith, G.S. *Journal of Chemical Physics*, **1995**, 103, 2320.

41) Currie, E.P.K.; Leermakers, F.A.M.; Cohen Stuart, M.A.; Fleer, G.J. *Macromolecules*, **1999**, 32, 721.

42) Ligoure, C. *Journal de Physique II (Paris)*, **1993**, 3, 1607.

43) Kent, M.S. *Macromolecular Rapid Communications*, **2000**, 21, 243.

44) Barentin, C.; Muller, P.; Joanny, J.F. *Macromolecules*, **1998**, 31, 2198.

45) Taunton, H.J.; Toprakcioglu, C.; Fetters, L.J.; Klein, J. *Macromolecules*, **1991**, 23, 571.

46) Field, J.B.; Toprakcioglu, C.; Ball, R.C.; Stanley, H.P.; Dai, L.; Barford, W.; Penfold, J.; Smith, G.; Hamilton, W. *Macromolecules*, **1992**, 25, 434.

47) Miller, A.F.; Richards, R.W.; Webster, J.R.P. *Macromolecules*, **2001**, 34, 8361.

Chapter Five

Surface Quasi-Elastic Light Scattering

5-1 Introduction

The dynamic surface behaviour of the surface excess of adsorbed aqueous solutions of fluorocarbon end-capped polyethylene oxide (PEOF) at the air-water interface has been investigated using surface quasi-elastic light scattering (SQELS). This chapter reports the results obtained for the three different molecular weight PEOF from SQELS experiments.

Firstly, variation of the frequency, ω_0, and damping, Γ, of the capillary waves as studied as a function of solution concentration using a fixed scattering vector, $q = 480 \pm 5$ cm^{-1}. The most straightforward analysis to extract the frequency and damping of such systems was by non-linear squares fit of a damped cosine function[1] as discussed in Chapter Two, section 2-4-1. Subsequently, values for the viscoelastic parameters, the surface tension (γ_0), the dilational modulus (ε_0) and the dilational viscosity (ε') were evaluated using the direct spectral fitting method[2]. The results are presented as follow: 2k PEOF results are initially discussed followed by comparison with higher molecular weight PEOFs in the main discussion. The dynamic behaviour of the surface capillary waves is correlated with the surface organisation of PEOF obtained from neutron reflectometry experiments and discussed.

Secondly, both the capillary wave propagation (frequency and damping) and viscoelastic parameters were analysed as a function of q and the results from the damped cosine and spectral fits are presented for all three molecular weight polymers and interpreted.

The effect of solution concentration, capillary wave frequency and polymer molecular weight on the dynamic properties of adsorbed solutions of end fluorinated PEO are summarised and discussed.

5-2 Experimental Details

5-2-1 Sample Preparation

Solutions were prepared in ultra pure water (80 M ohm cm^{-1} resistivity) and left overnight to ensure complete dissolution of the polymer. Desired solution concentrations were obtained by dilution. The polymer solution was poured (25 ml) into a circular, thermostatically controlled (298 K) stainless steel trough equipped with a lid having a window on the top for the incident and scattered laser beams. Prior to each experiment the apparatus was calibrated by determining the wavenumber, q, of each light spot incident on the surface of pure UHQ water (instrumental details are discussed in Chapter Two, section 2-4-3). Ten correlation functions (60 s each) were collected for each spot, each function was fitted using the damped cosine fit and the average of the fitted frequency and damping values calculated. A typical correlation function with damped cosine fit is shown in figure 5.2.1.

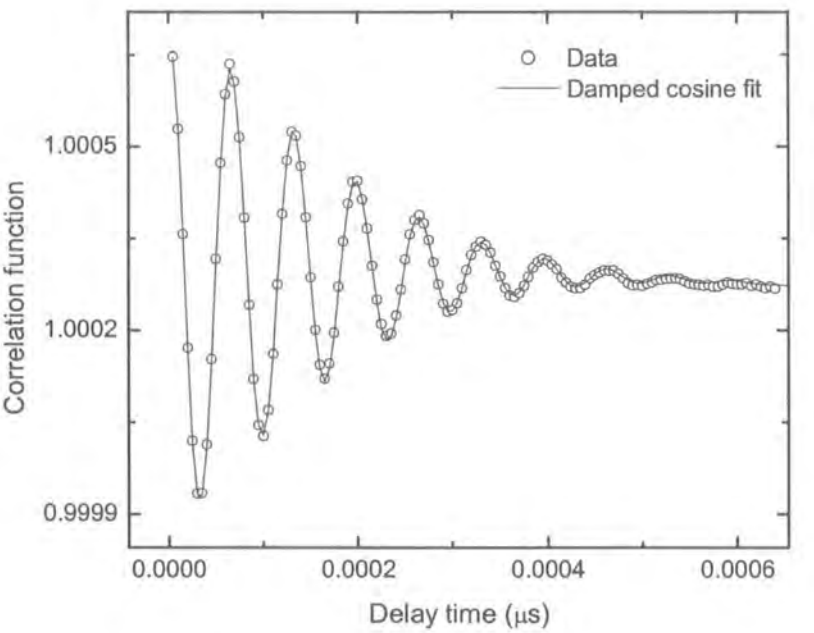

Figure 5.2.1: Experimental correlation function (circles) and a fit to the data (solid line) for pure UHQ water (q = 480 cm^{-1}).

By using the program CANICE the dispersion equation is solved to provide theoretical values of wave frequency and damping as a function of q, the experimental wavenumbers for each diffracted beam were determined by plotting the calculated wave frequency against q, then extracting the q value that corresponded to each experimentally obtained frequency value.

The first experiment undertaken examined the time dependence on both frequency and damping of capillary waves at fixed q values.

5-2-2 Time Dependence

To check if equilibrium time was necessary for both frequency and damping values of capillary waves, a time dependence experiment was performed for a solution concentration of 10^{-3} g ml^{-1} for 2k PEOF. Correlation functions were repeatedly recorded at regular time intervals over a period of 2 hours, figure 5.2.2.

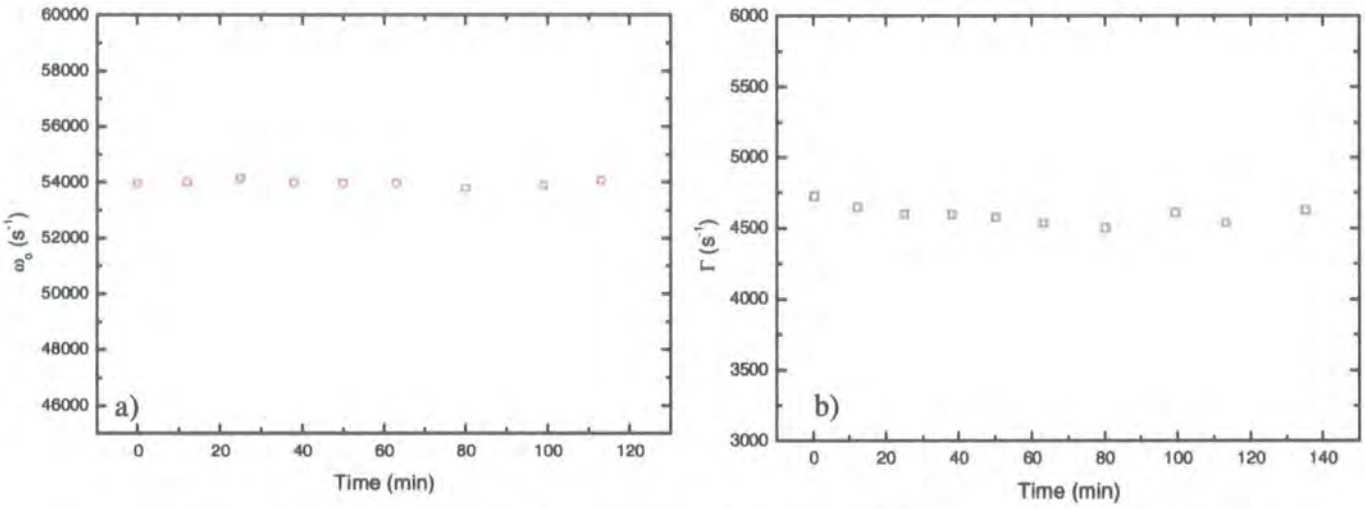

Figure 5.2.2: Capillary wave frequency (a) and damping (b) as a function of time for 2k PEOF at bulk concentration of 10^{-3} g ml^{-1} where q = 480 cm^{-1} at 298 K.

It is evident from figure 5.2.2 that both frequency and damping of capillary waves are time independent as no fluctuation in amplitude is observed suggesting that 2k PEOF forms homogeneous monolayers at the air-water interface. The same observations were also observed for 5k and 10k PEOF. Subsequently, polymer solutions were poured into the trough and left for 15 min to reach the desired temperature (298 K) only with no further need for equilibration.

5-3 Dependence on Solution Concentration

5-3-1 Damped Cosine Fit Analysis

The dependence of capillary wave frequency and damping on solution concentrations of 2k PEOF was investigated and ten correlation functions were collected at a fixed wavenumber (q = 480 cm^{-1}) for a range of concentrations between 10^{-7} g ml^{-1} and 10^{-3} g ml^{-1} and up to 10^{-2} g ml^{-1} for 5k and 10k PEOF. The experiments were repeated several times and reproducible results were obtained provided the height of the liquid surface was constant. This was achieved by using a teflon dipstick between each measurement to ensure that no variation in height was observed. The data was fitted using the damped cosine function to extract capillary wave frequency and damping. Model correlation functions were generated from initial estimates, and the model non-linearly least squares fitted to the data. This was a relatively fast process providing reasonable starting parameters were used. A typical example is shown in figure 5.2.1.
The parameters from the fits were averaged to give final values for frequency and damping.

5-3-2 Results: Capillary Wave Frequency and Damping

Values for frequency and damping of the capillary wave were determined for each solution concentration using the damped cosine fit. Figures 5.3.1. and 5.3.2 show the variation in frequency and damping with bulk concentration for 2k PEOF, where each point is the average from ten correlation functions.

The frequency of the capillary waves decreases gradually with an increase in bulk concentration, starting with the value of a pure water surface (90 510 s^{-1}) at very low concentrations and decreasing down to nearly half that value (55 000 s^{-1}) at circa 5×10^{-5} g ml^{-1} to reach a constant value of ~50 000 s^{-1} at 5×10^{-4} g ml^{-1}. The change in the magnitude of the frequency is extremely large but significant as they are highly reproducible. At low concentration the damping is already relatively high starting at circa 5 500 s^{-1} compared to 3 810 s^{-1} for a clean water surface and rising rapidly to reach a maximum value of ~6 600 s^{-1} at 10^{-6} g ml^{-1}. As the bulk concentration increases further, the damping falls gradually to reach a constant value (~4 400 s^{-1}) at $c = 10^{-3}$ g ml^{-1}.

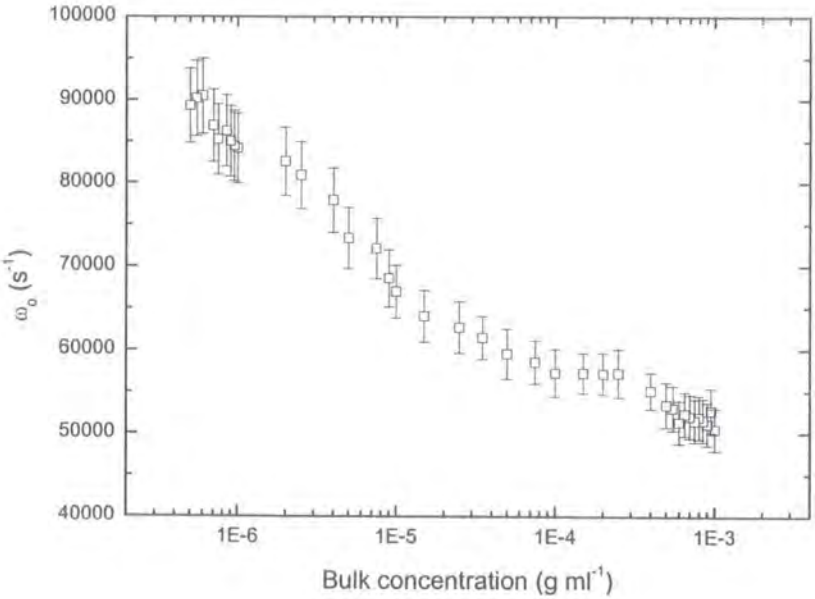

Figure 5.3.1: Frequency of capillary waves as a function of bulk concentration for 2k PEOF, $q = 480$ cm^{-1}.

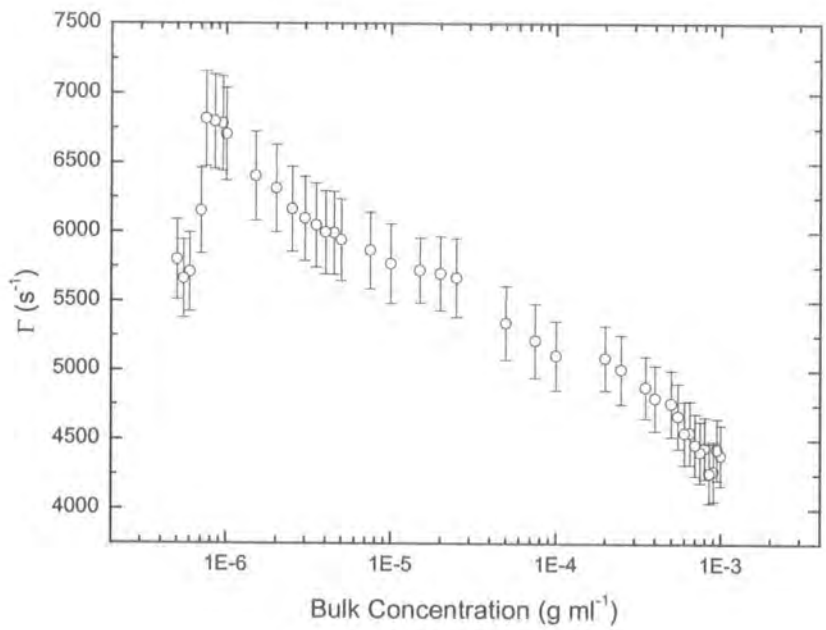

Figure 5.3.2: Damping of capillary waves as a function of bulk concentration for 2k PEOF, $q = 480$ cm^{-1}.

5-3-3 Spectral Fit Analysis

The data were analysed in accordance with the recent molecular theory for SQELS developed by Buzza and co-workers[3]. Basically, the data were treated using a spectral fitting procedure by allowing the three viscoelastic parameters, i.e. surface tension (γ_0), dilational modulus (ε_0) and dilational viscosity (ε') to float and by using the static surface tension as a first approximation. However, both γ_0 and ε_0 were restricted to values between 0 and 100 mN m^{-1} and the dilational viscosity was allowed to explore both negative and positive values ranging from -10^{-3} to 10^{-3} mN s m^{-1}. The bulk viscosity was set to the bulk viscosity of water and the transverse shear viscosity (γ') was assumed to be zero. Indeed, the solution viscosities were determined using a Ostwald tube viscometer and were found to be solution concentration independent and similar within experimental errors to that of pure water. Both viscosities (solution and pure water) were used during spectral fitting and identical results were returned, justifying the use of the bulk viscosity of pure water in this study.

The three viscoelastic parameters were initially estimated and a theoretical power spectrum of the scattered light generated, which gave a model correlation function when Fourier transformed. The generated correlation function was then non-linearly least squares fitted to the experimental data and the parameters varied until a minimum in the sum of the square of the difference was obtained. The fitting process was repeated several times until physically realistic values and good quality of the fit were returned. A typical example is shown in figure 5.3.3.

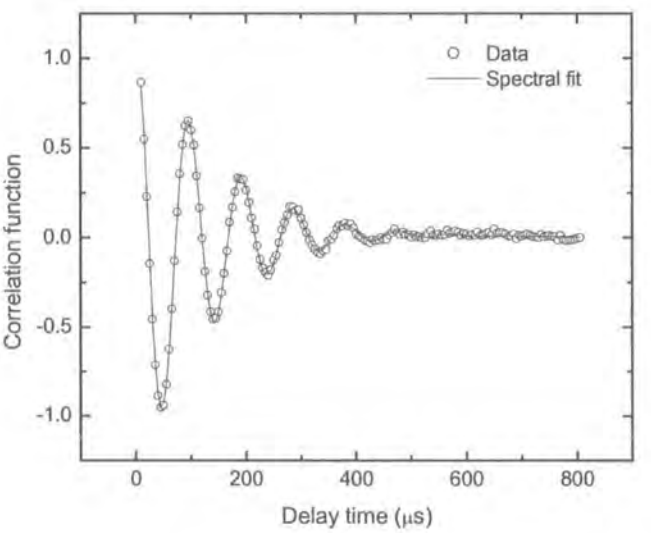

Figure 5.3.3: Experimental correlation function (circles) with fit overlaid (solid line). The data is recorded for 2k PEOF at 10^{-3} g ml^{-1}, $q = 480$ cm^{-1}.

The average values were determined from those obtained for each correlation function.

5-3-4 Results: Viscoelastic Parameters

The results obtained for the surface tension from SQELS (dynamic data) for 2k PEOF are given in figure 5.3.4 and the static surface tension values (solid line) obtained from digital tensiometer (Wilhelmy plate) are overlaid for comparison.

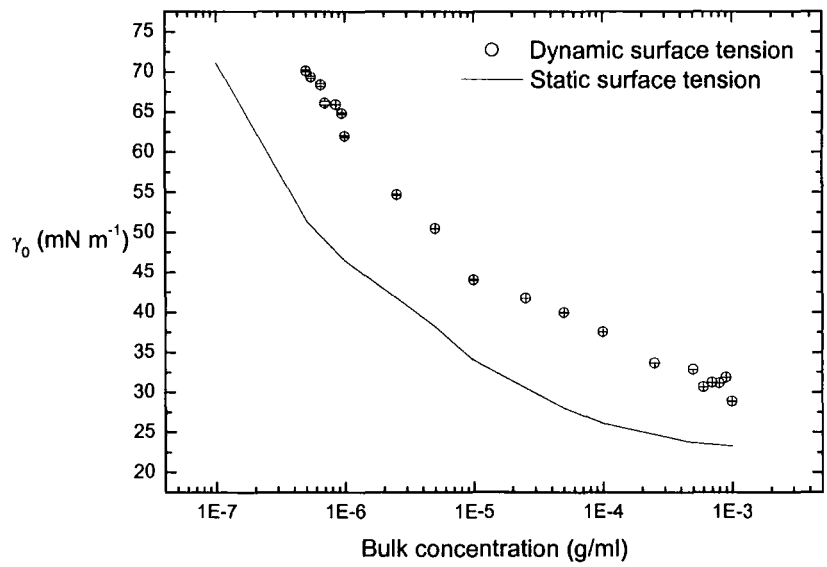

Figure 5.3.4: Bulk concentration dependence of the dynamic (symbol) and static (solid line) surface tension values obtained for 2k PEOF from SQELS and digital tensiometer respectively.

It is clear from the plot that the dynamic and static values exhibit qualitatively similar characteristics with increasing bulk concentration. However, quantitatively, the dynamic and static values disagree as the dynamic values are circa 10 mN m^{-1} higher than the corresponding static values. This behaviour suggests that PEOF surface excess layer undergoes transverse mode relaxation processes when perturbed by capillary oscillations.

To check whether or not longitudinal chain relaxation effects occur, the static dilational modulus was calculated from both the surface tension and the neutron

reflectometry (NR) data and compared with the corresponding dynamic dilational modulus as a function of bulk concentration (figure 5.3.5).

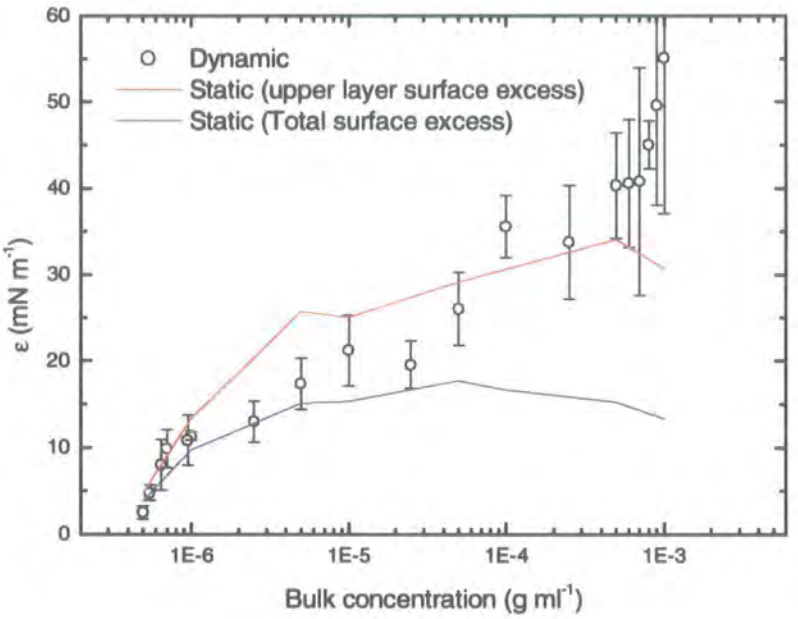

Figure 5.3.5: Bulk concentration dependence of the dynamic (symbol) and static (solid lines) dilational modulus values obtained for 2k PEOF from SQELS and neutron reflectometry respectively.

The static data, ε_{0ST}, corresponds to the Gibbs static elasticity and were calculated using the following relationship,

$$\varepsilon_{0ST} = \Gamma \frac{d\pi}{d\Gamma} \qquad \text{Equation 5.3.4.1.}$$

where $d\pi/d\Gamma$ is the slope of $\pi = f(\Gamma)$ with Γ being the surface excess determined by NR experiments and π being the surface pressure obtained by equation 5.3.4.2.

$$\pi = \gamma_0 - \gamma \qquad \text{Equation 5.3.4.2.}$$

where γ_0 and γ are the surface tension of pure water at 298 K and 2k PEOF solutions respectively.

In order to evaluate ε_{0ST} a least squares fitting routine was used to fit a second order polynomial function to the experimental surface pressure isotherm. The numerical derivative of this function was determined using both upper and total surface excess values obtained from neutron reflectometry results and substituted into equation 5.3.4.1.

Both static and dynamic dilational moduli depend on bulk concentration, a value of ~5 mN m^{-1} at low concentrations rising to ~45 mN m^{-1} at 10^{-3} g ml^{-1}, with no evidence of asymptotic values being reached. The error bars over the higher bulk concentration region are marginally larger in relation to the lower concentration data, however the sharp increase observed is not an artefact as the results were reproducible. Both static and dilational moduli exhibit similar qualitative and almost quantitative agreement. Indeed, almost exact agreement is seen at low bulk concentration but above 10^{-6} g ml^{-1}, divergence occurs. For higher bulk concentrations, although there is qualitative agreement between the two values of ε_0, absolute agreement is not obtained. By using both upper and total surface excess to calculate ε_{0ST}, it appears that ε_{0ST} (using the upper surface excess) reproduces the dilational modulus better at higher bulk concentrations suggesting that the polymer molecules present in the upper layer have the most influence on the dilational behaviour of the polymer film. It could be argued that the difference observed between dynamic and static dilational moduli above 10^{-6} g ml^{-1} reinforce the view that relaxation processes occur within the monolayer on perturbation by a capillary wave.

The dilational viscosity behaviour is presented in figure 5.3.6.

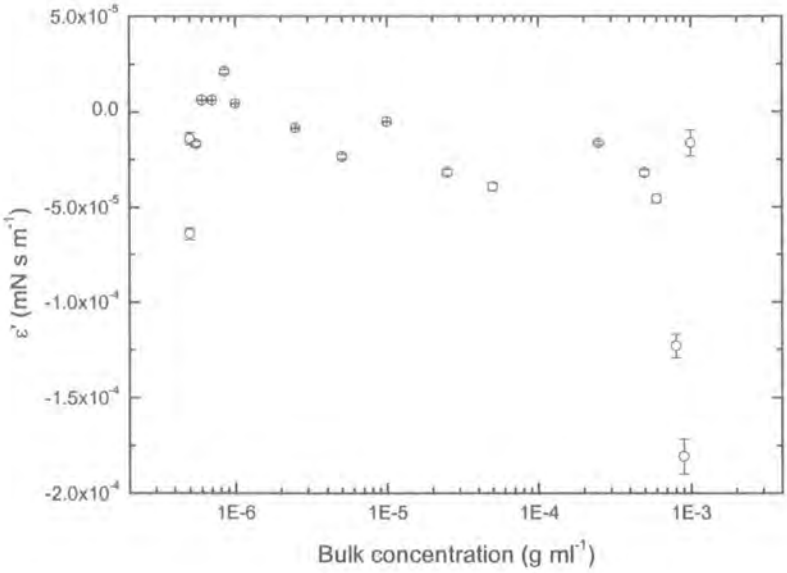

Figure 5.3.6: Variation in dilational viscosity for 2k PEOF as a function of bulk concentration.

The dilational viscosity data appears to be dependent on solution concentration. Negative dilational moduli are observed over almost the entire concentration range excepted around 10^{-6} g ml^{-1}, where a maximum is observed. This concurs with the maximum displayed in damping. Thereafter a slight decrease in dilational viscosity is observed whereas an increase in dilational modulus was evident. The sharp drop around 10^{-3} g ml^{-1} seems suspect and could be attributed to the large value of ε_0 in this particular region.

5-4 Discussion

5-4-1 Frequency and Damping for all PEOF Polymers

To ascertain the dependence of the capillary wave propagating characteristics on the molecular weight of fluorocarbon end-capped PEOF polymers, the frequency and the damping parameters were determined for 5k and 10k PEOF. The parameters (capillary wave frequency and damping) of all polymers are compared in figures 5.4.1a-b and plotted as a function of bulk concentration.

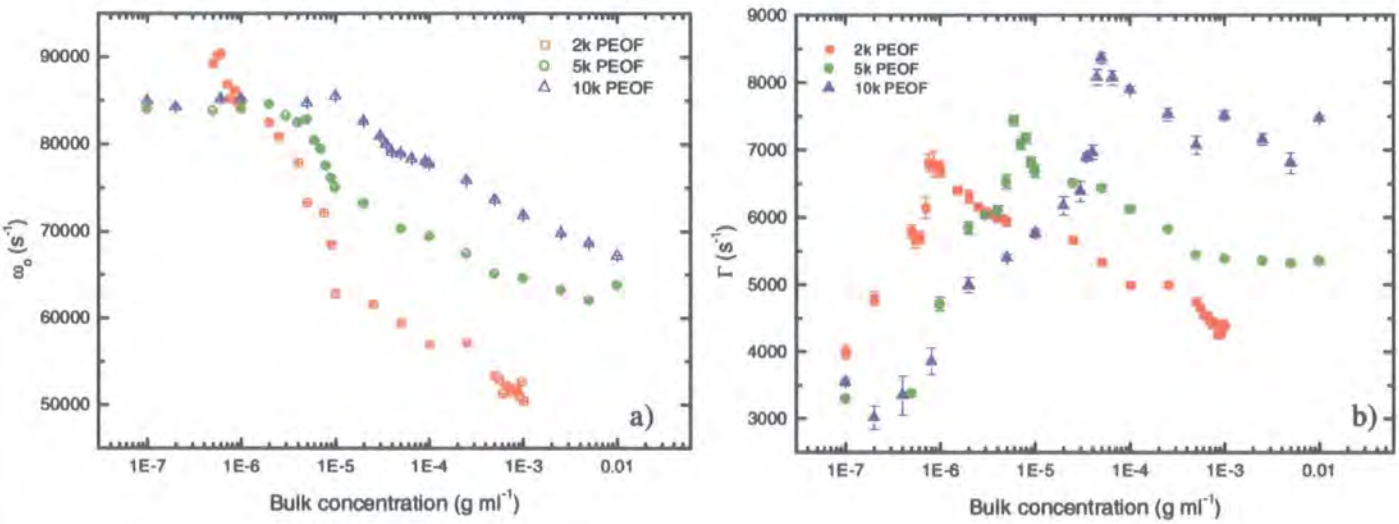

Figure 5.4.1: Comparison of the capillary wave frequency (a) and damping (b) for each PEOF polymer as a function of bulk concentration.

In general the frequency and damping of capillary waves exhibit similar dependencies on the bulk concentration for each fluorocarbon end capped PEO. However quantitatively, the frequency and damping of capillary waves vary significantly with bulk concentration. The frequency for the three polymers start approximately around 90 000 s^{-1} for 2k PEOF and 85 000 s^{-1} for higher molecular weight polymers and decrease with an increase in bulk concentration at different rate. Lowest values in frequency are reached by the lowest molecular weight polymer around 50 000 s^{-1} at 10^{-3} g ml^{-1} with a maximum in frequency (91 000 s^{-1}) observed at ~5×10^{-6} g ml^{-1} and a sharp break being observed at 10^{-5} g ml^{-1}. The same trend is observed for higher molecular weight polymers with a break in frequency observed at 10^{-5} and 5×10^{-5} g ml^{-1} for 5k and 10k PEOF

respectively. However, no maximum in frequency is observed for 5k and 10k PEOF. For the most concentrated solutions, ω_0 = 65 000 and 70 000 s^{-1} for 5k and 10k PEOF respectively. Constant values seem to be reached for 2k PEOF at high bulk concentrations but are not evident for 5k and 10k PEOF. However, the change in frequency mirrors that observed for static surface tension data as expected, since the frequency and surface tension are related, i.e. $\omega_0^2 \propto \gamma$.

The damping data (figure 5.4.1b) are qualitatively similar with a maximum in damping observed for all polymers with asymptotic values being reached at high bulk concentrations. For 2k PEOF, the maximum in damping (~7 000 s^{-1}) is observed at 10^{-6} g ml^{-1} and as the molecular weight increases, the maximum in damping is clearly shifted to 6×10^{-6} g ml^{-1} for 5k PEOF (Γ = 7 500 s^{-1}) and 5×10^{-5} g ml^{-1} for 10k PEOF (Γ = 8 500 s^{-1}). The maximum in damping is indicative of resonance between capillary and dilational modes[4].

The surface dynamics of various amphiphilic polymers containing PEO[5-10] have been reported in the literature but mainly as spread films. However, some SQELS experiments on adsorbed solutions of PEO have been reported[11-14]. Yu and co-workers[11,12] investigated spread and adsorbed film of PEO using a much higher molecular weight range to that used here for two bulk concentrations (10^{-4} and 10^{-3} % $^{w}/_{w}$) and found no difference in the adsorbed and spread film behaviour. This conclusion however was only based on the apparently identical variation in frequency and damping data as no further analysis to determine the viscoelastic parameters was undertaken. Cao *et al.*[13] have studied a range of concentrations for PEO of molecular weight 10^6 g mol^{-1} and again, frequency and damping data only were presented. Richards and co-workers[14], whilst repeating the earlier work, extended their study to encompass the frequency dependence. The results reported by the three main research groups for the variation in ω_0 and Γ with bulk concentrations at low q values, were similar as broad features were observed. The wave frequency decreases with increasing surface concentration whereas the damping increases from the value for water, passes through a maximum and then falls back to an asymptotic plateau at higher surface concentrations. However certain differences regarding the behaviour of ω_0 were observed as Yu *et al.* reported a sharp decrease from the value for water then a plateau interrupted only by a peak around 0.5 mg m^{-2}, whereas the data reported by Richards *et al.* exhibited a decrease, followed by a plateau but with no subsequent peak. The behaviour of ω_0 reported here follow the trend

reported by Richards *et al.* and a dependence on both surface concentration and molecular weight is evident.

The maximum damping values observed here are considerably more pronounced than that observed for both adsorbed solutions and spread films of PEO where the data exhibited a broad maximum centred at 0.4-0.6 mg m^{-2}. The maximum in damping was accounted for by the change in surface organisation observed from neutron reflectometry studies[15], where PEO chains begin to penetrate significantly the subphase moving from a 2 to a 3-dimensional molecular organisation as the PEO extends into the subphase as loops and tails above surface concentrations of 0.5 mg m^{-2}. Such an organisation change contrasts the sharp structural change observed for PEOF where the PEO chains are most likely to have a tail conformation due to stretching of the chains into the subphase. However the maximum in damping observed here do not correspond to a sudden change in surface organisation observed by NR experiments. For 5k and 10k PEOF polymers, a two-layer organisation is already evident at the lowest concentrations and little variation in layer thickness is observed for bulk concentrations corresponding to those where the maximum damping is observed. For the lowest molecular weight polymer, a single layer organisation is evident at 10^{-6} g ml^{-1} but most of the structural organisation takes place at ~3×10^{-5} g ml^{-1} where a two-layer organisation is generated. The maxima in damping do not seem to be influenced by the surface organisation or more specifically by the penetration of PEOF into the subphase but is clearly dependent on molecular weight.

To determine whether the maximum in damping is due to classical resonance observed when $\varepsilon_0/\gamma_0 = 0.16$, the surface viscoelastic parameters were extracted for all polymers using identical fitting procedure as that outlined earlier for 2k PEOF.

5-4-2 Surface Viscoelastic Parameters for all PEOF Polymers

The dependence on both static (solid lines) and dynamic (symbols) surface tension on bulk concentration is shown in figure 5.4.2 for all three polymers.

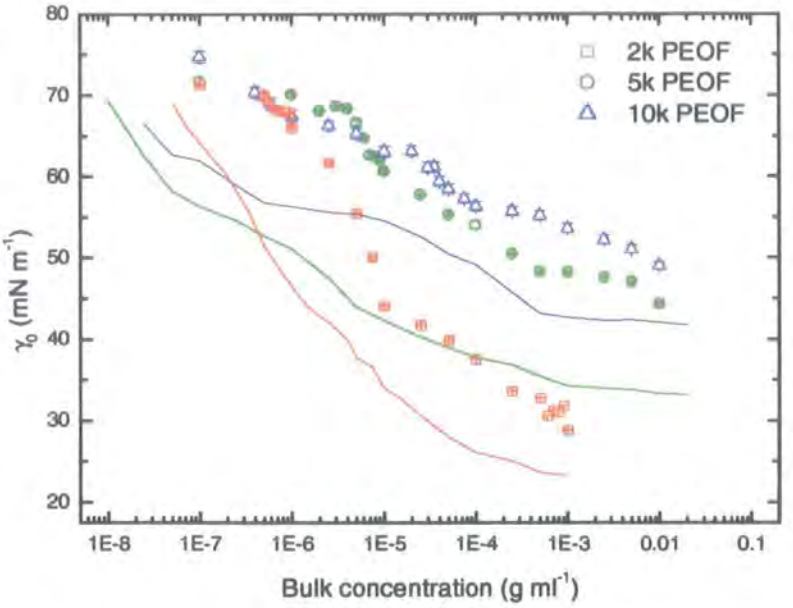

Figure 5.4.2: Comparison of the variation in dynamic (symbols) and static (solid line) surface tension as a function of bulk concentration for all fluorocarbon end-capped PEO.

The same observations made earlier for 2k PEOF are applicable to 5k and 10k PEOF. In all cases the dynamic surface tension are larger than the static values, always circa 10-15 mN m^{-1} higher. At low surface concentrations, dynamic surface tension data are independent of molecular weight as almost identical values, within experimental error, are returned for all polymers. As the surface concentration exceeds 10^{-6} g ml^{-1}, the surface tension values begin to separate and become dependent on molecular weight. The trend observed agrees with that observed in the static measurements as discussed in Chapter Four (section 4-2-1), i.e. a decrease in surface tension as the bulk concentration increases, lower surface tension values being observed for the lowest molecular weight polymer. Differences between surface tension of monolayers measured statically and dynamically by SQELS have been observed before in polymers[5,6,7,9,12], lipid[16] and surfactant[17,18]. The large difference in surface tension between the static and dynamic values were due to considerable relaxation undergone by the monolayer when perturbed by the capillary wave and will be discussed further (section5-5-3). As discussed previously, the data were analysed in accordance with the recent molecular theory for SQELS developed by Buzza and co-workers[3], stating that the value of the surface tension

used during spectral fitting should be the static one and $\gamma' = 0$. In an attempt to check this statement, the data was fitted using the spectral fit method and by fixing the surface tension to the static value. The fit returned is shown in figure 5.4.3.

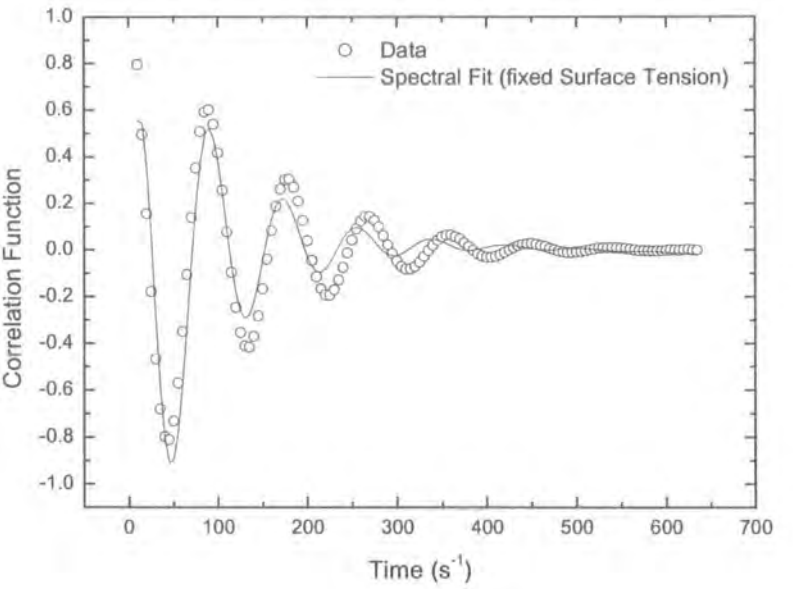

Figure 5.4.3: Experimental correlation function (circles) with fit overlaid (solid line). The data is recorded for 2k PEOF at 10^{-3} g ml^{-1}, q = 480 cm^{-1} and the surface tension is fixed to the static value.

It is evident that a fit is not obtained if the surface tension is fixed to a static value. If $\gamma' \neq 0$ and γ_0 are allowed to vary during fitting, the values of γ_0 returned are similar to those obtained when $\gamma' = 0$. It is concluded that the difference observed between the static and dynamic surface tension is not an artefact of the experiment but a real feature of PEOF dynamical behaviour. The same observations were obtained for 5k and 10k PEOF.

The dilational modulus for all polymers is shown in figure 5.4.4. Unfortunately, the static dilational moduli for 5k and 10k PEOF were not obtainable since a polynomial fit to the surface tension data was not feasible because the data were too scattered to extract reasonable values.

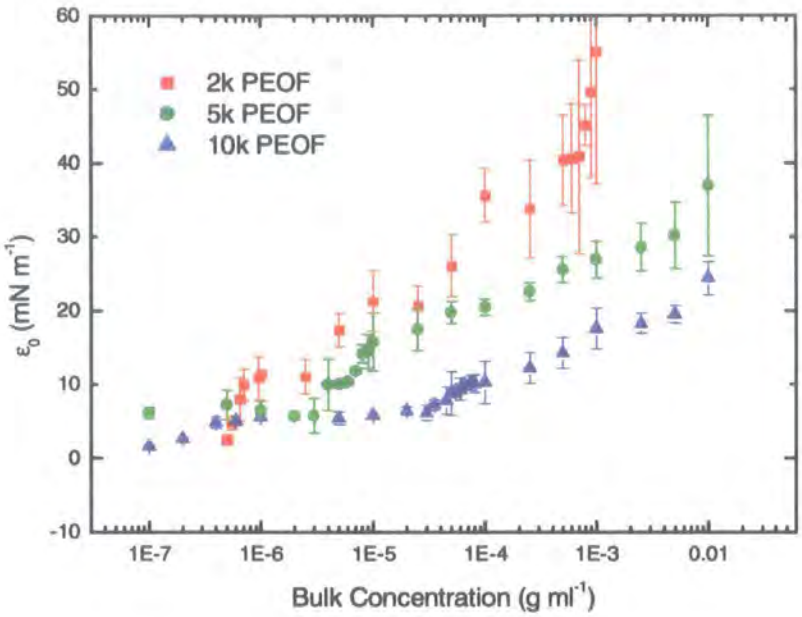

Figure 5.4.4: Comparison of the variation in dynamic dilational modulus as a function of bulk concentration for all polymers.

Above 10^{-6} g ml^{-1}, the dilational modulus diverges for each molecular weight polymer and increases with bulk concentration. The rate of increase varies with molecular weight, the 2k PEOF reaching higher values than that for the higher molecular weight polymers at equivalent bulk concentrations. No maximum is observed as the dilational modulus increases continuously with bulk concentration. However, a step-like increase in dilational modulus is evident for each polymer at the bulk concentration where a maximum in damping is observed. The values observed at higher concentrations differ with molecular weight suggesting that the dilational modulus decreases with increasing molecular weight. By analogy to NR experiments, it was found that the surface excess concentration for 2k PEOF was far greater than 5k and 10k PEOF and could explain the reason why the dilational modulus is higher for the lowest molecular weight polymer as the incompressible nature of the polymer layer is increased in proportion to the surface excess.

It was remarked earlier that the main feature observed for the frequency and damping data as a function of bulk concentration was the presence of a maximum, shifting to higher concentrations as the molecular weight increases, indicative of

resonance[4]. Classical resonance occurs when the ratio of dilational modulus (ε_0) to surface tension (γ_0), obtained from SQELS experiments, is equal to 0.16. The ratio of values for the moduli of each mode were plotted as a function of bulk concentration for all three molecular weight polymers as depicted in figure 5.4.5.

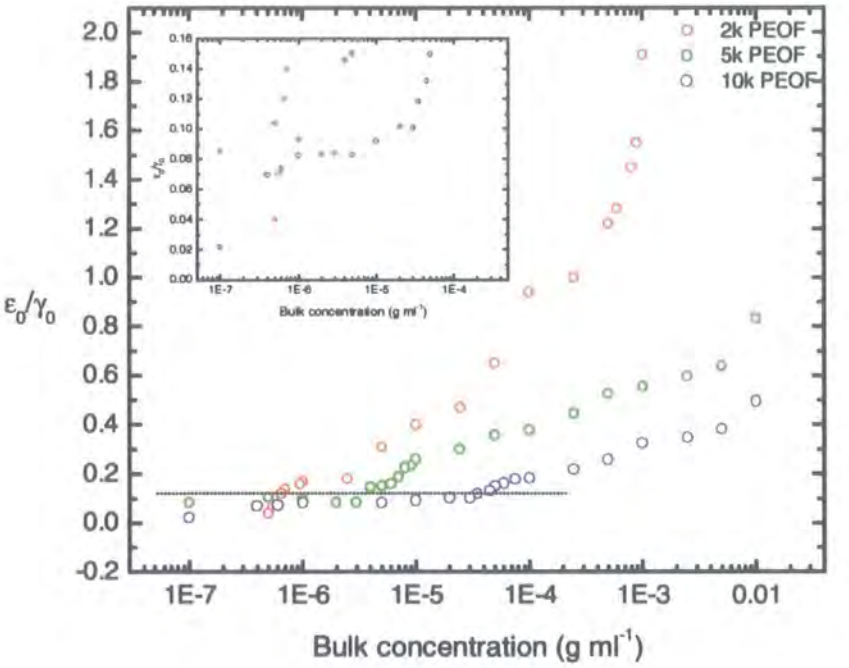

Figure 5.4.5: The ratio of ε_0/γ_0 versus bulk concentration. Classical resonance between the capillary and dilational waves occurs when $\varepsilon_0/\gamma_0 = 0.16$. The dashed line is a guide to the eye.

All polymers show a similar trend, i.e. a small ratio at low concentration independent of molecular weight. As the bulk concentration increases, the dependence of ε_0/γ_0 ratio on molecular weight is evident. The classical resonance conditions are met at 10^{-6}, 6×10^{-6} and 5×10^{-5} g ml^{-1} for 2k, 5k and 10k PEOF respectively and these concentrations concur with the maxima observed in the damping data.

First order approximations describing the propagating characteristics of the capillary and dilational modes were given in equations 2.4.8 and 2.4.9 (Chapter Two).

When the two modes are in resonance, the real frequencies are coincident, therefore $\omega_C = \omega_D$ which leads to,

$$q = \frac{(3/4)^3 \varepsilon^4 \rho}{\gamma^3 \eta^2} \qquad \text{Equation 5.4.2.1.}$$

By substituting the dilational modulus and surface tension values extracted at resonance for each polymer into equation 5.4.2.1, the q calculated was found to be between $475 \leq q / \text{cm}^{-1} \leq 489$, which is in good agreement with the experimental value of 480 cm^{-1}, reinforcing the idea that the two modes are in resonance.

The dilational viscosity dependence on bulk concentration for all three molecular weight polymers is shown in figure 5.4.6a-c.

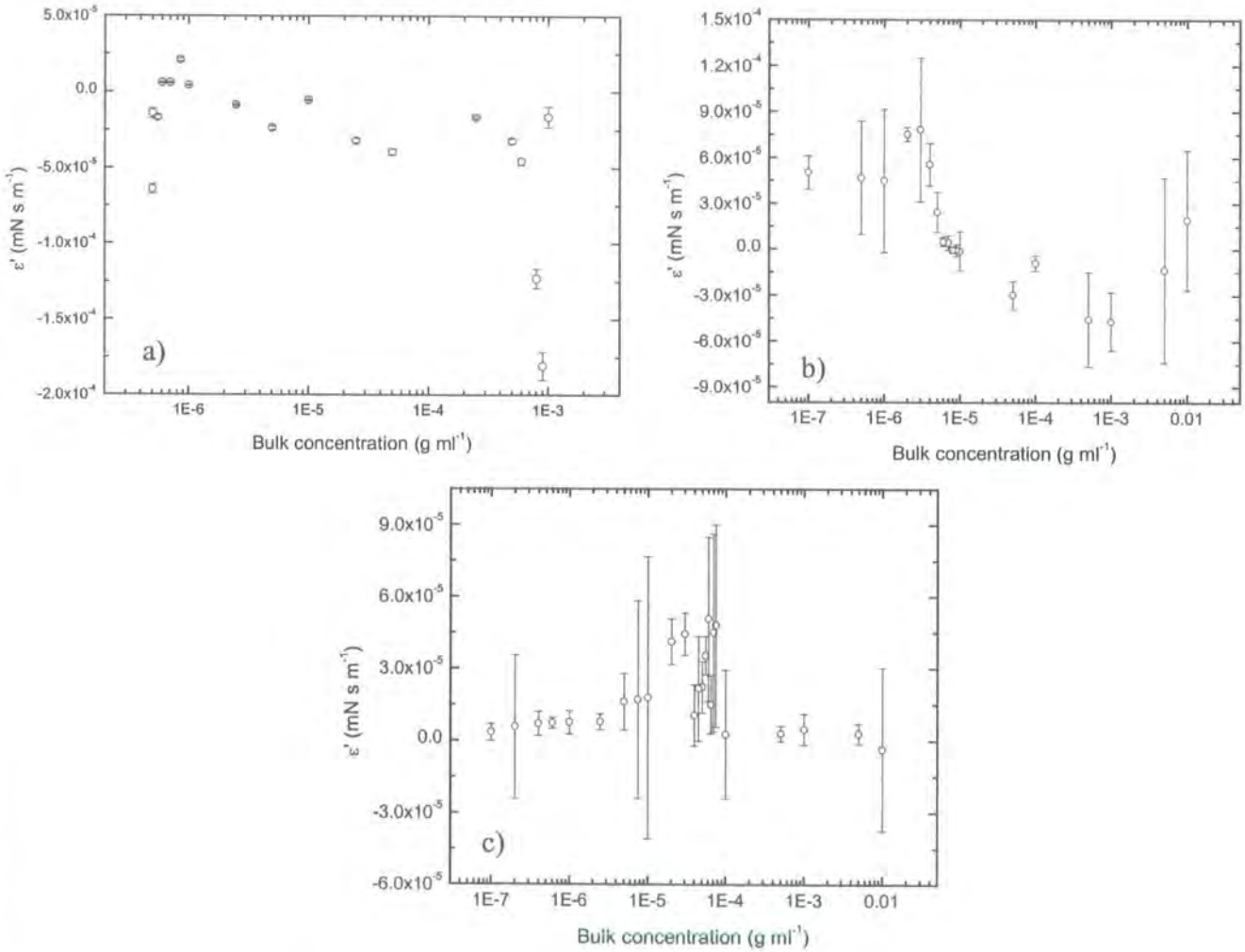

Figure 5.4.6: Comparison of the variation in dilational viscosity as a function of bulk concentration for a) 2k PEOF, b) 5k PEOF and c) 10k PEOF.

A dependence of dilational viscosity on molecular weight is evident especially when the comparison is made between 2k PEOF and the higher molecular weight polymers. Indeed, 2k PEOF displayed negative values over almost the entire concentration range except around 10^{-6} g ml^{-1} where a maximum is observed, thereafter, a decrease in dilational viscosity is evident. 5k PEOF and 10k PEOF exhibit a similar trend with the dilational viscosity being positive at low concentration and increasing with bulk concentration until a break is observed at the resonance concentration. Thereafter the dilational viscosity decreases sharply and negative values are observed for 5k PEOF whereas the dilational viscosity for 10k PEOF remains positive. At high concentrations, both 5k and 10k PEOF tend to ~zero within experimental error. The high error in dilational viscosity especially for 5k and 10k PEOF and dilational modulus for 2k PEOF when compared to the surface tension data is probably due to the presence of noise in the correlation function. However for all polymers, a discontinuity at the resonance concentration is evident, i.e. a sharp decrease in dilational viscosity takes place. The variation of the two dilational parameters close to resonance concentration is intriguing, ε_0 increases steadily with bulk concentration whilst ε' decreases sharply as the bulk concentration increases. At first sight these data may seem extraordinary but may be explained by considering the physics of forced oscillators and transfer functions. The relationship used to describe dilational behaviour by comparing it to the response of a system subjected to harmonic impulses is known as the Kramers-Kronig type relationships[19]. This relationship has been used successfully to describe the behaviour of dilational moduli in graft copolymer containing PEO[7,9]. Those graft copolymers were mainly composed of PEO blocks and the dilational behaviour was therefore attributed to the PEO content as similarities with homoPEO[6] behaviour were found.

Basically, Kramers-Kronig relations involve two equations that describe both the real and imaginary parts of the model system. However, Kramers-Kronig equations are typically given in terms of frequency rather than bulk concentration but they can still be applied here if the dilational behaviour is modelled by a spring that lies in the surface plane. At fixed q, the applied frequency ω is constant and it is the natural frequency ω_0 that varies as the concentration increases. The natural resonant frequency can be related to $\omega_0 = (k/m)^2$, where k is the spring constant and m the mass of the spring. When an oscillatory force is applied to the model spring, compression and expansion cycles are generated by the system. Consider that the compression and expansion cycles correspond

to the dilational behaviour of the monolayer. Any change in bulk concentration will have an affect on the dilational response. By increasing the bulk concentration, the natural resonance frequency, ω_0, is expected to increase as the monolayer stiffness hence k will be influenced. At some critical force (resonance concentration), the frequencies of the dilational mode and oscillatory driving force (capillary mode) are identical as they are in resonance. When a sinusoidal force, $F\exp(-i\omega t)$ is applied to the surface spring, the position (ξ) of the spring at time, t, is given by,

$$\xi(t) = \chi(\omega)F\exp(-\mathrm{i}\omega t) \qquad \text{Equation 5.4.2.2.}$$

where $\chi(\omega)$ is the transfer function which is the proportionality term relating the output (the response) of the system to the input (the force). The transfer function for the displacement response, $\chi_D(\omega_0)$ is expressed as,

$$\chi_D = -\frac{1}{m(\omega^2 - \omega_0^2 + 2\mathrm{i}\omega''\omega)} \qquad \text{Equation 5.4.2.3.}$$

where ω_0 is the natural frequency induced by the applied force and ω'' is its associated damping.

Any modification in the system induced by an applied force is taken into account by the transfer function and can be identified with a mechanical component such as the displacement or the velocity function. The qualitative behaviour can be obtained more directly if the resonance takes place between velocity components of the system rather than displacement components. If the velocity response of the surface film is considered, the transfer function is given by,

$$\chi_V(\omega_0) = -\mathrm{i}\omega\chi_D(\omega_0) = \frac{\mathrm{i}\omega}{\mathrm{m}(\omega^2 - \omega_0^2 + 2\mathrm{i}\omega''\omega)} \qquad \text{Equation5.4.2.4.}$$

By multiplying the denominator by its complex conjugate, the real and imaginary part of the transfer function can be identified as follow,

$$\chi'(\omega) = \frac{2\omega''\omega^2}{m\left[\left(\omega^2 - \omega_0^2\right)^2 + 4\omega''^2\omega^2\right]} \qquad \text{Equation 5.4.2.5.}$$

$$\chi''(\omega) = \frac{i\omega(\omega^2 - \omega_0{}^2)}{m\left[\left(\omega^2 - \omega_0^2\right)^2 + 4\omega''^2\omega^2\right]} \qquad \text{Equation 5.4.2.6.}$$

Figure 5.4.7a-b shows the behaviour of the real and imaginary parts of the velocity transfer functions calculated for the response of a system subjected to harmonic impulses where the real and imaginary parts correspond to the real and imaginary components of the dilational mode, i.e. the modulus and viscosity respectively of 2k PEOF.

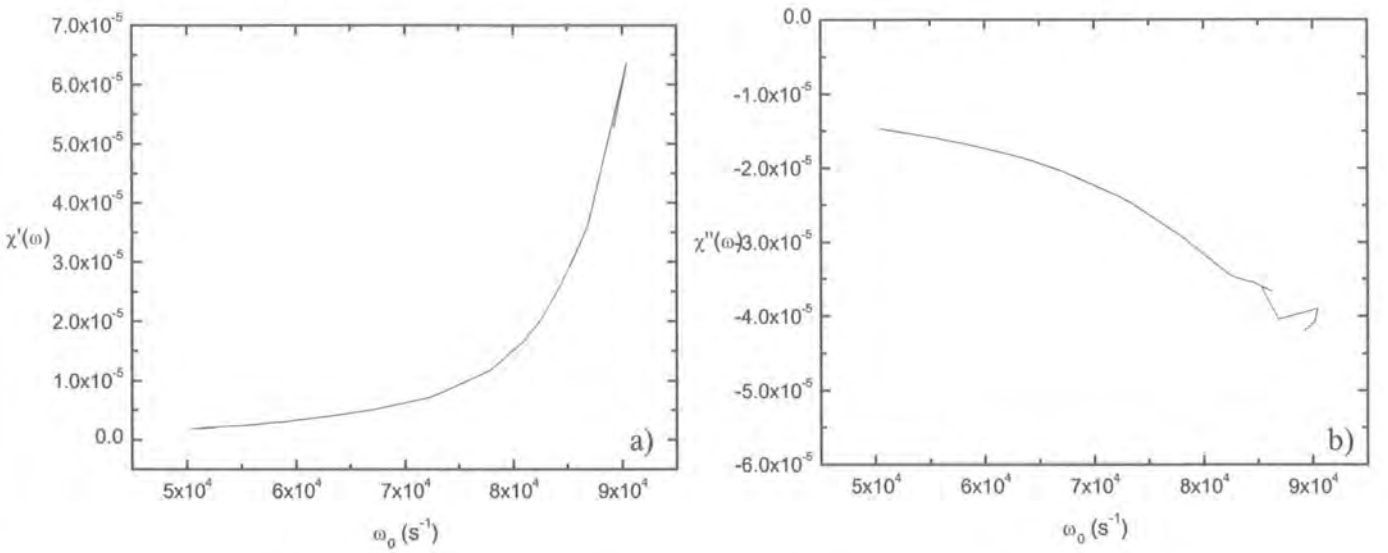

Figure 5.4.7: Transfer function for the velocity response of an oscillator (2k PEOF) subjected to an oscillatory force where a) represents the real component and b) the imaginary.

Figure 5.4.8a-b shows the behaviour of the real and imaginary parts of the velocity transfer functions calculated for the response (dilational modulus and dilational viscosity of 10k PEOF) of an oscillator subjected to an oscillatory force.

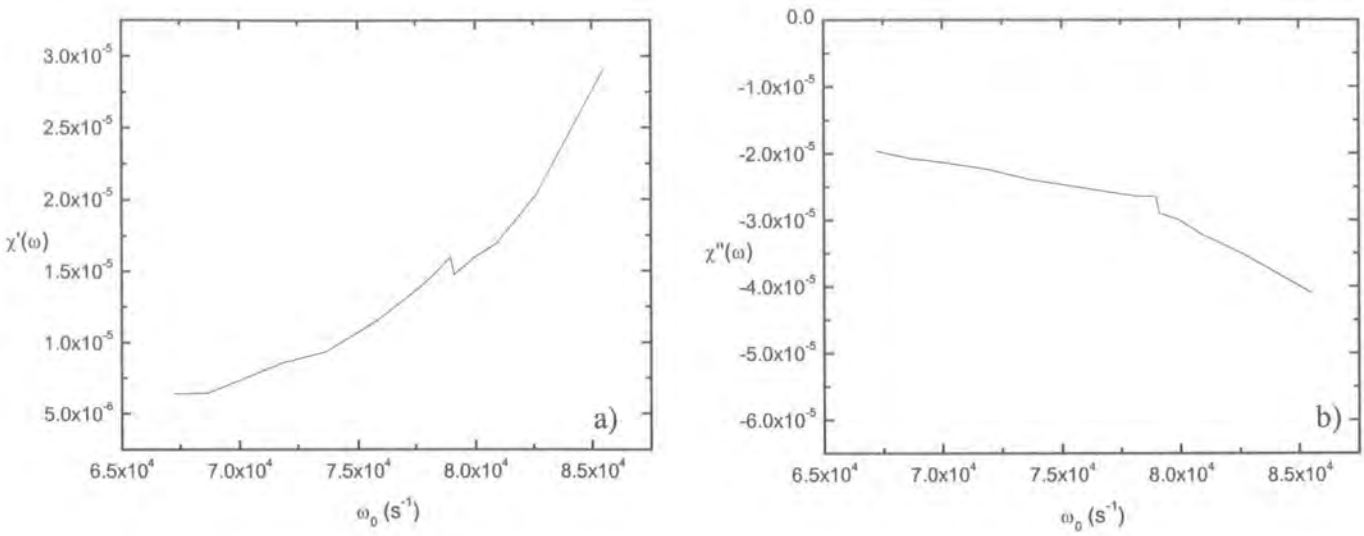

Figure 5.4.8: Transfer function for the velocity response of an oscillator (10k PEOF) subjected to an oscillatory force where a) represents the real component and b) the imaginary.

It is evident that these diagrams have some similarities with the trend observed for the experimentally dilational modulus and dilational viscosity of 2k and 10k PEOF. The plots for 5k PEOF are deliberately omitted since similar behaviour to the 10k PEOF was observed. The qualitative agreement obtained between the theoretical Kramers-Kronig behaviour and the experimental data revealed clearly that the dilational parameters represent the transfer function and thus altering the dynamical properties of the adsorbed film in response to some oscillatory force in the plane of PEOF monolayer. As this behaviour is observed at resonance condition, it seems that the oscillatory force is generated by the capillary waves due to strong coupling between both capillary and dilational modes.

As discussed previously, the viscoelastic parameters of an adsorbed or spread film of PEO at the air-water interface have been reported by mainly two groups, i.e. Yu and co-workers[11,12] and Richards *et al.*[6,14]. In comparing the surface viscoelastic parameters reported by the two groups the problem of the different data analyses is encountered as one group (Yu and co-workers) set the transverse shear viscosity to zero during spectral fitting whilst Richards *et al.* took it into account. The results reported here were obtained in accordance with current theory[3] with only three viscoelastic parameters being fitted ($\gamma' = 0$). However, both research groups agreed when analysing the data that

the experimental dilational modulus qualitatively followed the Gibbs elasticity, as determined from the surface pressure isotherm, although there was deviation at high concentrations. However big discrepancies were found for the dilational viscosity. The values of ε' reported by Yu and co-workers did not show any of the features reported by Richards et al. The discrepancy was accounted for the assumptions made regarding the transverse shear viscosity. The trend of ε_0 reported here is different to the one reported for PEO (parabolic shape). An increase of dilational modulus with bulk concentration is observed with a discontinuity occurring at resonance concentration. Only Richards and co-workers reported negative dilational viscosities for adsorbed solutions of PEO. Indeed at low surface coverage and below resonance concentration, the dilational viscosity increased proportionally with surface concentration. At resonance concentration and above, a sudden fall in ε' to negative values was observed, thereafter becoming increasingly positive at higher surface concentrations. This is precisely the behaviour detected in this study for 5k PEOF and 10k PEOF to a certain extent. The dilational viscosity of 2k PEOF was essentially negative over the entire concentration range investigated with a weak discontinuity observed at resonance concentration. For 10k PEOF, positive dilational viscosities are observed over the entire concentration range investigated and qualitative similarities between 5k and 10k PEOF are evident.

It is concluded that the dilational behaviour of PEOF is dramatically modified by the presence of the fluorocarbon group as unusual and unique values are obtained when compared to unmodified PEO. The sudden change in dilational viscosity for PEO was correlated to changes in monolayer organisation. In this study, it is clear that the surface organisation has little to do with the differences observed in dilational viscosity but it is evident that the dilational behaviour (modulus and viscosity) is definitely dependent on both bulk concentration and molecular weight.

Quantitative agreement with the experimental viscoelastic parameters (γ_0, ε_0 and ε') requires an appropriate theory to be developed. Buzza and co-workers[3] predicted that the viscoelastic parameters scale with polymer grafting density, σ, based on brush like layer at the air-water interface and are described as follow,

$$\pi \approx \sigma^{11/6} b^{5/3} N k_B T \qquad \text{Equation 5.4.2.7.}$$

$$\varepsilon \approx \sigma^{11/6} b^{5/3} N k_B T \qquad \text{Equation 5.4.2.8.}$$

$$\varepsilon' \approx \sigma^2 \eta b^5 N^3 \qquad \text{Equation 5.4.2.9.}$$

where N is the degree of polymerisation, b the monomer step length, T the temperature, η the viscosity of the water subphase and k_B the Boltzmanns constant.

As the surface density is directly proportional to surface concentration, it is therefore possible to assume that the above scaling relationship is still valid if Γ_{upper} is substituted for σ. It was found that the experimental data for the surface pressure scales as $\pi \sim \Gamma_{upper}^{1.92\text{-}3.89}$ above 10^{-6} g ml^{-1} for all three molecular weight polymers where a stretched configuration was observed according to NR observations. This experimental exponent is in good agreement with the theoretical value (11/6 = 1.83) for 2k PEOF (1.92 ± 0.1) whereas higher scaling exponents were returned for 5k (3.68 ± 1.1) and 10k (3.89 ± 0.1) PEOF, which do not agree well with the scaling equation 5.4.2.7. The dilational modulus was found to scale as $\varepsilon_0 \sim \Gamma_{upper}^{1.63\text{-}5}$ above 10^{-6} g ml^{-1}. Once again, good agreement between the theoretical (1.83) and experimental scaling exponent was found for 2k PEOF (1.63 ± 0.20) whereas higher scaling exponents were calculated for 5k and 10k PEOF (4.59 ± 0.60 and 5 ± 1 respectively). The qualitative analysis of the dilational viscosity has previously been discussed in terms of Kramers-Kronig relations. A quantitative interpretation of the data *via* equation 5.4.2.9 is impossible because negative values are not predicted by this equation. This reinforces the idea that the current dispersion equation is inadequate for the system investigated here (see section 5-5-3). This study reveals that agreement between experimental behaviour and the scaling relationships is only observed for the surface tension and dilational modulus of 2k PEOF confirming the observations made by NR experiments regarding the formation of a brush like layer configuration at the air-water interface for the lowest molecular weight polymer. Buzza and co-workers introduced two more parameters into the current theory known as the bending modulus (K) and the coupling constant (λ). However they have been disregarded here as the bending modulus of the film only becomes important for very low surface tension (near zero values) and the coupling coefficient is only significant for a very thick layer (~1 μm), which is not the case here.

To confirm that the real frequencies (capillary and dilational modes) coincide at resonance and also to understand the behaviour of each mode as a function of bulk

concentration, the individual capillary and dilational frequencies were calculated by using equation 2.4.7 and 2.4.8 (real part) given in Chapter Two. The frequencies of each mode are given in figure 5.4.9a-c for all polymers.

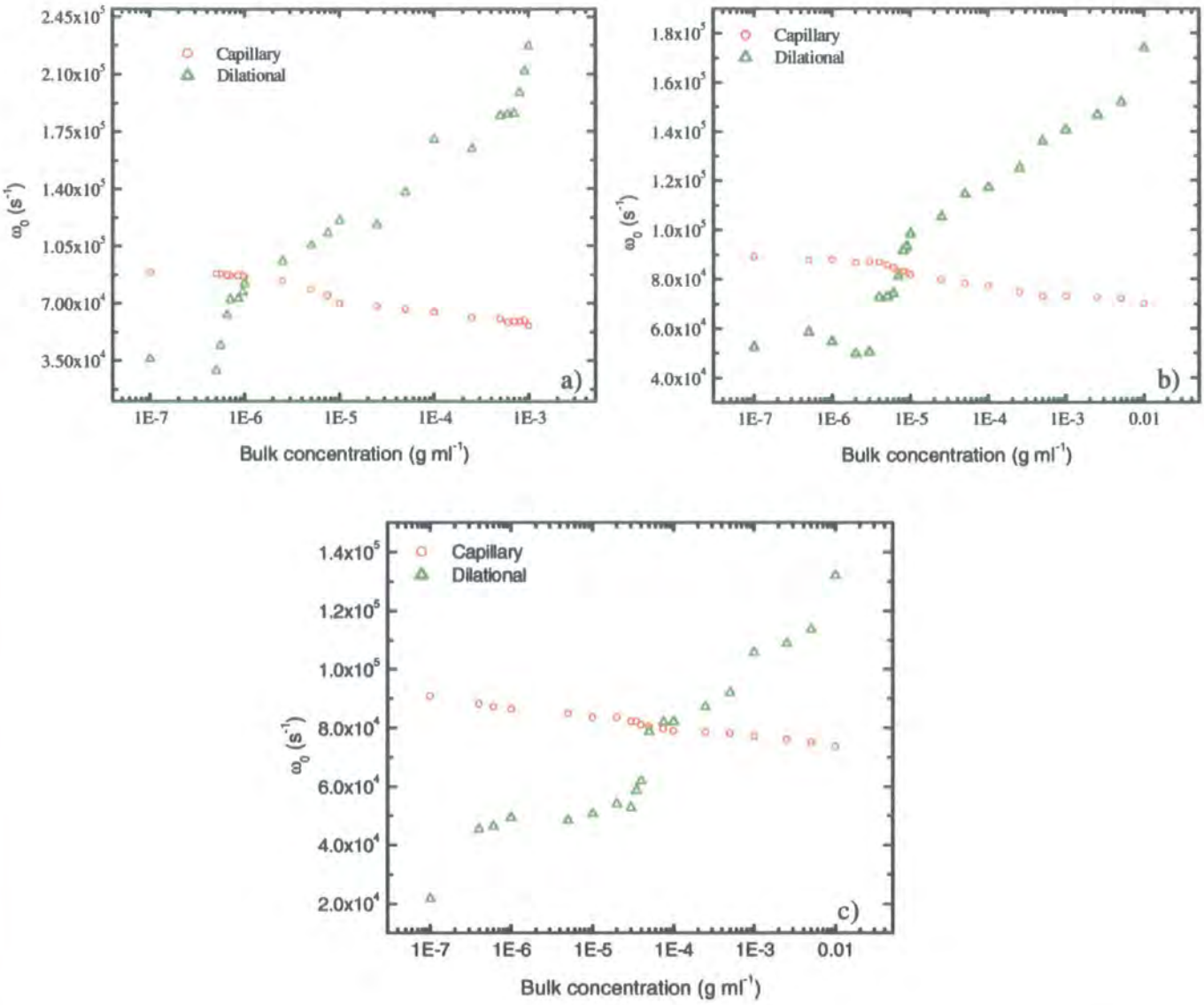

Figure 5.4.9: Comparison of capillary and dilational frequency for a) 2k PEOF, b) 5k PEOF and c) 10k PEOF as a function of bulk concentration.

From the results presented here, it is evident that the dilational and capillary modes converge and intersect at the resonance concentrations, i.e. 10^{-6}, 5×10^{-6} and 5×10^{-5} g ml^{-1} for 2k, 5k and 10k PEOF respectively. The capillary motion dominates the frequency mode below resonance concentration. Above resonance concentration, the two modes diverge with the dilational mode dominating the capillary motion. Constant values

of frequency are not reached by the dilational mode at high bulk concentration, a sharp increase being observed above resonance concentration. The frequency behaviour of the capillary mode is reminiscent of that observed experimentally in figure 5.4.1a. It can also be noted that the dilational frequency decreases with an increase in molecular weight suggesting that the dilational frequency is dependent on molecular weight.

In an attempt to improve our understanding of the behaviour of the individual capillary and dilational waves, the coupling between these modes can be described theoretically by a pair of oscillators[19,20]. The characteristics of the capillary and dilational modes are conceptualised by comparing their behaviour to two loss-free coupled oscillators. This model is simplified (dissipative effects influencing the surface wave characteristic are not included) and should be used as first approximation only. Imagine a system where two oscillators are connected but have different free frequencies Ω_1 and Ω_2. In the case where these two oscillators are linked together, any move in one will engender a response in the other and vice-versa. Consequently the frequency of both oscillators will be modified since the frequency of one oscillator will influence the other. Classically, the new frequencies ω of the coupled modes of two such oscillators are related to the complex frequencies Ω_1 and Ω_2 of the uncoupled modes via the coupling strength κ,

$$(\omega - \Omega_1)(\omega - \Omega_2) = \kappa^2 \qquad \text{Equation 5.4.2.10.}$$

The solutions of equation 5.4.2.10 are the normal frequencies (ω_1 and ω_2) associated with each mode. If two oscillators are coupled, the oscillations or modes of the coupled system will depend on the frequency of the free oscillations and the coupling strength. When $\kappa = 0$, there is no coupling between the mode and $\Omega_1 = \omega_1$ and $\Omega_2 = \omega_2$. As coupling is introduced, κ becomes positive and $\omega_1 > \Omega_1$ and $\omega_2 < \Omega_2$ as the individual frequencies start to diverge. Using this simplistic model it can be demonstrated that when the strength of the coupling is highest (i.e. at resonance) the frequency of the low frequency mode exhibits a minimum whereas the high frequency mode exhibits a maximum. By relating the polymer system to this simple model, the transverse and longitudinal modes would be propagating with free frequencies Ω_1 and Ω_2 and as these modes are always coupled, the real frequencies ω_1 and ω_2 are related to the capillary (high frequency) and dilational (low frequency) modes respectively. From this analogy it

is concluded that at resonance concentration, the coupling between the capillary and dilational waves is at maximum implying that the capillary and dilational frequency modes should display a maximum and minimum values respectively at resonance concentration. Such characteristic behaviour is observed for the individual frequencies of the three molecular weight polymers in figure 5.4.9a-c where the minima and maxima are observed around resonance concentration suggesting that the coupling behaviour between capillary and dilational frequencies can be interpreted by a two loss-free coupled oscillators.

5-5 Frequency Dependence

The results from the dependence of surface viscoelastic properties on wavenumber, q (capillary wave frequency), of each fluorocarbon end-capped PEO will be outlined here. In these experiments the resonance concentration was selected, i.e. 10^{-6}, 6×10^{-6} and 5×10^{-5} g ml^{-1} for 2k, 5k and 10k PEOF respectively. The resonance concentration is of particular interest as both dilational and capillary modes are optimised due to strong coupling between them. The dynamical behaviour of each polymer monolayer was monitored over a wide range of wavenumbers ($250 \leq q$ / cm^{-1} ≤ 1600) for a clean water surface.

5-5-1 Results: Frequency and Damping

A double logarithmic plot of the capillary wave frequency and damping is given in figure 5.5.1 for a solution of 2k PEOF at 10^{-6} g ml^{-1}. The symbols represent the experimental data and the lines are the theoretical values for a fluid surface calculated by substituting a surface tension of 47 mN m^{-1} (surface tension of polymer solution) and literature values for the density and viscosity of pure water at 298 K into the dispersion equation. All other parameters (γ', ε_0, ε') were set to zero (as they must be for pure water), any deviation between experimental and theoretical results will be due to the modulus and dilational viscosity of the surface. Theoretically, the propagating characteristics of the capillary waves are expected to scale as $\omega_0 \sim q^{3/2}$ and $\Gamma \sim q^2$ and the dilational damping as $\Gamma \sim q^{4/3}$.

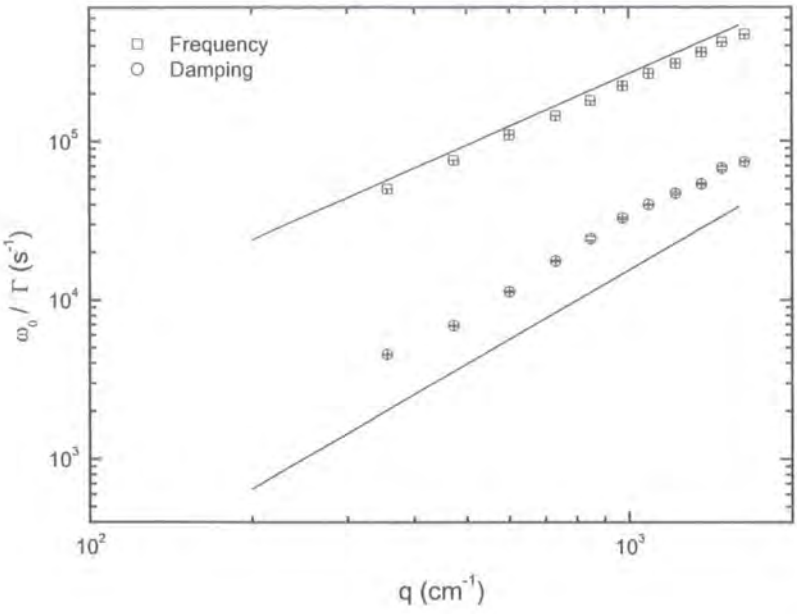

Figure 5.5.1: Double logarithmic plot of capillary wave frequency and damping as a function of wavenumber for 2k PEOF at 10^{-6} g ml^{-1} (symbols) and values calculated for a clean water surface (solid line).

The frequency data (ω_0) increase linearly with q and are qualitatively similar to that of pure water. However the values are slightly depressed due to the presence of the polymer molecules at the air-water interface. Linear least squares fit were applied to the data in order to check the theoretical predictions. The frequency was found to scale according to $\omega_0 \sim q^{1.48}$ which is in excellent agreement with the theoretical exponent. The experimental damping values are greater than those observed for a water surface as expected (no viscosity was included in the simulation). However, the trend of the damping is not as monotonic as the frequency as the data exhibits two separate regimes with a discontinuity at circa 850 cm^{-1}. This behaviour is neither an artefact of the experiment nor induced by an instrumental source[21] as this behaviour was highly reproducible, but is a real characteristic of the data, suggesting that a unique phenomenon is taking place in the polymer layer. The scaling exponent was determined for each set separately and the results are:

low q ($250 \le q$ / cm^{-1} ≤ 730)	$\Gamma \sim q^{1.72 \pm 0.1}$
high q ($849 \le q$ / cm^{-1} ≤ 1637)	$\Gamma \sim q^{1.89 \pm 0.1}$

For the low frequency data, the exponent is lower than the value expected by theoretical predictions (~2). For higher frequencies, the scaling exponent converges to the value expected and this behaviour (damping both diverged and converged towards the values predicted for water) has been reported before in polymer systems[9,21] and surfactants[22], suggesting that a change in coupling between the capillary and dilational modes is occurring.

The dependence of experimental frequency and damping as a function of q on molecular weight is shown in figure 5.5.2.

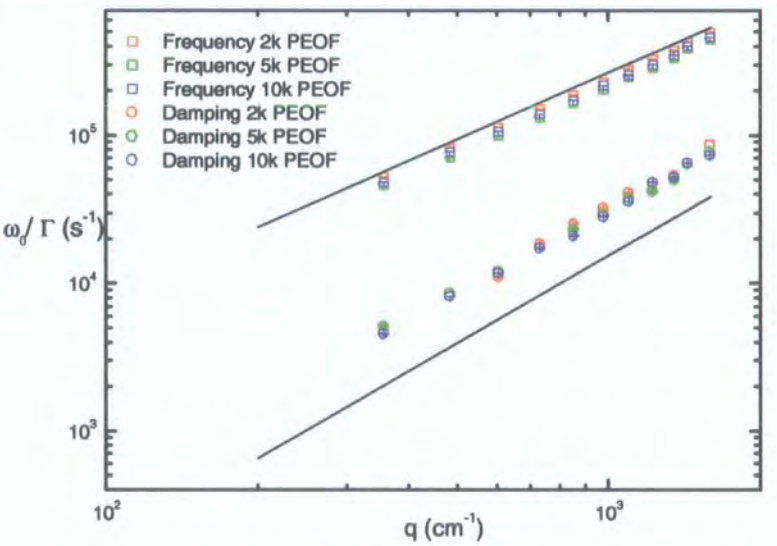

Figure 5.5.2: Comparison of frequency and damping behaviour as a function of q for the three molecular weight polymers.

Qualitatively, both frequency and damping exhibit similar features; both increase with q and the same discontinuity in damping is observed at ~850 cm^{-1}. Experimental frequencies are close to those expected for a pure water subphase and there is no discernible dependence on molecular weight. For all of the data the error is smaller than the size of the symbol. The surface tension and densities of the three polymer solutions are very similar, so the absence of molecular weight effect is expected. The damping data are somewhat more complicated: there are clear deviations from the behaviour predicted for a pure water subphase and two separate regimes are exhibited. However, a dependence on molecular weight could be debated as the departure between experimental

damping and theoretical prediction is slightly more marked for the lowest molecular weight polymer.

The scaling exponents for the frequency and damping of all PEOF polymers as a function of q have been determined and are shown in table 5.5.1.

Polymer	Frequency exponent	Low q Damping exponent	High q Damping exponent
2k PEOF	1.48 ± 0.01	1.72 ± 0.10	1.89 ± 0.10
5k PEOF	1.52 ± 0.02	1.69 ± 0.05	1.91 ± 0.10
10k PEOF	1.50 ± 0.01	1.74 ± 0.05	2.04 ± 0.10

Table 5.5.1: Comparison of scaling exponents for the frequency and damping behaviour of all PEOF polymers as a function of q.

For all three molecular weight polymers the frequency was found to scale according to $\omega_0 \sim q^{1.50}$, in excellent agreement with the theoretical prediction. In all polymers the damping behaviour at low q disagrees with the theoretical capillary dependence and the average scaling exponent predicts a weaker dependence on q than capillary mode but stronger than dilational mode (~1.33). For high q the damping behaviour appears to be dominated by capillary damping as all scaling exponents agree well, within experimental errors, with the theoretical capillary dependence.

5-5-2 Results: Viscoelastic Parameters

Again the spectral fitting method was used to determine the viscoelastic parameters. The transverse shear viscosity was set to zero whilst the other viscoelastic parameters were allowed to float as described previously. In this section the wavenumber dependence on each viscoelastic parameter is presented individually for all three molecular weight polymers.

Surface Tension

Surface tension data for each polymer are shown in figure 5.5.3.

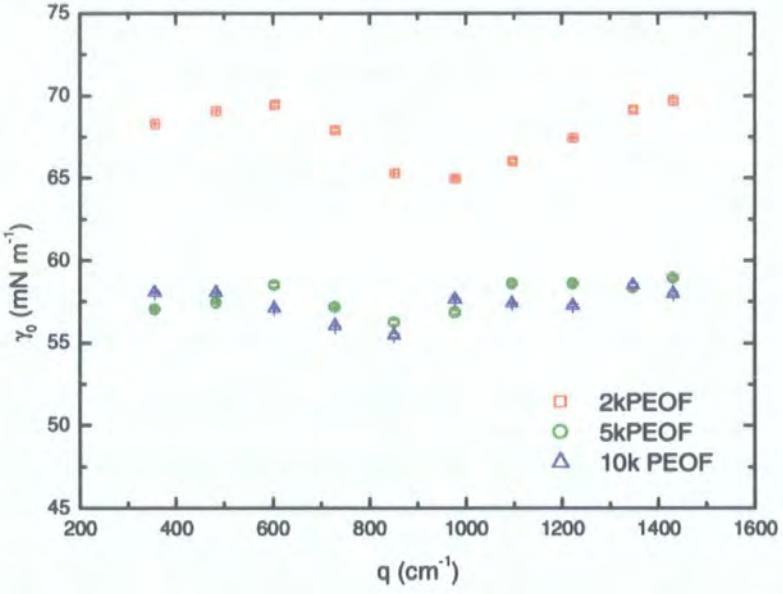

Figure 5.5.3: Wavenumber dependence of surface tension for an adsorbed film of three different molecular weight polymers at resonance concentration.

All polymers display scattered data fluctuating around 68 mN m^{-1} for 2k PEOF and 57 mN m^{-1} for 5k and 10k PEOF. A weak dependence on q is observed as the initial values are returned at high q values. The magnitude of the surface tension observed here (circa 68 mN m^{-1} for 2k PEOF and 57 mN m^{-1} for 5k and 10k PEOF) is almost identical than the dynamic values observed in the concentration dependence studies. However those values are still 10-15 mN m^{-1} bigger than the static surface tension (47, 43, 50 mN m^{-1} for 2k, 5k and 10k PEOF respectively) suggesting that the adsorbed polymer film undergoes considerable relaxation as remarked earlier (figure 5.4.2). This will be discussed further later.

Dilational Modulus

A plot of dilational modulus as a function of wavenumber is given in figure 5.5.4 for each polymer.

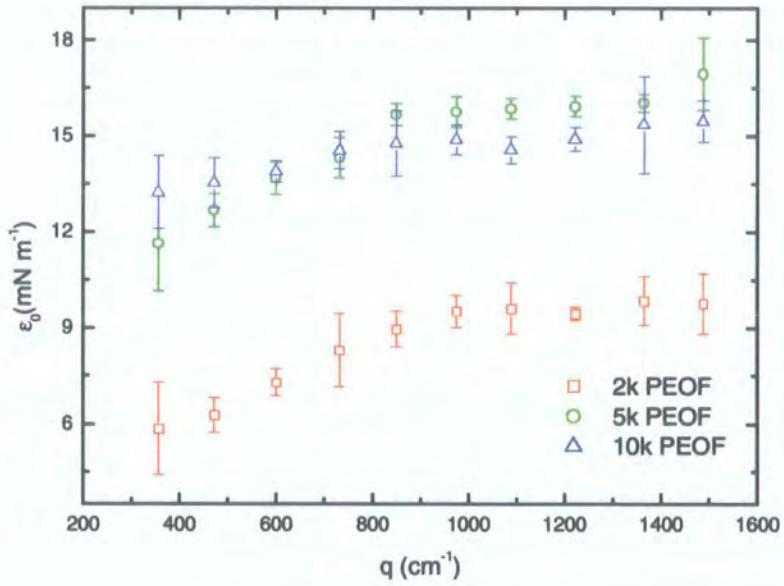

Figure 5.5.4: Wavenumber dependence of dilational modulus for an adsorbed film of three different molecular weight polymers at resonance concentration.

The dependence of the dilational modulus on wavenumber q is evident. All data exhibit a discernible trend, i.e. ε_0 increases with q until 1000 cm^{-1} where an asymptotic value for higher q values is noted. The magnitude of the dilational modulus for all polymers increases linearly and is ~3 mN m^{-1} higher than the values observed at ~260 cm^{-1}. The behaviour of PEOF polymers is again similar suggesting that surface behaviour does not depend on molecular weight. The difference in magnitude can be attributed to the difference in resonance concentration as the corresponding surface excess from NR results are 1.13, 1.98 and 1.54 mg m^{-2} for 2k, 5k, and 10k PEOF respectively. However, this frequency dependence of the dilational modulus suggests the existence of at least one relaxation process and this should be accompanied by a reduction in the magnitudes of the dilational viscosity as the frequency increases.

Dilational viscosity

The variation of dilational viscosity with surface wavenumber is given in figure 5.5.5 for all polymers.

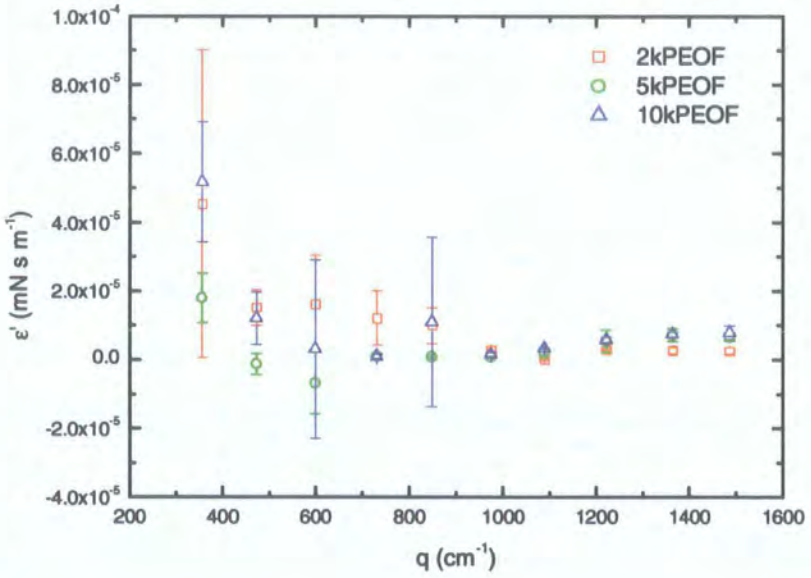

Figure 5.5.5: Wavenumber dependence of dilational viscosity for an adsorbed film of three different molecular weight polymers at resonance concentration.

Figure 5.5.5 shows clearly a reduction in the magnitudes of the dilational viscosities of the three polymer solutions with increasing frequency. Negative dilational viscosities were observed for 5k PEOF at q~500 and 600 cm^{-1}. 2k and 10k PEOF exhibit positive dilational viscosities over the entire q range investigated. The magnitudes of the dilational viscosities detected are identical within error for all polymers molecular weight.

5-5-3 Viscoelastic Relaxation

In an attempt to understand the complex viscoelastic behaviour of the system, simple models have been applied to experimental data to describe the relaxation processes occurring within the adsorbed polymer film. The simplest models describing viscoelastic relaxation in three-dimensional bulk solids are the Voigt-Kelvin and

Maxwell models[23]. Both of these models attempt to describe viscoelastic behaviour through some combination of elastic and viscous elements by using two mechanical components, a spring and a dashpot, connected in either series (Maxwell) or parallel (Voigt). Basically, the dashpot (piston moving in oil) accounts for the viscous nature of the film quantified by the frictional resistance and the spring represents the elastic contribution of the monolayer (shear modulus). When a surface excess layer is present at a liquid surface the capillary waves import an oscillatory stress and strain and these two properties are related via the complex dynamic modulus, $G^{*'}(\omega)$,

$$G^{*'}(\omega) = G'(\omega) + iG''(\omega) \qquad \text{Equation 5.5.3.1.}$$

where $G'(\omega)$, and $G''(\omega)$, are the storage and loss moduli respectively.

The storage modulus is related to the storage and release of energy with surface motion and is the dynamic surface tension. The loss modulus describes the dissipative properties of the motion and is conventionally related to $\omega^2\gamma'$. But, in the system presented here, $\gamma' = 0$, however theoretically a relaxation processes can also be observed through dilational waves. All data were collected at the resonance concentration where frequencies of the dilational waves are experimentally accessible. Therefore, at resonance, the following expressions for the storage and loss modulus can be used: $G'(\omega) = \varepsilon_0$ and $G''(\omega) = \omega^2\varepsilon'$.

The Voigt model predicts frequency-independence for the dilational and loss moduli, it is therefore disregarded here since both dilational parameters have a frequency dependence. The Maxwell model predicts a relaxation where ε_0 increases and ε' decreases with frequency and such behaviour is clearly reproduced experimentally at low q values ($\leq 850\text{cm}^{-1}$). Assuming that there is only one relaxation process for the Maxwell fluid model, the expressions for the storage and loss moduli for the Maxwell model are given by,

$$G'(\omega) = G_e + \frac{G_i\omega_0{}^2\tau^2}{1+\omega_0{}^2\tau^2} \qquad \text{Equation 5.5.3.2.}$$

$$G''(\omega) = \frac{G_i\omega_0\tau}{1+\omega_0{}^2\tau^2} \qquad \text{Equation 5.5.3.3.}$$

where G_e is the equilibrium (static) elastic modulus for an adsorbed film added to the Maxwell model to include the possibility of solid-like behaviour in the material. G_i is the strength of the relaxation process, which has a relaxation time τ.

Consequently by plotting $\varepsilon_0 = f(\omega_0)$ and $\omega_0^2\varepsilon' = f(\omega_0)$ and by fitting the data using equation 5.5.3.2 and 5.5.3.3 with G_e, G_i and τ as adjustable parameters of the fit, we expect the values for these parameters from separate fits to ε_0 and ε' data to be the same , within error, for a particular PEOF molecular weight.

A typical fit for ε_0 and ε' data of 2k PEOF is shown in figure 5.5.6a-b.

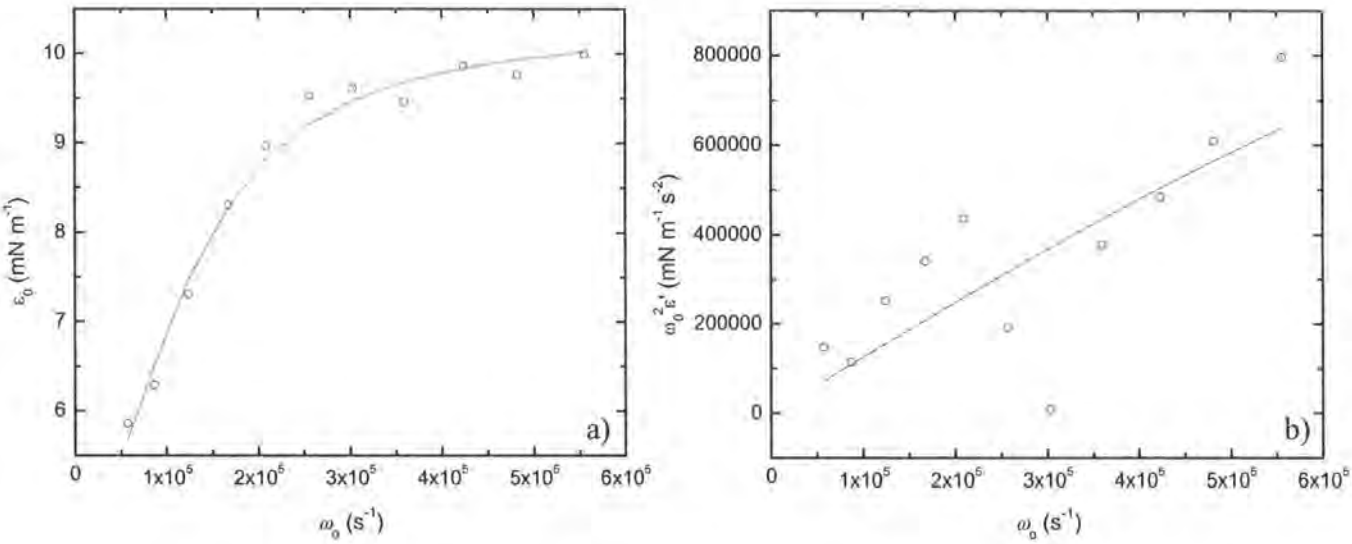

Figure 5.5.6: Fit of Maxwell fluid model to dilational modulus (a) and dilational viscosity (b) data for 2k PEOF.

The results are shown in table 5.5.2.

Dilational moduli	τ (s^{-1})	G_i ($mN\,m^{-1}\,s^{-2}$)	G_e ($mN\,m^{-1}$)	χ
ε_0	8×10^{-6} $\pm\ 9\times10^{-7}$	5.6 $\pm$ 0.32	4.6 $\pm$ 0.4	0.042
ε'	5.61×10^{-7} $\pm\ 1.4\times10^{-6}$	2.2×10^{6} $\pm\ 4\times10^{6}$		10^6

Table 5.5.2: Results from Maxwell fluid model fit to dilational modulus (ε_0) and dilational viscosity (ε') for 2k PEOF.

It is evident from table 5.5.2 that the Maxwell fluid model describes well the dilational modulus behaviour while failing to describe the dilational viscosity behaviour.

The same procedure was applied to 5k and 10k PEOF dilational modulus data and the results for all three molecular weight polymers are shown in table 5.5.3.

Polymer	τ (s^{-1})	G_i ($mN\,m^{-1}\,s^{-2}$)	G_e ($mN\,m^{-1}$)	χ
2k PEOF	8×10^{-6} $\pm 9\times10^{-7}$	5.57 $\pm$ 0.32	4.6 $\pm$ 0.4	0.042
5k PEOF	8×10^{-6} $\pm 1.1\times10^{-6}$	6.33 $\pm$ 0.41	10.6 $\pm$ 0.5	0.091
10k PEOF	6×10^{-6} $\pm 1.4\times10^{-6}$	2.64 $\pm$ 0.27	13.0 $\pm$ 0.3	0.051

Table 5.5.3: Results from Maxwell fluid model fit for 2k, 5k and 10k PEOF.

For the data obtained at each q for a fixed concentration (resonance concentration), the dependence of the dilational modulus on frequency can be fitted by equation 5.5.3.2 with a relaxation time around 8×10^{-6} s^{-1} for all three molecular weight polymers and an equilibrium ($\omega_0 = 0$) dilational modulus (G_e) of 4.6, 10.6 and 13 for 2k, 5k and 10k PEOF respectively. These latter values are in fair agreement with the static dilational modulus calculated using equation 5.3.4.1, i.e. 6, 11 and 14 mN m^{-1} for 2k, 5k and 10k PEOF respectively. The strength of the relaxation process is almost identical for 2k and 5k PEOF but much reduced for 10k PEOF. By assuming that the relaxation is described by the Maxwell model, the relaxation time at different bulk concentrations for a fixed capillary wave frequency can be obtained by combining equation 5.5.3.2 or 5.5.3.3 (equation 5.5.3.4).

$$\tau = \frac{[G'(\omega_0) - G_e]}{[\omega_0 G''(\omega_0)]}$$

Equation 5.5.3.4.

$$= \frac{\varepsilon_0(\omega_0) - \varepsilon_{0ST}}{\omega_0^2 \varepsilon'(\omega_0)}$$

However as depicted in equation 5.5.3.4 τ is related to the dilational viscosity, which is negative over the entire concentration range investigated for 2k and 5k PEOF (except at low bulk concentration) and a negative relaxation time is physically unrealistic.

Equation 5.5.3.4 has been applied to 10k PEOF. Unfortunately, the values of ε_{0ST} returned by using equation 5.3.4.1 are too scattered over the concentration range investigated as discussed earlier and a negative relaxation time was also returned as $\varepsilon_{0ST} > \varepsilon_0(\omega_0)$. It is therefore concluded that the variations of relaxation time with bulk concentration were inaccessible due to a lack of information regarding the dilational viscosity and ε_{0ST}. The implications of negative dilational viscosity are not understood fully. Conventional thinking would regard a negative viscosity as unphysical since the viscosity is associated with the dissipation of mechanical energy, and thus a negative viscosity implies energy being input from an external source[24]. Negative dilational viscosities have now been reported numerous times for various PEO-containing system[6,7,14,21] but also surfactant[22] and other polymer systems[8,25]. For systems where a surface excess layer is present, negative values are associated with an adsorption barrier[26] and the diffusive exchange[27] of polymer molecules from the bulk solution to the surface layer until equilibrium is reached. Whilst the data indicate that additional forces are influencing surfaces wave evolution, ε' is currently best viewed as an effective parameter indicating that modification of current theories is required due to the dispersion equation not describing the surface dynamic behaviour adequately.

Although a Maxwell fluid model has been applied successfully here for ε_0 and other models such as surface films of spread PEO film[14] and block copolymer containing PEO[5], they are only phenomenological, i.e. the notional spring and dashpot cannot easily be related to real physical parameters. For the specific case of the dilational properties of surfactant surface excess layers, numerous models have been developed describing relaxation effects due to processes such as surface-bulk exchange and micelle formation and these relaxation models have been reviewed elsewhere[21].

5-5-4 Discussion

The only unusual feature of the viscoelastic parameters is the difference observed between the static and dynamic surface tension (determined as the bulk concentration dependence studies and frequency dependence studies), suggesting that the excess layer undergoes significant relaxation when perturbed by capillary wave. The dilational modulus increases with frequency as expected and this increase in dilational modulus is compensated by a decrease in dilational viscosity.

PEO is the major component of the fluorocarbon end-capped PEO therefore it seems appropriate to discuss the characteristics viscoelastic parameters in relation to those exhibited by a surface excess in dilute solutions of PEO[14]. As discussed previously, the transverse shear viscosity was fitted for adsorbed PEO films but here, this parameter has been disregarded, as its effect on the viscoelasticity was minimal. The only difference between experiments is the molecular weight (much higher molecular weight were investigated by Richards *et al.*).

This comparison reveals some similarities between the viscoelastic properties of PEO and the fluorocarbon end-capped PEO investigated here. The surface tension values for both PEO and PEOF exhibit weak dependencies on frequency. For PEO, some scatter in the data is observed but no evidence of any increase in surface tension with increased frequency is reported. The average surface tension for all polymers was found to be ~62.2 $\pm$ 2 mN m^{-1} and no significant deviation from the static value of surface tension was observed. The surface tension values for PEOF are also frequency independent but large deviations from the static values are reported here. It is interesting to notice that the average surface tension for 5k and 10k PEOF is almost identical to the average values observed for higher molecular weight PEO.

Qualitatively, the dilational modulus of PEO and PEOF exhibit the same behaviour with ε_0 increasing with an increase in frequency (low q). At higher frequencies, PEO dilational modulus starts to decrease whereas PEOF dilational modulus remains constant. An increase from low values or zero at zero frequency to approximately 3 mN m^{-1} at a capillary wave frequency of 20 kHz was observed for PEO dilational modulus. The same order of magnitude is reported for PEOF but the dilational modulus is 3 times bigger for 2k PEOF and approximately 5 times bigger for the higher

molecular weight polymers when compared to PEO, suggesting that the high frequency surface waves are affected by the incompressible nature of the adsorbed PEOF.

The frequency dependence of the dilational viscosity observed here is similar to PEO, both displaying a decay with increasing frequency until constant values around zero are reached for higher frequencies. However, quantitatively, total agreement is not obtained as PEO dilational viscosities are negative over the entire frequency range whilst ε' for PEOF are positive, except for 5k PEOF, at low q range (480 and 605 cm^{-1}). Interestingly when the trend in results is compared (PEO and PEOF) as a function of frequency they are mirror images, reflected in the x-axis.

For the dilational mode (modulus and viscosity), only qualitative agreement between PEO and PEOF is found. Therefore, the fluorocarbon group and the resulting tethering organisation of the PEO chains must influence the dilational behaviour; the magnitudes of ε_0 and ε' being dramatically different. The similarity of the results for the series of polymers reveals a lack of dependence of behaviour for the frequency and viscoelastic properties on molecular weight.

Mode mixing

All the results presented here have been obtained at resonance concentration where the coupling between the dilational and capillary modes is maximised. As discussed earlier, the damping dependence studies on q (table 5.5.1.) revealed two separate regimes indicative of mode mixing.

Mode mixing[22,28,29] (i.e. splitting of the mode frequencies) occurs at a specific point where the normal modes become mixed and the behaviour of each mode cannot be isolated. Theory predicts two routes to mode mixing for waves on a liquid surface. One involves the dilational viscosity[28] and the second the transverse shear viscosity[29]. The second route is not relevant to this work since $\gamma' = 0$. Briefly, an increase in transverse shear viscosity increases the damping of the capillary waves and reduces the damping of the dilational mode until both damping converge at a critical value of γ', inducing mode mixing.

Earnshaw and co-workers predicted theoretically[28], and observed in surfactant solutions[22], that changes in the dilational viscosity bring about the conditions for mode mixing. It is expected in theory that an increase in dilational viscosity increases the

damping of the dilational mode therefore tending to separate the two damping constants, whereas convergence is required for mode mixing. However if the dilational mode becomes unstable, then negative viscosities are generated, which effectively cause the damping to converge. As the dilational viscosity decreases further, the real frequencies begin to separate leading to mode mixing.

Negative dilational viscosities were not observed over the frequency range investigated for all three molecular weight polymers suggesting that mode mixing does not occur. However, the change in the q dependence of the damping (figure 5.5.2) suggests the opposite. To check whether or not mode mixing is occurring, the normalised frequency (equation 5.5.4.3) and normalised damping (equation 5.5.4.3), which is the experimentally obtained damping divided by the first-order approximation of the damping of the pure liquid, are plotted in the complex plane.

$$\omega_{0\ norm} = \frac{\omega_0}{\sqrt{(\gamma_0 q^3 / \rho)}} \qquad \text{Equation 5.5.4.3.}$$

$$\Gamma_{norm} = \frac{\Gamma}{(2\eta q^2 / \rho)} \qquad \text{Equation 5.5.4.4.}$$

If mode mixing is occurring, as q increases, the values on the plot should decrease and bend to the left followed by a curving bend to the right to give a characteristic hook-like curve[22]. Such plots are given in figure 5.5.7a-c for all three molecular weight polymers.

It is evident from figure 5.5.7a-c that no trend indicative of mode mixing is observed. The data are rather scattered and confirmed that PEOF does not exhibit mode mixing.

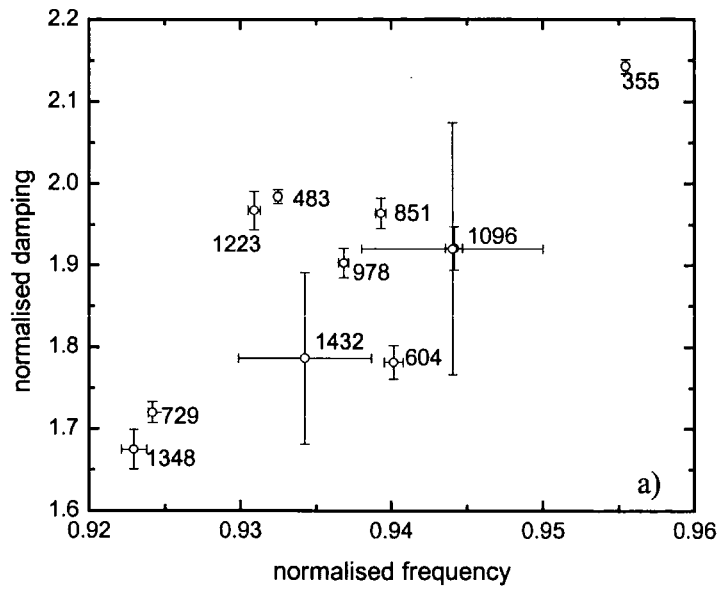

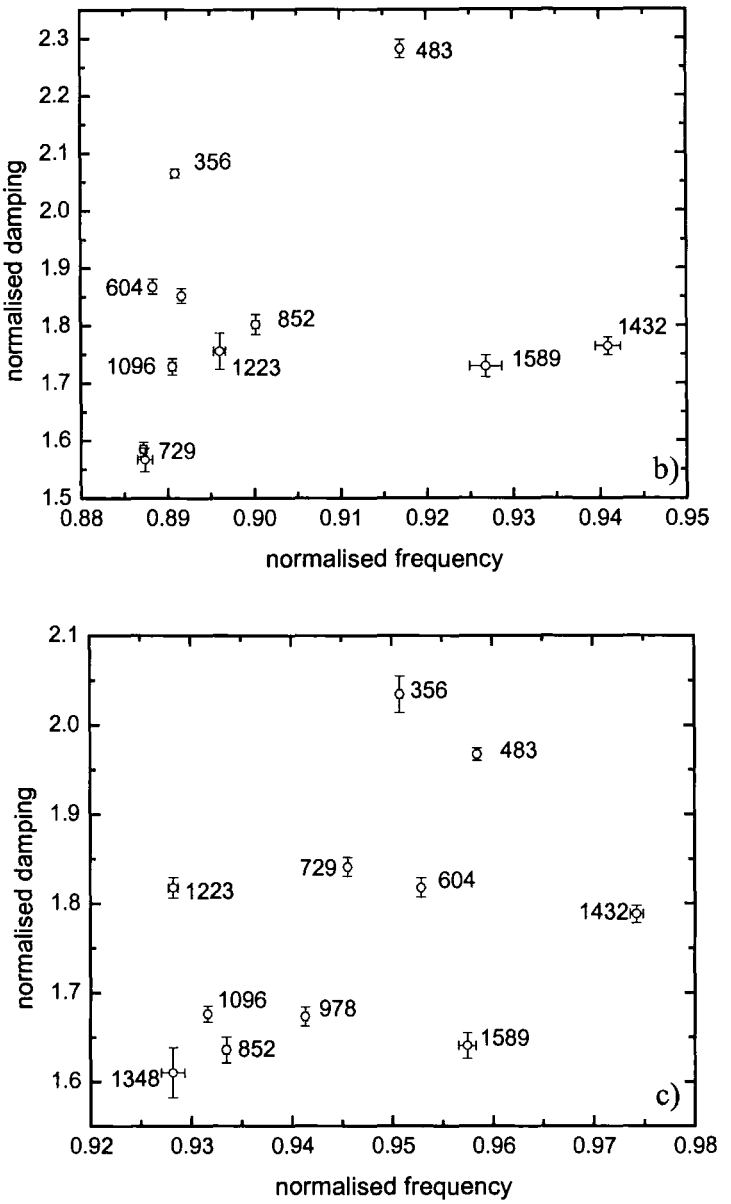

Figure 5.5.7: Normalised frequency and damping behaviour for a) 2kPEOF, b) 5k PEOF and c) 10k PEOF plotted in the complex plane. The numbers are the associated q values for each data point.

It is therefore concluded that the discontinuity observed in the q dependence of the damping (figure 5.5.2) was not attributed to mode mixing but certainly due to the presence of an adsorbed film at the air-water interface. Indeed due to cohesion between molecules in the adsorbed layer, extension of the film by a perturbing transverse capillary wave is resisted and the wave is damped. In all polymers, the damping behaviour at low q disagrees with the theoretical capillary dependence and the average scaling exponent predicts a weaker dependence on q than capillary mode but stronger than dilational mode.

These results reinforce the idea that the dispersion equation does not properly describe the system investigated here; i.e. there are processes other than transverse shear (capillary mode) and in-plane dilation (dilational mode) contributing to the surface motion and thus affecting capillary waves. The primary conclusion of this study of high frequency thermally excited capillary waves on the surface of solutions of PEOF is that there exists some process (or processes) which influences the damping behaviour but is not yet possible to state with any assurance what the underlying mechanism is in the present case as more theoretical effort is required to take account of all the processes that influence the thermally excited waves.

5-6 Conclusions

Surface quasi-elastic light scattering has been performed on three molecular weight fluorocarbon end-capped PEO to determine the dynamic behaviour of the air-solution interface. The damping and frequency of capillary waves have been extracted using a cosine fit and their dependence on time, bulk concentration and surface frequency evaluated. Three viscoelastic parameters have been determined using spectral fitting and examined as a function of bulk concentration and surface frequency.

Solution concentration studies revealed that the capillary and dilational modes were not influenced by the surface organisation of PEOF but dependent on solution or surface concentration and polymer molecular weight. The change in capillary wave frequency with concentration for all molecular weight was that anticipated from the relation between frequency and surface tension, i.e. $\omega_0^2 \propto \gamma$.

Damping dependence on molecular weight and solution concentration displayed a maximum identified as a point of resonance between dilational and capillary modes. The maximum damping occurred at higher bulk concentrations for the higher molecular weight polymer probably due to a delay in the rise of the dilational modulus with bulk concentration as the molecular weight increased. Consequently, given that to a first approximation the surface tension is constant, the concentration at which the dilational modulus reaches the appropriate characteristic value for maximum damping is therefore also delayed to higher bulk concentrations for the higher molecular weight PEOF. However, the maximum in damping did not coincide with any major changes in organisation of polymer in the surface excess layer determined from NR experiments but was dependent on both solution concentration and molecular weight. The behaviour of dynamic surface tension was found to be much higher than the static values suggesting that a transverse relaxation process takes place in the surface excess layer. The dilational modulus and solution concentration showed an increase with bulk concentration with a step increase observed at the resonance concentration. The dilational viscosity has also been found to be molecular weight and solution concentration dependent. The general trend was similar for all three polymers investigated and in general a drop in viscosity was observed at the resonance concentration whereas the dilational modulus increased. It was found that qualitatively, both dilational modulus and dilational viscosity displayed Kramers-Kronig-type characteristics. Negative dilational viscosities were observed for 2k

and 5k PEOF and were interpreted as effective parameters where energy is probably transferred from one of the other surface modes (splay or twist not accessible by light scattering). The viscoelastic parameters were examined for agreement with scaling relationships predicted by brush-like layer configuration for the polymer. Agreement between experimental behaviour and theoretical scaling relationships is only observed for the 2k PEOF polymer confirming the observations made by NR experiments regarding the formation of a brush like layer configuration at the air-water interface for the lowest molecular weight polymer.

Frequency dependence studies undertaken at the resonance concentration revealed intriguing behaviour. Whilst the capillary wave frequency followed the theoretical dependency with q for a capillary wave, a discontinuity was observed in the damping. This effect was not attributable to mode mixing but certainly due to the presence of other processes influencing the surface motion but unfortunately inaccessible by SQELS. For the dilational mode (modulus and viscosity), only qualitative agreement with unmodified PEO was found, indicating the influence of the fluorocarbon end group on the dilational behaviour of PEOF. The similarity of results for the different molecular weights showed the absence of any dependence of frequency and viscoelastic properties on molecular weight. Frequency dependent values of the dilational modulus could be fitted to a Maxwell fluid model and a relaxation time obtained. Unfortunately, the concentration dependence of this relaxation time was inaccessible due to negative dilational viscosities, the latter being considered as an effective parameter. Use of dilational parameters produces relaxation times of the same order for all polymers, which suggests that the same molecular process is involved in the relaxation process. It is interesting to point out that a Maxwell fluid model was also successful in describing the relaxation process of spread film of PEO[6] with a relaxation time = 8.7×10^{-6} s^{-1}. This value is fairly similar to the one obtained for PEOF suggesting that the relaxation process is mainly attributable to the PEO chains rather than the fluorocarbon end group.

5-7 References

1) Earnshaw, J.C.; McGivern, R.C. *J. Colloid Interface Sci.*, **1988**, 123, 36.
2) Earnshaw, J.C.; McGivern, R.C.; McLaughlin, A.C.; Winch, P.J. *Langmuir*, **1990**, 6, 650.
3) Buzza, D.M.A; Jones, J.L.; McLeish, T.C.B.; Richards, R.W. *J. Chem. Phys.*, **1998**, 109, 5008.
4) Lucassen-Reynders, E.H.; Lucassen, *J. Adv. Colloid Interface Sci.*, **1969**, 2, 347.
5) Richards, R.W.; Rochford, B.R.; Taylor, M.R. *Macromolecules*, **1996**, 29, 1980.
6) Richards, R.W.; Taylor, M.R. *J. Chem. Soc., Faraday Trans.*, **1996**, 92, 601.
7) Peace, S.K.; Richards, R.W. *Langmuir*, **1998**, 14, 667.
8) Milling, A.J.; Richards, R.W.; Hiorns, R.C.; Jones, R.G. *Macromolecules*, **2000**, 33, 2651
9) Miller, A.F. *Ph.D. Thesis*, **2000**, Durham University.
10) Milling, A.J.; Hutchings, L.R.; Richards, R.W. *Langmuir*, **2001**, 17, 5297.
11) Sauer, B.B.; Yu, H. *Macromolecules*, **1989**, 22, 786.
12) Kawaguchi, M.; Sauer, B.B.; Yu, H. *Macromolecules*, **1989**, 22, 1735.
13) Cao, B.H.; Kim, M.W.; Schaffer, H.; Cummings, H.Z. *J. Chem. Phys.*, **1991**, 95, 9317.
14) Richards, R.W.; Taylor M.R. *Macromolecules*, **1997**, 30, 3892.
15) Henderson, J.A.; Richards, R.W.; Penfold, J.; Thomas, R.K., Lu, J.R. *Macromolecules*, **1990**, 26, 4591.
16) Crowford, G.E.; Earnshaw, J.C. *Biophys. J.*, **1987**, 52, 87.
17) Earnshaw, J.C.; McGivern, R.C.; Winch, P.J. *J. Phys.*, **1988**, 49, 1271.
18) Earnshaw, J.C.; Sharpe, D.J. *J. Chem. Soc., Faraday Trans.*, **1996**, 92, 611.
19) Pippard, A.B. *The Physics of Vibration*, **1989**, Cambridge University Press, Cambridge, UK.

20) Pippard, A.B. *Response and Stability*, Cambridge University Press, **1988**, Cambridge, UK.

21) Brown, A.S.; Richards, R.W.; Buzza, D.M.A.; McLeish, T.C.B. *Faraday Discuss.*, **1999**, 112, 1.

22) Earnshaw, J.C.; McCoo, E. *Langmuir*, **1995**, 11, 1087.

23) Ferry, J.D. *Viscoelastic Properties of Polymers 3rd ed.*, **1980**, John Wiley and Sons: New York.

24) Earnshaw, J.C.; McLaughlin, A.C. *Proc. R. Soc. Lond. A*, **1993**, 440, 519.

25) Booth, C.; Richards, R.W.; Taylor, M.R.; Yu, G.E. *J. Phys. Chem. B*, **1998**, 102, 209.

26) Van den Tempel, M.; Lucassen-Reynders, E.H. *Adv. Colloid Interface Sci.*, **1983**, 18, 281.

27) Hennenberg, M.; Chu, X.L.; Sanfeld, A.; Velarde, M.G. *J. Colloid Interface Sci.*, **1992**, 150, 7.

28) Earnshaw, J.C.; McLaughlin, A.C. *Proc. R. Soc. Lond. A*, **1993**, 440, 519.

29) Earnshaw, J.C.; McLaughlin, A.C. *Proc. R. Soc. Lond. A*, **1991**, 433, 663.

Chapter Six

Conclusions and Further Works

6-1 Conclusions

The surface organisation and surface wave dynamics of a series of surface adsorbed solutions of fluorocarbon end-capped PEO (PEOF) at the air-water interface have been investigated. There were three main aspects to this work. Initially a series of fluorocarbon end-capped PEO were synthesised. They were subsequently dissolved in water forming surface excess layers at the air-water interface and their surface tensions were recorded and analysed. Neutron reflectometry was applied to determine the surface organisation of PEOF as a function of bulk concentration and molecular weight. Finally, surface quasi-elastic light scattering experiments were undertaken to investigate the influence of adsorbed layers on the long wavelength dynamics and viscoelasticity of the air-solution interface.

A series of novel polymeric surfactants have been prepared by combining anionic polymerisation and an end-capping reaction via isophorone diisocyanate. By using anionic polymerisation, control over the molecular weight distribution and polydispersity was achieved. Three molecular weight PEOs varying from 2 000, 5 000 and 10 000 g mol^{-1} were successfully synthesised; for each molecular weight a hydrogenous and a deuterated version was prepared. The end-capping reaction was first attempted using perfluorodecanoyl chloride acid and seemed successful. However, after diluting the sample in water and subsequent recovery, ^{19}F NMR showed that the fluorocarbon group had been removed implying that hydrolysis occurred. In an attempt to increase the strength of the chemical bond between the PEO chains and the fluorocarbon end group, isophorone diisocyanate was used. This method was successful.

Surface tension measurements as a function of bulk concentration for all three molecular weight polymers were made and a dependence of surface tension on both molecular weight and bulk concentration was evident, the adsorption characteristics being much enhanced by the fluorocarbon group at one end.

The interfacial organisation of each PEOF polymer was investigated using neutron reflectometry. Indeed, when polymer chains are grafted by one end, a brush-like layer configuration is expected. Hence PEO chains with one end capped by perfluorodecanoyl groups were conjectured to form a brush-like structure at the

air/water interface. Two methods were adopted to analyse the data collected, the optical matrix and the kinematic approximation methods, both of which are model dependent. The optical matrix analysis predicted a two-layer organisation at the air-water interface for all three molecular weight polymers with an increase in solution concentration. Optical matrix analysis revealed that accurate segmental concentration profiles can be obtained provided the models adopted are carefully selected and all data sets are rigorously analysed. The kinematic approximation agreed with the results obtained from optical matrix analysis and more details regarding the polymer distribution and water distributions as well as the separation between them were available. Both analyses predicted a two layer organisation at the air-water interface and that the surface organisation was molecular weight and solution concentration dependent. The upper layer was made of PEO chains anchored at the surface by the fluorocarbon group. To determine the extent of stretching of the PEO chains, the layer thickness was compared to their respective radius of gyration and analysed as a function of grafting density to compare with theoretical predictions for brush configuration (scaling theory). Only the lowest molecular weight polymer seemed to formed a brush-like configuration at the air-water interface as the layer thicknesses returned for higher molecular weight polymers were not compatible with brush configuration. However, higher scaling exponents were returned. The lower layer was further examined by dynamic light scattering and small-angle neutron scattering to check for micelle formation. Only the lower molecular weight polymer seemed to generate micelles with a well-defined morphology whereas higher molecular weight PEOFs seemed to adopt a random coil conformation. From self-partial and cross-partial structure factors analyses, the PEOF chains are totally immersed into the subphase at high bulk concentrations with the fluorocarbon group attached at the air-water interface.

The next logical step for neutron reflectometry is to attempt to address the distribution of the fluorocarbon group within the subphase. Indeed, unusual self-partial structure factors of water were returned using the kinematic approximation, indicating the influence of the fluorocarbon group on the distribution. An attempt to determine the distribution of the fluorocarbon end group was undertaken (Chapter Four, equation 4.3.2.13). Unfortunately, the experimental contrasts used seemed inadequate as unrealistic partial structure factors were returned. It would therefore be interesting to determine new experimental contrasts in order to identify the exact

distribution of the fluorocarbon group within the water layer. Contrasts such as a mixture of D_2O and H_2O in order to match the PEO scattering length density could be investigated to obtain reflectivity from the fluorocarbon end group only.

Following the determination of the organisation of the polymer at the air-water interface, attention was then focussed on the wavelength dynamics of each PEOF adsorbed surface excess using surface quasi-elastic light scattering. Both frequency and damping of capillary waves were examined as a function of time, bulk concentration and surface frequency. Time dependent studies revealed that both frequency and damping of capillary waves were time independent suggesting that PEOF formed homogeneous and stable layers when adsorbed at the air-water interface. Bulk concentration studies revealed a dependence of both frequency and damping on molecular weight and bulk concentration. A maximum in damping was evident for all three molecular weight PEOF indicating resonance between capillary and dilational modes. This resonance concentration was shifted to higher bulk concentration for higher molecular weight polymers. However, the maximum in the damping coincided with no major change in organisation of polymer in the surface excess layer determined by NR. From spectral fitting, three viscoelastic parameters were extracted and studied as a function of bulk concentration and surface frequency. The variation of the dilational modulus and the associated viscosity displayed Kramers-Kronig type behaviour, which was attributed to changes within mechanical properties of the adsorbed film as it was compressed. Negative dilational viscosities were reported and have been interpreted as effective parameters and possibly arise from the exchange of energy from one of the other surface modes not accessible by light scattering. The three-viscoelastic parameters exhibited solution concentration and molecular weight dependence. The results obtained from frequency studies revealed a lack of dependence of behaviour for the frequency and viscoelastic properties on molecular weight while the damping dependence on molecular weight could be argued. Frequency dependent values of the dilational modulus could be fitted to a Maxwell fluid model and a relaxation time obtained. Unfortunately, the concentration dependence of this relaxation time was inaccessible due to negative dilational viscosities.

The next logical step for SQELS is to attempt to address the ambiguity of negative dilational viscosities as it implies that the dispersion equation used to describe the polymers at the air-water interface is inadequate and would therefore

benefit from further development. Improving our understanding of the wavelength dynamic of polymers at the air-water interface would be beneficial and could therefore be extended to liquid-liquid interfaces, where most of industrial applications take place. There is also the interesting question as to whether spread PEOF films will have the same surface organisation and dynamics at the air-water interface when compared to adsorbed solutions of PEOF.

It would also be of great interest to modify the length of the fluorocarbon end group with fixed molecular weight to check the influence of the end-capping group on PEO surface organisation and wavelength dynamics at the air-water interface.

Appendices

APPENDIX 1

c (g ml^{-1})	Layer	$d \pm 2$ (Å)	$\rho \pm 0.02$ (10^{-6} Å^{-2})	Interfacial roughness (Å)	$\phi_{PEO(F)}$	ϕ_w	$n_{EO} \times 10^{-4}$ (Å^{-3})	$\Gamma_T \pm 0.03$ (mg m^{-2})	$\Gamma_{upper} \pm 0.05$ (mg m^{-2})
1.E-02	1	45	2.18	4	0.45	0.55	0.55	2.26	1.76
	2	41	0.72	14	0.14	0.86	0.17		
5.E-03	1	47	2.27	7	0.47	0.53	0.57	2.45	1.91
	2	41	1.19	15	0.23	0.77	0.29		
1.E-03	1	45	2.55	6	0.52	0.48	0.64	2.46	2.05
	2	41	0.59	10	0.12	0.88	0.14		
5.E-04	1	43	2.58	7	0.53	0.47	0.65	2.50	1.99
	2	40	0.74	9	0.15	0.85	0.18		
1.E-04	1	43	2.44	8	0.50	0.50	0.61	2.37	1.87
	2	39	0.73	10	0.14	0.86	0.18		
5.E-05	1	43	2.39	6	0.49	0.51	0.60	2.59	1.84
	2	38	1.16	9	0.23	0.77	0.28		
1.E-05	1	42	2.43	4	0.50	0.50	0.71	2.39	1.92
	2	37	0.42	11	0.10	0.90	0.10		
5.E-06	1	40	2.30	5	0.47	0.53	0.58	1.98	1.65
	2	36	0.54	10	0.11	0.89	0.13		
1.E-06	1	43	2.10	6	0.43	0.57	0.53	2.16	1.62
	2	40	0.80	10	0.16	0.84	0.19		
5.E-07	1	46	2.01	5	0.41	0.59	0.51	1.67	1.67
1.E-07	1	35	1.56	5	0.32	0.68	0.39	0.97	0.97

Table A.1: Layer thickness, scattering length density, interfacial roughness, volume fraction, number density and surface excess of the individual components from double uniform layers for 5k PEOF.

APPENDIX 2

c (g ml^{-1})	Layer	$d \pm 2$ (Å)	$\rho \pm 0.02$ (10^{-6} Å^{-2})	Interfacial roughness (Å)	$\phi_{PEO(F)}$	ϕ_w	$n_{EO} \times 10^{-4}$ (Å^{-3})	$\Gamma_T \pm 0.03$ (mg m^{-2})	$\Gamma_{upper} \pm 0.05$ (mg m^{-2})
1.E-02	1	36	1.54	5	0.29	0.71	0.20	1.66	1.14
	2	39	0.75	20	0.14	0.86	0.084		
1.E-03	1	37	1.81	8	0.34	0.66	0.19	1.67	1.12
	2	40	0.77	30	0.14	0.86	0.087		
1.E-04	1	32	1.74	2	0.33	0.67	0.20	1.64	1.02
	2	39	0.91	20	0.17	0.83	0.10		
5.E-05	1	32	1.68	5	0.32	0.68	0.19	1.54	0.97
	2	43	0.75	20	0.14	0.86	0.084		
1.E-05	1	33	1.76	5	0.33	0.67	0.18	1.68	0.94
	2	42	0.99	30	0.18	0.82	0.11		
5.E-06	1	32	1.62	3	0.31	0.69	0.19	1.52	0.97
	2	45	0.69	25	0.13	0.87	0.078		
1.E-06	1	27	1.92	5	0.36	0.64	0.22	1.73	0.94
	2	41	1.05	35	0.19	0.81	0.12		
1.E-07	1	25	1.75	5	0.33	0.67	0.20	1.39	0.89
	2	42	0.80	30	0.15	0.85	0.090		

Table A.2: Layer thickness, scattering length density, interfacial roughness, volume fraction, number density and surface excess of the individual components from double uniform layers for 10k PEOF.

APPENDIX 3

Concentration (g ml^{-1})	n_m (Å^{-2})	a_m (Å^2)	D (Å)
1.E-02	2.48E-03	404.04	20.10
5.E-03	2.68E-03	373.27	19.32
1.E-03	2.88E-03	347.22	18.63
5.E-04	2.80E-03	357.78	18.92
1.E-04	2.62E-03	381.24	19.53
5.E-05	2.58E-03	387.60	19.69
1.E-05	2.98E-03	335.35	18.31
5.E-06	2.32E-03	431.03	20.76
1.E-06	2.28E-03	438.79	20.95
5.E-07	2.35E-03	426.26	20.65
1.E-07	1.37E-03	732.60	27.07

Table A.3.a: Number of molecules per unit area, area per molecule and distance between molecules for 5k PEOF.

Concentration (g ml^{-1})	n_m (Å^{-2})	a_m (Å^2)	D (Å)
1.E-02	7.20E-04	1388.89	37.27
1.E-03	7.03E-04	1422.48	37.72
1.E-04	6.40E-04	1562.50	39.53
5.E-05	6.08E-04	1644.74	40.56
1.E-05	5.94E-04	1683.50	41.03
5.E-06	6.08E-04	1644.74	40.56
1.E-06	5.94E-04	1683.50	41.03
1.E-07	5.00E-04	2000.00	44.72

Table A.3.b: Number of molecules per unit area, area per molecule and distance between molecules for 10k PEOF.

APPENDIX 4

c (g ml^{-1})	$d \pm 2$ (Å)	$n_i \pm 3\times10^{-6}$ (Å^{-3})	$\Gamma \pm 0.1$ (mg m^{-2})
1.00E-02	σ 50	n_1 6.00E-05	2.72
	τ 47	n_2 2.00E-05	
5.00E-03	σ 50	n_1 6.00E-05	2.72
	τ 48	n_2 2.00E-05	
1.00E-03	σ 49	n_1 6.00E-05	2.71
	τ 47	n_2 2.00E-05	
5.00E-04	σ 49	n_1 6.00E-05	2.75
	τ 48	n_2 2.00E-05	
1.00E-04	σ 47	n_1 6.00E-05	2.63
	τ 44	n_2 2.00E-05	
5.00E-05	σ 45	n_1 6.00E-05	2.58
	τ 44	n_2 2.00E-05	
1.00E-05	σ 45	n_1 6.00E-05	2.58
	τ 46	n_2 1.00E-05	
5.00E-06	σ 41	n_1 5.00E-05	1.72
	τ 40	n_2 1.00E-05	
5.00E-07	σ 43	n_1 5.00E-05	1.71
1.00E-07	σ 33	n_1 4.00E-05	1.05

Table A.4: Number densities (n_1 and n_2) of polymer molecules at the maximum of each Gaussian peak and widths (σ and τ) at half height of Gaussian distributions and total surface excess, Γ, for 5k DPEOF with bulk concentration.

APPENDIX 5

c (g ml^{-1})	$d \pm 2$ (Å)	$n_i \pm 3\times10^{-6}$ (Å^{-3})	$\Gamma \pm 0.1$ (mg m^{-2})
1.00E-02	σ 36	n_1 2.00E-05	1.91
	τ 39	n_2 5.20E-06	
1.00E-03	σ 35	n_1 2.00E-05	1.92
	τ 37	n_2 5.10E-06	
1.00E-04	σ 32	n_1 2.00E-05	1.93
	τ 37	n_2 5.20E-06	
5.00E-05	σ 30	n_1 2.00E-05	1.93
	τ 40	n_2 5.22E-06	
1.00E-05	σ 33	n_1 2.00E-05	1.95
	τ 49	n_2 6.49 E-06	
5.00E-06	σ 32	n_1 2.00E-05	1.88
	τ 49	n_2 6.17E-06	
1.00E-06	σ 31	n_1 2.00E-05	1.89
	τ 50	n_2 6.34E-06	
1.00E-07	σ 27	n_1 2.00E-05	1.64
	τ 44	n_2 5.69E-06	

Table A.5: Number densities (n_1 and n_2) of polymer molecules at the maximum of each Gaussian peak and widths (σ and τ) at half height of Gaussian distributions and total surface excess, Γ, for 10k DPEOF with bulk concentration.

APPENDIX 6

c (g ml^{-1})	$ds_i \pm 2$ (Å)		$ns_i \pm 3\times10^{-4}$ (Å^{-3})	
1.00E-02	ds_1	29	ns_1	4.90E-03
	ds_2	52	ns_2	2.00E-02
5.00E-03	ds_1	30	ns_1	5.10E-03
	ds_2	67	ns_2	2.00E-02
1.00E-03	ds_1	30	ns_1	5.10E-03
	ds_2	64	ns_2	2.10E-02
5.00E-04	ds_1	29	ns_1	5.10E-03
	ds_2	63	ns_2	2.21E-02
1.00E-04	ds_1	27	ns_1	5.00E-03
	ds_2	55	ns_2	2.07E-02
5.00E-05	ds_1	28	ns_1	4.50E-03
	ds_2	56	ns_2	2.20E-02
1.00E-05	ds_1	26	ns_1	4.10E-03
	ds_2	58	ns_2	2.50E-02
5.00E-06	ds_1	23	ns_1	4.50E-03
	ds_2	52	ns_2	2.40E-02
5.00E-07	ds_1	32	ns_1	4.00E-03
	ds_2	67	ns_2	2.50E-02
1.00E-07	ds_1	25	ns_1	3.00E-03
	ds_2	61	ns_2	2.60E-02

Table A.6: Number densities (ns_1 and ns_2) of water molecules with appropriate thickness (ds_i) obtained by double uniform layer fit for 5k HPEOF with bulk concentration.

APPENDIX 7

c (g ml^{-1})	$ds_i \pm 2$ (Å)	$ns_i \pm 2\times10^{-4}$ (Å^{-3})
1.00E-02	ds_1 31	ns_1 3.30E-03
	ds_2 39	ns_2 1.00E-02
1.00E-03	ds_1 35	ns_1 3.20E-03
	ds_2 39	ns_2 1.00E-02
1.00E-04	ds_1 40	ns_1 3.00E-03
	ds_2 44	ns_2 1.00E-02
5.00E-05	ds_1 36	ns_1 3.00E-03
	ds_2 40	ns_2 8.50E-03
1.00E-05	ds_1 31	ns_1 3.20E-03
	ds_2 39	ns_2 8.40E-03
5.00E-06	ds_1 31	ns_1 3.00E-03
	ds_2 41	ns_2 6.80E-03
1.00E-06	ds_1 32	ns_1 2.90E-03
	ds_2 42	ns_2 4.60E-03
1.00E-07	ds_1 33	ns_1 2.80E-03
	ds_2 42	ns_2 4.70E-03

Table A.7: Number densities (ns_1 and ns_2) of water molecules with appropriate thickness (ds_i) obtained by double uniform layer fit for 10k HPEOF with bulk concentration.

APPENDIX 8

c (g ml^{-1})	δ ± 0.5 (Å)
1.E-02	36
5.E-03	35
1.E-03	33
5.E-04	30
1.E-04	30
5.E-05	35
1.E-05	30
5.E-06	27
1.E-06	23
5.E-07	21
1.E-07	10

Table A.8.a: δ values obtained from kinematic approximation for 5k PEOF with bulk concentration.

c (g ml^{-1})	δ ± 0.5 (Å)
1.E-02	50
1.E-03	52
1.E-04	52
5.E-05	50
1.E-05	40
5.E-06	41
1.E-06	34
1.E-07	35

Table A.8.b: δ values obtained from kinematic approximation for 10k PEOF with bulk concentration.